Facoltà di Scienze Matematiche, Fisiche e Naturali
Dottorato di Ricerca in Scienze Chimiche
XXXI Ciclo

Glass Ceramics for High-Temperature Sealing Applications: Synthesis and Physicochemical Properties of Modified CaO-MgO-Al_2O_3-SiO_2 Materials, with a view to recycling of industrial waste

PhD Candidate:

Giulia Simonetti

Supervisor:

Dott. Andrea Ciccioli

Abstract

Solid Oxide Fuel cells (SOFC) and dense gas separation membranes based on mixed ionic and electronic conductors have gained increased interest the resent years due the search for new technologies for clean energy generation. These technologies can be utilized to produce electricity from fossil fuel with low CO_2 emission compared to conventional gas or coal based energy plants. One crucial challenge with SOFCs is the sealing of the active membranes/electrolytes to prevent leakage of air to fuel side or vice versa. Due to the high operating temperatures of typical 600-1000°C the selection of reliable sealing materials is limited. The seals have to remain gas tight during the life time of the reactor/SOFC, they need to be chemical compatible with the sealed materials and stable in reducing and oxidizing atmospheres containing water vapor and CO2, and finally they should be cheap, readily available and easy to process. The main purpose of the present work was to evaluate rigid bonded glass ceramic seals for dense oxygen ion and proton conducting membranes and electrolytes for SOFCs. First, a review of sealing technologies has been carried out with emphasis on SOFC and ceramic membranes technologies applicable for zero emission power plants. Regarding sealing, the best and cheapest materials at the present time are based on silicate glass and glass ceramics.

The aim is to provide a systematic study of the properties of glasses and glass-ceramics as a function of the glass composition in the CaO-MgO-Al_2O_3-SiO_2 system, which represent the most advanced sealing technology for high-temperature Solid Oxide Fuel Cells (SOFC).

Two glass systems have been evaluated, aluminosilicate and boroaluminosilicate and their variants obtained adding five different oxides acting as nucleating agents, like TiO_2, MnO_2, ZnO and SnO_2. Fabrication and characterization of the glasses are reported with special focus on the thermal and thermochanical properties, glass forming ability, kinetic crystallization and phase evaluation. The influence of different additives in glass and glass ceramic properties has been analyze in depth.
In the last section, the research has been extended to the recycling of aluminosilicate basted waste to characterize a new type of glass ceramic derived from industrial waste, like Kaolin clay waste.

Table of contents

List of abbreviations

SOFC	Solid Oxide Fuel Cell
AFC	Alkaline Fuel Cell
PEMFC	Proton Exanche Membrane Fuel Cell
DMFC	Direct Methanol Fuel Cell
DEFC	Direct Ethanol Fuel Cell
PAFC	Phosphoric Acid Fuel Cell
MCFC	Molten Carbonate Fuel Cell
MEA	Membrane Electrode Assembly
PEN	Positive electrode – Electrolyte – Negative electrode
TSOFC	Tubular Solid Oxide Fuel Cell
APU	Auxiliary Power Units
YSZ	Yittrum stabilized- Zirconia
CGO	Ceria stabilized- Gadilinum
LSM	$La_{1-x}Sr_xMnO_3$
LSCF	$La_{1-x}Sr_xCo_{1-y}Fe_yO_3$
LC	$LaCoO_3$
LCCF	Lanthanum Calcium Cobaltite Ferrite
SSC	Samarium Strontium Cobaltite
PVB	Polyvinyl Butyral
CTE, α	Coefficient of thermal expansion
T_g	Glass transition temperature
T_m	Melting temperature
T_O	Temperature of crystallization onset
T_S	Temperature of sintering
T_C	Temperature of crystallization
T_{FS}	Temperature of first shrinkage
T_{MS}	Temperature of maximum shrinkage
T_{HB}	Temperature of half ball
T_N	Temperature of nucleation
T_D	Dilatometric softening temperature
T_{CG}	Maximum temperature of exothermic peak for samples nucleated
NBO	Non-Bridging Oxygens
BO	Bridging Oxygens
F	Field strength of ions
z	Valence of ions
r	Ionic radius
E_a	Activation Energy for Crystallization
E_b	Water absorption coefficient
p	Porosity percent
V	External volume
V_o	Volume of closed pores
V_1	Volume of open pores
T	Apparent density in the fraction of sample with less easily refillable porosities
K_T	Stability of glass by Turnbull
K_1	Stability of glass
K_2	Stability of glass
K_W	Stability of glass by Weinberg
K_H	Stability of glass by Hruby
K_3	Stability of glass by Saad and Poulain

η	Viscosity of materials
x	Crystallization fraction
k_o	Frequency factor
n	Avrami exponent
m	Numerical factor of crystallization mechanism
β	Heating rate
BAS	Boroaluminiosilicate
CMAS	Calcium Magnesium Aluminosilicate
CMASTi	Calcium Magnesium Aluminosilicate modified by Titanium
CMASMn	Calcium Magnesium Aluminosilicate modified by Manganese
CMASZn	Calcium Magnesium Aluminosilicate modified by Zinc
CMASSn	Calcium Magnesium Aluminosilicate modified by Tin
CMASB	Calcium Magnesium Boroaluminiosilicate
CMASBTi	Calcium Magnesium Boroaluminiosilicate modified by Titanium
CMASBMn	Calcium Magnesium Boroaluminiosilicate modified by Manganese
CMASBZn	Calcium Magnesium Boroaluminiosilicate modified by Zinc
CMASBSn	Calcium Magnesium Boroaluminiosilicate modified by Tin
CMASX	Calcium Magnesium Aluminosilicate with X is nucleating oxide
XRF	X-Ray Fluorescence
ICP-OES	Inductively Coupled Plasma- Optical Emission Spectroscopy
HSM	Hot Stage Microscope
DTA	Differential Thermal Analyses
DSC	Differential Scanning Calorimetry
XRD	X-ray diffraction
SEM	Scanning Electron Microscopy
EDX	Energy Dispersive X-Ray Analysis
SE	Secondary Electrons
BSE	Backscattered Electrons
CER	European Waste Catalogue

List of tables

List of figures

Introduction and objective

Over the last decades public awareness has been raised on the pressing need to reduce greenhouse gas emission. One of the most significant greenhouse gases, carbon dioxide, is released to the atmosphere by burning fossil fuels. CO_2 emissions could be significantly reduced by increasing the efficiency of energy conversion system. In central power plants, the overall efficiency could be increased by combining several complementary engines: combined cycle thermal power plants with gas turbines or steam turbines fed by exhaust gases were demonstrated in different places with efficiencies up to 58%[1]. In decentralized energy conversion systems, both electrical and thermal energies can be utilized in cogeneration systems, providing higher overall efficiencies. In comparison with conventional thermal engines, where fossil fuels are burned to produce electric energy after several conversion steps, fuel cells present the advantage to convert the chemical energy directly to electricity. Solid Oxide Fuel Cells (SOFC) are a class of fuel cells working at high temperatures of 700°C to 1000°C, thereby providing high electrical efficiencies of about 60 to 65%, with the possibility to use various fuel gases. Since a single cell unit usually generates a relatively small voltage, in order to achieve higher voltage output individual cells are connected together in series to form a stack. But significant limitations to the broad utilization of SOFC-based system are their high investment costs as well as their insufficient long-term stability. Besides the loss of performances of the cell under prolonged utilization, the gas tightness and electrical insulation of the sealing system represent critical point of fuel cell stack technologies. Seal and sealing processes are an important part of the construction process for complex devices as SOFCs. More generally, seals are probably the most challenging components for high temperature applications. Examples include sealing SiC/SiC parts in thermonuclear fusion reactors, separation membrane reactors, and planar solid oxide fuel cell (SOFC) stacks.

In SOFCs, sealing parts should fulfill stringent requirements regarding their compatibility with other cell and interconnect materials, their chemical stability at high temperature under dual atmospheres (oxidizing atmosphere on the cathode side, humidified reducing atmosphere on the anode side) and long-term constancy of their physical properties. Indeed, in planar SOFCs, fuel gas and air must be kept separate from each other to prevent a decrease in the efficiency of the production of electrical energy as well as direct combustion and local overheating of the components. Therefore, gas-tight sealing is essential along the edges of the electrodes, electrolyte and interconnects as well as between individual cells to bond the cell stacks, preventing the gases from mixing in the anode or the cathode, and providing electrical insulation to avoid shunting.

Several physical and chemical properties should be fulfilled simultaneously for a sealing material to allow proper SOFC operation. The most important are high temperature stability (between 750°C-900°C), electrical insulation (> $2 k\Omega \cdot cm^2$), gas tightness, sufficient adaptation of the coefficient of thermal expansion (CTE) to the other components of the SOFC (CTE of anode substrate $\sim 12 \cdot 10^{-6}\ K^{-1}$), good adhesion to steel and the

electrolyte, chemical stability in oxidizing and (humid) reducing atmospheres, plasticity at the joining temperature ($\eta \sim 10^6$-10^8 Pa·s) and sufficient mechanical strength to withstand thermal stresses.

A great number of materials and approaches have been investigated as sealants for planar-type SOFC stacks, such as glass sealants, glass-ceramic sealants, glass-ceramic composite sealants and cement sealants. The best of these approaches succeed in sealing the cells with acceptable leakage rates. Today, glasses and glass-ceramics are widely used as sealing materials for several joining partners (glass, ceramic and metal) because they easily form hermetic seals in useful shapes. They provide electrical insulation and are also chemically stable under corrosive or oxidizing environments. Nevertheless, some problems appear with these seals during long-term operation, due to corrosion effects or cracking associated with multiple thermal cycles. Currently, the strength of the glass-ceramic sealants is considered a very important feature and for this reason over the last decade, have developed and improved glass-ceramics sealants to fulfill the requirements of planar SOFC stacks.

The main purpose of the present work is to evaluate rigid bonded glass ceramic seals for planar SOFCs. Our research aims to perform a systematic study of the properties of glasses and their counterparts glass ceramic in a particular glass-forming oxide system, the SiO_2-Al_2O_3-CaO-MgO quaternary system, as a function of the chemical composition. First, a review of sealing technologies has carried out with the aim to illustrate the requirements that a material must satisfy to be suitable for use as a sealant in the construction of the stack. Regarding sealing, the best performing and cheapest materials at the present time are based on silicate glass and glass ceramic. In this thesis, various aluminosilicate and boroaluminosilicate glass-ceramics with different nucleating agents have been examined as candidate for sealing materials. The main reason for studying aluminosilicate system is that this kind of materials are used in the ceramic industry for producing different types of manufactured goods, such as dishes, vessel, but also sanitary ware for example washbasins, sinks and water closets. The coarse fraction that remains after refining process is normally reburied as a waste product. In the last few years, in fact, numerous silicate based wastes, such as coal combustion ash, slag from steel production, fly ash and filter dusts from waste incinerators, mud from metal hydrometallurgy, different types of sludge as well as glass cullet or mixtures of them have been considered for the production of glass ceramics. The basic idea is to use wastes from ceramic industry as a starting material for glass ceramic seal production.

Chapter 1

Solid Oxide Fuel Cells (SOFC) and sealing concept

1.1 State of art of sealants for high-temperature applications

Sealants for high temperature applications have been developed with a focus on electrochemical devices such as SOFCs and high-temperature separation membrane reactors for oxygen separation and purification. In both cases, the sealant is responsible for gas tightness and electrical insulation. Oxygen ionic or proton-conducting ceramic membranes are technologically important in high temperature gas separation and membrane reactor processes. In practical applications, the operating temperatures are typically between 600°C and 1000°C. The joining of machined SiC/SiC composites for thermonuclear fusion reactor is another interesting application, demanding sealants capable of withstanding high temperatures. Choosing the sealing materials for high temperature applications can be very challenging because several requirements need to be respected in order to achieve a successful combination. These include good thermal and chemical compatibility, good wettability, specific viscosity, matching CTEs and an adequate bonding with the other metal or ceramic components. The high operating temperatures (650°C-1000°C) considerably limit the variety of sealing options, i.e. practically no organic or polymer seal can be employed. In Fig. 1.1.1 an overview of conventional high temperature seals is presented.

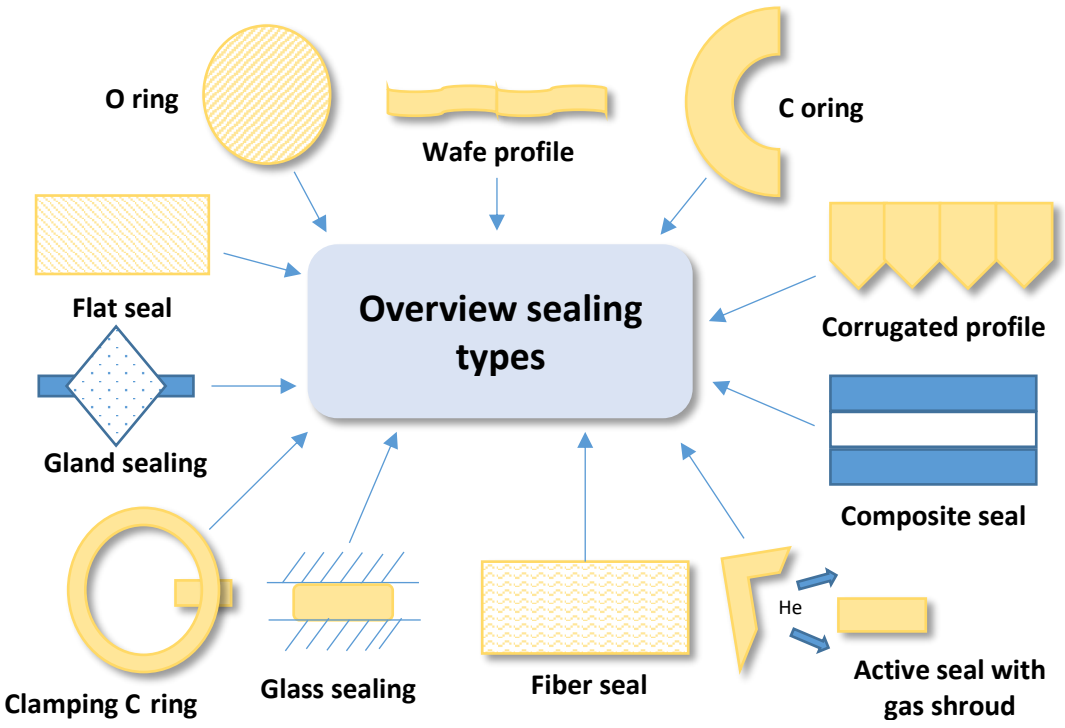

Figure 1.1.1 Overview of current sealing types for high temperature applications.

Inorganic materials with high melting points can be used to seal the ceramic membranes at high temperatures above 600°C. Noble ductile metals, for example silver and gold, pure glass or ceramic are among the possible materials that can be used as high temperature seals, nevertheless, none of them meet all of the desired parameters. Metal seals for instance usually have higher CTEs than the joining partners, and pure glass seals can easily react with the joining surfaces provoking failure at the interfaces. Glass-ceramic seals perform better than pure metal, glass or ceramic seal because the properties of the composite seal can be tailored to match those of the joining partner materials.

1.2 Fuel cells

Fuel cells are electrochemical devices for direct conversion of chemical energy into electrical power. Different types of fuel cells were developed that follow the same basic principles and share generic component. They are composed of an oxygen electrode (cathode), an ionic conducting electrolyte and a fuel gas electrode (anode). Either on the cathode or on the anode side, gas is transported to the electrolyte where is adsorbed, dissociated and ionized. The driving force for ionic diffusion across the electrolyte is the partial pressure difference between cathodic and anodic atmospheres.

Different categories of fuel cells are defined by the employed electrolyte. The electrolyte determines the domain of operating temperatures, the choice of materials for components, conception design, possible fuel gases, efficiency and potential fields of application. Different categories are represented in Table 1.2.1., with their operating temperatures, oxidant and fuel gases, diffusing species, electrolyte and possible applications.

	Alkaline Fuel Cell (AFC)	Proton-Exchange Membrane Fuel Cell (PEMFC)	Direct Methanol/Ethanol Fuel Cell (DMFC/DEFC)	Phosphoric Acid Fuel Cell (PAFC)	Molten Carbonate Fuel Cell (MCFC)	SOLID OXIDE FUEL CELL (SOFC)
Operating temperature	60-80°C	70-90°C	70-90°C	150-200°C	600-650°C	650-1000°C
OXIDANT	O_2	AIR / O_2	AIR	AIR	AIR / CO_2	AIR
IONIC CONDUCTION	OH-	H^+	H^+	H^+	CO_3^{2-}	O^{2-}
FUEL	H_2	H_2	CH_3OH / CH_3CH_2OH	H_2 ref. CH_4	H_2 / CH_4 / CO	H_2 / CH_4 / CO
ELECTROLYTE	POROUS MATRIX SATURED IN AN ACQUEOUS ALKALINE SOLUTION OF 35-50% KOH	POLYMER MEMBRANE (the membrane is covered with a catalyst layer of Pt or Pt/Ru)	POLYMER MEMBRANE (the membrane is covered with a catalyst layer of Pt or Pt/Ru)	CONCENTRATED PHOSPHORIC ACID	ELECTROLYTE COMPOSED A MOLTEN CARBONATE SALT MIXTURE (Li_2CO_3, K_2CO_3 OR Na_2CO_3) SUSPENDED IN A POROUS CERAMIC MATRIX OF BETA ALUMINA	DENSE, GAS-TIGHT OXIDE CERAMIC ELECTROLYTE, TYPICALLY YTTRIA STABILIZED ZIRCONIA (YSZ)
CATHODE ANODE	CARBON, NiO/Ni or POLYMER DOTED WITH A NOBLE METAL CATALYST	GRAPHITE	GRAPHITE	THE ELECTRODES ARE MADE OF CARBON PAPER BONDED WITH A POLYMER (PTFE), COATED WITH A FINELY DISPERSED PLATINUM CATALYST	- CATHODE: Ag_2O or LITHIUM-COATED NiO - ANODE: Ni with 10 wt.% Cr	- CATHODE: PEROVSKITE CERAMIC - ANODE: CERMET OF Ni-YSZ
MAX. ELECTRICAL EFFICIENCY	63%	40-55%	35%	40%	55%	65%
POWER OUTPUT	10-100 kW	1-250 kW	1-100 W	UP TO 1 MW	UP TO 100 MW	UP TO 100 MW
APPLICATION	AREOSPACE	- AEROSPACE - AUTOMOTIVE INDUSTRY	THEY ARE ILL-SUITED FOR POWER APPLICATION BUT IDEAL FOR CONSUMER GOODS SUCH AS BATTERIES FOR MOBILE PHONES OR LAPTOPS	PAFC HAS BEEN WELL ESTABLISHED IN THE STATIONARY FUEL CELL MARKET, SYSTEM OF 200kW ARE COMMERCIALISED IN THE USA AND JAPAN	DEVELOPED FOR NATURAL GAS AND COAL-BASED POWER PLANTS, UNITS OF 250Kw HAVE SHOWN OVERALL EFFICIENCIES OF UP TO 65% COMBINED TO A STEAM TURBINE	AUXILIARY POWER UNITS (APU)
LIMIT	INCOMPATIBILITY OF THE ELECTROLYTE WITH CO_2	- WATER MANAGEMENT FOR THE MEMBRANE PERFORMANCE - POISONING OF THE CATALIST BY CO	- HIGH PERMEATION OF CH_3OH THROUGH THR MEMBRANE - LOW ELECTRICAL EFFICIENCY OF ABOUT 20% TO 30% FOR SYSTEM UP TO 100 W	- SOLIDIFICATION OF PHOSPHORIC ACID AT 40°C	HIGHLY CORROSIVE ENVIROMENT REDUCING CELL LIFE	HIGH COST OF MATERIALS

1.2.1 Solid Oxide Fuel Cell (SOFC)

The SOFC [2] is a solid-state device for electro-chemical electricity production that uses a dense metal oxide ion-conducting ceramic material as an electrolyte, placed between a porous cermet anode or "fuel electrode" and a porous ceramic cathode or air electrode. Together, these three components are often denoted as the membrane electrode assembly (MEA)[3]. The electrolyte should be a good ionic conductor and should have no electronic conductivity (it remains electrically insulating at high temperatures), while the electrodes should be good electronic conductors and possibly also ionic conductors. Each electrode should have a high catalytic activity for adsorption, dissociation and electrochemical reactions of the oxidant or fuel species. Depending whether the electrolyte is a pure oxygen ion conductor or a proton conductor, two types of SOFC can be considered. Figure 1.2.1.1. illustrates the operating principle of a SOFC based on an oxygen ion conducting electrolyte.

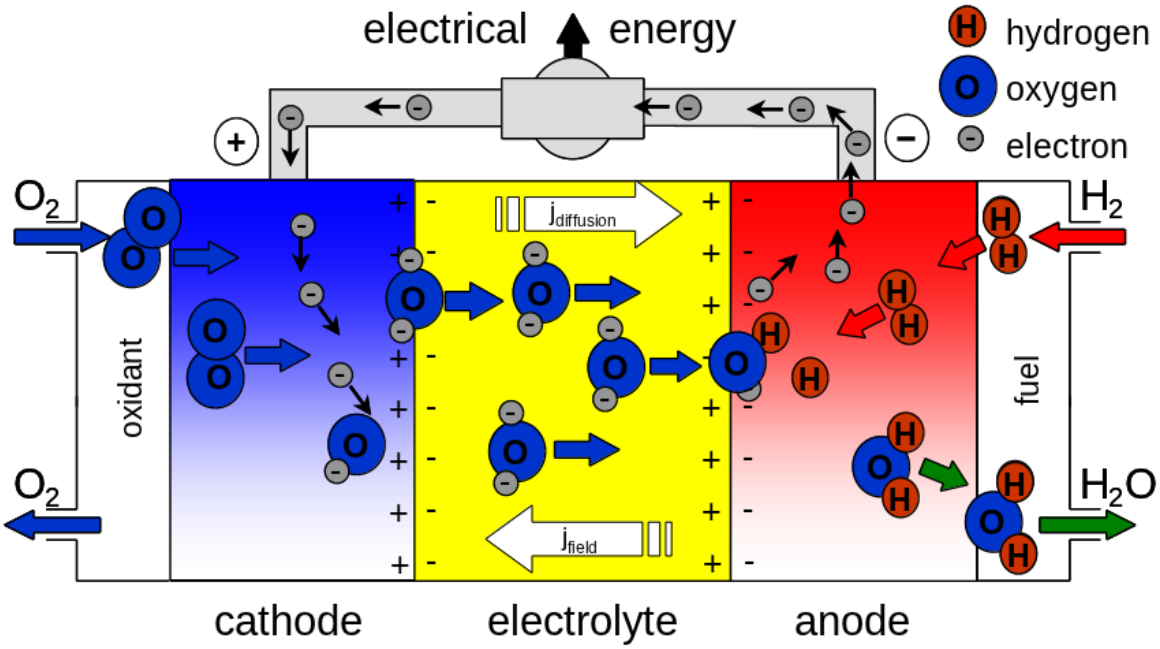

Figure 1.2.1.1 Schematic representation of operating principle of a planar SOFC.

The fuel (H_2 in the figure) is brought into the anode compartment and the oxidant (air) into the cathode compartment. Oxygen as a constituent of air at the cathode side is transformed into ions (oxygen gas is electrochemically reduced to O^{2-}) as a result of receiving electrons from the external circuit. O_2 molecules are adsorbed on the catalytic surface of the cathode material, dissociated and ionized to O^{2-}, following the reaction:

$$O_2 + 4e^- \rightarrow 2O^{2-}$$

Driven by differences in potential and concentration, oxygen ions migrate to the anode through oxygen vacancies in the electrolyte[4]. The fuel at the anode side is oxidized to water by reacting with oxygen ions, releasing electrons to the external circuit. On the anode side, the fuel molecules reach the so-called "three-phase" boundaries between metal, oxide and atmosphere. They are adsorbed and react with the diffused oxygen ions:

$$H_2 + O^{2-} \rightarrow H_2O + 2e^-$$

If the fuel is, for instance, CO, the anode reaction becomes

$$CO + O^{2-} \rightarrow CO_2 + 2e^-$$

Electrons charge the anode negatively compared to the cathode. The ionic current between the electrodes within the electrolyte maintains the overall electrical charge balance. Finally, the flow of electrons in the external circuit generates the electrical power output. The resulting voltage can be used to feed an external circuit, returning the electrons to the cathode side. The global reaction in the fuel cell is hence given by:

$$2H_2 + O_2 \rightarrow 2H_2O$$

or for CO

$$2CO + O_2 \rightarrow 2CO_2$$

If the fuel gas is methane the reaction at the anode is $CH_4 + 4O^{2-} = CO_2 + 2H_2O + 8e^-$ and that at cathode $4O_2 + 8e^- = 4O^{2-}$, resulting in the total reaction $CH_4 + 2O_2 = CO_2 + 2H_2O$. Compared with other fuel cells, the main feature of SOFCs is the utilization of solid oxide as the electrolyte, which also prevents leakage or vaporization and makes the cell design more flexible[2]. Solid oxides used in SOFCs typically possess sufficiently high ionic conductivity at elevated temperatures of 600°C-1000°C. Advantages of SOFCs are high energy conversion efficiency, long-term stability, fuel flexibility, low levels of NO_x and SO_x emissions. The largest disadvantage is the high operating temperature, which result in longer start-up times as compared to low-temperature fuel cells as well as mechanical and chemical compatibility issues[5].

1.2.1.1 Cell and stack designs

In order to obtain high voltage and high power from SOFCs, single cells are stacked together in different ways. Two major stack design, tubular (Fig. 1.2.1.1.1) and planar (Fig. 1.2.1.1.2), are widely used, each with specific benefits and drawbacks.

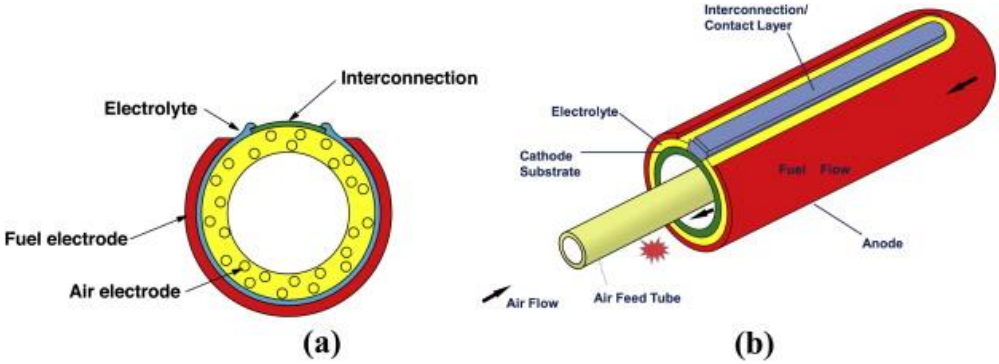

Figure 1.2.1.1.1 Schematic of a single cathode-supported tubular SOFC (a) Cross sectional view (b) Three dimensional view of the cell.

The tubular SOFC (TSOFC) can be manufactured with different diameter, and the main advantage of this desing is that it does not require a high-temperature seal to separate the oxidant from the fuel. This gives the system long-term reliability. A limit to the use this kind of SOFC is the long current path around the circumference of the single cell tube which basically decreases the power density to typically 200 mW/cm^2 at 1000°C [6]. A problem is also the higher fabrication costs.

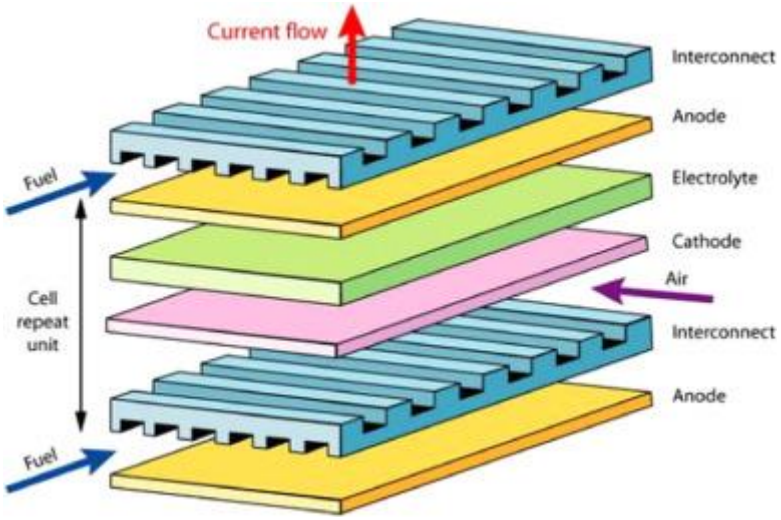

Figure 1.2.1.1.2 Schematic representation of planar SOFC.

The development of planar SOFCs for large electrical power units started before that of tubular SOFCs. The planar configurations more closely resemble a stacking arrangement, with a simple series of electrically connected cells avoiding the long current path of the tubular cell. The main advantage of the planar design over other concepts is the potential to achieve higher power densities due to the short transport paths across the cell. An additional advantage lies in the simpler fabrication technology, with the possibility to use low cost processes like screen-printing or tape-casting, representing a largescale production potential [7]. The inconvenience of the design is the need of a high-temperature sealing. Furthermore, the ceramic layers show a lower tolerance to thermally induced stresses that can cause the cracking of the cells upon thermal cycling. Planar SOFC design can be divided in two categories:

1. Self-supported configuration, where one of the cell components acts as the structural support (Fig. 1.2.1.1.3)

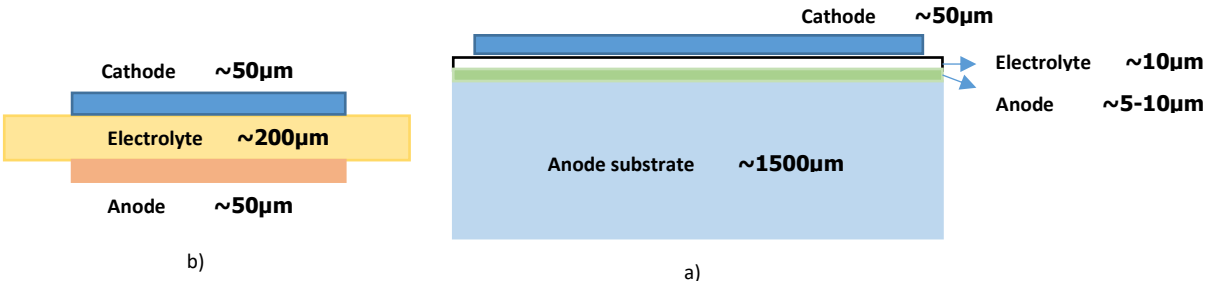

Figure 1.2.1.1.3 Self-supported cell concept: a) anode-supported cell, b) electrolyte-supported cell.

A kind of this configuration is electrolyte-supported cells that offers a strong support from a dense thick electrolyte, but require a high operating temperature of about 900-1000C° to minimize the ohmic losses of the electrolyte. Anode- or cathode-supported cells with thin electrolytes (5-20µm) allow operating temperatures lower that 800°C. High conducting anode cermets have been favored as substrate but have a lower stability due to potential re-oxidation [8].

2. Externally supported configuration, including interconnect-supported cells that provide a lower electrical transport limitation than anode-supported and a stronger metallic support. However, an issue is the interconnect oxidation. Porous metallic substrate is an alternative to improve the support properties.

The advantages of reduced operation temperature include a wider choice of materials, especially low-cost materials for interconnect, reduced thermal stresses, improved reliability and longer cell life, together with reduced cell cost. Main drawbacks are slower electrode reaction kinetics and reduced thermal energy extracted from hot exhaust steams of the cell.

The actual stack design for stationary applications is presented in Fig. 1.2.1.1.4.

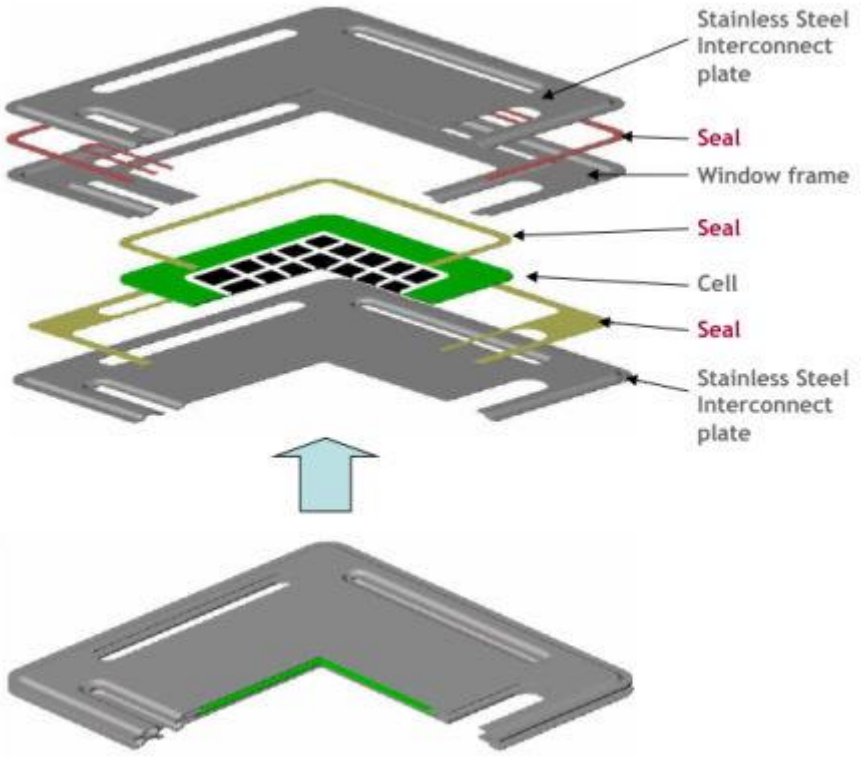

Figure 1.2.1.1.4 Planar stack design.

A typical planar SOFC consists of a sandwich-like structure with a thin ionic oxygen-conducting electrolyte layer, an anode usually acting as the mechanical support that is exposed to the gaseous fuel, a cathode that is exposed to air, and an interconnect material [9]. The cathode side is typically contacted using a ceramic contact layer. In addition, high temperature hermetic sealants are needed and play an important role in the planar

SOFCs to prevent leakage during operation and mixing of fuel and oxidant [10]. The interconnect layer is placed between each individual cell made up of an anode, an electrolyte and a cathode, connecting them in series. Between interconnect and cell, a nickel mesh is typically inserted to work as anode current collector. The entire building up of the individual cells and the interconnect is called the stack (Fig. 1.2.1.1.2). In practical applications, a positive electrode-electrolyte-negative electrode plate (PEN), is fabricated by sintering anode, electrolyte and cathode together at high temperatures [11]. The voltage and the power of a single cell are limited. In order to obtain higher voltage and power, interconnects with high electrical conductivity and gas-separation ability are used to provide electrical conduction between several PEN plates in a serial connection [12]. Each of the components of an SOFC stack anodes, cathodes, electrolytes and interconnects must be thermally, chemically, mechanically and dimensionally stable at the operating conditions and compatible, in terms of thermal expansion and chemical reactivity, with the other layers to which they come into contact. [13].

The cell concept presents the following advantages:

- a thin electrolyte of 5 to 10 µm, with low resistance provides high power densities at low operating temperatures of 750° - 850°C.
- a thick anode substrate gives the cell mechanical stability; different thicknesses can be obtained by warm pressing or tape casting, with dimensions up to 250 x 250 mm^2
- the anode functional layer and electrolyte can be coated successively by different methods including vacuum slip casting and screen-printing and co-fired
- low operating temperatures allow the use of ferritic steels as interconnect plates instead of expensive high-temperature alloys or ceramics

A major issue of planar SOFC is the need for gas-tight sealing around the edge of the cell components, but a positive point of this design is that the sealing contours for manifold are located in-plane (Fig. 1.2.1.1.4) which makes assembling easier.

1.2.1.2 Electrolyte

From a material point of view the electrolyte is one of the most demanding components in a SOFC. The electrolyte has to be physically and chemically stable in both oxidizing (P_{O2}>0.2 bar at the anode) and reducing conditions (P_{O2}<10^{-19} bar)[14]. The function of the electrolyte is to transport oxygen ions from the cathode to the anode, and it should have no electronic conductivity. The oldest and still most used electrolyte for oxygen ion conduction is ZrO_2 stabilized with 8 mol% Y_2O_3 (YSZ). The operating temperature is typically 800-1000°C. Yttrium-stabilized-Zirconia is an appropriate material for this task at elevated temperatures [15] due to its low cost, acceptable ionic conductivity, high mechanical and chemical stability [16]. YSZ is also highly stable with respect to the anode and cathode materials during operation. The ionic conduction of YSZ is based on oxygen vacancies, which are induced by replacement of Zr^{4+} ions by Y^{3+}ions [17] in the fluorite crystal structure of

zirconia. Considering the requested ionic conductivity, the electrolyte layer must be manufactured as thin as possible to yield a good cell performance. Ceria with 10-20 mol% Gd, (CGO) offers excellent promise as a potential electrolyte for lower temperature SOFC (500-600°C). However, unfortunately under the reducing atmosphere at the anode, ceria becomes an electronic conductor, which significantly reduces the efficiency of the SOFC. Extensive research is going on to tackle this problem [18-19].

1.2.1.3 Anode materials

In view of the reducing atmosphere at the anode side, metallic anodes can be used. The most commonly used material is a porous Ni-YSZ cermet with 40-50% nickel evenly distributed in a porous YSZ matrix. The Ni metal phase provides the required electronic conductivity and catalytic activity [20], whereas the 8YSZ ceramic phase lowers the thermal expansion coefficient of the anode to match it with that of the electrolyte, prevents the Ni phase from coarsening, and offers a conduction path for oxide ions and thus the potential to extend the active zones for anode reactions [21]. Ni-YSZ anodes have been used for more than twenty years. They are also used as anode substrates due to the high mechanical strength and good operation performance. Other anode materials are perovskites (ABO_3) of the $LaCrO_3$type doped with Ca, Sr, or Ti, and $SrTiO_3$ doped with niobium or lanthanum e.g. $Sr_{0.6}Ti_{0.2}Nb_{0.8}O_3$ and $La_{0.4}Sr_{0.6}TiO_3$ [22-23-24].

1.2.1.4 Cathode materials

Possible SOFC cathode materials have been investigated for many decades. Noble metals could be used but are excluded for the high cost. Most cathode materials are perovskite materials. Indeed, ceramics with perovskite structure possessing high electronic conductivity have so far been the materials of choice for cathodes. The most common cathode material is lanthanum manganite doped with strontium $La_{1-x}Sr_xMnO_3$ (LSM), it has been used for almost one decade due to its high electrochemical activity for oxygen reduction at operation temperatures, good stability, and good thermal expansion match with YSZ anode and electrolyte materials [25]. Another important benefit is that it shows no chemical reaction with common electrolyte materials. Recently the focus has shifted towards lanthanum cobaltite doped with Sr and Fe of the type $La_{1-x}Sr_xCo_{1-y}Fe_yO_3$ (LSCF), due to its better performance at lower temperatures (750°C and below) envisaged for future SOFC developments. Other option could be lanthanum cobaltite $LaCoO_3$ (LC), lanthanum calcium cobaltite ferrite (LCCF), samarium strontium cobaltite (SSC) [23-26-27]. The cathode is often made of two layers, one consisting of a porous mix of electrode and electrolyte (e.g. LSM/YSZ) and the other pure electrode material (e.g. LSM). These two-layers cathode give a better match of the thermal expansion coefficients between electrolyte and the cathode and better chemical compatibility without reducing the performance of the cathode.

1.2.1.5 Interconnect materials

To obtain functional fuel cell units, the single cells have to be assembled in stacks in order to give enough power for commercial use. This can only be accomplished by some interconnects between each cell. Indeed, the main purpose of the interconnect plates is to provide electrical connection between two successive cells, separation between both atmospheres and distribution of the fuel and oxidant gases, avoiding the electrical contact between the anode of one individual cell and the cathode of the neighboring one in the stack. The materials for the interconnect parts are selected for their high electronic conductivity, low thermal expansion mismatch to cell components (coefficient of thermal expansion, CTE, of about $10.5\text{-}12.5 \cdot 10^{-6}\ ^{\circ}C^{-1}$ between room temperature and the operating temperature in the range 750°C to 850°C [28-29]) and chemical stability in both high and low oxygen partial pressures corresponding to cathode and anode atmospheres, respectively. Interconnect materials should not undergo significant shape changes with temperature or oxygen partial pressure changes [30]. The materials should show a high thermal conductivity to allow a uniform heat distribution across the stack, as well as a good chemical compatibility with adjacent stack components. In addiction the interconnect parts should be fabricated with a high density to ensure gas tightness and a high creep resistance, as the bottom cells of the stack are under a large weight load.

Different types of interconnect materials were successively developed for different ranges of operating temperature (Table 1.2.1.5.1).

Operation temperature	Ceramic materials 900-1000°C	Metallic materials BELOW 800°C
EXAMPLES OF SUITABLE MATERIALS	- $LaCrO_3$ doped with divalent cations, e.g. $La_{1-x}M_x\ CrO_3$ (M= Sr^{2+}, Ca^{2+} or Mg^{2}) - Y CrO_3	- Ni-alloys - Cr-alloys or FeCr-alloys - Ferritic stainless steels
PROPERTIES	- They can easily be modified to fulfil the main requirement - The electrical conductivity of these perovskites is improved by substituting divalent ions, such as Sr^{2+}, Ca^{2+} or Mg^{2+}on either the A or the B sites of the ABO_3 lattice - CTE could be markedly increase by doping the perovskites with aliovalent ions such as Co^{+}. In the lattice ABO_3, the replacement of a trivalent by a divalent ion is electrically compensated by the formation of tetravalent chromium ions at high P_{O2}.	- Higher electrical and thermal conductivity - Easier fabrication with low machining costs - High oxidation resistance with CTEs close to the ceramic components - The chromium content has to be higher than 17 wt% to ensure the formation of a protective chromium oxide layer, but larger amounts are required to achieve low CTE values and offer a chromium reservoir. - Al and Si contents are avoided to prevent the formation of an external protective layer, which low electronic conductivity would increase the resistance at the interface are fabricated by power metallurgy from mixture of Cr flakes, Fe and Y_2O_3 powders, and additional alloying elements like Mn, Ti and Mo to improve the physical and chemical properties of intermediate temperature alloys.

		- The alloys are fabricated by powder metallurgy from mixture of Cr flakes, Fe and Y_2O_3 powders, an additional alloying element like Mn, Ti, Mo to improve the physical and chemical properties of intermediate temperature alloys. A fine distribution of Y_2O_3 particles is essential to improve the oxidation resistance of the alloys, as well as their mechanical properties. - Small amount of Mn and Ti could be added to provide an external $(Cr,Mn)_3O_4$ spinel formation of volatile Cr-species and to obtain fine internal titania precipitates for strengthening of the near-surface region. - Lanthanium appears the most beneficial because it becomes distributed in the alloy rather that forming intermetallics at grain boundaries like Y or Ce.
LIMITS	- The change of valence state, together with a variation of the oxygen vacancy concentration in a reducing atmosphere, leads to a volume expansion generating mechanical stresses within the interconnect - Low thermal conductivity (< $5Wm^{-1}\cdot K^{-1}$) that causes strong thermal gradients in the stack - Drawback of chromite materials are related to their fabrication process, they are difficult to sinter up to high density under high $P_{o2,}$ and lack a proper workability to large dimensions due to their brittleness	- Commercially available high temperature oxidation resistant alloys could not directly be used to their high CTE - The electrical conductivity is controlled by the oxide scale formed at high temperature - Under either oxidizing or reducing atmospheres, Cr- and FeCr-based alloys form a chromium oxide layer, which growth rate id strongly affected by size and distribution of the oxide dispersion. Small dispersion size and small distances between the particles insure an optimum reduction of the oxide growth rate

Table 1.2.1.5.1 Different type of interconnect materials.

1.2 Sealing

In this research work the attention will be focused in particular on the study of new materials for sealing applications in solid oxide fuel cells. Several seal concepts for SOFCs have been developed during the last 20 years but few have been tested for long time (> 2 years) under realistic conditions. A key challenge in assembling planar SOFC systems is to create and maintain a hermetic seal between a thin dissymmetric stack of ceramic layers and the metallic interconnect plate.

The schematic cross-section of the sealing in Fig.1.3.1 highlights the main problems related to joining of planar SOFCs.

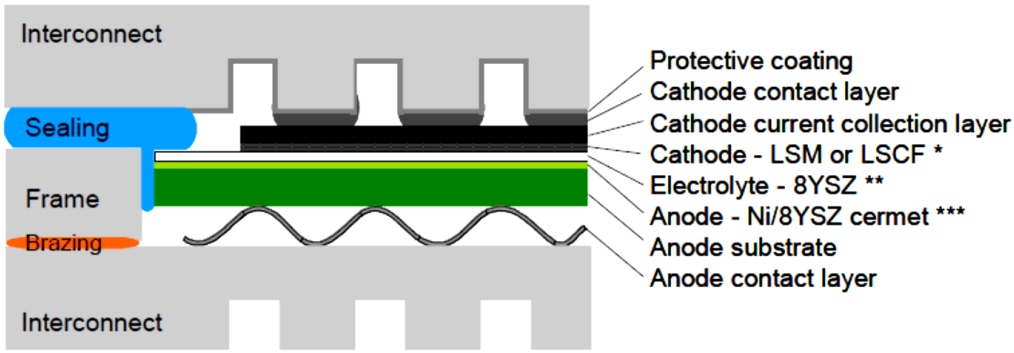

Figure 1.3.1 Schematic cross-section of a layer in a planar stationary SOFC stack with state of the art materials for each layers.

*LSM: $(La, Sr)_{1-x}MnO_{3-\delta}$ or LSCF: $(La, Sr)_{1-x}(Co, Cu, Fe)O_{3-\delta}$ perovskites
**8YSZ: 8mol% Yttria-Stabilized Zirconia
***Ni/8YZS cermet: cermet of 8YSZ with 40 vol% Ni
Interconnect and frame: 17-26 wt% Cr ferritic steel or powder metallurgy alloy

Finding solutions for the seal challenges are crucial for large scale use of SOFC technology. The main functions of sealing materials for fuel cells are to ensure the gas separation between both gas atmospheres, i.e. air on the cathode side and fuel gas on the anode side, and to guarantee electrical insulation between two successive interconnect planes. Solid oxide fuel cells typically work under a gradient of oxygen partial pressure across a dense, gas-tight electrolyte. Leaks due to fabrication defects or degradation of the components or interfaces during operation, reduce the system performance drastically, if not lead to complete failure of the stack [31]. The seal has to match the electrolyte, cathode and interconnect materials with respect to thermal expansion. Depending on the design, the seal might have to join ceramic to ceramic, ceramic to metal or metal to metal. For air and fuel supply, the SOFC stacks need manifolds with corresponding sealing as shown in Fig. 1.3.2.

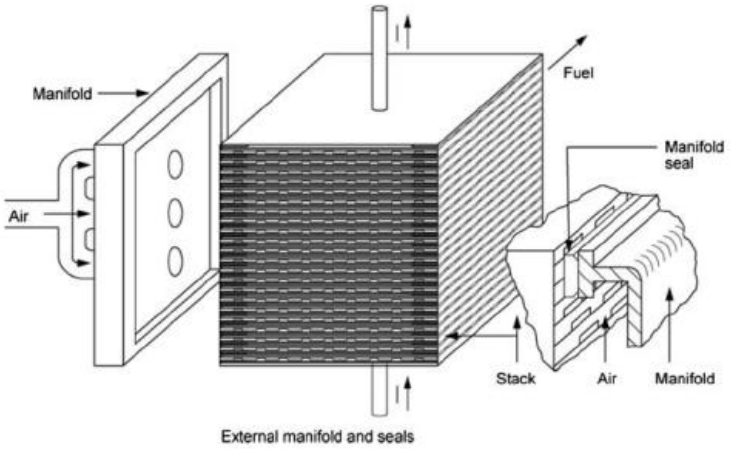

Figure 1.3.2 Schematic of one possible design for sealing the air supply manifold to a planar SOFC stack. A corresponding manifold is needed for the fuel supply.

Hence the sealant must be tailored to match the thermal expansion coefficient of the adjacent materials, cell (anode substrate) and interconnect [32]. Even a modest degree of thermal expansion mismatch can cause

substantial bowing of the cells, which can lead to fuel and air mal-distribution in the stack and hence poor system performance [33] as well as fracture of sealant and/or cells.

Sealants need to withstand thermal cycles during the routine operation of SOFC stacks in a stationary design, the envisaged operation lifetimes being more than 40000 h with up to 100 thermal cycles for stationary application and 5000 h with at least 2000 cycles under high heating rates (short start-up time) for mobile applications at high operating temperature (600 °C and more). Given the importance of its role, there are some severe conditions which the sealants material must satisfy [34]. A critical problem is the chemical stability of the sealing materials at high temperature, for this reason they should show a limited reactivity with adjacent components, typically the yttria-stabilized zirconia (YSZ) electrolyte and chromium-rich ferritic steel interconnect and should be stable against evaporation. Besides these stringent requirements, other specifications are closely tied to the cell and stack design as well as the system application, i.e. either mobile or stationary application. The functional requirements of sealing systems for SOFCs can be summarized as follows (Table 1.3.1):

CHEMICAL PROPERTIES	MECHANICAL PROPERTIES	ELECTRICAL PROPERTIES	DESIGN AND FABRICATION
Long-term stability under dual air//wet fuel atmospheres up to 850°C	Hermetic sealing or low, non–localized leakages	Electrical insulation between interconnect plates (ρ=1MΩ·cm)	Simple processing and flexible design
Limited reactivity with adjacent components, low corrosion of ferritic steel interconnects	CTE matching the cell substrate and interconnect ($\Delta\alpha \leq 1.5 \cdot 10^{-6} °C^{-1}$) or dissipation of thermal stresses		High reliability and reproducibility
	High bond strength to joined components or applied compressive load		Low cost
	Tolerance to thermos-mechanical and externally applied stresses		

Table 1.3.1 Functional requirements of sealing systems.

Different approaches have been imagined to fulfill those demanding specifications and can be classified into three categories:

1. Rigid bonded seals

   In a rigid sealing design, the sealant material (non-deformable at room temperature) forms a joint (chemical bond) that is non-deformable. Due to the inherent brittle nature of the materials, suitable materials for this type of sealant are glass, glass-ceramics and ceramics. Another option for rigid seals is composite sealants, where the addiction of either an inert or a reactive filler material to a glass matrix in controlled proportion, allow to tailor the thermo-mechanical properties of the composite [35]. For high temperature purposes seals based on glass or glass-ceramics are the most promising concept because of their high chemical stability at high temperature. Nevertheless, due to the inherent brittle nature of these materials, they are sensitive to tensile stresses, caused by thermal

expansion mismatches between the sealant and adjacent components. Glass is cheap, readily available and can be supplied as a paste or paint of powder mixed with a liquid binder. The glass powders can be also tape cast in thin sheets, which can be cut into special shapes to fit the parts to be sealed. The sealing function is achieved by heating the membrane assembly with the "green" seals to a temperature high enough for the seal to sinter completely. The maximum temperature for the sealing cycle should be lower than for all the fabrication steps of the cell components and higher than the operational temperature. The seal must wet the components during sealing, but not react in a way that reduces the performances of the seal or the sealed components.

2. Compliant bonded seals

   In contrast to rigidly bonded seals, compliant seal forms a bond that undergo plastic deformation at operating temperatures. In this way stresses that arise from external expansion mismatch between the cell components of the stack can be relaxed to a certain extent. However, this approach raises different issues like the possible bend of non-constrained cells, which in turn implies losses in electrical contact and non-uniformity of gas distribution across the cell. In addition, similar problems of electrical conduction are encountered like with metal gaskets, if metal-based materials are used. Therefore, the approach requires the development of insulating layers to prevent internal short-circuiting. The implementation of this technology remains difficult due to the need of reliable high temperature sealing materials.

3. Compressive seals

   Compressive seal is based on deformable materials that do not bond to the adjacent components but rather serve as a gasket. That is, the sealing parts need to conform to the adjacent surfaces and require constant compressive load during use. Because not rigidly bonded, the sealing surfaces can slide along on another and components are free to expand and contract during thermal cycling with no need to consider CTE matching. Additionally, they open the possibility to replace damaged cells or interconnect part during service time, by release of the compressive load on the stack during operation, which should be tolerable for the cell components. Further problems are related to the load frame oxidation, load relaxation due to creep, and increased weight and thermal mass that reduce the specific power of the overall system.

Each of these concepts has advantages and limitations. In table 1.3.2 [36-37] the properties of each type of seal are described.

<table>
<tr><th colspan="2">Sealing concept</th><th colspan="2">ADVANTAGES</th><th colspan="2">DISADVANTAGES</th></tr>
<tr><td rowspan="3">Rigid bonded seals</td><td>Glass ceramic</td><td>Electrical insulation
Gas tightness
Paste processing</td><td rowspan="3">• Hermetic seal
• Tailorable performance by composition design
• High electrical resistivity
• Suitable for stationary and mobile applications
• Flexible in design and fabrication</td><td>Control of phase content
Chemical reactivity
Fragile fracture</td><td rowspan="3">• Brittle at low temperature
• Poor resistance to thermal cycling
• Chemical reaction with other cell components</td></tr>
<tr><td>Ceramic</td><td>Chemically inert</td><td>Pyrolysis processing
Non-adapted CTE
Fragile fracture</td></tr>
<tr><td>Composite</td><td>Tailored CTE</td><td>Filler phase stability
Control of viscous flow
Fragile fracture</td></tr>
<tr><td rowspan="3">Compressive seals</td><td>Metal gasket</td><td>Plastic stress relaxation
Enable disassembling</td><td rowspan="3">• Easy replacement of seals in a malfunctioning cell stack.
• Resistance to thermal cycling</td><td>Non-adapted CTE
Permanent gas leakage
Creep under high load</td><td rowspan="3">• Application of external load
• Complex design and high cost
• High gas leakage rate
• Unsuitable for mobile application
• Poor stability
• Electrically conductive</td></tr>
<tr><td>Mica-based</td><td>Elastic</td><td>High leakage rates
High permanent load</td></tr>
<tr><td>Metal-mica</td><td>Elastic
Plastic stress relaxation
Enable disassembling</td><td>Electrical conductivity
High permanent load
Complex processing</td></tr>
<tr><td rowspan="3">Compliant seals</td><td>Metal brazing</td><td>Gas tightness
Plastic stress relaxation
Paste, sheet processing</td><td rowspan="3">• Low thermal stress</td><td>Electrical conductivity
Chemical reactivity
Processing (T, atm)</td><td rowspan="3">• Non-wetting to other SOFC components
• Poor oxidation resistance
• Hydrogen embrittlement
• Electrically conductive</td></tr>
<tr><td>Glass</td><td>Electrical insulation
Gas tightness
Plastic deformation</td><td>Chemical reactivity
Stability against evaporation</td></tr>
<tr><td>“Wet” seal</td><td>Gas tightness
Plastic “self-healing”</td><td>Chemical reactivity
Stability against evaporation
Electrical insulation</td></tr>
</table>

Table 1.3.2 Overview of potential sealing concepts for SOFCs.

Rigidly bonded seals have many advantages compared to compressive and compliant seals and are preferred for SOFCs. For this reason, the emphasis of this work is mainly put on developing a new glass ceramic for rigid bonded seals.

Glass and glass ceramic seals are flexible in design, easy to fabricate, and cost-competitive. A wide range of materials' properties required for sealing can be achieved with glass and glass-ceramic seal by compositional design [38]. These materials have a good resistance to the oxidizing and reducing atmospheres in the stack, hermetically separate anode and cathode gas supply, are chemically stable to any component materials or gaseous species in the stack environment, and possess a sufficient bonding strength to withstand the operation-induced stresses [39]. Moreover, the glass paste can be manufactured to the sealing surface due to the good wetting behavior and can be designed to have a good matching of the thermal expansion coefficient to those of the adjacent layers [40]. Glasses and partially crystallized glass-ceramics are characterized by a glass transition temperature (T_g), above which the mechanical properties of the material change from brittle to

ductile behavior [40]. During the joining process, the glass might partially or fully crystallize. Furthermore, it will react with the joining partner (or oxide layer) to form a rigid bonding. The resulting interfacial phases might thicken and become porous during long annealing times implying a susceptibility to micro-cracking when thermally cycled [41]. Crystallization is advantageous since the resulting microstructure is mechanically stronger than the initial glass [42].

1.3.1 Glass material

Glass is an amorphous solid material which possesses no long-range atomic order and, upon heating, gradually softens to finally reach a molten state [43]. The glass components can be classified mainly into network formers, network modifiers and intermediates (Fig. 1.3.1.1).

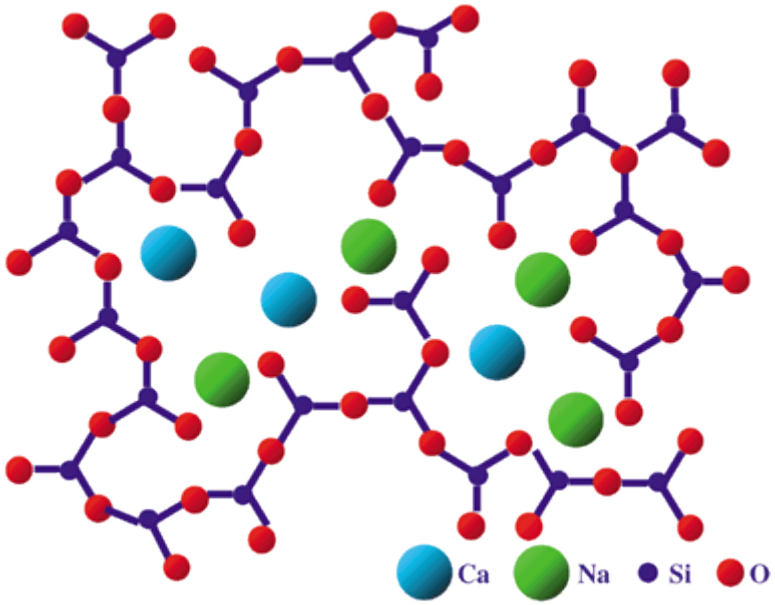

Figure 1.3.1.1 Schematic representation of the random network of alkali silicates.

Inorganic glasses consist of one or several network formers, one or several network modifier and often also some intermediates [44]. The network formers build the main structure of the glass. The network modifiers strongly influence the glass properties. The intermediates stabilize the glass structure depending on their mole fraction. The functions of different oxide constituents in glass are listed in table 1.3.1.1. [45]

Glass constituent	Oxide	Function
Network former	SiO_2, B_2O_3	Form glass network Determine T_g and T_s Determine thermal expansion coefficient (CTE) Determine adhesion/wetting with other SOFC components
Network modifier	Li_2O, Na_2O, K_2O BaO, SrO, CaO, MgO	Maintain charge neutrality Create non-bridging oxygen species Modify glass properties such as Tg, Ts and CTE
Intermediate	Al_2O_3, Ga_2O_3	Hinder devitrification Modify glass viscosity
Additive	La_2O_3, Nd_2O_3, Y_2O_3	Modify glass viscosity Increase thermal expansion coefficient

	ZnO, PbO NiO, CuO, CoO, MnO Cr_2O_3, V_2O_5 TiO_2, ZrO_2	Improve glass flowability Improve seal glass adhesion to other cell components
	TiO_2, ZrO_2	Induce devitrification

Table 1.3.1.1 Function of different oxide constituents in a seal glass.

While glasses are amorphous solids, they can also be partly or totally crystallized (also denoted inverted) to give a glass ceramic. Oxide glasses can be described as a continuous network of atoms linked together by oxygen atoms. Common network formers are SiO_2, B_2O_3, P_2O_5, TeO_2, SeO_2, As_2O_3, SbO_2 and V_2O_5. The most common seal glasses contain only SiO_2 or B_2O_3 or a combination of SiO_2 and B_2O_3 as glass former. Other oxides as P_2O_5 are reduced by hydrogen at 750°C and cannot be used as a SOFC [46]. B_2O_3 addition to silicate glass generally decreases the viscosity and the tendency to crystallization, which are favorable effects. Addiction of more of than 12 mol% B_2O_3 increases the thermal expansion[46]. One disadvantage with B_2O_3 addition is that boron oxide forms volatile compounds with water vapor at elevated temperatures resulting in seal degradation [46]. The use of B_2O_3 in silicate glasses thus has to be a compromise between the favorable and less favorable properties of B_2O_3. The majority of suggested silicate seal glasses for SOFC contain B_2O_3. Common network modifiers are alkali oxides (such as Li_2O, Na_2O and K_2O) and alkaline earth oxides (such as BaO, SrO, CaO and MgO) and some other oxide such as ZnO, PbO, Y_2O_3, TiO_2 and La_2O_3. The effect of glass modifiers is related to their effects on the network structure. Field strength, ionic radius, polarizability, and coordination number of a network modifier need to be considered. Addiction of network modifiers into pure glass-forming oxides disrupts glass network structure and creates non-bridging oxygen. The modifiers affect the chain structure so that physical properties such as viscosity, thermal expansion, density, refractive index, chemical durability can be tailored. While alkali oxides are common in glasses for use at ambient temperatures, for glasses that are to be used at high temperatures they present the drawbacks of high reactivity and high ionic mobility. The most common modifiers in a glass for high temperature application are the alkaline earth oxides. Intermediate oxide candidates are Al_2O_3, Cr_2O_3, TiO_2, ZnO, ZrO_2, HfO_2, Ta_2O_5 and rare earth oxides. Al_2O_3 and ZrO_2 are stable oxides even in strongly reducing atmospheres. TiO_2 is often added as a nucleating agent for the purpose of achieving homogeneous nucleation in the glass. TiO_2 may be reduced in H_2 at 800°C. ZnO is reduced under dry H_2 at temperatures as low as 300 °C, but it shows no reduction in wet H_2 even at much higher temperatures. Carbon-containing fuel gases – e.g. CH_4 / CH_3OH, reduce ZnO under both wet and dry conditions. ZnO has similar effect as boron oxide regarding the viscosity and thermal expansion. Alumina is an important constituent in many glasses. Al_2O_3 increases the viscosity of molten glasses and promotes microcrystalline growth, which is an attractive property for glass-ceramic seals. Alumina also increases the chemical durability, hardness and other mechanical properties [47]. On the basis of their chemical and physical properties the following oxides are potential components for SOFC seal: SiO_2, B_2O_3, Al_2O_3, BaO, SrO, CaO, MgO, Y_2O_3, ZnO, La_2O_3 and Ta_2O_3[48].

Structural features of silicates and aluminosilicates

Aluminosilicates are the most common minerals owing to the abundance of silicon and aluminum in the Earth's crust. Different silicates are composed of individual SiO_4^{4-} tetrahedrons which can be either bonded to other cations or linked together through corner oxygens shared with other SiO_4^{4-} groups (Figure 1.3.1.2).

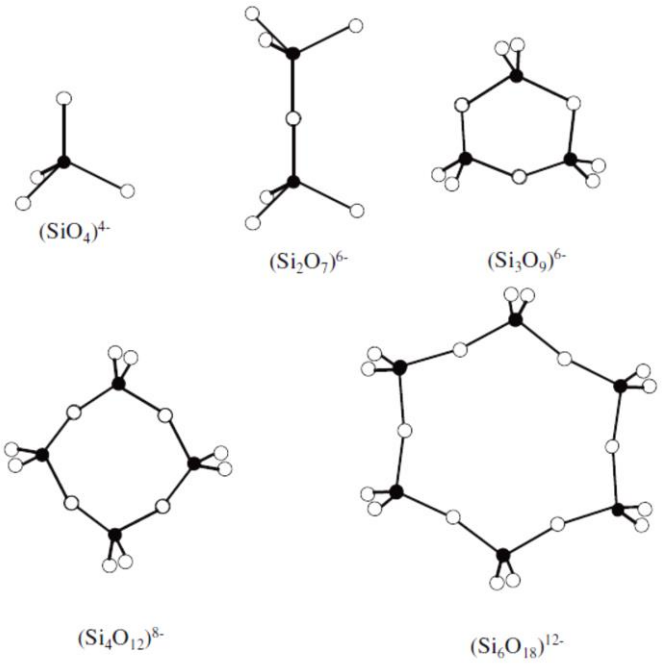

Figure 1.3.1.2 The simple tetrahedron and more complex groups built from [SiO_4] tetrahedrons.

Aluminum plays a special role in silicate structures being six- or four-fold coordinated with oxygen and giving rise to various aluminosilicates. In the latter case $(AlO_4)^{5-}$ groups substitute for SiO_4^{4-} ones, while charge balancing is satisfied by cations of alkali (Li, Na, K), alkaline-earth (Be, Mg, Ca) or transition (Fe, Mn, Ti, Zr, etc.) metals. SiO_4^{4-} tetrahedrons shared with octahedral groups are basic units of nesosilicates (island silicates) also known as orthosilicates (Figure 1.3.1.3).

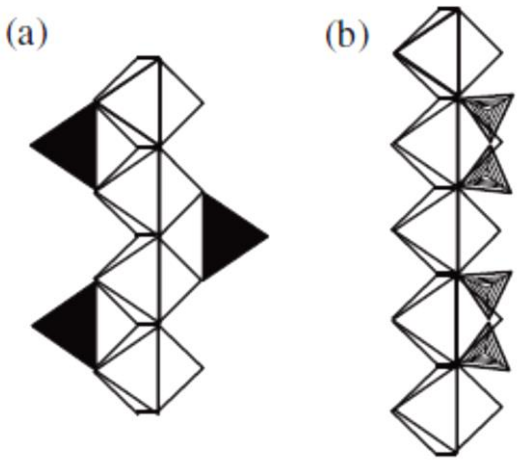

Figure 1.3.1.3 The elements of silicates structure: (a) orthogroups of [SiO_4] tetrahedrons; (b) diorthogroups of [Si_2O_7].

This combination is possible due to matching edge sizes of isolated SiO_4^{4-} tetrahedrons (2.64 Å) and octahedral groups that contain relatively small cations like Mg^{2+}, Fe^{2+}, Zr^{2+}, etc. Zircon ($ZrSiO_4$), forsterite (Mg_2SiO_4), fayalite (Fe_2SiO_4), montichellite ($CaMgSiO_4$) are some representatives of nesosilicates.

Diorthogroups $Si_2O_7^{6-}$ are formed through sharing of corner oxygens from tetrahedrons and are the basic units of silicates referred to as sorosilicate group. $Si_2O_7^{6-}$ groups have dimensions (4.1-4.2Å) comparable with the edges of octahedral groups formed by larger cations like Ca^{2+}, Sr^{2+}, Ba^{2+}, etc. (Fig. 1.3.1.4). A good example of sorosilicates are the minerals from melilite family, in particular akermanite $Ca_2MgSi_2O_7$ that forms continuous solid solutions along with gehlenite $Ca_2Al_2SiO_7$. Cyclosilcates (ring silicates) are composed of several SiO_4^{4-} tetrahedrons that share oxygens in a ring structure creating $Si_3O_9^{6-}$, $Si_4O_{12}^{8-}$, $Si_5O_{15}^{10-}$ and $Si_6O_{18}^{12-}$ groups (Fig. 1.3.1.5). Some examples of cyclosilicates are cordierite - $Mg_2Al_3AlSi_5O_{18}$ and beryl - $Be_3Al_2Si_6O_{18}$. Inosilicates (single chain silicates) are formed when SiO_4^{4-} tetrahedrons share oxygens in a way to create long single chains with the basic structural units SiO_3^{2-} or $Si_2O_6^{4-}$. Minerals from pyroxene group such as the enstatite $MgSiO_3$ or diopside $CaMgSi_2O_6$, wollastonite $Ca_3Si_3O_9$, rhodonite $Mn_5Si_5O_{15}$[49] are representatives of single chain silicates (Figure 1.3.1.4).

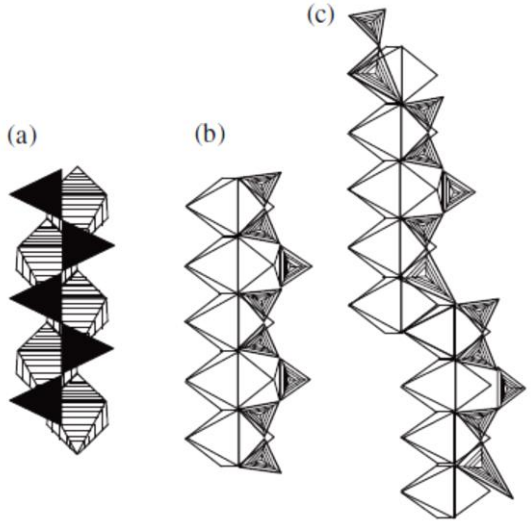

Figure 1.3.1.4 Structures of some inosilicates (single chain silicates): (a) diopside – $CaMg[Si_2O_6]$; (b) wollastonite - $Ca_3[Si_3O_9]$; (c) rodonite - $Mn_5[Si_5O_{15}]$.

Inosilicates with double chain structure (basic structural unit $Si_4O_{11}^{6-}$) are formed from two chains of SiO_4^{4-} tetrahedrons linked together in a way to share three oxygens from each tetrahedral group.

Phyllosilicates (sheet silicates) are composed of tetrahedrons that join together in form of sheets. Thus, in the clay minerals three of the four oxygens in each tetrahedron are shared with other tetrahedrons giving a continuous sheet as shown in Fig. 1.3.1.2. Three of four oxygens in each tetrahedron are valence-satisfied. As the fourth oxygen is only bonded to one Si, the silica layer can join cations of similar structures like gibbsite layer. The basic formula of silica sheets is therefore $(SiO_{2.5})^-$ or $(Si_2O_5)^{2-}$. Besides clay, minerals such as micas, talc, serpentines, etc. belong to sheet silicates. In tectosilicates (framework silicates) like quartz and in its polymorphs (tridymite and cristobalite) each SiO_4^{4-} tetrahedron shares the corner oxygens with other four tetrahedrons. Likewise feldspars are the framework silicates in which Al^{3+} can substitute for some Si^{4+} ions

resulting in different arrangements of Na^+, K^+ and Ca^{2+} cations within the framework structure to achieve charge balance.

The thermodynamic properties of aluminosilicate glasses are mainly related to their composition and network connectivity. When introducing Al_2O_3 in the fully connected cornersharing tetrahedral network of amorphous silicates, the Al atoms substitute for the Si atoms in the center of the tetrahedra thus leading to charged $(AlO_4)^{5-}$ units. In order to maintain local charge neutrality, $(AlO_4)^{5-}$ units can be charge compensated by alkali cations (K^+, Li^+) which must be present in the vicinity of each such tetrahedron. Therefore, the $(AlO_4)^{5-}$ tetrahedra substitute directly into the network for silicon-oxygen tetrahedra, and simultaneously tend to suppress the immiscibility while raising the glass transition temperature and decreasing the CTE of glasses [50-51]. However, if the concentration of these cations becomes larger than needed for a full compensation of the $(AlO_4)^{5-}$ units, then the cations play the role of modifiers. Indeed, they create non-bridging oxygens (NBO) by breaking T-O-T linkages (T=Si, Al) and/or play the role of charge balancing, by neutralizing the AlO_4 entities. Considering the abovementioned features, alkali or alkaline-earth oxides such as Na^+, K^+, Ca^{2+}, Mg^{2+}, Sr^{2+}, Ba^{2+} etc., can serve both as charge compensators and/or as network modifiers in aluminosilicate glasses. These cations perturb silicate frameworks linked by bridging oxygen (BO) and by forming non-bridging oxygens (NBO), which play essential roles in many dynamic properties of melts. In principle, the number of NBO atoms in a glass is directly related to the viscosity of the glass forming liquid [66]. The types of cations in oxide glasses can cause different states of disorder depending on their characteristics, such as ionic radius, charge, field strength, and on their local environments. In Figure 1.3.1.5 is illustrated the $(Si_2O_5)_n^{2n-}$ tetrahedral silica layer.

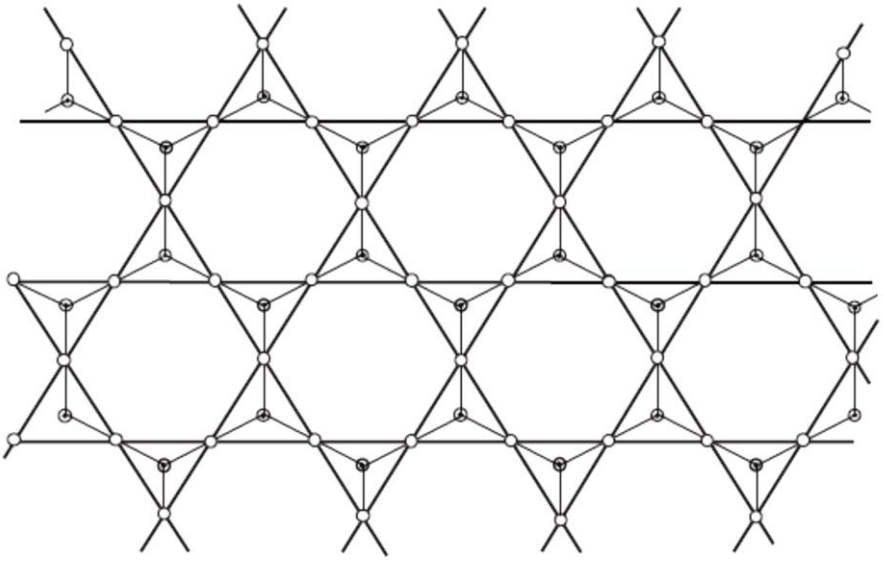

Figure 1.3.1.5 $(Si_2O_5)_n$ $^{2n-}$-tetrahedral silica layer.

Generally speaking, if a molten glass material is cooled sufficiently fast from the liquid state so that there is not enough time to form crystalline structure, the glassy state is formed. Ideally, when a liquid is slowly cooled from high temperature to room temperature so that crystallization takes place, its specific volume decreases continuously until the melting point is reached, then a rather large jump occurs associated with a large volume

change (ΔV^m) as the material transforms from the liquid state into a crystalline solid state [52]. This behavior is shown in the Figure 1.3.1.6 for path 1: as soon as the temperature falls below the crystallization temperature, T_C, the volume of the system contracts from A to B and a crystalline material is formed. On the other hand, in the path 2 an undercooled liquid continues to shrink further to point C; and if the cooling is sufficiently slow even further to point D. Here, the curve flattens out towards F. By fast cooling the glass continues to shrink linearly directly from C to E. In both case, it will always remain above the line B-G of the crystalline system.

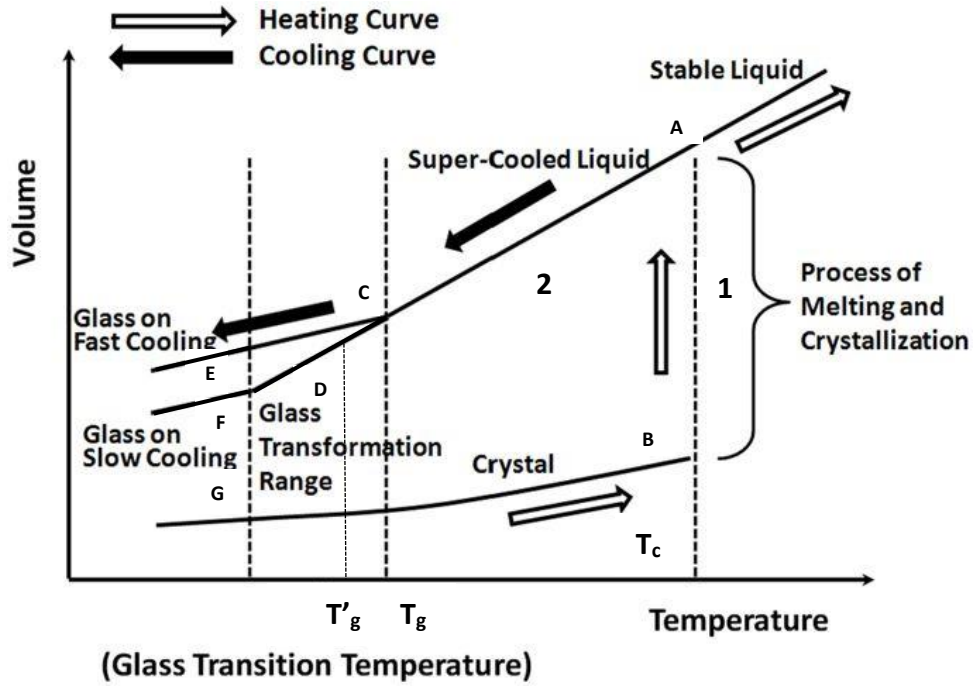

Figure 1.3.1.6 Volume changes versus temperature for a crystalline system (1) and a glass system (2). Path CE-fast cooling, CF-slow cooling. Glass transition temperature T_g depend on the cooling rate.

The temperature T_g where the glass cooling curve flattens out, is called the glass transition temperature or glass transformation temperature. Actually, T_g represents the onset and T'_g the end of the glass transition range since T_g is not a unique material property but depends on the cooling rate. Below T'_g the glass is considered as a solid material where mechanical stresses can build up. The transition from the viscous state to the elastic state occurs within the viscosity range $10^{12.0}$-$10^{13.5}$ Pa·s. In this range, which is also denoted as *annealing range,* mechanical stresses that may have developed during cooling below T_g can be eliminated. At $10^{13.5}$ Pa·s, the elimination of stresses may take several hours [53]. This temperature range is dependent on the heating rate and accordingly it represents no precise definition.

During the heating of a glass, the dilatometric softening point, A_t, or deformation point is reached above T_g as shown in Figure 1.3.1.7.

At this temperature the force from the dilatometer pushrod will deform the glass.

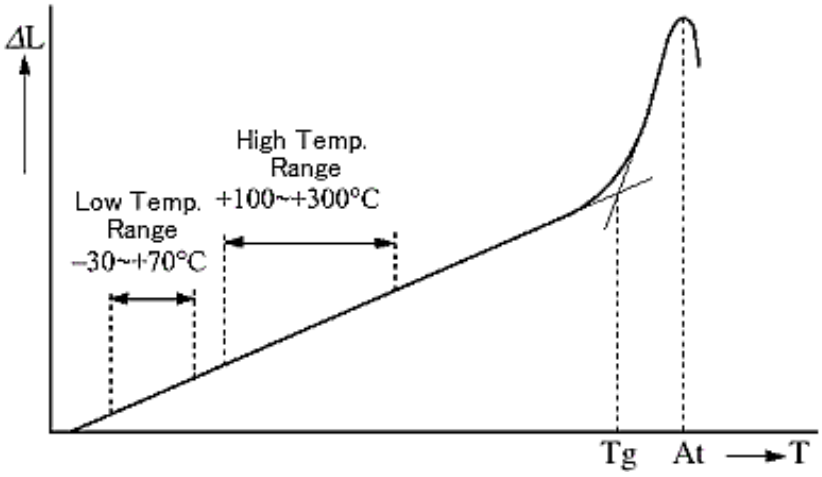

Figure 1.3.1.7 Typical thermal expansion curve of a glassy materials.

A typical viscosity of a silicate glass at A_t is $10^{10.3}$Pa·s, which is much higher than the typical viscosity at the softening point T_s ($10^{6.6}$ Pa·s) where the glass deforms under its own weight. The glass can be easily shaped at a viscosity about 10^3Pa·s (working point). To make a homogeneous glass, the glass must be heated to a temperature where the viscosity is below 10 Pa·s [54]. At T_g and T_s, the viscosity of pure SiO_2 are typically ~ 10^{11} and 10^9 Pa·s, respectively [43]. Generally, SOFC sealing glasses need to have lower viscosities than SiO_2 to achieve appropriate processing properties (Figure 1.3.1.8[55]).

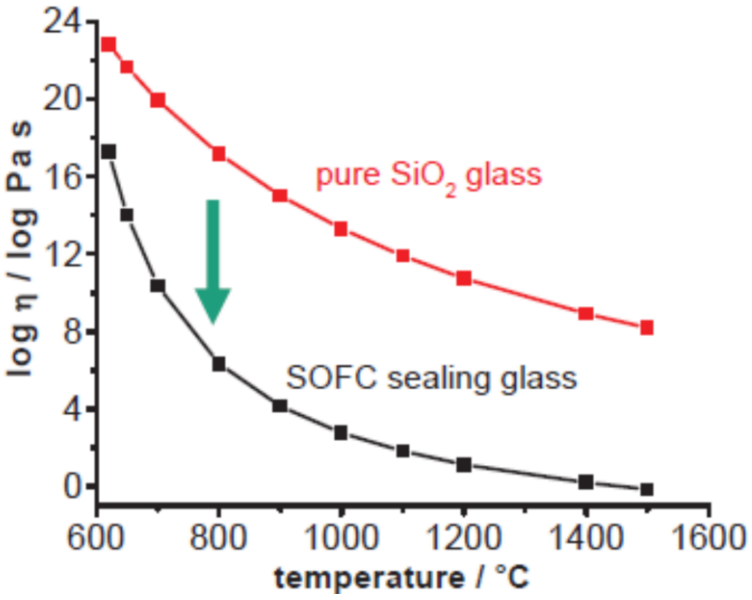

Figure 1.3.1.8 General relationship between viscosity and temperature.

T_g and T_s can be controlled by the composition of the glass material. However, the softening point of a remaining glass component can limit the maximum operating temperature to which the joint may be exposed [56]. The most important criteria for the initial design and development of a sealant glass are T_g (glass transition temperature), T_s (glass softening temperature), CTE (thermal expansion coefficient) and viscosity [57].

Glass must show an adequate viscous behavior to enable joining by softening, while maintaining a sufficiently high viscosity not to flow out. The glass transition temperature (T_g) and softening temperature (T_s) are needed to predict the flow characteristics of a glass. In the scientific literature as well as in commercial applications, glass sealants with low T_s show high thermal expansion and vice versa. Hence, for specific applications like SOFCs, the development of new sealing materials is required.

The target range for both parameters, T_g and CTE, suggested by Geasee et al.[58] is shown in Figure 1.3.1.9.

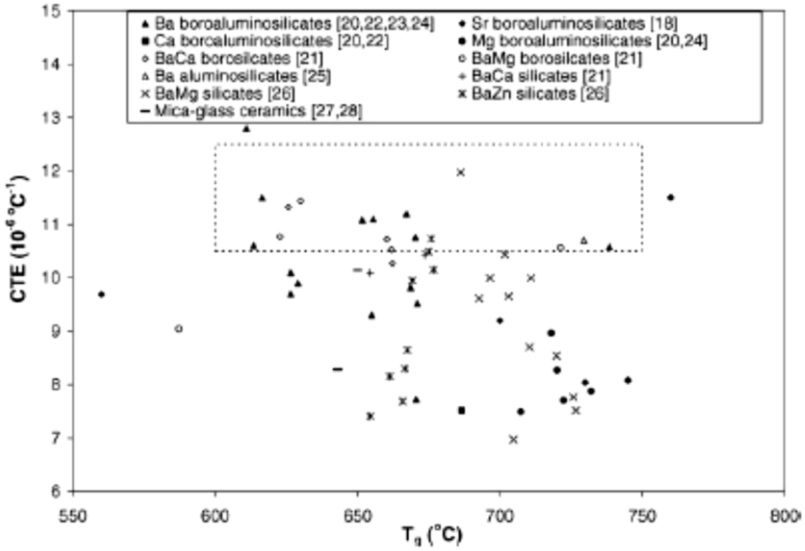

Figure 1.3.1.9 Glass transition temperature and coefficients of thermal expansion of sealant glasses for SOFC. The frame represents the target range defined by Geasee et al.[58].

The thermal expansion behavior of glass sealants depends on the chemical composition of the parent glass. Glasses in both BaO-MO-SiO_2 (M=Mg, Zn) systems show CTE rising with increasing BaO content at constant SiO_2 content [59].

The increase can be related to the lower field strength, as defined by Dietzel, of Ba^{2+} compared to Mg^{2+} and Zn^{2+}. Due to its lower field strength, the glass modifier is responsible for a higher weakening of the SiO_2 network structure, hereby enhancing its CTE. Indeed, both the glass transition temperature and the thermal expansion behavior of glass sealants depend on the chemical composition of the parent glass, with the presence of modifier cations usually having a considerable influence on these properties. For this reason, it's important to consider the effect of the field strength of alkaline and alkaline earth cations expressed as

$$F = \frac{z_1 z_2 e^2}{r^2}$$

where z_1 and z_2, respectively, are the valences of cation, *e* is the charge of ions, and *r* is the ionic radius.

The field strength of modifier cations follows the order: K^+ (0.17)<Na^+ (0.19)<Li^+ (0.23) for alkaline metals and Ba^{2+}(0.24)<Sr^{2+}(0.27)<Ca^{2+}(0.33-0.35)<Mg^{2+}(0.45-0.51) for alkaline metals [60]. T_g and T_s of a seal glass increase in the same order when these species are involved. T_g and T_s of alkaline earth oxide containing glasses are higher than alkali oxide containing glasses because of the higher field strength and lower mobility of alkaline earth ions.

On the contrary, the increase of CTE can be related to the lower field strength of the cations, therefore glass modifier is responsible for a higher weakening of the SiO_2 network structure, hereby enhancing its CTE. However, the thermo-elastic properties of glasses change upon progressive crystallization at high temperature. [58-61].

1.3.2 Glass ceramic

One of the most important class of materials utilized in high temperature joining are glasses and glass-ceramic [62-63]. Glasses and glass ceramics are suitable candidates as their properties can be tailored to the specific requirements of this technology by choosing the adequate components of the glasses and their proportions [64-65-66]. Experience shows that the glass partially or fully crystallizes during the sealing process to form a rigid bonded seal, representing the optimum.

Glass-ceramic materials share many properties with both non-crystalline glasses and crystalline ceramics.

They are formed as glasses, and then partially crystallized by heat treatment.

In general, glasses and partially crystallized glass ceramics possess a transition temperature, above which the material changes from a rigid and brittle state to a ductile behavior, which is needed to provide a sufficient flow and thus an adequate sealing [67-68].

However, the sealing material should not become too fluid as it can flow out from between the joining partners resulting in open gaps and subsequent leakages. In addition, a sufficient rigidity is crucial for maintaining the mechanical integrity. Crystallization is advantageous since the resulting microstructure is typically stronger than the amorphous glass. It is also a key aspect to minimize thermal expansion coefficient mismatches and hence thermally induced residual stresses.

In many cases, the CTE of glass ceramics is usually lower than that of the interconnect or electrodes. It has been reported in literature, that CTE is usually between 8 and $11.5 \cdot 10^{-6}$ °C^{-1}as compared to $12.5 \cdot 10^{-6}$ °C^{-1} for the interconnect [69]. Furthermore, it has been reported that to avoid thermally induced cracking a CTE difference of less than around $1 \cdot 10^{-6}$ °C^{-1} should be warranted [70].

The major advantages of glass ceramics compared to glasses are a lower chemical reactivity and higher durability of their physical and mechanical properties. In particular, a wide range of more stable thermal expansion coefficients can be obtained by controlling the crystalline phase content and their volume fraction.

To form a glass ceramic from a glass, the heating cycle show in Figure 1.3.2.1 is used.

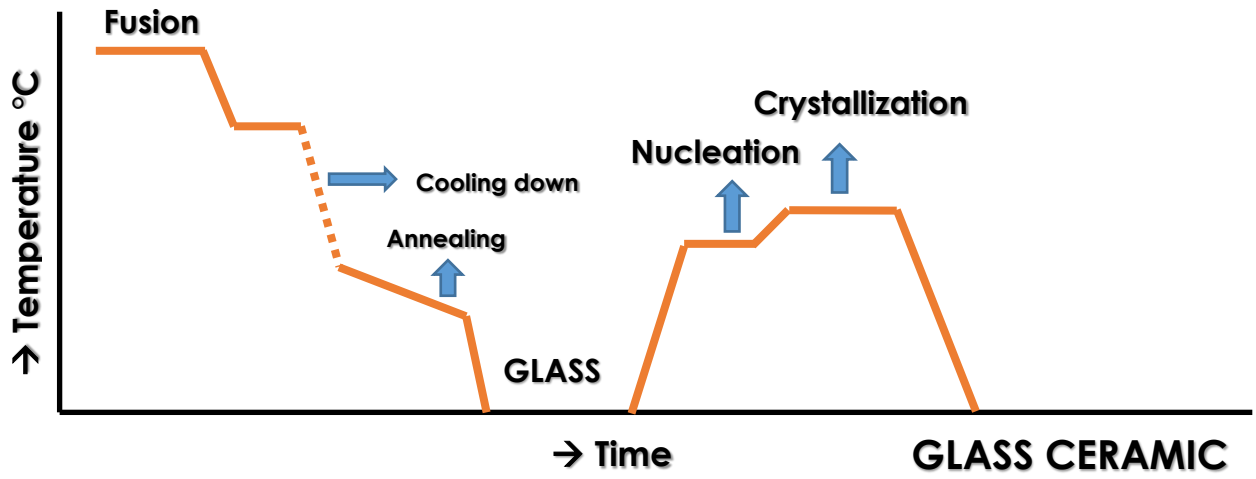

Figure 1.3.2.1 Heating cycle for glass ceramic synthesis.

Normally a glass powder (frit) already processed at high temperature is the starting material. The frit is heated to high temperature in order to get rid of gas bubble (fining). Then the temperature is lowered to the proper temperature for the material to be formed the final shape. When the forming step is finished, the temperature is lowered to the optimum temperature for nucleation and held constant for 10-15 min. When nucleation is finished the temperature is raised to the value for crystal growth. The crystallization temperature and the holding time depend on the intended crystal structure. To obtain a glass ceramic with high strength, the crystals should be numerous and small (<1µm). To achieve a large number of small crystals, the crystallization temperature should be "low". After crystallization the glass is cooled to room temperature. If the glass is reheated to temperatures corresponding to the crystallization temperature the crystals will continue to grow. In a glass that has to be used as a high temperature seal, the crystals should have completed their growth so that the system can achieve volumetric stability. This fact has to be considered when determining the sealing temperature cycle. It is an advantage to have only one crystalline phase. To avoid microcracking the thermal expansion of different phases should be similar to within a few % glassy phase operating at a temperature in the glassy stability region, just above T_g to avoid complete crystallization. However, in this temperature range there is a high nucleating activity. If the temperature is held constant in this range for long time, the glass will become completely crystalline.

As already mentioned, the main criteria for selection of suitable initial glass compositions are T_g and CTE, the task becomes more challenging in multi-component glass system typically used as sealants. Besides controlling the crystalline phase content of the glass-ceramic, an important point is to control the crystallization kinetics as well. Sealant glasses are usually processed by powder technology, and require sintering to full density as well as wetting of the substrate prior to crystallization, which increases the viscosity of the glass [71-72-73]. If crystallization occurs before complete sintering and wetting of the substrate, a high porosity or a poor adherence of the seal will result.

However, the thermo-elastic properties of glasses change upon progressive crystallization at high temperature. The key point is to control the thermal expansion behavior of the resulting stable, rigid glass-

ceramic. In binary or ternary glass system, it can be predicted by thermodynamic calculation of coexistent crystalline phases, using their individual CTE and the relative amount of residual glass [61-74]. Kinetic factors, problems of phase stability intervene in the equation and influence the physical properties of the material. For instance, barium and strontium aluminosilicates crystallize to form Celsian ($RAl_2Si_2O_8$, R=Ba, Sr) in addition to barium silicates [75-76-77-78-79-80]. Both the high temperature metastable hexagonal ($\alpha_{20\text{-}600°C}$ = 7-8·10^{-6} °C^{-1}) and the stable monolithic ($\alpha_{20\text{-}600°C}$ = 2-3·10^{-6} °C^{-1} [81-82]) forms have low coefficients of thermal expansion. In addition, the hexagonal forms undergo a structural transformation into orthorhombic at about 300°C, associated with large volume change [81-83]. In some compositions, Quartz or Cristobalite can also appear, whose large CTE ($\alpha_{20\text{-}600°C}$ = 23.3·10^{-6} °C^{-1} and $\alpha_{20\text{-}600°C}$ = 27.1·10^{-6} °C^{-1}, respectively [63]) could be detrimental. Cristobalite is particularly problematic due to a transformation that occurs upon cooling with a large decrease of about of 8% causing cracking [84]. The formation of detrimental phases affect the material properties after long-term annealing treatments by reducing the CTE and/or affecting the thermomechanical integrity. Among earth-alkaline modified aluminosilicates glasses, barium-based glasses show faster crystallization than calcium- and magnesium- based glasses [76-85]. The lower activation energy for crystallization with barium as a network modifier is attributed to the lower field strength of Ba^{2+} (0.27) compared to Ca^{2+} (0.36) and Mg^{2+} (0.47), implying a higher weakening of the SiO_2 structure. As a consequence, barium aluminosilicate glasses crystallize at lower temperatures and more completely than other earth-alkaline-based glasses. The crystallization kinetics can be modified by addition of the so-called nucleating agents [76-86]. In magnesium aluminosilicate glasses, small addition of TiO_2, Cr_2O_3 and Ni enhanced the activation energy for crystallization, whereas ZrO_2 decreased it. The first group of additives can adopt tetrahedral oxygen coordination besides having higher coordination as network modifiers, whereas the latter solely acts as a modifier favoring crystallization. Additional agents also enable to control the phase content of glass-ceramics. Chromium and titanium oxides have the beneficial effect of inhibiting the formation of cordierite ($Mg_2Al_4Si_5O_{18}$) which has a very low CTE (α= 1·10^{-6} °C^{-1} [82]). Titania and zirconia both decrease the CTE of barium-as well as magnesium-aluminosilicate glasses, but show contrasted effects on the glass transition, indeed TiO_2 additions decrease the T_g of glasses while ZrO_2 additions increases it. In order to tailor the viscous behavior of glasses for sealing in a particular temperature range (750°-950°C), compositions have to include additional glass-forming and flux oxides. Compositions that match the criteria for T_g and CTE are essentially alumino- and borosilicate glasses. Aluminum oxide is introduced to extend the glass-forming region in earth-alkali modified silica glasses, with significant effect up to 10wt% [77]. The effect of intermediate oxides on T_g and T_s is less straightforward because of their dual functional on glass network structures. The most well-known intermediate is Al_2O_3, which has been added into many of the SOFC seal glass compositions. Al_2O_3 behaves as a glass network former when Al^{3+}ion is 4-coordinated and as a glass network modifier when Al^{3+}ion is 6-coordinated. In a silicate glass, Al^{3+} ions exist as AlO_4^- tetrahedra and T_g and T_s increase with addition of alkali or alkaline earth oxides until other modifier ions and Al^{3+} ions reach 1:1 ratio. Once ratio is greater than one then Al^{3+}ions exist in AlO_6^- octahedra

and Al_2O_3 acts as a glass network modifier, resulting in a decrease of T_g and T_s. Low field strength modifiers (such as Ba^{2+} and Sr^{2+}) favor the formation of AlO_4^- tetrahedra and high field strength modifier ions (such as Mg^{2+}) favor the formation of AlO_6^- octahedral for borate glass [87]. For a borosilicate glass, modifier ions generally favor AlO_4^- tetrahedra formation. Once the amount of Al^{3+}ions exceeds the amount of modifier ions, formation of borate tetrahedra is favored [88]. Again, T_g and T_s increase for 4-coordinate Al^{3+}ions and decrease for 6-coordinates Al^{3+}ions. Higher contents led to fast crystallization of glasses upon cooling. Hence, depending on the glass composition, aluminium at low amounts can adopt a tetrahedral coordination and play a role of a glass former, but a larger amount becomes six-fold coordinated and acts as a glass modifier. Due to its dual role, aluminium has been reported both to inhibit and to enhance crystallization, inducing phase separation [76-89]. Furthermore, glasses containing alumina formed hexacelsian upon crystallization, which low CTE and instability is critical to thermomechanical properties. Boron oxide is a glass-forming oxide that decrease the T_g and T_s of the sealant [58-89-90-91]. It is also found to increase the CTE in borosilicate compositions, but the effect is overlaid by the variation in other components at low amounts of boron oxide. Boron oxide is expected to stabilize the amorphous structure as a glass-former, however its effect on the crystallization kinetics is not clear. Since it lowers the viscosity of a glass, boron oxide both favor crystal growth at lower temperatures, but decreases the crystal growth rates[92]. Beside silicate glasses, other glass-forming systems have been investigated for application as sealant SOFCs. Boro-aluminophosphate glasses were developed by Larsen and James [93-94]. These glasses present low CTE but at the same time, they show high evaporation rates at an operating temperature of 1000°C, both in air and in wet fuel gas (> 0.2 $mg \cdot cm^{-2} \cdot h^{-1}$). Despite an attempt to stabilize phosphate glasses by partial substitution of phosphorus by silicon oxide, the improvement in glass stability was balanced by a loss in the CTE, so that the glass properties were insufficient for an application in SOFC conditions. Borate and borosilicate glasses with high boron oxide contents show a low stability against evaporation in wet fuel atmospheres. Alkaline oxides, which are commonly used as flux oxides in commercial glass sealants, also show high evaporation rates in humidified atmospheres. In addition, alkali species enhanced the chromium evaporation rates from interconnect materials at high temperatures, hereby leading to accelerated degradation of both the interconnect and cathode materials [95-96]. The chemical compatibility of sealing materials with yttria stabilized zirconia is generally good. Earth-alkali boro- and aluminosilicate glasses show a limited interaction with 8YSZ, with no diffusion of the glass species into the electrolyte and limited diffusion of yttrium and zirconium into glass. Phase formation observed in powder mixtures of barium, calcium and magnesium aluminosilicate glasses with nickel and YSZ after annealing at 1000°C for 1000 h showed that only zirconia reacted with Ba, Ca and Si to form mixed zirconate phases, in both air and humidified Ar/4% H_2. The compatibility of glasses with interconnect materials is more problematic due to the high reactivity of alkaline earth oxides with chromium, which is a component of both ceramic and metallic interconnects. Among earth-alkali aluminosilicate glasses, those containing barium oxide show the highest reactivity whereas glasses based on magnesium oxide show the least interaction with a chromium-based alloy.

While a mixed spinel $(Mg,Fe)(Cr,Al)_2O_4$ is observed at the interface of magnesium aluminosilicates, chromate phases like $Ca_3Cr_2(SiO_4)_3$ and $BaCrO_4$ are formed in calcium and barium aluminosilicates, respectively [85]. Secondary phases that arise due to reaction or interdiffusion between the seal and the joining materials can be detrimental not only to the seal, but also to membranes, electrolytes, electrodes and interconnects. The number and composition of the secondary phases are determined by composition of joining materials and of the temperature and atmosphere they are exposed to. It is beyond the scope of this work to make a full review of all systems that have been evaluated but it is of crucial importance to understand the interfacial reactions in order to be able to make stable and reliable power systems based on SOFCs. Generally, secondary phases with low or high thermal expansion compared to the pure seal and the joining components must be avoided. Due to the high chemical activity of barium oxide at high oxygen partial pressure, the reactions leading to formation of barium chromate are the most extensive in air, whereas in a reducing atmosphere chromium dissolves into the glass [97-98].

Formation of $BaCrO_4$ is likely to occur when using glasses containing BaO as seal against chromium containing materials, i.e. the high temperature ferrochromium alloys. These alloys form a Cr_2O_3 protective scale during peroxidation before sealing. During the sealing process $BaCrO_4$ is formed. Two possible reactions are shown in eq. 1.1 and 1.2.

$$2Cr_2O_3(s) + 4BaO(s) + 3O_2(g) = 4BaCrO_4(s) \quad (1.1)$$

$$CrO_2(OH)_2 + BaO = BaCrO_4(s) + H_2O(g) \quad (1.2)$$

The first reaction involves BaO and the Cr_2O_3 scale (eq.1.1). In humid atmosphere chromium oxyhydroxide $CrO2(OH)_2$ (g) can be present, resulting in formation of $BaCrO_4$ and water vapor (eq. 1.2). The gas can in turn result in bubble formation in the seal.

$BaCrO_4$ has an orthorhombic structure with high linear coefficients of thermal expansion $\alpha_a = 16.5 \cdot 10^{-6}$ °C $^{-1}$, $\alpha_b = 33.8 \cdot 10^{-6}$ °C $^{-1}$, and $\alpha_c = 20.4 \cdot 10^{-6}$ °C^{-1} in the temperature range 20-813°C [99]. Due to the large mismatch with the CTE of interconnect materials, the formation of the phase lead to cracking at the interface between glasses and interconnect upon cooling. These are two reasons why BaO-containing glass ceramic should be avoided as seal for chromium containing components.

In addition to the compatibility with other components, the sealant should withstand the specific atmospheric conditions of a fuel cell, where it is simultaneously exposed to air on the cathode side, and wet fuel on the anode side. Several studies reported on an anomalous oxidation behaviour of metallic interconnect materials under dual atmosphere exposure, where a fast growth of ferrous oxide nodules was observed on the air side of the seal [96-100-101]. Such behavior could not be fully explained by hydrogen permeation through the metal, as it is significantly reduced by the formation of a protective oxide layer in chromia-forming materials. In the first case, the reaction of alkaline elements from the sealant, a Pyrex glass, with the chromium oxide scale

could stand for its decomposition and subsequent fast oxidation of the bare ferritic steel to form a thick Fe-oxide scale. In another case the phenomenon occurred as a consequence of inner oxidation of the ferritic steel, under the combined presence of minor oxides in the glass composition and certain impurity content in steel. The initiation of the corrosion was related to the reduction of PbO from the glass in the H_2/H_2O atmosphere, because the oxygen partial pressure is lower than its dissociation pressure, and subsequent liquid phase (T_m (Pb) = 328°C) internal oxidation of the steel. The internal attack along grain boundaries resulting in a local volume change in the steel caused a crack formation at the glass-ceramic-to-steel interface. By propagation of the process along the interface, the internal oxidation reached the air side, where chromium depletion in the steel is accompanied by a loss of the ability to maintain a protective chromia layer. The rate of the corrosive attack was observed to depend both on the presence of easily reducible species like PbO in the glass, and on the content of impurities such as Si and Al in the ferritic steel. Nevertheless, barium calcium aluminosilicate glasses have been successfully used as sealants in fuel cell stacks operated at 800°C beyond 6000 h of continuous operation [102-103].

1.3.1 Seal glasses for SOFCs

During the last 20 years several seal glass compositions for SOFCs have been proposed and evaluated. The main focus has been on tailoring CTE, T_g, T_s and T_C values to specific design and temperature of operation in order to find glass-ceramic seals that are stable and chemically compatible for long time operation. The majority of the proposed seal glasses for SOFCs can be divided in two groups; one B_2O_3-containing and one without B_2O_3. Boron-silicate glasses can be used for low to intermediate temperature systems, while those without boron oxide are best suited for high temperature systems.

Most of the proposed seal glasses in this group consist of the oxides such as B_2O_3, SiO_2, Al_2O_3, BaO, CaO and SrO. Boron silicates have excellent seal performance due to high wetting ability and low viscosity during sealing. Glasses in this group might have chemical stability in both dry and humid H_2 atmosphere at 800°C [104]. These compositions also show good seal performance during thermal cycling between room temperature and 800°C. The effect of the different components on the glass properties depends on the overall composition of the glass. Normally, B_2O_3 lowers T_s and T_g, but if the B_2O_3/SiO_2 ratio is held constant B_2O_3 additions have little effect on the two temperatures. This was demonstrated by Sohn et al. [89] for the glass (20-40)BaO-10Al_2O_3-5La_2O_3-(12.5-21.7)B_2O_3-(29.2-43.3)SiO_2 where the ratio B_2O_3/SiO_2 is held constant at 0.5. T_g and T_s for all compositions were in the range 668-671°C and 735-745°C respectively. The thermal expansion can also be tailored within wide ranges for these glasses but the effect of different oxides differs for the various glass systems. Jinhua et al.[105] evaluated a series of glasses with composition (mol%) 33.3SiO_2-16.7B_2O_3-10Al_2O_3-5La_2O_3-35(CaO+BaO) where CaO is gradually substituted with BaO in the range 0-35mol%. For this range the CTE varied from $7.6 \cdot 10^{-6} °C^{-1}$ to $13.0 \cdot 10^{-6} °C^{-1}$. The glass with 35% CaO has the lowest CTE while the highest is observed for the glass with 35% BaO. This shows that CaO lowers the CTE while BaO increases it. La_2O_3

addictions will also have a positive effect on increasing the CTE [89-106]. SiO_2 and Al_2O_3 have normally a negative impact on the CTE. In a series of boron silicate glasses with constant B_2O_3/SiO_2 ratio of 0.5 the effect of MgO, SrO, Al_2O_3, La_2O_3 and Y_2O_3 on the CTE is investigated. The result shows that Y_2O_3 and SrO increased CTE, MgO and Al_2O_3 lower the CTE, while La_2O_3 has little influence. The aluminosilicate seal glasses, with the formula $MO\text{-}Al_2O_3\text{-}SiO_2$ (M=Ca, Ba, Mg, Sr and Zn) are reported in many research works [79-107-108-109-110]. By adding up to 75 vol% MgO filler to a sodium-aluminium-silicate glass (NAS), the CTE increased linearly from 11.5 to $13.7 \cdot 10^{-6}$ °C^{-1}. 32 vol. % MgO seemed to be the maximum due to reduced mechanical properties for higher MgO contents. The glass/MgO composite seal worked well above 850°C as seal material for the interconnect alloy Crofer22APU. The sintering and thermo-physical properties of glasses in the system $30BaO\text{-}5Al_2O_3\text{-}50SiO_2\text{-}15RO$ (mol%) where R=Ca, Mg, Ba and Zn have been investigated [79]. T_g varied between 692°C and 719°C with the addition of Zn, Ba, Mg and Ca, respectively. ZnO-addition had the largest effect on lowering T_g compared to the other. The pure barium-aluminium-silicate glass (BAS-glasses) with 45% BaO has a CTE of $13.2 \cdot 10^{-6}$ °C^{-1} while for the other 3 additives the same CTE of 9.7±0.1 10^{-6} °C^{-1} is observed. In BAS-glasses thermal expansion can be modified within wide limits by changing the BaO-content. For the same glass system, the glass transformation temperature and the softening temperature could be effectively tailored by varying the alumina content.

Chapter 2

Experimental

2.1 Experimental method

The CaO-MgO-Al_2O_3-SiO_2 (CMAS) quaternary system is one of the most promising glass-ceramic materials for its excellent mechanical properties and good chemical resistance related to the precipitation of different type of crystals. CMAS glass-ceramics have become good candidates for functional applications such as sealants for solid oxide fuel cells, architectural applications such as building materials for interior and exterior walls, and heavy industrial applications such as protective materials for bunker, funnel and chute [111-112-113]. As mentioned, in this research work the attention is placed on the study of the properties of the CMAS system for a new kind of sealant materials for SOFCs.

Two series of aluminosilicate glasses have been evaluated with a view to the application as high-temperature glass ceramic seals, based on the CaO-MgO-Al_2O_3-SiO_2 and CaO-MgO-Al_2O_3-SiO_2-B_2O_3 systems. While these systems have already been demonstrated to show adequate properties for the application as sealants in SOFCs, a full understanding of the relationship between the glass chemical composition and its relevant properties has not been achieved, and the crystallization kinetics as well as related properties of the glass-ceramics were only partly investigated.

The crystallization of CMAS glass-ceramics is known to be very difficult to control, which severely limits the preparation and application of CMAS-glass ceramics [114]. Sintering process and body crystallization process are the two main preparation methods for CMAS- glass ceramics. The former is derived from sintering of fine ceramics, consisting of glass melting and high temperature sintering, while the body crystallization process is similar to the production procedure of plate glass, and includes glass melting, annealing and crystallization. In comparison with body crystallization processes, it is relatively easy to control the crystallization of CMAS glasses by the sintering process, but it is very difficult to obtain the fully dense glass ceramics. Recently, a significant improvement in the crystallization of CMAS glasses was achieved by adding nucleation agents. On of the aim of this research is to analyze the effect of different types of nucleating agent on the CMAS system and to study the effect of substituting a glass former as SiO_2 with another glass former like B_2O_3 in the sintering and crystallization (see Chap. 3) processes.

2.2 Preparation of glass

All glasses were prepared from the pure powder raw materials shown in Table 2.2.1.

Chemical	Supplier	Purity
SiO_2	Minerali industriali S.p.A.	>99.0%
$CaCO_3$	Minerali industriali S.p.A.	>99.0%
$MgCO_3$	Minerali industriali S.p.A.	>99.0%
Al_2O_3	Minerali industriali S.p.A.	P.a.
H_3BO_3	Carlo Erba Reagents S.r.l.	99.6%
TiO_2	Carlo Erba Reagents S.r.l.	99.5%
MnO_2	Keramtone S.r.l..	P.a.
ZnO	Keramtone S.r.l.	P.a.
SnO_2	Keramtone S.r.l.	P.a.

Table 2.2.1 Raw material used for glass preparation.

Carbonates are used as the alkaline earth oxide precursors. These raw materials lose weight under firing due to the well-known thermal decomposition leading to the corresponding oxide and CO_2. Before the individual batch compositions are made, the weight loss was measured on each raw material by heating well above the decomposition temperature to find the oxide content. For the synthesis of glasses, the traditional solid state route has been employed.

In the first step, the raw materials for each system are mixed together by dry mixing for 2h in a high-speed alumina ball milling (Nannetti Faenza, Italy). The homogeneous mixtures of batches (~300 g) are melted in fire clay crucible in a globar furnace. Heating is carried out in four steps with the following rates:

1. 20-400°C at 200°C/h
2. 400-1000°C at 100°C/h
3. Isothermal step at 1000°C for carbonate decomposition
4. 1000-1400°C at 100°C/h

After reaching the maximum temperature, an isothermal step at 1400°C for 90 min is performed to melt the powder. The melt is then quickly cooled (50°C/min) to produce the glass by operating the controlled cooling mechanism of the oven. To prevent cracking during cooling the sample is kept inside the furnace. The residual stress is removed by annealing at 800°C for 1 hour followed by cooling at a rate of 30°C/min. The glass yield is calculated by comparing the weight of glass product with the theoretical yield calculated from batch weight.

Samples of 100 g glass are milled in 30 g acetone with 0.3 g PVB (Polyvinyl Butyral) as a dispersive agent. A vibratory agate mill is used at a speed of 300 rpm to grind the glasses with agate balls of three different sizes during the following times: 30 min. with four 30 mm diameter balls, followed by two times 10 min. with sixteen 20 mm and then with fifty 10 mm size balls. The grinding process is modified to obtain different distributions of particle size. Fine powders are produced either by increasing the grinding times to 1.5 h with medium and

small size balls, or by grinding smaller shares of 30 g of glass. Coarse powders are obtained by milling only with big size balls. The glass powders are subsequently dried at 60°C for one day.

2.3 Characterization of glass and glass-ceramic

2.3.1 Glass properties

Chemical Analysis

Two methods were used for determining the composition of glass powders.

For aluminosilicate glasses without boron oxide, X-Ray Fluorescence analysis (AXIOS – PANALYTICAL) was performed. To this end, glass powder (8 g) is mixed with a $C_{18}H_{36}O_2N_2$ wax (2.5g), and a tablet with a diameter of 4.5 cm is prepared by uniaxial pressing (80 MPa). Since this technique is known to be inappropriate for light elements such as boron, B_2O_3-containing glasses were analysed by optical emission spectroscopy (OES). 100 mg of powder were mixed with 1 g NaOH and melted at 500°C for about 30 min enclosed in a fire clay crucible. The melt is dissolved in water and poured in 50 ml HCl (3%). The solution is fed into an inductively coupled plasma (ICP), and the resulting characteristic radiations emitted were analyzed. This method enables a quantitative analysis of main elements (> 1 wt.%) with a relative experimental error of ± 3 %, while minor elements (> 0.1 %) and impurities (> 0.01 %) are detected with larger errors of 10 to 20 %.

Particle size analysis

Particle size distributions was measured by the laser scattering method (Alfatest, Mastersize Hydro 2000). The method relies on the principle of laser light scattering, where interference fringe patterns resulting from the low angle light scattering on particles of different sizes can be related to their dimensions. The apparatus enables to measure sizes down to 0.1 µm. The analysis is performed in a water dispersant.

Hot-stage microscopy

In order to determine the sintering behavior and the characteristic temperatures of glasses, a Hot Stage Microscope (HSM) equipped with image analysis system and electrical furnace Expert System Solution – MISURA ODLT 1600°C. was used The microscope projects the image of the sample through a quartz window and onto the recording device. The computerized image analysis system automatically records and analyzes the geometry changes of the sample during heating. The image analyzer takes into account the thermal expansion of the alumina substrate while measuring the height of the sample during firing, with the base as a reference. The HSM software calculates the percentage of decrease in height of the sample during firing, with the base as a reference. The measurements were carried out in air with a heating rate of 15°C/min. Cylindrical shaped samples with height and diameter of ~ 3mm were prepared by pressing glass powders. The cylindrical

samples were placed on a 10x15x1 mm alumina (>99.5 wt% Al_2O_3) support. The temperature was measured with Pt/Rh (6/30) thermocouple contacted under the alumina support. The temperatures corresponding to the characteristic viscosity points (first shrinkage, maximum shrinkage, softening, half ball and flow) were obtained from the photographs taken during the hot-stage microscopy experiments following the Sholze's definitions and refs [115-116].

Dilatometry of glassy samples

The primary criteria for the selection of glasses for sealing purposes are the combination of a high glass transition temperature T_g with a high coefficient of thermal expansion (CTE). Bulk glass samples are tested after annealing them in a temperature range higher than their glass transition temperature for about 2 h. Rectangular bar free of thermal stresses with dimensions of 5mm x 5mm x 50mm are prepared by uniaxial pressing (80MPa). Samples are placed in the dilatometer and heated up with a rate of 10°C/min. The measurement proceeds until the glass has reached its softening point, at which the sample relaxed the applied load and the measurement stopped automatically. Characteristic temperature ranges corresponding to glass transition (T_g) and softening point (T_s) are extracted from the expansion curve. The former is obtained from the change of slope characteristic for glassy materials; the latter corresponds to the maximum expansion reached in the run. The thermal expansion of reference samples is previously measured to account for the thermal expansion of the apparatus, including the alumina housing. Two reference materials are measured, which thermal expansion behavior is well known, 738 stainless steel and alumina bar. The thermal expansion values obtained on glass samples are subsequently corrected accordingly. Measurements are performed in an optic dilatometer (Expert System Solution – MISURA ODLT 1600°C). Thermal expansion coefficients are calculated between room temperature and high temperature by the ratios of length change to the temperature difference.

Differential Thermal Analysis and theoretical models for the analysis of crystallization kinetics

Differential thermal analyses (DTA) were performed using a Netzsch STA 409C apparatus to investigate the crystallization behavior of glass powders. By measuring the difference of temperature between the sample and a reference empty alumina crucible in air, it is possible to estimate when heat is being used or provided by the sample, i.e. endothermic or exothermic reactions can be detected by the deviation of heat flux compared to the reference material. Glass powders were heated in air in an alumina crucible with a heating rate of 10°C/min up to a temperature of either 1200 or 1400°C. Characteristic temperatures of glass transition T_g, crystallization onset T_o or peak T_p, and "melting point" T_m are extracted from the characteristic endo- or exothermic signals. T_m is not properly a melting point but corresponds rather to the decomposition of the crystalline phase(s) formed during the run. Decomposition may occur with different mechanisms, and can be

influenced by the surrounding glass, whose chemical composition changes during phase formation, by melting of adjacent phases, and subsequent diffusion of species to the interface.

Different methods are developed to analyze the kinetics of glass devitrification in the last decades, which rely on a set of preliminary assumptions. The choice of the method and the interpretation of the experimental data must be done with caution. The values determined for activation energies may actually be overall values corresponding to nucleation and growth processes, or to the overlap of several crystalline phases, rather than specific to a single process.

The use of thermal analysis techniques such as differential thermal analysis (DTA) and differential scanning calorimetry (DSC) is quite widespread for the kinetic study of crystallization processes in amorphous solids, giving the potential for obtaining useful data with practical and simple procedures. In this work, the crystallization parameters, such as reaction order (n) and activation energy (E_a), were obtained by non-isothermal DTA experiments. In the non-isothermal method, the sample is heated at a fixed heating rate and the change in enthalpy is recorded as a function of temperature. When a reaction occurs during a thermal analysis run, the change in the heat content and in the thermal properties of the sample is indicated by a deflection of the DTA trace. It is conventional to represent an endothermic effect by a negative effect and an exothermic effect by a positive deflection. The activation energy and the position of the peak of a given reaction changes with changing the heating rate. The variation in the peak position may be used to determine the activation energy for first order reactions.

Many reactions of interest to materials scientists involve transformations in the solid state, such as recrystallization of a cold-worked material, precipitation of a crystalline polymer from an amorphous phase, or growth of an equilibrium phase from a non-equilibrium structure, the driving force for which is brought about by cooling. If we assume the initial phase to be α and the resulting phase to be β, the reaction is the following:

$$\alpha \rightarrow \beta \tag{2.1}$$

The total volume of the sample is the sum of the volumes of α and β

$$V = V^{\alpha} + V^{\beta} \tag{2.2}$$

The transformed fraction is usually represented in the literature as x

$$x = \frac{V^{\beta}}{V} \tag{2.3}$$

Let us assume that the transformation from α to β is controlled by nucleation and growth, that is, the nucleation of phase β within α and then the rate of growth of β, and let's indicate with N the nucleation rate per unit volume and with G the growth rate in one direction ($G = \frac{dr}{dt}$, assuming spherical form of β). The time line from zero to a time *t* is represented in Figure 2.3.1.1 below.

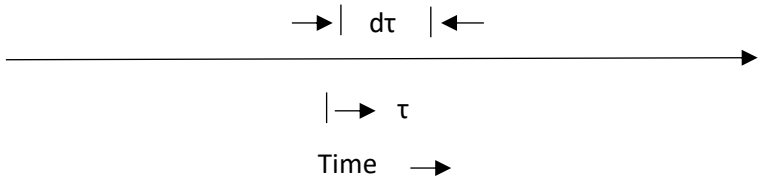

Figure 2.3.1.1 Definition of t and τ for derivation of solid state transformation equations.

We will consider another measure of time (τ), which starts when the nucleus is formed. The number of nuclei (*n*) formed in a differential time *dτ* is equal to

$$dn = NV^{\alpha}d\tau \tag{2.4}$$

Assuming that the particles nucleated as spheres, the radius of the particles after they have grown to time *t* is

$$\int_0^r dr = \int_\tau^t G \cdot dt \tag{2.5}$$

$$r = G\,(t-\tau) \tag{2.6}$$

and the volume of the particle nucleated at time *t* is

$$dV^{\beta} = \frac{4}{3}\pi G^3(t-\tau)^3(NV^{\alpha})d\tau \tag{2.7}$$

$$dV^{\beta} = \frac{4}{3}\pi G^3 N\left(V - V^{\beta}\right)(t-\tau)^3 d\tau \tag{2.8}$$

Early in the transformation, when V^{β} can be considered negligible compared to V, the transformed fraction may be calculated as follows:

$$\int_0^{V^{\beta}} dV^{\beta} = \int_0^t \frac{4}{3}\pi G^3 NV\,(t-\tau)^3 d\tau \tag{2.9}$$

$$V^{\beta} = V\frac{\pi}{3}G^3 N t^4 \tag{2.10}$$

$$x = \frac{V^{\beta}}{V} = \frac{\pi}{3}G^3 N t^4 \tag{2.11}$$

To treat the regime beyond the early transformation stages, the extended volume concept is adopted. In this case, the nucleation and growth rates are separated from geometrical considerations such as impingement. The extended volume (V_e) is the volume that would have been formed if the entire volume had participated in nucleation and growth, including the transformed portion $\left(V^{\beta}\right)$. In this case

$$dV_e^{\beta} = V\frac{4}{3}\pi G^3 N(t-\tau)^3 d\tau \tag{2.12}$$

$$V_e^{\beta} = \frac{4}{3}\pi V\int_0^t G^3 N(t-\tau)^3 d\tau \tag{2.13}$$

But the total volume is equal to the sum of the volumes of α and β

$$V = V^{\alpha} + V^{\beta} \tag{2.14}$$

$$\frac{V^{\alpha}}{V} = 1 - \frac{V^{\beta}}{V} = 1 - x \tag{2.15}$$

where $x = {V^{\beta}}/{V}$

The amount of β formed, dV^{β}, is the fraction of α times dV_e^{β}

$$dV^{\beta} = \left(1 - \frac{V^{\beta}}{V}\right)dV_e^{\beta} \tag{2.16}$$

Integrating Eq.2.15.

$$V_e^{\beta} = -V\ ln\left(1 - \frac{V^{\beta}}{V}\right) = -V\ ln(1-x) \quad (2.17)$$

Combining Eq. 2.13 and 2.17 yields

$$-\ln(1-x) = \frac{4}{3}\pi \int_0^t G^3 N(t-\tau)^3 d\tau \quad (2.18)$$

and if *G* and *N* are constant

$$-\ln(1-x) = \frac{4}{3}\pi G^3 N \int_0^t (t-\tau)^3 d\tau = \frac{4}{3}\pi G^3 N t^4 \quad (2.19)$$

$$x = 1 - exp\left(-\frac{\pi}{3} G^3 N t^4\right) \quad (2.20)$$

The resulting equation relating the transformed fraction to nucleation rate, growth rate and time is called the Johson-Mehl equation.

A similar treatment of the subject was given by Avrami. In general, he expresses the fraction transformed as

$$x = 1 - exp(-kt^n) \quad (2.21)$$

where *n* is called "Avrami exponent". To determine the value of Avrami *n* from Equation 2.20, the following mathematical manipulation is performed

$$x = 1 - exp(-kt^n) \quad (2.22)$$

$$1 - x = exp(-kt^n) \quad (2.23)$$

$$\ln(1-x) = -kt^n \quad (2.24)$$

$$ln[ln(1-x)] = \ln k - n \ln(t) \quad (2.25)$$

Thus the Avrami *n* is the slope of the plot of the logarithm of the logarithm of $(1-x)$ versus the negative of the logarithm of *t*.

Solid state reactions such as the nucleation and growth of crystalline phases in a glass can be described by the above reported Johson-Mehl equation [117-118] where *x* is the volume fraction crystallized at a given temperature T in the time *t, k* is the reaction rate constant and *n* the order of reaction. The reaction rate constant is related to the activation energy of the process, E_a, through the well-known Arrhenius relation:

$$k = \nu \exp\left[-\frac{E_a}{RT}\right] \quad (2.26)$$

Where v is a frequency factor, R the universal gas constant and T the absolute temperature.

Taking logarithms of relations 2.22 and 2.26 one obtains:

$$\ln\left[\frac{1}{(1-x)}\right] = n\ ln(k) + n\ ln(t) \quad (2.27)$$

$$ln(k) = \ln \nu - \frac{E_a}{RT} \quad (2.28)$$

Values of the crystallization parameters *k*, *n*, *v* and E_a are determined from a series of isothermal experiments performed in a narrow range of temperatures where crystal growth occurs with a steady rate, well below the temperature of maximal growth rate. The plot of the fraction crystallized, *x*, versus the isothermal hold time at different temperatures can be used to estimate the time to reach a given crystalline fraction at a given

temperature. Values of *k* and *n* are then determined plotting $\left[ln\left[\frac{1}{(1-x)}\right]\right]$ versus $ln(t)$ for different temperatures. A plot of $ln(k)$ versus $\frac{1}{T}$ is used to provide values of the activation energy E and the frequency factor v. The method may actually be not valid for transformations involving nucleation and growth unless a number of conditions are satisfied. In particular, the relation $x = 1 - exp(-kt^n)$ is defined under the following assumptions:

1. the boundary conditions can be ignored, i.e. the system is infinite
2. the nucleation occurs randomly and uniformly
3. the growth of particles ends up at their points of mutual contact but continues unrestricted elsewhere [119-120].

Therefore, the method can be reasonably applied only in a limited range of crystalline fractions, $x = 0.2 - 0.5$ to minimize the influence of early and later stages of crystallization.

The crystallized fraction can be estimated using different techniques. One of the well-established techniques is the analysis by DTA of either bulk glass samples, or glass powders of a well-defined particle size. DTA characteristics are produced by isothermal runs in a range of temperatures were a steady crystallization rate is expected. Under the assumption that the transformation rate is proportional to the heat flux evolved during the experiment, the fraction crystallized at any time is proportional to the amount of heat evolved, i.e. to the partial area under the exothermal peak. Hence the fraction x_i crystallized in time t_i is calculated by the ratio of the integral of the peak from t_0 to t_i, to the total integral of the peak.

In order to describe non-isothermal crystallization kinetics, the JMA equation has to be modified.

When the temperature follows a linear variation with time:

$$T = T_0 + \alpha\, t \tag{2.29}$$

where T_0 is the starting temperature and α is the heating rate, the reaction rate *k* is no longer a constant but varies with temperature and time

$$k = v\, exp\left[-\frac{E_a}{R(T_0+\alpha\, t)}\right] \tag{2.30}$$

and the equation (2.22) should be replaced by

$$x = 1 - exp(-u) \tag{2.31}$$

where $u = \int_0^t \left[\frac{d(k\,t)^n}{dt}\right] dt = \int_{T_0}^{T} \left[\frac{d(k\,t)^n}{dT}\right] dT$ (2.32)

Eq. 2.32. has been integrated by different authors under certain assumptions.

Matusita and Sakka [121-122-123] as well as Marotta et al. [124-125] derived eq. 2.32 to find that the rate of the chemical reaction associated with crystal precipitation in a glass is described by an equation of the type:

$$\frac{dx}{dt} = A_0\, \alpha^{-(n-1)}\, f(x) \exp\left(-\frac{m\, E_a}{RT}\right) \tag{2.33}$$

where A_0 is a constant, α the heating rate, $f(x)$ a function of the extent of reaction (in the form $f(x) = (1-x)^r$ with r is the order of reaction), n and m are numerical factors depending on the crystallization mechanisms and E_a the apparent activation energy for crystal growth.

Kinetic parameters, such as the apparent activation energy, E_a and the order of the reaction, can be derived from the non-isothermal methods of thermal analysis. Several methods were proposed, based either on the analysis of the peak height [124-126-127-128] or shape [129], or on the change of the peak crystallization temperature with the heating rate [130-131-132,133-134]. These different methods were employed in several studies to interpret experimental data obtained either by Differential Thermal Analysis (DTA) or by Differential Scanning Calorimetry (DSC).

Analysis of the peak height

One of the simplest methods is based on the studies of chemical reaction kinetics carried out by Borchardt and Daniels [126-127] and was developed by Piloyan [128]. The method is based on the assumption that the deviation of the signal from the baseline in the initial stages of the reaction is proportional to the reaction rate:

$$\Delta y = S \cdot \frac{dx}{dt} \tag{2.34}$$

where Δy is the deviation of the DTA or DSC signal from baseline, S the integral of the thermal effect, x the fraction reacted and $\frac{dx}{dt}$ the reaction rate.

Substituting equation 2.33 into equation 2.34 and taking logarithms gives:

$$ln\Delta y = \ln f(x) - \frac{m \cdot E_a}{R \cdot T} + C \tag{2.35}$$

where the constant C includes all constant terms. In the initial part of the reaction, the change in temperature has a larger effect on Δy than the change in x at heating rates commonly used in thermal analysis (10 to 20 °C/min) [128]. Therefore, the equation can be approximated by:

$$ln\Delta y = -\frac{m \cdot E_a}{R \cdot T} + C_1 \tag{2.36}$$

Given the knowledge of the crystallization mechanism and the corresponding value of m, the method enables to calculate an apparent activation energy for crystal growth from a single DTA run at a standard heating rate. Alternatively, it can be used to estimate the value of m for a glass if the activation energy is known. The shortcoming of the method is that complementary investigations are required to clarify the crystallization mechanisms.

Analysis of the peak shape

Another method to analyze the crystallization mechanisms was proposed by Augis and Bennett [129]. These authors pointed out that reactions with the same activation energy but different order of reactions will show crystallization events with the same peak temperature. The value of n determines the shape of the peak, with

higher the value of n, the narrower the peak. Augis and Bennett derived the following relation from the work of Kissinger [130]:

$$n = \left[\frac{2.5}{\Delta T_{1/2}}\right] \cdot \left[\frac{T_p^2 \cdot R}{E_a}\right] \quad (2.37)$$

where $\Delta T_{1/2}$ is the width at half-maximum of the crystallization peak. This expression is used to estimate the value of n for a glass whose activation energy is known.

Variation in the peak temperature with the heating rate

Several methods have been proposed to determine an apparent activation energy from the variation in the crystallization peak temperature with the heating rate, as observed by thermal analysis techniques.

The method was originally described by Kissinger to analyze first order reactions [130-131]. Matusita et al. [121] subsequently modified the equations to adapt the method to nth order reactions of crystallization in glasses. The method relies on the assumption that the crystallization mechanisms, i.e. the parameters n and m, do not change with temperature and heating rate. Furthermore, the maximum rate of a reaction is supposed to occur at the peak temperature.

Starting from equation 2.32, the rate of change of the volume fraction of crystals, $\frac{dx}{dt}$, reaches its maximum at the peak temperature, T_p. Solving the equation $\frac{d(\frac{dx}{dt})}{dt} = 0$, the following equation is derived:

$$\frac{\alpha^n}{T_p^2} = \left[\frac{A_o \cdot p \cdot R}{m \cdot E_a}\right] \cdot \left(1 - x_p\right)^{r-1} \cdot exp - \frac{m \cdot E_a}{R \cdot T_P} \quad (2.38)$$

where x_p is the volume fraction crystallized at T_p. It has been found empirically in several non-isothermal kinetic studies that the fraction crystallized at the peak temperature is insensitive to the heating rate and remains constant for usual heating rates of 1 to 20 °C/min. As a consequence, equation 2.38 can be rewritten as:

$$ln\left(\frac{\alpha^n}{T_p^2}\right) = -\frac{m \cdot E_a}{R \cdot T_p} + C_2 \quad (2.39)$$

If the crystallization mechanisms are precisely known and do not change with the heating rate, the plot of $ln\left(\frac{\alpha^n}{T_p^2}\right)$ versus $\frac{1}{T_p}$ for a range of heating rates provides a value for the apparent activation energy E_a, given the corresponding values of n and m. Appropriate values of the parameters n and m for various crystallization mechanisms are given in Table 2.2.1.1. In the particular case where surface crystallization is the dominant mechanism, equation 2.38 reduce to the equation defined by Kissinger for first order reactions [131]:

$$ln\left(\frac{\alpha^n}{T_p^2}\right) = -\frac{E_a}{R \cdot T_p} + C_2 \quad (2.40)$$

Another method was proposed by Ozawa [132-133], who extended the model of Johnson-Mehl-Avrami to non-isothermal crystallization kinetics. He developed a simplified method of analysis applicable to the fast

crystallization kinetics of polymer materials. The model was subsequently modified by Matusita et al. [122-123] in a similar way to the Kissinger model:

$$ln(\alpha) = -\frac{m \cdot E_a}{n \cdot R \cdot T_p} + C_3 \quad (2.41)$$

where *n* and *m* are the same crystallization parameters as in the previous equations (Table 2.2.1.1). The analysis gave results comparable to the Kissinger method, but with slightly higher values of activation energies. Similarly, equation (2.41) is reduced to the model of Ozawa in the particular case where surface crystallization is dominant.

Variation of crystallized fraction with the heating rate

Subsequently, Ozawa developed a simple method to evaluate the crystallization mechanisms from non-isothermal analysis, i.e. the parameter *n* and the reaction rate *k* as a function of the temperature [134]. He found the following relation, similar to equation 2.27:

$$ln\left[ln\left[\frac{1}{(1-x)}\right]\right] = n \cdot ln[k \cdot (T - T_0)] - n \cdot ln\alpha \quad (2.42)$$

Similar to isothermal studies, the crystallized fraction, *x*, between T_0 and a given temperature T is evaluated in a series of non-isothermal runs performed at various heating rates α. Values of *k* and *n* are then determined by plotting $ln\left[ln\left[\frac{1}{(1-x)}\right]\right]$ versus $ln\alpha$ for different temperatures.

The drawback of the method is the difficult estimation of the crystallized fraction at the same temperature for different heating rates, due to the shift of the exothermal peak.

Crystallization mechanisms

In both the modified models of Kissinger and Ozawa, an independent knowledge of the crystallization mechanism is necessary to assign the correct values to parameters *n* and *m* (Table 2.2.1.1).

Crystallization mechanisms are traditionally evaluated by isothermal crystallization kinetic studies, where the values of kinetic parameters *k* and *n* are the nearest to their equilibrium values at the given temperature. Therefore, the pre-exponential factor v and the activation energy E determined by equation 2.26 should be the closest to their correct values.

As an alternative to extensive isothermal studies, non-isothermal methods enable a faster evaluation of mechanisms, although with a lower accuracy. A combination of different methods of analysis (peak height, peak shape, variation of crystallized fraction with the heating rate) to the modified Kissinger or Ozawa method can be employed to determine the correct values to be assigned to the crystallization parameters.

Crystallization mechanism	Limiting mechanism for growth rate:			
	Interface-controlled		Diffusion-controlled	
	n	m	n	m
Bulk nucleation with a constant number of nuclei N (indep. of heating rate)				
3-dimensional growth	3	3	1.5	1.5
2-dimensional growth	2	2	1	1
1-dimensional growth	1	1	0.5	0.5
Bulk nucleation with a constant nucleation rate (N invers. prop. to heating rate)				
3-dimensional growth	4	3	2.5	1.5
2-dimensional growth	3	2	2	1
1-dimensional growth	2	1	1.5	0.5
Surface nucleation	*1*	*1*	*1*	*1*

Table 2.2.1.1. Nucleation and crystal growth mechanisms and corresponding values of parameters n and m for the modified Kissinger and Ozawa models, after Matusita et al. [121], and Henderson [119]

If surface nucleation (or heterogeneous nucleation) is dominant, then *n = m = 1* and equation 2.39 is reduced to the Kissinger equation 2.40 valid for a first order reaction. If bulk nucleation (or homogeneous nucleation) dominates, two different cases should be distinguished. In the first case, the crystal growth rate is controlled by reactions at the crystal-glass interface. If the growth occurs from a fixed number of nuclei, then *n = m = 1, 2* or *3* for 1-, 2- or 3-dimensional growth of crystallites, respectively, whereas if the nucleation rate is constant then *n = 2, 3* or *4* depending on the dimensionality of crystal growth, and m = n-1 [137].

In the second case the crystal growth is limited by diffusion in the volume of the glass. In such case, the coefficients are reduced due to the time-dependency of the growth rate in $t_{1/2}$. If crystal growth occurs from a fixed number of nuclei, then *n = m = 0.5, 1* or *1.5* for 1-, 2- or 3-dimensional growth of crystallites, respectively. If the nucleation rate is constant during crystal growth, then *n = 1.5, 2* or *2.5* depending on the dimensionality of crystal growth, and *m = n-1* [119].

Values of the parameters n and m in the various cases are grouped in Table 2.2.1.1.

2.3.2 Characterization of glass ceramic properties

A key challenge in selecting glass compositions for a sealant is to control the thermal expansion coefficient of the partly to fully crystallized glass-ceramics.

Thermophysical properties of glass-ceramics can be in principle predicted by a thermodynamic approach of phase coexistence in multicomponent glass systems [61-74]. However, this approach may be unsatisfactory in complex systems where the domains of phase stability are not fully known, and additional species such as additional glass formers may strongly influence the phase formation processes. In such complex systems, empirical investigations may be helpful to tailor the physical properties of glass-ceramics by controlling the crystalline phase content and their volume fraction, and by analyzing their long-term stability.

Thermal treatments of crystallization

The phase formation was investigated in the basic glass systems by thermal treatments performed in a systematic way with variation of temperature and time of the crystallization regime. The range of temperature

where crystallization occurs was revealed by exothermic DTA signals depending on the chemical composition of glasses. Samples were pressed with terpineol as a solvent, either in cylindrical pellets 5 mm high and 8 mm in diameter, or in bars of 5 x 5 x 40 mm, under a load of 100 or 200 MPa. Heat treatments were performed at a heating rate of either 15 °C/min, with a step of 1 hour at a temperature between 850 and 1100°C depending on the glass composition. Samples were then cooled down to room temperature with a cooling rate of either 2 °C/min or 5 °C/min. In other cases, quenching was done either in air or in ice water.

The series of glass compositions with various contents of additional oxides were investigated with the same methods. Thermal treatments were performed 1 h at temperatures between 850 and 1100°C. Sintering, nucleation and crystal growth mechanisms were investigated in-depth on glass compositions, which were thermally treated with various heating rates. Samples were cut after thermal treatment and analyzed by different characterization techniques.

X-Ray Diffraction analysis (XRD)

To identify the phases obtained upon thermal treatment, sintered samples were ground to fine powders and analyzed by X-ray diffraction (XRD, Axio Panalytical, Cu Kα radiation). The principle of the measurement is the interference of a crystalline lattice with the radiation emitted by a monochromatic X-ray source. Monochromator and sample can rotate to different relative positions. Under specific incidence angles 2θ, constructive interferences generate a reflection whose intensity is detected. The occurrence of such interferences obeys the well-known Bragg law:

$$n \cdot \lambda = 2d \cdot sin\,\theta \qquad (2.43)$$

where d is the lattice plane spacement, θ the incidence angle, λ the wavelength of the X-ray source (Cu Kα: 1.54Å) and n the order of the interference. By scanning a range of incidence angles 2θ, a pattern of interference reflexes is obtained which is characteristic for the phases present in the crystalline body. The identification of the phases is performed with a specific program that enables to compare the pattern to standard patterns of pure phases, grouped in the JCPDS database (Joint Committee on Powder Diffraction Standards). The indexing of interference patterns must be done with caution in the case of glass-ceramic materials. The formation of mixed compositions leads to variations in crystal lattice parameters, which generate a shift of the peaks in the 2ϑ-scale compared to a reference pure phase pattern. Moreover, the texturing of crystal morphologies often leads to a relative increase of the intensity of particular peaks in one phase. In glasses the amorphous structure provides no interference, but a diffusion of the X-ray signal. This is recognizable by a broad halo at low 2ϑ values independent of the glass composition. Hence, XRD enabled to verify the amorphous state of glass powders after melting.

Phase contents of glass-ceramic samples were analyzed by X-ray diffraction on half-samples ground to fine particle size, after various thermal treatments.

Microscopy (SEM- Scanning Electron Microscopy)

In parallel to the identification of the crystalline structure of phases formed upon thermal treatment of glasses, analyses were performed to observe the microstructure and estimate the stoichiometry of the phases. Cross-sections of sintered samples were mounted in epoxy resin, grinded with grinding paper of up to granularity 1200 or 2400, and then successively polished with several diamond suspensions (9, 3 and 1 µm) for 30 to 60 min. each. Some of the samples were subsequently etched in hydrofluoric acid (HF, 48 %) for 10 to 30 sec. to selectively remove remaining glass around the crystallites.

Samples were first inspected by light microscopy and subsequently analysed by scanning electron microscopy (SEM, Quanta FEI) combined with energy dispersive X-ray analysis (EDX, Edax). Different detector modes were used for the analysis of the surface (secondary electrons, SE) or the mass of the sample (backscattered electrons, BSE), providing either a high resolution or a high material contrast. Point elemental analyses were performed by EDX to estimate the stoichiometry of the different phases. Statistical point analyses were performed to determine the stoichiometry of the major phases, in case one phase could not be ordered to any of the crystalline structures detected by XRD. However, the technique is spoiled by a large error inherent to the size of the detected area. The EDX detector receives a signal from a large spot (> 2µm) that can easily surpass the grain boundaries of phases and mix elemental composition of a phase with the surrounding phases or glass matrix.

Dilatometry of partially crystallized samples

Subsequently to investigation of the crystallization behavior of glasses in dependence of their chemical composition, the thermomechanical properties of the resulting glass-ceramics were studied. Dilatometric measurements were performed on pressed glass powder samples after various thermal treatments to determine the influence of the phase content on the thermal expansion behavior of the material. Thermal treatments of the samples before measurements were tailored to obtain fully sintered samples prior to their crystallization. In this way the risk of mechanical weakness of samples with highly porous structures is minimized. An evaluation of the “free” sintering of samples was carried out on a few sets of samples by a thermal treatment step at temperatures selected from shrinkage curves previously measured. An optimization of the temperature and time of the sintering treatment by density measurements led to optimal conditions at the inflection point of shrinkage curves, i.e. at temperatures ranging from 700 to 800°C for 1 to 2 h, depending on the viscosity of the material. Similar methods were reported in the literature [73-79]. Subsequently to the sintering stage, a crystallization stage was performed at various temperatures corresponding to exothermal events in DTA. By comparison with XRD and SEM /EDX analyses, dilatometry experiments show the influence of each crystalline phase on the thermal expansion behavior of the thermally treated glass-ceramic. In such a way, it was intended to relate thermomechanical properties of glass-ceramics to their phase content and volume ratio.

Chapter 3

Synthesis and characterization of CMAS glass ceramics and their variants containing TiO_2, MnO_2, ZnO and SnO_2

In the first part of this study, the purpose is to analyze aluminosilicate-based glasses of the CaO-MgO-Al_2O_3-SiO_2 system. This is considered the basic system from which to start for studying the influence of different network modifier oxides on the properties of the glass. Our choice has fallen upon this composition because it is one of the most promising glass ceramic systems, exhibiting excellent properties to be exploited for sealing purposes in SOFCs. Glass-ceramic materials, prepared by the controlled crystallization of glasses, have a variety of established uses that depend on their uniform reproducible fine-grained microstructures, absence of porosity and other wide-range properties, which can be tailored by adjusting the composition and the heat treatment procedures. In particular, CaO-MgO-Al_2O_3-SiO_2 glass ceramics have become good candidates for functional application in several areas. Recently, glass-ceramics based on chain silicate structures have been developed [135-136]. Materials in this system were revealed to be potential candidates for SOFC seal because of several valuable features:

1. the CTEs may be tailored to match those of the interconnector materials
2. an easy sealing is achieved below 1000°C
3. good wettability behavior is observed towards the interconnect materials under various atmospheric conditions
4. they are Ba-free

Some work has been done on the diopside ($CaMgSi_2O_6$)–anorthite ($CaAl_2Si_2O_8$)–celsian ($BaAl_2Si_2O_8$) system [137-138-139]. Furthermore, a number of studies have been recently reported on the synthesis of CaO-MgO-Al_2O_3-SiO_2 glass ceramics using various wastes as starting materials. Numerous studies have been dedicated to the recycling of aluminosilicate-based waste. Because glass and glass ceramics are known to have many commercial applications, the transformation of waste into these materials provides an opportunity for making use of products out waste, with important economic, technological and scientific consequences. In this scenario, the last part of our study aims to investigate the potential for reuse of kaolin waste to obtain new type of glass ceramics. In particular, the attention is here focused on the waste generated from ceramic industry in the processes of silica sand and kaolin clay refining. My research work has been carried out in the chemical laboratory/facilities of the X-Tech Spa, a corporation working for ceramic industry in the sanitary-ware sector. X-Tech lab is located in Civita Castellana (Italy), which has been for longtime one of most famous

areas in Italy for sanitary ware production. The development of ceramic industry in this area is related to the local availability of good clay sources. Large amounts of kaolin clay are mined every year. The production is accompanied by generation of a huge amount of waste (about 500.000 t per year), pointing to the need to find an alternative use for waste materials. In this context, the sanitary-ware companies have an obligation to landfill the solid process scrap at least one time each year. Our work was designed with a view to reconvert the waste derived from the preparation of ceramic bodies and glaze into glass ceramics which can be used as sealants for SOFCs. The waste consists mainly of quartz, clay (kaolinite - $Al_2Si_2O_5(OH)_4$) and/or mica and feldspars (orthoclase - $KAlSi_3O_8$ or albite - $NaAlSi_3O_8$) and contains small amounts of coloring components such as Fe_2O_3 and TiO_2. For this reason, it is important to study the effect of the additives on the properties of the aluminosilicate based glasses.

In the first step of this work, we will investigate the basic aluminosilicate system (CMAS). Subsequently, we will study the effect of the addition of nucleation agents to improve the crystallization of CMAS. The selection of intermediate oxides has been carried out considering that the waste derived from industrial processing may contain different types of oxides. Indeed, in developing a glaze for sanitary-ware purposes, four classes of oxides with different functions are used in the chemical formulation:

1. Vitrificant oxides such as SiO_2 and B_2O_3
2. Stabilizing oxides (mainly A_2O_3)
3. Fluxing oxide such as PbO, Na_2O, K_2O, CaO, MgO, BaO, Li_2O, ZnO
4. Coloring oxides such as SnO_2, ZrO_2, Fe_2O_3, CuO_2, Co_3O_4, Cr_2O_3, MnO_2, NiO, V_2O_5 and TiO_2

Hence, to study the influence of some fluxing and coloring oxides on the properties of the aluminosilicate quaternary system, nucleation agents such as TiO_2, MnO_2, ZnO and SnO_2 were added to the CMAS system.

In summary, we aimed at exploring a as large as possible portion of a “composition space” working both on the nucleating agents and on the network modifier effects. A number of glass compositions have been developed to identify the respective contribution and the influence of each added element. Moreover, a series of borosilicates has been also analyzed (Chapter 4) in order to investigate how the addition of a different network former could influence the glass and glass ceramic properties.

3.1 Chemical compositions

In the case of the basic CMAS system, four different compositions have been examined to study the effect of alkaline earth oxides CaO and MgO on the aluminosilicate glass properties. Furthermore, the role of the intermediate oxide Al_2O_3 will be also analysed.

In Table 3.1.1. the investigated compositions are presented (wt%, the error on results is ±0.01). The samples are designated with the acronym CMAS referring to their general composition, with a progressive number indicating the increasing fraction of SiO_2.

Sample ID	SiO_2 (wt%)	Al_2O_3 (wt%)	CaO (wt%)	MgO (wt%)	Impurities (wt%)
CMAS1 basic system	46.53	36.89	13.93	1.91	0.74
CMAS2 basic system	50.35	19.55	27.85	1.47	0.78
CMAS3 basic system	51.89	14.45	30.70	2.51	0.45
CMAS4 basic system	53.07	14.03	26.25	6.35	0.30

Table 3.1.1 Chemical composition of the CMAS glasses investigated in this work.

The compositions of the samples are designed with the purpose to analyze the influence of the modifier oxides. The first sample (CMAS1) can be distinguished from the others because the ratio between the alkaline earth oxide and Al_2O_3 $\left[\frac{(CaO+MgO)}{Al_2O_3}\right]$ is less than one. Based on this ratio, it is possible to predict the configuration of Al^{3+} ions in the glass structure. Indeed, if the ratio is less than one, Al^{3+}ions exist in the form of AlO_4^- tetrahedra and Al_2O_3 acts as glass network former, whereas if the ratio is larger than one, Al^{3+} ions exist as AlO_6^- octahedral groups and Al_2O_3 acts as glass network modifier. The systems named CMAS2, CMAS3 and CMAS4 will be compared to study effect of different amounts of the modifier oxide.

As mentioned, the basic system has been subsequently modified by adding four types of intermediate oxides. Table 3.1.2 shows the composition in wt% of glass batches after X-Ray Fluorescence analysis (the error is ±0.01).

Sample ID	SiO_2 (wt%)	Al_2O_3 (wt%)	CaO (wt%)	MgO (wt%)	TiO_2 (wt%)	MnO_2 (wt%)	ZnO (wt%)	SnO_2 (wt%)	Impurities (wt%)
CMASTi1	45.03	33.25	15.69	1.78	4.25	-	-	-	0.01
CMASTi2	50.35	19.55	24.79	1.47	2.56	-	-	-	1.10
CMASTi3	51.89	14.45	26.21	2.51	4.49				0.45
CMASTi4	53.07	14.03	19.91	6.35	6.35	-	-	-	0.74
CMASMn1	45.03	33.25	15.69	1.78	-	4.25	-	-	0.01
CMASMn2	50.35	19.55	24.79	1.47	-	2.56			1.10
CMASMn3	51.89	14.45	26.21	2.51	-	4.49	-	-	0.45
CMASMn4	53.07	14.03	19.91	6.35	-	6.35	-	-	0.74
CMASZn1	45.03	33.25	15.69	1.78	-	-	4.25		0.01
CMASZn2	50.35	19.55	24.79	1.47	-	-	2.56		1.1
CMASZn3	51.89	14.45	26.21	2.51	-	-	4.49	-	0.45
CMASZn4	53.07	14.03	19.91	6.35	-	-	6.35	-	0.74
CMASSn2	50.35	19.55	24.79	1.47	-	-	-	2.56	1.1
CMASSn3	51.89	14.45	26.21	2.51	-	-	-	4.49	0.45

Table 3.1.2 Chemical compositions of glass batches with nucleation agents.

These systems were obtained by modifying each glass of the CMAS series in order to analyze how the intermediate oxides may influence the properties In CMAS1 glass the change consists in replacing a fraction of the network former, such as Al_2O_3, with an intermediate oxide such as TiO_2, MnO_2 and ZnO. For the glasses CMAS2, CMAS3 and CMAS4, in which Al_2O_3 acts as a network modifier, the change involves a partial

substitution of the alkaline earth oxide CaO with the nucleating agents, whereas the concentrations of silicon oxide and magnesium oxide remain unchanged.

Studying these modified glasses allows us to investigate how the presence of nucleation oxides influences the crystallization kinetics. In particular, the ratio of the intermediate oxide to CaO will be considered.

3.2 Density of glass and glass ceramic

The Archimede's method (immersion in diethyl phthalate) was employed to measure the apparent density of the bulk annealed glass and glass ceramic. The so obtained density values are then used to calculate the molar volume. The density of all the glasses is given in Table 3.2.1. The second column in this table reports the density of the as quenched samples (glassy material), while the third column shows the density for the inverted glasses after crystallization for 3 hours at 1200°C.

Sample ID	Density of glass (g/cm^3)	Density of glass ceramic (g/cm^3)	Molar volume of glass (cm^3/mol)	Molar volume of glass ceramic (cm^3/mol)
CMAS1 basic system	2.66±0.01	2.69±0.01	21.327±0.008	21.218±0.008
CMAS2 basic system	2.91±0.01	2.95±0.01	22.375±0.008	21.201±0.008
CMAS3 basic system	2.51±0.01	2.58±0.01	21.147±0.008	21.001±0.008
CMAS4 basic system	2.71±0.01	2.73±0.01	21.402±0.008	21.414±0.008
CMASTi1	2.65±0.01	2.71±0.01	21.352±0.008	21.287±0.008
CMASTi2	2.44±0.01	2.45±0.01	21.058±0.008	21.102±0.008
CMASTi3	2.61±0.01	2.63±0.01	21.243±0.008	21.251±0.008
CMASTi4	2.60±0.01	2.66±0.01	21.517±0.008	21.505±0.008
CMASMn1	3.02±0.01	3.07±0.01	20.895±0.008	20.625±0.008
CMASMn2	2.98±0.01	3.00±0.01	20.788±0.008	20.685±0.008
CMASMn3	3.08±0.01	3.11±0.01	20.567±0.008	20.451±0.008
CMASMn4	3.03±0.01	3.08±0.01	20.645±0.008	20.511±0.008
CMASZn1	2.78±0.01	2.81±0.01	21.486±0.008	21.322±0.008
CMASZn2	2.71±0.01	2.76±0.01	21.631±0.008	21.576±0.008
CMASZn3	2.64±0.01	2.71±0.01	21.354±0.008	21.269±0.008
CMASZn4	2.69±0.01	2.73±0.01	21.493±0.008	21.251±0.008
CMASSn2	2.92±0.01	2.93±0.01	21.861±0.008	21.774±0.008
CMASSn3	2.81±0.01	2.86±0.01	21.734±0.008	21.716±0.008

Table 3.2.1 Density measured for glasses and crystalline samples (1200 °C for 3h) by the immersion method

The density for glassy samples of the CMAS-series for n=1 to 4 is similar, while a slight increase is observed for the resulting glass ceramic.

For the glasses in the CMASX series (with X=nucleating oxide), density is in the range from 2.44 to 3.08 g/cm^3, with no large differences observed between the series and compared with the CMAS basic systems. The density for the resulting glass ceramics shows a slight increase.

3.3 Chemical resistance

The chemical resistance of glasses in acid and basic environments was examined by immersing each sample in 5% HCl and in 5% NaOH solutions, respectively, at 95°C for 1h. No evident changes were noticed for all glasses following these chemical treatments, indicating that all the examined glass compositions are suitable for applications, as far as chemical corrosion resistance properties are concerned.

To understand the behavior of the glasses towards water, two tests have been carried out:

1. Durability in water
2. Water absorption according to the ISO standard method 10545-3:1995

With regard to the durability test, reaction with water was noticed for all the glasses after different periods of time. All series of glasses were tested placing a fragment of bulk glass in a beaker containing deionized water for 15 minutes, 3 days and 70 days. After a couple of days, the glasses belonging to the CMASn series showed evident signs of reaction. The examined glasses were covered by a white dusty layer, which over time also covers the walls and the bottom of the beaker.

The CMAS3 glass was found to react especially fast, as evidenced by gas bubbles appearing on the surface after only 15 minutes of soaking. After about 3 days, bubbles could also be seen on CMAS2 and CMAS4 samples. The pH value of the water containing fine grained powder of CMAS3 composition stabilized at ~10.6 after an hour and the powder turned into hard aggregates. XRD analysis of the CMAS3 sample after 24 hour exposure to water demonstrated the formation of hydrate phases such as $Ca_3Al_2(OH)_{12}$ (Katiote) and hydrate carbonate $Ca_4Al_2CO_9{\cdot}11H_2O$. The visible changes caused by the reaction with H_2O are illustrated in Figure 3.3.1.

Figure 3.3.1 Visual evidence of the reaction between distilled water and CMAS3, CMAS2 and CMAS4 glasses. Pictures of dried glass samples after 70 days.

For the glasses belonging to the CMASX series (with X=nucleating oxide) the effects of reaction with water were less noticeable. Only in the CMASSn1 and CMASSn2 samples a thin layer on the surface was displayed, due to the larger amount of CaO in the chemical formulation.

The substitution of network formers for alkaline earth oxides, especially CaO, decreases the durability in water. From the XRD-pattern of the water-treated powder of CMAS samples the white coating was ascertained to be a mixture of hydroxides and carbonates. Alkaline earth elements such as Ca and Mg can easily form carbonates and the reaction is accelerated when water is involved. The first reaction step results in the formation of a hydroxide, which reacts further leading to carbonate, as shown in equations 3.1 and 3.2 below, where M=Mg or Ca.

Step 1: $MO + H_2O = M(OH)_2$ (3.1)

Step. 2: $M(OH)_2 + CO_2 = MCO_3 + H_2O$ (3.2)

At elevated temperatures, hydroxides and carbonates decompose. However, in steam-containing atmospheres the hydroxide phase $C_{12}A_7O_{32}(OH)_2$ can be formed in the temperature range 950°C-1350°C. In conclusion, the durability tests have demonstrated that the parent glasses with high CaO content are not stable in contact with water at ambient temperature. The same evidence has been found in the other glasses with high content of CaO, indicating that the presence of nucleation agents do not limit this process.

Water absorption tests have been carried out on bulk glasses following the ISO 10545-3:1995 standard. This method consists in placing dried samples in boiling water for 2 hours and then leaving them in soaking for 4 hours. The weight difference between dried and wet samples allows to calculate the water absorption coefficient from the Equation 3.3:

$$E_b = \frac{m_{2b} - m_1}{m_1} \cdot 100 \quad (3.3)$$

where m_1 is the dried sample mass and m_{2b} is the wet sample mass.

Moreover, the method could be implemented by placing the bulk glasses in a vacuum chamber at a pressure of 10±1 kPa for a period of 30 minutes by slowly adding distilled water. The penetration of water in open pores can be evaluated in a similar manner:

$$E_v = \frac{m_{2v} - m_1}{m_1} \cdot 100 \quad (3.4)$$

where m_1 is the dried sample mass and m_{2v} is the wet sample mass under vacuum.

From the relation between the volume of open porosities and the external volume of bulk sample, the porosity percent can be estimated according to eq. 3.5:

$$p = \frac{m_{2v} - m_1}{V} \cdot 100 \quad (3.5)$$

where m_{2v} is the wet sample mass obtained under vacuum conditions.

The external volume of the sample is expressed by

$$V = m_{2v} - m_3 \quad (3.6)$$

i.e. by the weight difference between the wet sample (m_{2v}) and the sample immersed under vacuum impregnation (m_3).

Thee volume of open pores, V_0, and the volume of closed pores, V_1, are defined by the following equations:

$$V_0 = m_{2v} - m_1 \quad (3.7)$$

$$V_1 = m_1 - m_3 \quad (3.8)$$

The results of this analysis are presented in Table 3.3.1.

Sample ID	E_b	E_v	V(cm^3)	p	V_0(cm^3)	V_1(cm^3)
CMAS1 basic system	2.07	1.92	0.10	30.00	0.03	0.07
CMAS2 basic system	2.22	2.04	0.09	33.33	0.03	0.06
CMAS3 basic system	3.55	1.62	0.14	31.43	0.03	0.11
CMAS4 basic system	2.52	3.03	0.13	38.46	0.05	0.08
CMASTi1	3.01	1.95	0.12	33.33	0.04	0.08
CMASTi2	2.14	2.87	0.14	50.00	0.07	0.07
CMASTi3	3.76	4.25	0.09	66.66	0.06	0.03
CMASTi4	3.25	4.58	0.01	60.00	0.06	0.04
CMASMn1	1.88	1.81	0.07	57.14	0.04	0.03
CMASMn2	2.03	1.97	0.11	36.36	0.04	0.07
CMASMn3	2.16	1.57	0.09	33.33	0.03	0.06
CMASMn4	2.92	2.73	0.09	55.55	0.05	0.04
CMASZn1	2.78	3.31	0.07	61.43	0.05	0.02
CMASZn2	4.51	2.55	0.08	50.00	0.04	0.04
CMASZn3	3.25	2.07	0.01	30.00	0.03	0.07
CMASZn4	3.36	2.34	0.06	50.00	0.03	0.03
CMASSn2	3.46	2.01	0.16	31.25	0.05	0.11
CMASSn3	3.39	2.67	0.13	38.46	0.05	0.08

Table 3.3.1 Characteristic values calculated from the ISO 10545:1995 method.

The results show that all the examined glasses present low absorption coefficients (up to 4.50), the CMASZn series exhibiting the maximum values. The porosity percent is in the range between 30% and 60%. The absorption coefficients obtained in vacuum conditions are in agreement with the values derived in standard conditions. The data obtained by this procedure could be used to calculate the apparent density T in the fraction of sample with less easily refillable porosities:

$$T = \frac{m_1}{m_1 - m_3} \tag{3.9}$$

In Table 3.3.2 the values of apparent density for all glasses are reported.

Sample ID	T(g/cm^3)
CMAS1 basic system	22.28
CMAS2 basic system	22.51
CMAS3 basic system	22.78
CMAS4 basic system	21.43
CMASTi1	22.31
CMASTi2	21.89
CMASTi3	22.02
CMASTi4	22.47
CMASMn1	21.99
CMASMn2	22.78
CMASMn3	22.02
CMASMn4	22.37
CMASZn1	21.88
CMASZn2	21.79

CMASZn3	22.05
CMASZn4	22.12
CMASSn2	22.27
CMASSn3	22.18

Table 3.3.2 Calculated apparent density for all series of glasses.

The so obtained results are in good agreement with the values determined by the Archimede's method.

3.4 Powder glass particles sizes

Before studying the thermophysical properties of the glasses, it is important to determine the particle size distributions of the glass powders. Milling and particle size measurements were performed to this end.

Milling process proved to be relatively reproducible. A milling time of 2 hours was selected.

In Figure 3.4.1 the size distributions of glasses CMAS 1-4 are presented.

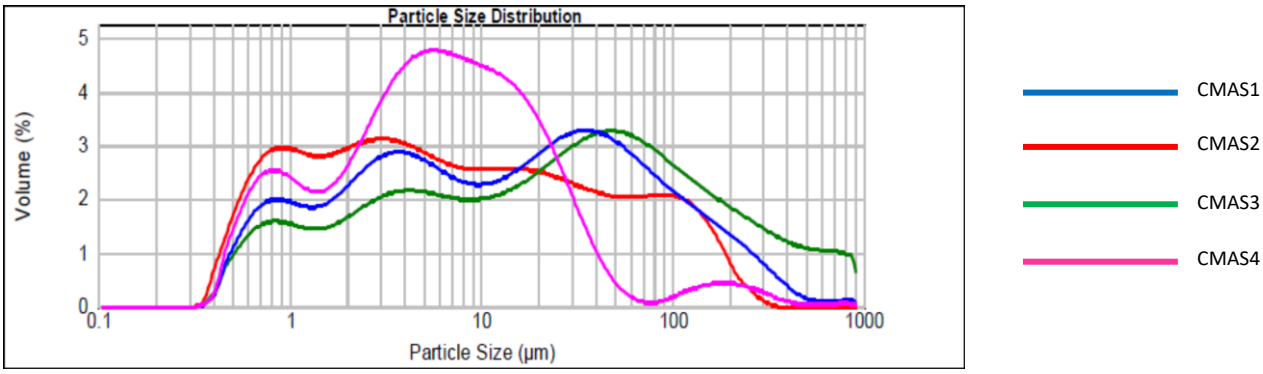

Figure 3.4.1 Particles size distribution of CMAS basic glass series.

Differences between the distributions are related to the hardness of the material, which in turn depends on the chemical compositions. Another important aspect is that the particle size affects the temperature of fusion, the smaller the size the lower the melting temperature.

Typical resulting grain sizes are reported in the Table 3.4.1 below.

GLASS SAMPLE ID	d(0.1) µm*	d(0.5) µm**	d(0.9) µm***
CMAS1 basic system	1.089± 0.030	13.819± 0.030	123.025± 0.030
CMAS2 basic system	0.825± 0.030	6.613± 0.030	89.505± 0.030
CMAS3 basic system	1.301± 0.030	25.895± 0.030	254.630± 0.030
CMAS4 basic system	0.911± 0.030	5.898± 0.030	26.065± 0.030

Table 3.4.1 Particle size distribution of the CMAS glass powders.

d(0.1) µm*: 10% of the particles have dimensions below the value obtained
d(0.5) µm**: 50% of the particles have dimensions below the value obtained
d(0.9) µm***: 90% of the particles have dimensions below the value obtained

Considering the results of the grain size analysis, glasses belonging to CMAS basic system are concluded to have different hardness, with the CMAS3 sample being the hardest material.

In the Figures 3.4.2 - 3.4.5 the particle size distribution of the modified glasses are shown, namely CMASTi glass series, CMASMn glass series, CMASZn glass series and CMASSn glass series.

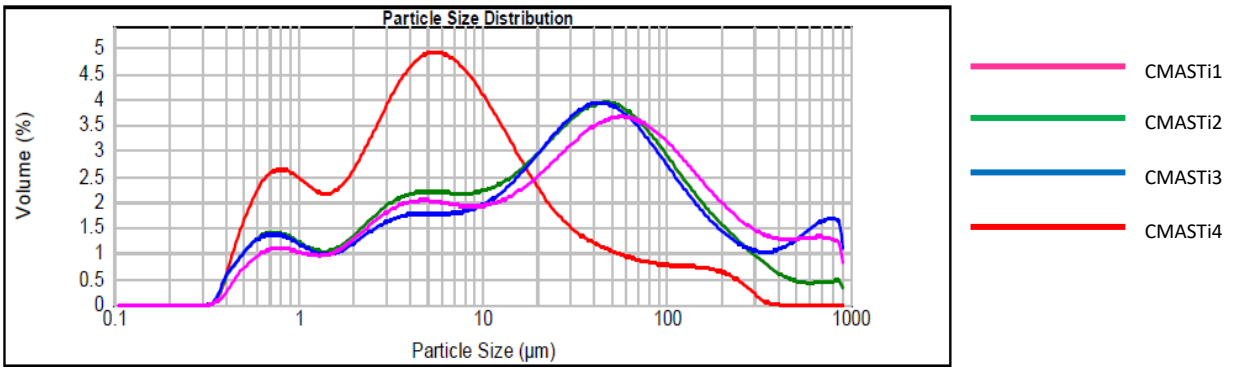

Figure 3.4.2 Particle size distribution of CMASTi glass series.

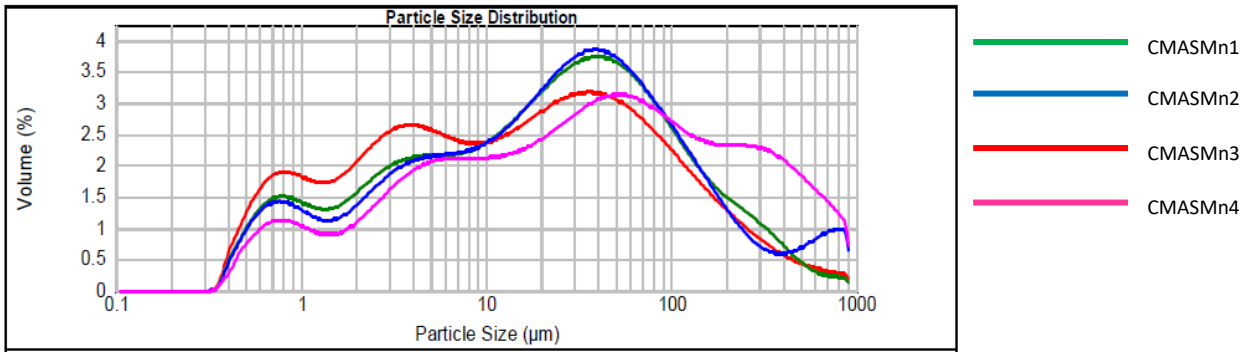

Figure 3.4.3 Particle size distribution of CMASMn glass series.

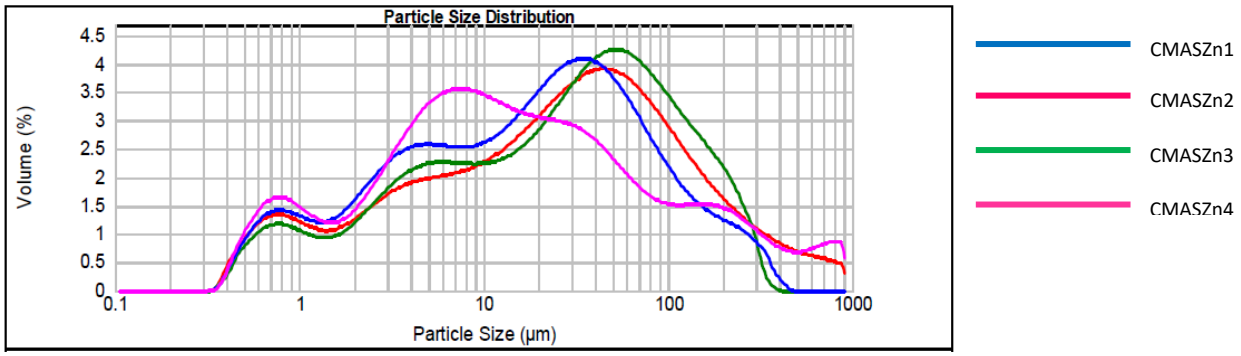

Figure 3.4.4 Particle size distribution of CMASZn glass series.

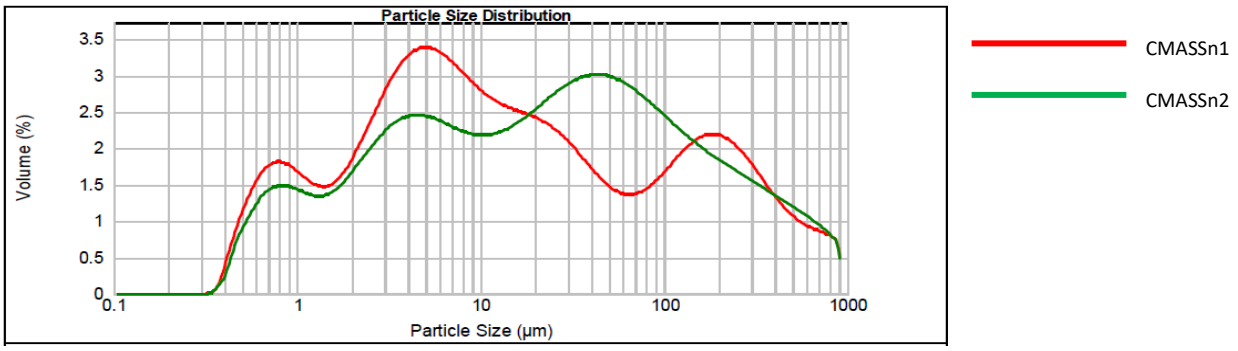

Figure 3.4.5 Particle size distribution of CMASSn glass series.

The resulting grain sizes are reported below in the Table 3.4.2

GLASS SAMPLE ID	d(0.1) µm	d(0.5) µm	d(0.9) µm
CMASTi1	2.002± 0.030	35.169± 0.030	291.282± 0.030
CMASTi2	1.468± 0.030	25.440± 0.030	160.001± 0.030
CMASTi3	1.551± 0.030	30.983± 0.030	299.636± 0.030
CMASTi4	0.858± 0.030	5.576± 0.030	41.705± 0.030
CMASMn1	1.331± 0.030	22.084± 0.030	153.426± 0.030
CMASMn2	1.453± 0.030	23.960± 0.030	167.712± 0.030
CMASMn3	1.049± 0.030	14.999± 0.030	136.879± 0.030
CMASMn4	2.038± 0.030	36.645± 0.030	368.386± 0.030
CMASZn1	1.471± 0.030	18.820± 0.030	111.269± 0.030
CMASZn2	1.568± 0.030	27.125± 0.030	181.058± 0.030
CMASZn3	1.919± 0.030	28.734± 0.030	145.570± 0.030
CMASZn4	1.271± 0.030	13.292± 0.030	188.729± 0.030
CMASSn2	1.130± 0.030	11.898± 0.030	261.773± 0.030
CMASSn3	1.397± 0.030	23.089± 0.030	261.901± 0.030

Table 3.4.2 Particle size distribution of the CMASX glass powders.

Particle size distributions of the modified glasses highlight that the hardness of these materials is higher compared with the CMAS corresponding basic glass due to the presence of additives.

In the CMASTi series, the lowest hardness is found for the highest TiO_2 content, whereas in the CMASMn glass series, CMASMn4 exhibits the hardest behavior. The results for glasses belonging to the CMASZn series do not show large differences. CMASSn2 and CMASSn3 also presents a similar behavior. It is important to note that in all glasses 90% of the particles have dimensions below 500 µm. The particles size plays an important role during the crystallization stage, so to monitor the distribution of grain size is important. In general, an increase in glass particle size should increase the onset and the maximum temperature of the exothermic peak due to the decreased surface area and nucleation sites for heterogeneous nucleation.

3.5 Thermophysical properties

In order to meet the requirements of seal glass in terms of thermal stability, T_g, T_S, and CTE, the glass composition design should take into account the role of individual oxides on glass network structures. In a seal glass, the number of constituents should be as low as possible. Too many constituents increase the configurational entropy and microheterogeneity due to coexistence of different structural units [140], which in turn could be detrimental to thermal stability [141-142]. A lack of understanding of the effects of individual oxides on the glass structure limits the design capability of a seal glass. Systematic studies are then needed to understand the effects of different glass constituents on the thermal properties of a glass system. With regard to modifiers, alkali oxides decrease T_g, T_s, and network connectivity due to their low field strength and creation of non-bridging oxygen species and should be avoided for a seal glass. Alkaline earth oxides increase immiscibility in the glass and cause phase separation [143], in the order of $Mg^{2+} > Ca^{2+} > Ba^{2+}$. So, lower field strength alkaline earth oxides such as BaO and SrO are more desirable than higher field strength alkaline earth

oxides such as CaO and MgO. However, BaO causes poor thermal stability due to its devitrified Celsian polymorphs and should be avoided.

3.5.1 Glass stability and glass forming ability

Thermophysical properties of glasses were investigated in dependence of the main oxide contents by hot stage microscope and differential thermal analysis. Characteristic temperatures of the glasses were obtained from these measurements. The main target parameters for statistical analyses are the glass transition temperature, T_g, and the melting temperature, T_m. Alternatively, a third parameter can be considered which is related to the glass stability toward crystallization, either the parameter K_T proposed by Turnbull [144-145], or one of the parameters K_1 and K_H defined by Hrubÿ [146], as well as K_W defined Weinberg [147]. Several parameters are hence proposed to evaluate the glass stability against crystallization upon heating.

A classic parameter was defined, as mentioned, by Turnbull, under the assumption that the nucleation frequency in an undercooled melt is inversely proportional to its viscosity. The term K_T is obtained from the ratio of the glass transition (T_g) to the melting point temperature (T_m):

$$K_T = \frac{T_g}{T_m} \tag{3.10}$$

This relationship is derived from the classical nucleation theory of Johnson-Melh-Avrami and mentioned earlier on by Kauzmann.

Later on, different criteria including characteristic temperatures of the crystallization event were proposed to evaluate the glass stability upon heating. Simple parameters are defined as the interval between two characteristic temperatures:

$$K_1 = T_m - T_g \tag{3.11}$$

$$K_2 = T_c - T_g \tag{3.12}$$

Where T_c is the crystallization temperature, i.e. either the onset T_o or the maximum of the exothermal peak T_p. From the two above expressions, the larger is the interval, that higher the glass stability.

The factor K_2 was found to give a relatively good estimate of the glass stability in the literature. However, other criteria were proposed that include the melting point, which is taken from HSM analysis. A first parameter is defined by Weinberg as a ratio of the interval to the melting point:

$$K_w = \frac{[T_c - T_g]}{T_m} \tag{3.13}$$

A second parameter is that of Hruby defined as the ratio of the same interval to the interval between melting point and crystallization temperature:

$$K_H = \frac{[T_c - T_g]}{[T_m - T_c]} \tag{3.14}$$

Other criteria were proposed, which include two characteristic crystallization temperature like that one defined by Saad and Poulain:

$$K_3 = \frac{[T_o - T_g][T_c - T_o]}{T_m} \quad (3.15)$$

An assessment of the ability of various parameters to evaluate glass stability against crystallization by heating was performed by Nascimento et al. [148]. The study focused on finding whether a relationship exists between those parameters and classical criteria used to evaluate the glass forming ability by cooling from a melt. In this respect, different studies led to contrasting conclusions [147-149]. Parameters like K_W and K_H including three characteristic temperatures were found to provide a good correlation between glass stability and glass forming ability.

In the present work, DTA and HSM measurements, under the same heating conditions, were utilized to observe sintering and devitrification behavior in the glass systems. In order to determine the characteristic temperatures of the glasses, typical curves of the percentage linear shrinkage versus temperature are represented for each CMAS glasses together with the differential thermal analysis. Thanks to HSM it is possible to derive the sintering behavior of glass powders. A comparison between the results obtained from these experimental methods allows to analyze what happens during the heat treatment of the glass and can be useful to investigate the effect of glass composition on sintering and devitrification phenomena. In general, two different trends can be observed related to the sintering and crystallization behavior of the glasses [150]. In the first case, the beginning of crystallization (T_O) occurs after the final sintering stage. Thus, under such circumstances, sintering and crystallization are independent processes. In the other case, T_O appears before maximum density has been reached. In this case, the crystallization process starts before complete densification occurs, thus preventing further sintering. Figure 3.5.1.1 - 3.5.1.4 represent the HSM and DTA curves for each glass system in the CMAS series. HSM curves present the variations in the relative area of glass powder compact and the DTA curve analysis reports the heat flow with respect to temperature. Both curves have been recorded at heating rate of 15 °C·min^{-1}.

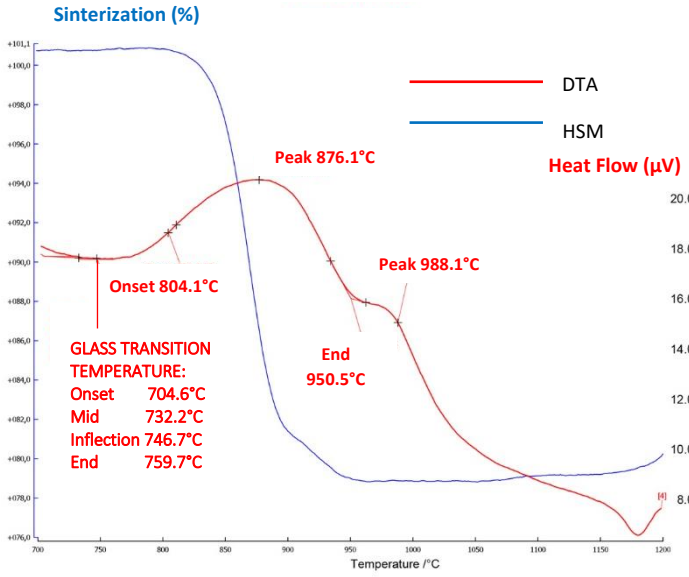

Figure 3.5.1.1 HSM and DTA curves for CMAS1.

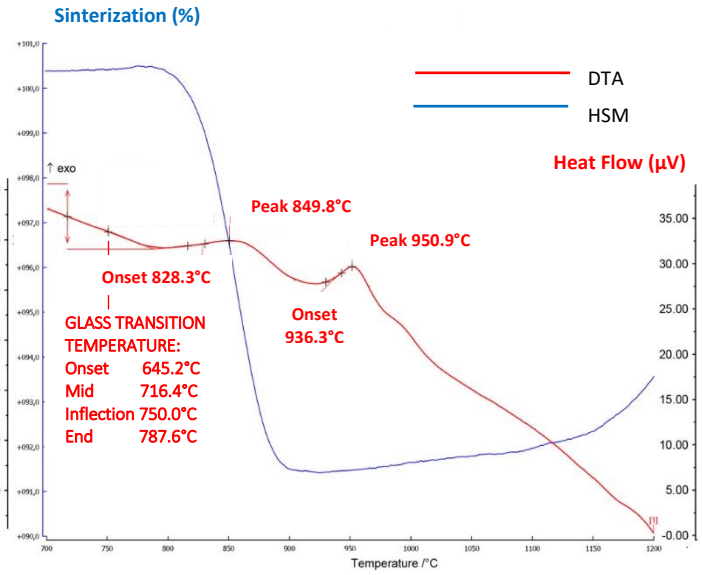

Figure 3.5.1.2 HSM and DTA curves for CMAS.

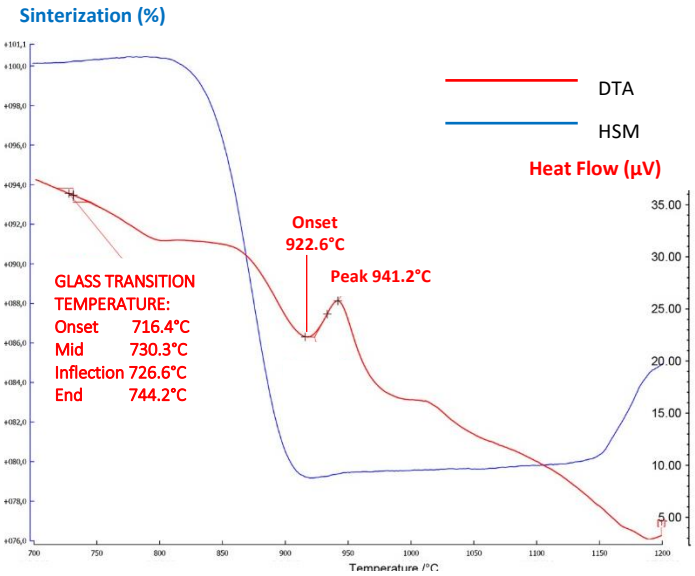

Figure 3.5.1.3 HSM and DTA curves for CMAS3.

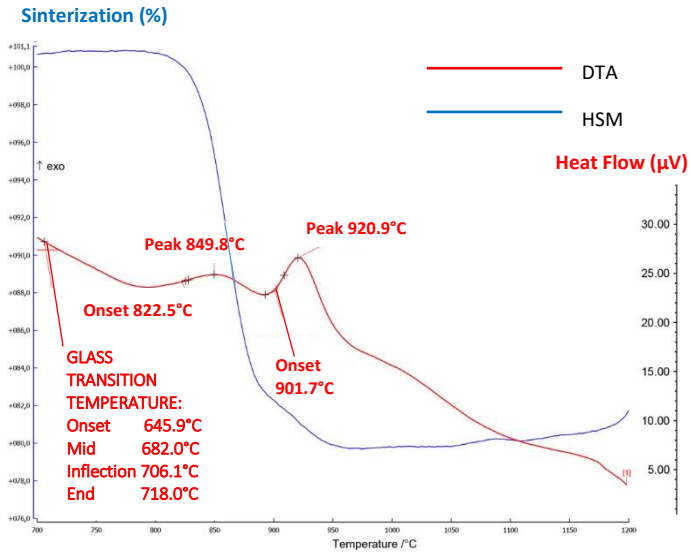

Figure 3.5.1.4 HSM and DTA curves for CMAS4.

Table 3.5.1.1 summarizes the data obtained from HSM and DTA measurements for all glasses belonging to CMAS series. From HSM analysis the sample morphologies and contact angles are determined by a computer program in accordance to the norm DIN 51730 and the results obtained show the characteristic temperatures:

1. T_{FS}, first shrinkage: the temperature at which the pressed sample start to shrink
2. T_S, sintering: the temperature at which the sample turns from a powder into a indivisible material
3. T_{MS}, maximum shrinkage: the temperature at which maximum shrinkage of the glass powder compact takes place before it starts to soften
4. T_{HB}, half ball temperature: the temperature at which the section of the observed sample forms a semicircle on the microscope grid.

Temperatures corresponding to the onset (defined at 5% of shrinkage) and to the completion of sintering are extracted from the shrinkage curves.

For an optimal glass ceramic to be used as a sealant, the softening temperature, T_s, should be higher than the SOFC operating temperature to avoid excessive glass flow, but at the same time should remain below 1000°C to avoid excessive oxidation of the metallic interconnects during sealing.

During the sintering of a glass-powder compact with a size distribution of glass particles, small particles get sintered first as shown by Prado et al.[151]. Thus, sintering kinetics at first shrinkage is dominated by the neck formation among smallest particles by viscous flow and is best described by the Frenkel model of sintering [152]. Maximum shrinkage is reached when large pores (pores formed from cavities among larger particles) have disappeared due to viscous flow that reduces their radii with time. This region of sintering kinetics may the described by the Mackenzie-Shuttleworth model of sintering [153]. However, various physical processes (entrapped insoluble gases or crystallization) and sintering processes might affect the densification kinetics.

The DTA measurements allow one to derive the crystallization temperature (T_C) together with its onset temperature (T_O) and the glass transition temperature (T_g). The glass transition temperature is an important

parameter for choosing a suitable glass for SOFC seal. A seal glass is brittle below T_g but viscous above T_g. The stress between the seal glass and the adjoining SOFC components induced by thermal expansion mismatch during thermal cycling can generate cracks, which are potential paths for gas leakage. These cracks can "self-heal" by viscous flow of the seal above T_g. The viscosity of the seal glass should be > 10^9Pa s to provide hermetic sealing at cell operating temperatures. This means that hermeticity of a seal glass can be maintained by T_g values slightly below the SOFC operating temperatures while relieving thermal stresses and self-healing cracks. T_g is generally between 650°C and 800°C. The aim of this work is to identify new types of glass ceramic sealants for SOFC operating in the range of temperatures between 600° and 800°C. Obviously, T_s and T_g of a seal glass depend on the glass composition.

In Table 3.5.1.1. are shown the characteristic temperatures for all the glasses belonging to the CMAS series.

GLASS SAMPLE ID	T_s (°C)	T_{FS}(°C)	T_{MS}(°C)	T_{HB} (°C)	T_F (°C)	T_g (°C)	T_c(°C)	T_o (°C)	T_{c1}(°C)	T_{o1} (°C)
CMAS1 basic system	860	828	939	1257	1262	746	876.8	804.0	988.1	950.5
CMAS2 basic system	854	806	894	1243	1252	749	849.8	828.3	950.9	936.3
CMAS3 basic system	858	820	915	1254	1263	733	941.2	922.6	-	-
CMAS4 basic system	852	821	936	1271	1285	726	849.8	822.5	920.9	901.7

Table 3.5.1.1 Characteristic temperatures of CMAS basic glasses.

The glass transition temperatures and the sintering temperatures are in the same range for the whole range of chemical compositions. The comparison of HSM and DTA curves reveals that CMAS1, CMAS2 and CMAS4 glasses belonging to CMAS series exhibit a single sintering stage behavior with the maximum densification being achieved after the first crystallization peak. In the DTA thermograms there are two crystallization peaks, with the first appearing about 50°C after the first shrinkage stage.

T_{MS}>T_c demonstrates that crystallization precedes sintering of the glass powder and, therefore, not well sintered and mechanically weak glass powders should be expected in the first stage of heat treatment. In these cases, as the onset of crystallization extracted from DTA measurements is located within the range of sintering temperature, crystallization may have hindered the completion of sintering by increasing the viscosity of the material. Such behavior is clear in CMAS1 DTA analysis, in which the first crystallization peak is broad and not well defined.

From the above evidence, we can conclude that the CMAS1 glass is not suitable as a sealant material for SOFCs, because the crystallization onset is evident before the sintering process starts. In CMAS1 the first peak in the DTA curve represents the main crystallization peak. This kind of glass, as mentioned above, has a ratio between the alkaline earth oxide and Al_2O_3 $\left[\frac{(CaO+MgO)}{Al_2O_3}\right]$ less than one and Al^{3+}ions act as former network. Hence, the low content of network modifiers compared with the network former tend to decrease the crystallization

temperature below T_{MS}. Furthermore, as a general tendency, the addition of high amounts of alumina transforms the sharp crystallization peak into a broadened peak splitted into multiple components.

The three glasses CMAS1, CMAS2 and CMAS4 present a low sintering ability. It is thus very important to investigate how the addition of intermediate oxides may change the thermal properties. In the case of CMAS3 the situation is different, because only one crystallization peak is recorded in the DTA curve and the main crystallization temperature appears after the sintering process is complete. The behavior of CMAS3 can be explained by the presence of high amounts of network modifiers, in particular CaO, that control the crystallization step. The sintering ability parameter S_c ($S_C=T_C-T_{MS}$) [154] calculated for the CMAS3 glass is significantly high, indicating delayed nucleation and crystallization events, and so a wider processing window to attain maximum densification. The parameter S_c is a measure of the ability of sintering versus crystallization: the greater is the difference, the more independent are the kinetics of both processes. Furthermore, a DTA thermogram displaying a single crystallization exothermic peak suggests that the resulting glass ceramic consists of a single crystalline phase or of several crystalline phases precipitated simultaneously. This feature gives this glass good suitability as sealant for SOFCs. For CMAS2 and CMAS4 the DTA curves show evidence of similar thermal events in different compositions, related to the formation or transformation of the same crystalline compounds, sharing the same maximum temperature of the first exothermic peak.

The influence of chemical composition of glasses on the evolution of the characteristic temperatures, T_g, T_o and T_c, is represented in Fig. 3.5.1.5.

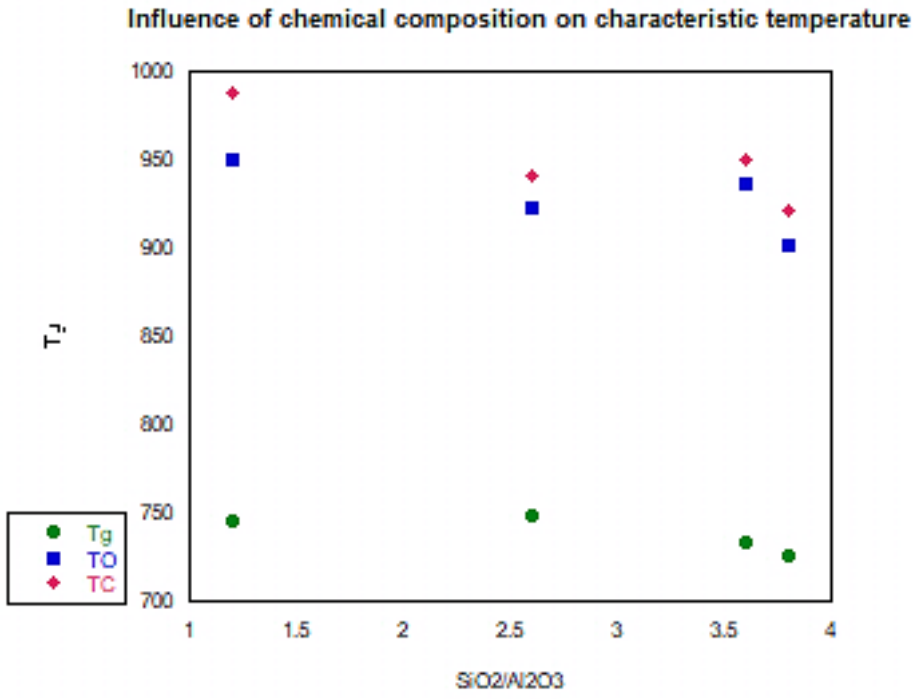

Figure 3.5.1.5 Influence of chemical composition of basic glasses CMAS on the evolution of characteristic temperatures.

This figure shows that the glass transition temperature decreases with increasing the SiO_2/ Al_2O_3 ratio and that a similar trend is observed for the crystallization temperature.

No significant evolution of T_g could be directly related to the ratio $\left[\frac{CaO}{MgO}\right]$, whereas a relationship between the ratio $\left[\frac{CaO}{MgO}\right]$ and crystallization temperatures could be noted for CMAS4, CMAS3 and CMAS2. A different situation was found for CMAS1, where the crystallization temperature is higher than expected. This behavior is due to the role of Al^{3+} ions as network former, in turn related to the high ratio between network formers and network modifiers, $\left[\frac{SiO_2+Al_2O_3}{CaO+MgO}\right]$ (5.28). For the other glasses, the ratio between network formers and network modifiers is different and equal to $\left[\frac{SiO_2}{CaO+MgO+Al_2O_3}\right]$, because Al^{3+} ions act as modifiers.

Considering the results obtained for the CMAS glass series, it is important to understand how the addiction of an additive can influence the thermal properties of glasses. TiO_2 is the first oxide that has been used. Glasses modified by substitution of either part of alumina in CMAS1 or part of alkaline earth oxide CaO in the other systems are investigated for their sintering behavior as well.

In Figure 3.5.1.6 the comparison between DTA and HSM curves measured at the same heating rate (15°C/min) is reported for the CMASTi1 sample. The plots for the other members of the CMASTi series are reported in the Appendix 1 (Figure A1, A2 and A3.)

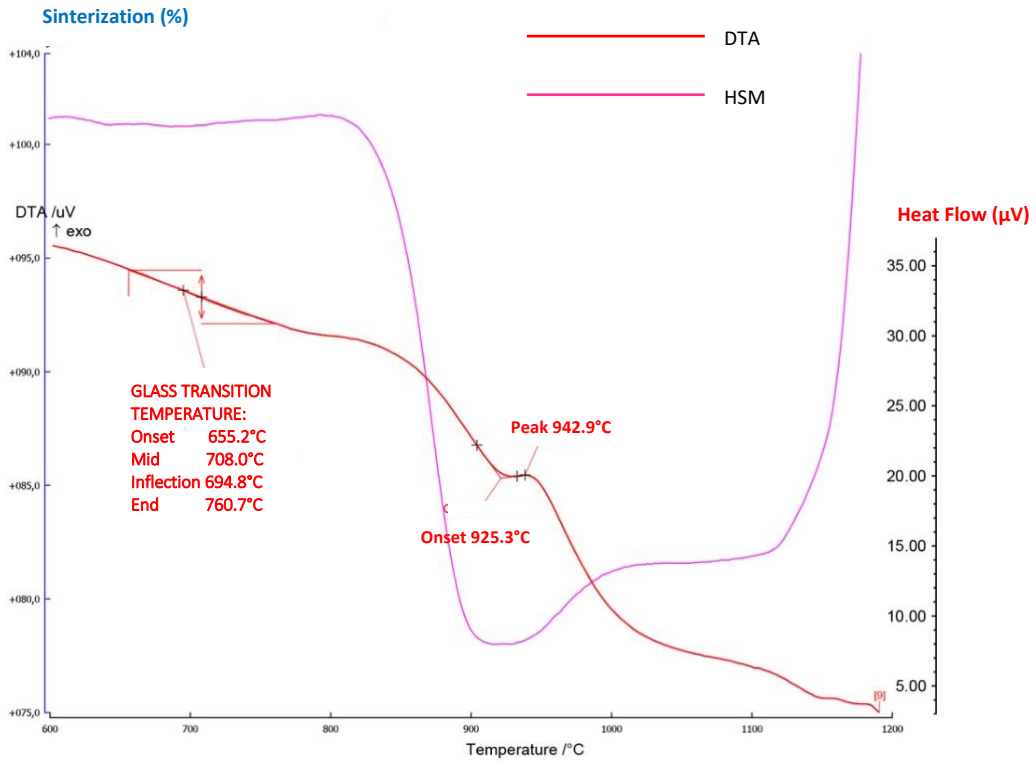

Figure 3.5.1.6 HSM and DTA curves for CMASTi1.

In Table 3.5.1.2. the corresponding characteristic temperatures are listed.

GLASS SAMPLE ID	T_s (°C)	T_{FS}(°C)	T_{MS}(°C)	T_{HB} (°C)	T_F (°C)	T_g. (°C)	T_c(°C)	T_o (°C)
CMASTi1	857	817	907	1235	1249	720	942.9	925.3
CMASTi2	854	815	920	1280	1303	699	922.4	898.1
CMASTi3	831	802	888	1233	1241	750	957.9	946.6
CMASTi4	843	809	891	1239	1248	723	930.7	916.3

Table 3.5.1.2 Characteristic temperatures of CMASTi glasses.

While the modified glasses show a sintering behavior similar to that of the corresponding basic glasses, the crystallization properties are different. Transition metal oxides strongly influence the thermal stability of the glass by changing its devitrification tendency. The thermal stability can be thus improved by introducing TiO_2 into the system.

As a result, the addition of TiO_2 makes uniform the crystallization process and only one peak is observed in the DTA curve. The maximum crystallization temperature lies in the range 930°C-960°C for all glasses belonging to the CMASTi series. Furthermore, for all glasses the temperatures of maximum shrinkage are recorded before the crystallization starts. As mentioned, this is a very important feature giving the glasses good mechanical properties which are crucial for sealing applications. The shrinkage onset of glasses is in the same TEMPERATURE range (800-820°C) for all glasses, whereas the maximum sintering temperatures are different. The sintering ability parameter values, S_c, is significantly high, especially for CMASTi3 glass (∼70°C), hence a strong glass powder compact should be expected before the crystallization starts.

In the CMASTi1 sample, even though Al_2O_3 acts as network former, the addiction of TiO_2 promotes the crystallization process to occur after the sintering is over, though the peak is not well defined because the effect of Al_2O_3 is still evident. This behavior is different from that shown by the CMAS1 sample, in which the network formers control the crystallization stage.

In the other samples, Al_2O_3 acts as network modifier and the presence of TiO_2 continues to control the crystallization step. The only exception is evident in the DTA thermogram of the CMASTi2 sample: in this case the onset of the crystallization peak is recorded at lower temperature. An explanation for this behavior can be found in the high ratio between the alkaline earth oxides, CaO and MgO, and TiO_2, determining a minor effect of the additive during the heat treatment. In this situation, the network modifiers and the additive compete to improve the crystallization step. Furthermore, according to Morimoto and Kuriyama [155], because the ionic radius of Ti^{4+} is larger than Si^{4+} this ion prefers octahedral or cubic co-ordination at lower temperatures near the annealing point (at $T<T_g$). In some glasses containing lower amounts of alkaline earth oxides titanium gradually becomes six-fold coordinated as nucleation occurred.

In previous works [156-157], it was reported that nucleating agents such as TiO_2 tend to form titanate groups that can separate from silicate glasses, leading to phase separation, which plays a role in the crystallization of the glass ceramic. In particular, TiO_2 in amounts >5 wt% resulted in phase separation phenomena. An example of

this phenomenon in our study is the CMASTi4 composition. Also in glasses with relatively large amounts of alkaline earth oxides, owing to the existence of a large number of non-bridging oxygen ions, Ti^{4+} cations can attain a coordination number of 6 with no coordination change during heat treatment.

The influence of MnO_2 on thermal properties of CMAS has not been studied in literature. The study of this additive is important in this work because this oxide is usually contained in wastes from industrial processing, and can affect the properties of CMAS glasses. In Figure 3.5.1.7 we show a typical example of DTA and HMS curves for a glass modified by adding a given amount of MnO_2 (CMASMn2 sample).

This behavior was investigated for all the glasses belonging to the CMASMn series (see the Figures A4, A5 and A6. in Appendix 1). These glasses exhibit the same trend observed in glasses modified by substitution with TiO_2, with DTA thermograms characterized by only one main peak in the range of temperatures between 950°C and '970°C.

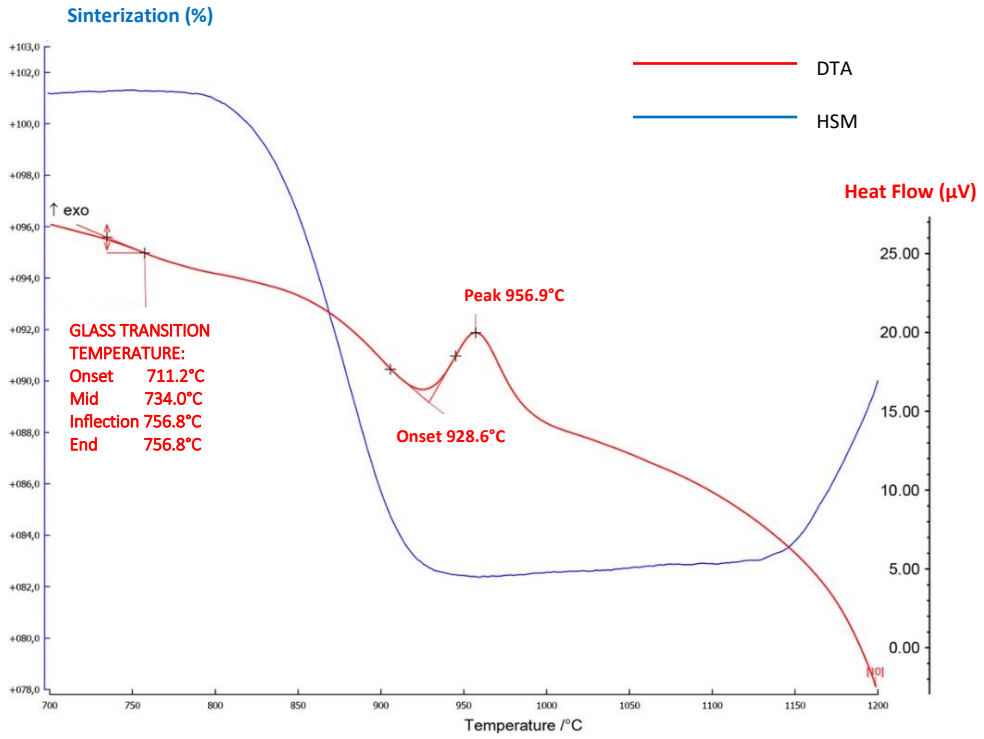

Figure 3.5.1.7 HSM and DTA curves for CMASMn2.

In the case of CMASMn3, a second peak at high temperature could be noted.

In Table 3.5.1.3. are listed the characteristic temperatures extracted from the analysis.

Glass sample ID	T_s (°C)	T_{FS}(°C)	T_{MS}(°C)	T_{HB} (°C)	T_F (°C)	T_g (°C)	T_c(°C)	T_o (°C)
CMASMn1	858	813	919	1456	1460	719	941.2	922.6
CMASMn2	859	810	925	1409	1420	716	956.9	928.6
CMASMn3	854	812	911	1259	1283	720	950.7	920.8
CMASMn4	861	816	913	1421	1428	716	956.1	926.9

Table 3.5.1.3 Characteristic temperatures of CMASMn glasses.

The glass transition temperatures increase with the content of the main glass former silicon dioxide (SiO_2).

In the sample CMASMn1, where Al^{3+} ions act as network formers, the nucleating agent dominates the crystallization process differently from the parent glass CMAS1. As a result, the presence of an additive like MnO_2 makes the crystallization process homogeneous because MnO_2 controls totally the formation of new phases and the alkaline earth oxide plays a minor role in the crystallization step. In contrast to the results obtained for the CMASTi glasses series, for CMASMn glasses, the higher is the amount of MnO_2, clearer and sharper becomes the exothermic peak in the DTA curves. It can be then concluded that the resulting glass ceramic consists of a single or of more simultaneously precipitated crystalline phases. Figure 3.5.1.7 indicates that complete densification takes place below the crystallization temperature, though the onset of crystallization is very close to the temperature of maximum densification. The significant difference between T_g and T_c for all the glasses belonging to the CMASMn series suggests a large ability of the glasses to flow, to accommodate mechanical stresses arising from any CTE mismatch and to act as self-healing materials. The larger sintering ability values, greater than 25°C, are related to larger final densities, which indicate better sintering/crystallization behavior. CMASMn2 shows good properties as far as thermophysical data are concerned.

In the case of Zn-doped glasses, the data obtained from the comparison of HSM and DTA curves display a behavior similar to that exhibited by glasses belonging to CMASMn series. In Figure 3.5.1.8. an example of this kind of modified glass is presented, namely the CMASZn2 sample (the results for the other samples are reported in Appendix 1, Figures A7, A8 and A9).

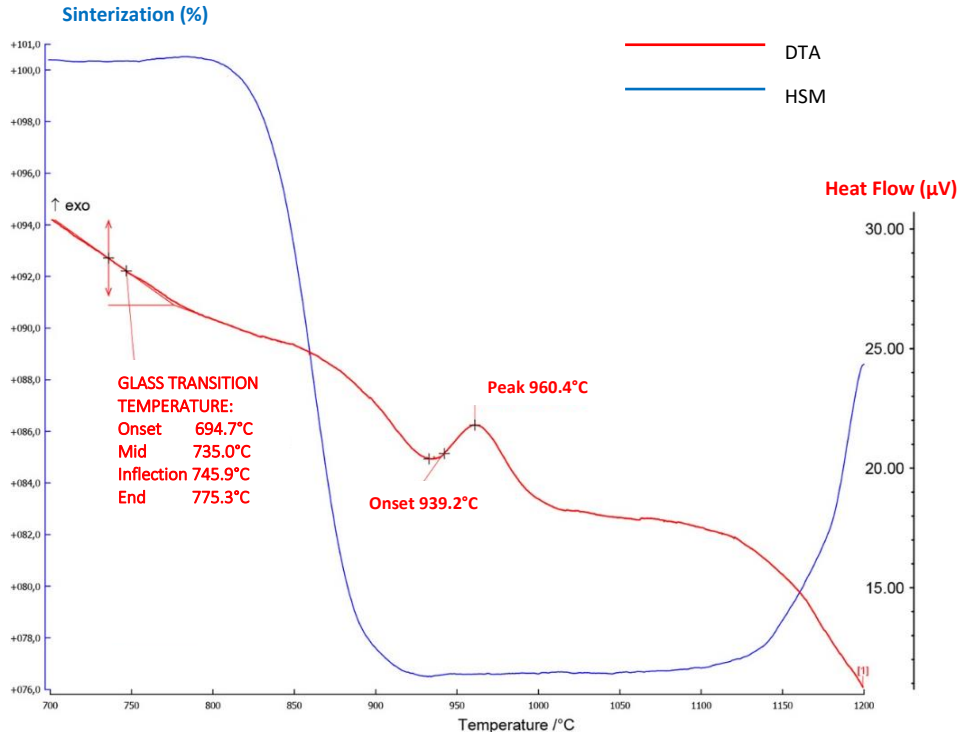

Figure 3.5.1.8 HSM and DTA curves for CMASZn2.

Comparing the CMASMn2 and CMASZn2 samples is evident how the influence of the nucleating agents is the same. Well compact glasses are formed before the crystallization step with high sintering ability. The maximum densification temperatures are lower than those recorded in other samples for all series.
In Table 3.5.1.4 are listed the results obtained from the analysis.

GLASS SAMPLE ID	T_s (°C)	T_{FS}(°C)	T_{MS}(°C)	T_{HB} (°C)	T_F (°C)	T_g (°C)	T_c(°C)	T_o (°C)
CMASZn1	839	801	898	1252	1266	730	958.2	934.8
CMASZn2	847	809	913	1221	1231	735	960.4	939.2
CMASZn3	855	815	919	1244	1253	718	959.4	933.7
CMASZn4	834	800	905	1257	1263	712	914.6	884.8

Table 3.5.1.4 Characteristic temperatures of CMASZn glasses.

The main crystallization peak is located around 960°C for the first three glasses, the only exception is evident in CMASZn4 sample, in which the high amount of ZnO moves the exothermic peak to lower temperature (~914°C). The presence of ZnO improves the kinetic of crystallization. Hence, the presence of ZnO_2 controls the development of crystallization step. Except for CMASZn4, complete dense and well sintered glasses are subjected to devitrification process. Indeed, ZnO enhances sintering and crystallization over MgO and CaO in glass, when $\frac{CaO+Mgo}{ZnO}$ is high, generally greater that 4, thus resulting into dense sintered and mechanically strong glass powders. Moreover, it has been observed that ZnO acts in a manner similar to B_2O_3 with regard to the viscosity. In a number of alkaline-earth aluminosilicate glasses, addiction of small amount of ZnO decreases viscosity in the transition temperature range, lowering T_g by around 20°C while at the same time slightly increasing CTE (see the Par.3.6). Also, unlike B_2O_3, ZnO remains more stable in wet hydrogen atmospheres [158-159]. The behavior of T_g and CTE suggests that the addition of ZnO results in a weakening of the glass network and decreasing of the glass viscosity. In CMASZn4, where the content of ZnO is equal to the content of MgO, these oxides improve in opposite ways the starting of sintering and crystallization: MgO promotes the crystallization of new phases due to Mg^{2+} diffusion, while ZnO acts favoring the sintering ability, so that the onset of crystallization is observed at temperatures near to the end of the sintering process.
It is interesting to note that in these two last series the ratio between the alkaline earth oxides and additive doesn't play an important role in the formation of glass ceramic material.

The last series of glasses was obtained for addition of SnO_2. Only two modified glasses were analyzed because of the SnO_2's critical behavior during the heat treatment to form the glass melt from powders of raw materials. In fact, it has been observed that when the amount of network former and SnO_2 is too high, it is difficult to achieve the fusion temperature. In Figure 3.5.1.9 and 3.5.1.10 the comparison of HSM and DTA curves for the CMASSn1 and CMASSn2 glasses is shown.

The sintering curves of both samples are different from the other glasses, because the first sintering temperature is high (around 840°C), but at the same time the maximum densification temperature keep around 910°C, meaning that the sintering range is reduced. The values of sintering ability (S_C) are high as the crystallization is delayed. From HSM curves a considerable expansion is observed in CMASSn1 and CMASSn2 glasses in the temperature range in which the crystallization takes place (900-1000°C). This phenomenon can probably be due to the formation of phases with larger volume, which is generally an undesirable effect for sealing.

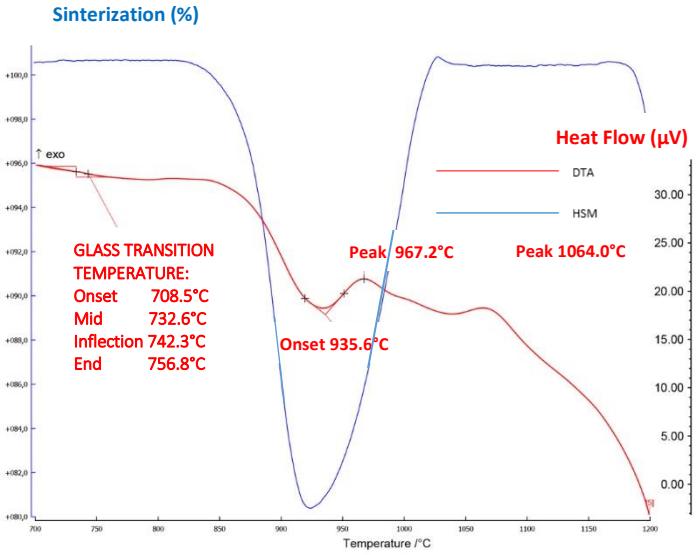

Figure 3.5.1.9 HSM and DTA curves on the temperature scale for CMASSn2.

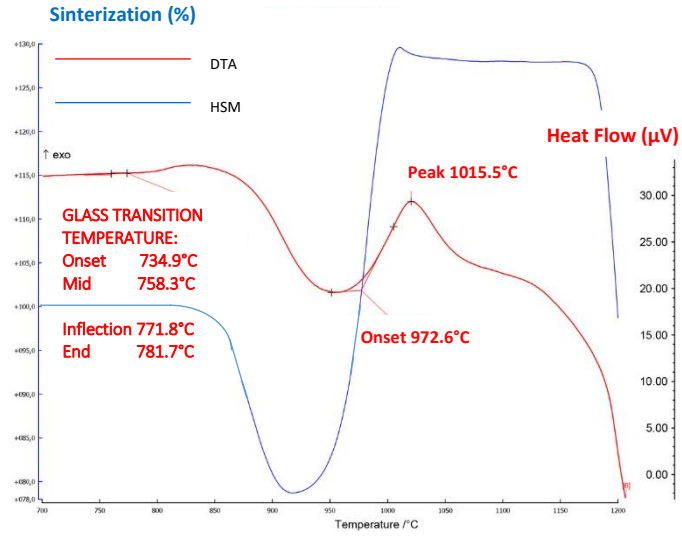

Figure 3.5.1.10 HSM and DTA curves on the temperature scale for CMASSn3.

In Table 3.5.1.5 are listed the results obtained from the analysis of the above reported curves.

GLASS SAMPLE ID	T_s (°C)	T_{FS}(°C)	T_{MS}(°C)	T_{HB} (°C)	T_F (°C)	T_g (°C)	T_c(°C)	T_o (°C)
CMASSn2	882	838	918	1228	1245	742	967.2	935.6
CMASSn3	865	843	907	1221	1236	748	1015.5	972.6

Table 3.5.1.5 Characteristic temperatures of CMASSn glasses.

From DTA analysis is clear that the behavior of these two samples is quite different. CMASSn2 display two exothermic peaks, one at a temperature of 966°C and the other at 1064°C. On the contrary, CMASSn3 exhibits just one exothermic peak at high temperature, around 1015°C, and the peak is well defined and clear. These results could be explained by the amount of SnO_2 in the glass composition in comparison with the amount of network modifiers. This explains why the influence of SnO_2 is larger in CMASSn3.

To complete the analysis of thermophysical properties, the glass stability and the glass forming ability were evaluated. Glass stability and glass forming ability could be calculated from HSM and DTA data. The results were derived considering the first crystallization temperature recorded. To this end, we resort to the use of the previously discussed equations 3.10-3.15 based on slightly different approaches. These equations allow to

determine the glass stability using different characteristic temperatures. In the Table 3.5.1.6. are presented all the results obtained for all series of glasses.

GLASS SAMPLE ID	K_T	K_1	K_2	K_W	K_H	K_3
CMAS1 basic system	0,59	516	130.8	0.10	0.34	3.35
CMAS2 basic system	0,60	503	100.8	0.08	0.25	1.36
CMAS3 basic system	0,58	530	208.2	0.16	0.65	2.79
CMAS4 basic system	0,56	559	123.8	0.10	0.28	2.05
CMASTi1	0,58	529	222,9	0,18	0,73	2,89
CMASTi2	0,54	604	223,4	0,17	0,59	3,71
CMASTi3	0,60	491	207,9	0,17	0,73	1,79
CMASTi4	0,58	525	207,7	0,17	0,65	2,23
CMASMn1	0,49	741	222,2	0,15	0,43	2,59
CMASMn2	0,50	704	240,9	0,17	0,52	4,24
CMASMn3	0,56	563	230,7	0,18	0,69	4,68
CMASMn4	0,50	712	240,1	0,17	0,51	4,31
CMASZn1	0,58	536	228,20	0,18	0,74	3,79
CMASZn2	0,60	496	225,40	0,18	0,83	3,52
CMASZn3	0,57	535	241,40	0,19	0,82	4,42
CMASZn4	0,56	551	202,60	0,16	0,58	4,08
CMASSn2	0,60	503	225,20	0,18	0,81	4,91
CMSASn3	0,61	488	267,50	0,22	1,21	7,80

Table 3.5.1.6 Results of glass stability parameters for all examined glasses.

Apart from the glasses CMAS1, CMAS3 and CMAS4 belonging to the basic system, in which the crystallization events occur soon during heat treatment, all other tested materials exhibit a good glass stability. Considering the different parameters, K_1 and K_2 could be considered as the best indicators to estimate the glass stability, the larger is the interval, the higher the glass stability. From the result in table 3.5.1.6, it is evident that glasses belonging to CMASMn series exhibit the highest K_1 values, i.e they present high glass stability ranges due to their high melting temperatures. All the other glasses show a glass stability range about 500°C. The other three parameters, K_W, K_H and K_3 put into relation the crystallization temperature with the melting temperature and are closely related to the effect of the nucleating agents. For the glasses modified by partial substitution of the alkaline earth oxide, CaO, or alumina, the crystallization events are shifted to higher temperatures, therefore the glass stability is expected to increase. The study of crystallization kinetics could help to understand better the effect of additional oxides on the glass stability. Considering the Turnbull's value of glass stability, as reported in literature [144-145], samples with K_T greater than 0.5 exhibit good stability. As result, the parameters, K_W and K_3, calculated for all glasses, falls within the range established in literature by Weinberg for simple

system of glasses, i.e. $0.1< K_W<0.5$ and $K_3>1.5$. The same remark could be applied to K_H according to the Hruby interpretation. K_H must fall in the interval between 0.3 and 2.0. Only CMASSn2 presents a value higher than the upper limit due to the high temperature of crystallization. It can be concluded that the addition a nucleating agent could increase the stability of the basic glasses depending on the chemical composition.

3.6 Thermomechanical properties

The Coefficient of Thermal Expansion (CTE) is one of the most important thermal properties for sealing applications in SOFCs. In order to avoid thermal stresses, it should strictly match with those of other SOFC components. During cell operation, thermal stress arises due to difference(s) in CTEs between the joined SOFC component and seal glass. Both tensile ($CTE_{component}>CTE_{glass}$) and compressive ($CTE_{component}<CTE_{glass}$) stresses are possible at the interface [160-161]. CTE differences should not exceed $1\cdot10^{-6}$ °C^{-1} [162]. Tensile stress often leads to cracks at the interface and in the glass. Compressive stress to some extent can be tolerated because the compressive strength of a seal glass is much higher than tensile strength, but excessive compressive stress causes the delamination of the glass from interfacing SOFC components. The CTE of a common Ni–ZrO_2 cermet (hydrogen electrode), usually containing more than 30 vol.% nickel, varies between 10.0 10^{-6} and 14.0 10^{-6} °C^{-1} depending on temperature and nickel content [163-164-165], partly because the CTE of nickel increases with temperature [166]. The CTEs of lanthanum manganate electrode (air electrode), ZrO_2 electrolyte, and metallic interconnects are 12.4 10^{-6} °C^{-1}[167], 8.5–10.5 10^{-6} °C^{-1} [163], and 11.0– 15.0 10^{-6} °C^{-1} [168], respectively. To seal these cell components, the CTE of a seal glass should be 8.5–15.0 10^{-6} °C^{-1}. In practice, a CTE ranging from 8.0 10^{-6} °C^{-1} to 12.0 10^{-6} °C^{-1} is the target for SOFC applications. The CTE of a seal glass depends on the glass structure symmetry, bond-bending, and molar-free volume. For example, pure SiO_2 glass has 0.6 10^{-6} °C^{-1} CTE due to its high symmetry and B_2O_3 has 14.4 10^{-6} °C^{-1} CTE due to its low symmetry [169]. Modifiers in silicate glasses create non-bridging oxygen species which decrease the average symmetry of the Si–O bonds and thus increase the CTE [88]. Unlike T_g and T_s, CTE does not depend on the polarizability of ions [169]. Roles of different constituents on the CTE of a seal glass generally follow the opposite trend as on T_g and T_s. Specific effects can be analyzed based on the functions of the glass constituents and the operating conditions and duration of a SOFC. The thermal expansion characteristics of bulk glasses were analyzed for all kind of glasses to verify that their CTEs measured in common ranges of temperature between 200°C and 500° and between 200°-700°C matched the target interval of 8.0 10^{-6} °C^{-1} to 12.0 10^{-6} °C^{-1}.

Dilatometric experiments were performed on pressed tablets of glass powder (<45 µm). The dilatometry measurements were made at 5°C·min^{-1} on a minimum of three specimens from each glass and the standard deviations for the reported CTE values are within the range $\pm0.1\cdot10^{-6}$ °C^{-1}. Besides CTE, also T_g and the dilatometric softening point, T_D, can be retrieved from dilatometric measurements. All samples have a linear expansion up to the glass transition temperature. The dilatometric softening temperature, T_D, is determined at the point of maximum thermal expansion. This parameter was also used to determine the viscosity of the

glasses. To study the influence of different additives on the CMAS glasses, the thermal expansion curves obtained for all the series of glasses will be analyzed simultaneously. The results for each series are presented in Figures 3.6.1. - 3.6.4 (CMAS1, CMAS2, CMAS3, CMAS4 series, respectively).

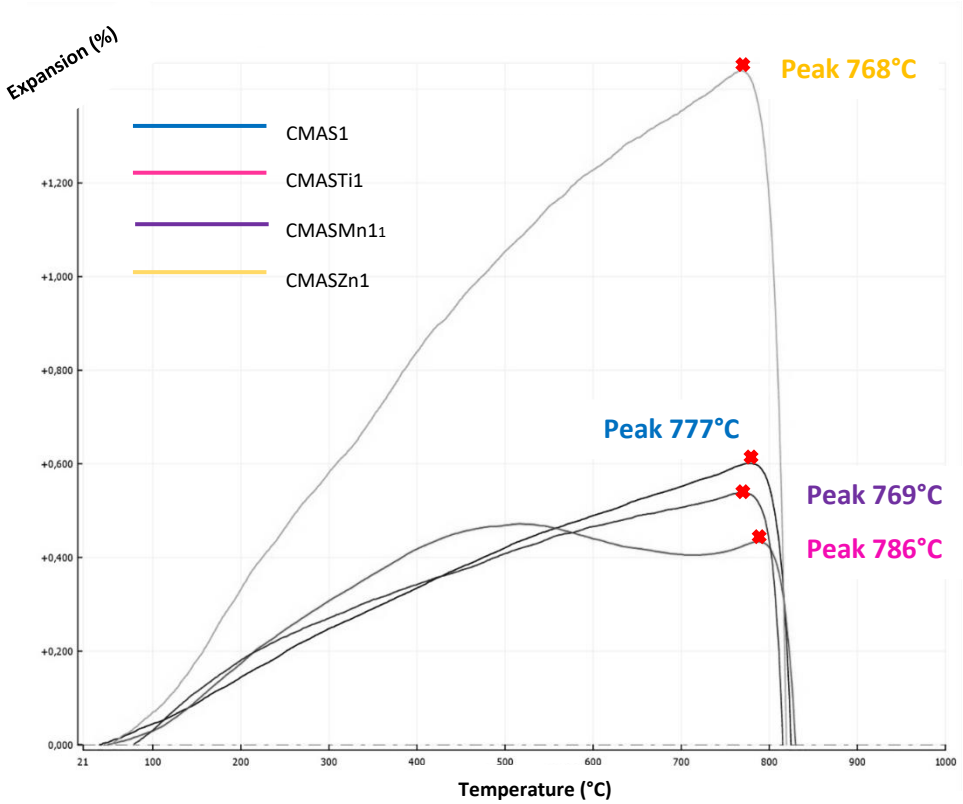

Figure 3.6.1 Expansion curve for CMAS1 glass system.

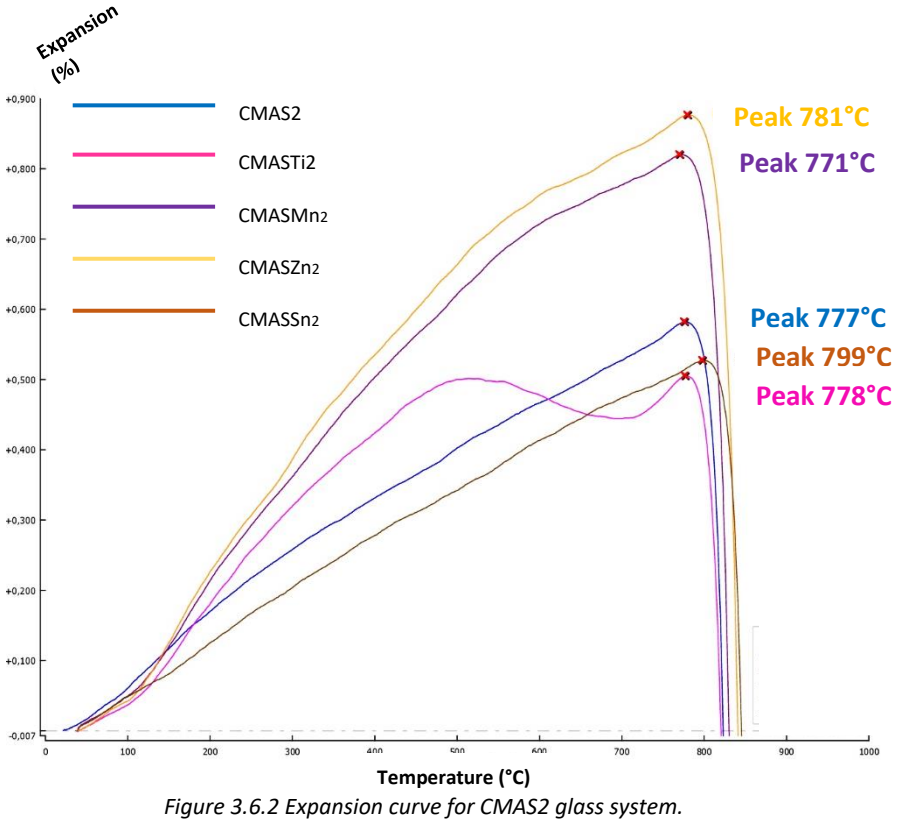

Figure 3.6.2 Expansion curve for CMAS2 glass system.

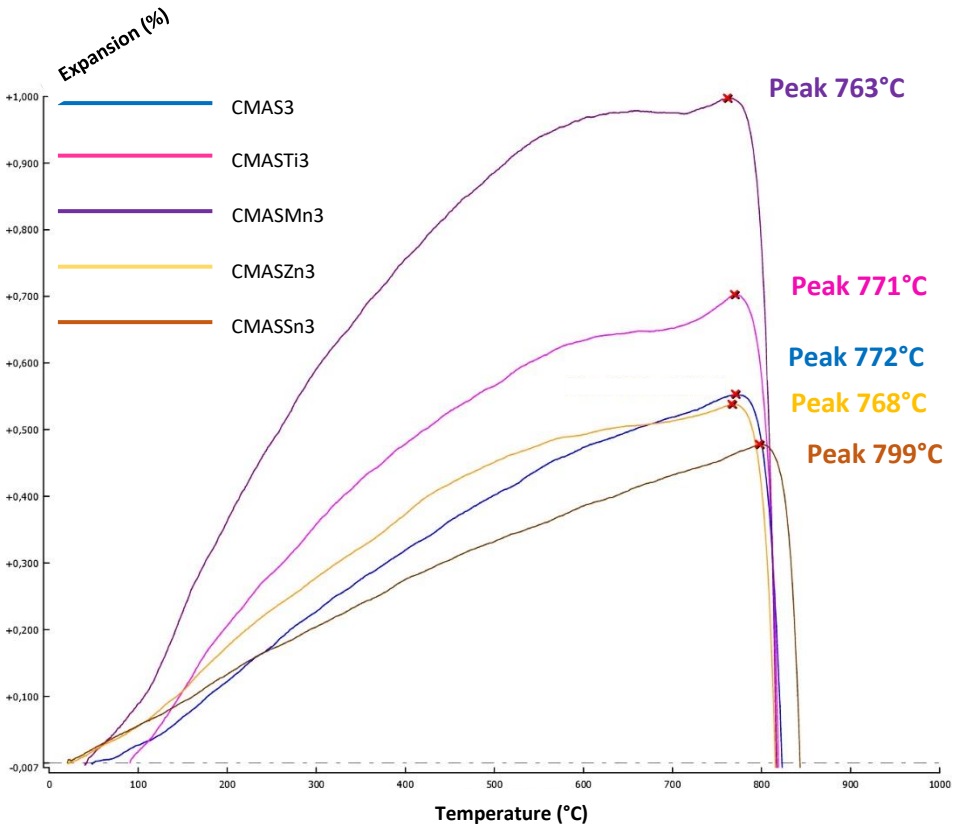

Figure 3.6.3 Expansion curve for CMAS3 glass system.

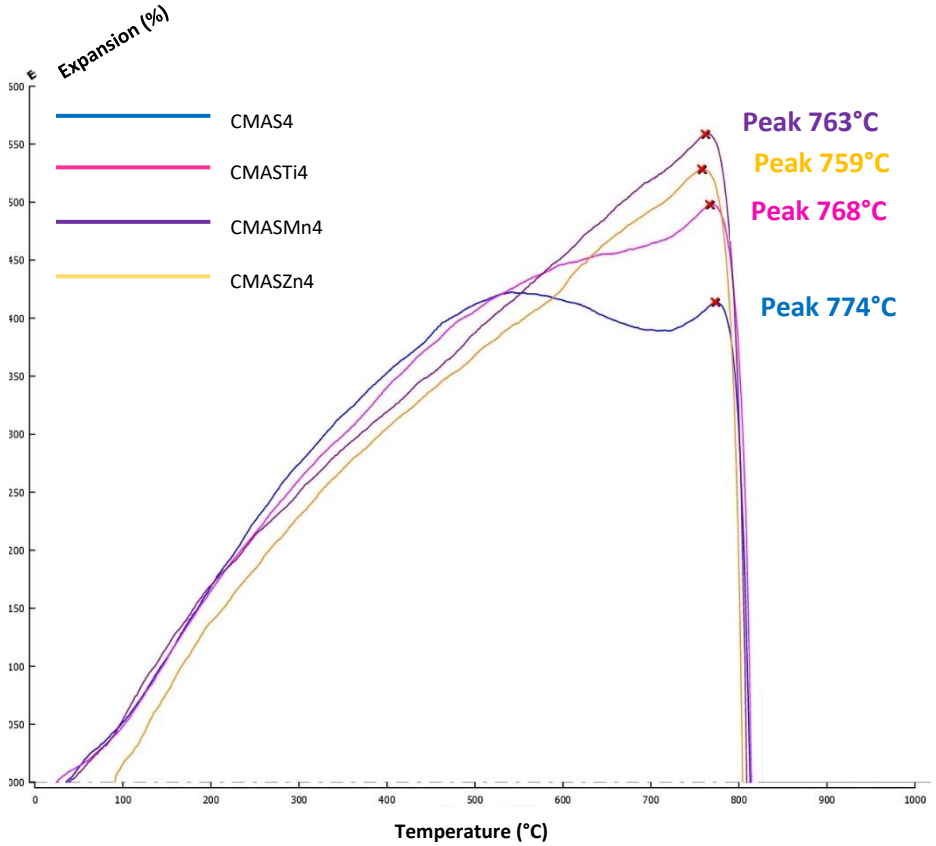

Figure 3.6.4 Expansion curve for CMAS4 glass system.

In Table 3.6.1. are listed the CTE values recorded in the common temperature ranges of 200°C-500°C and 200°C-700°C (error within the range $\pm 0.10 \cdot 10^{-6}$ °C^{-1}).

GLASS SAMPLE ID	$\alpha_{(200°-500°C)}$ (°C^{-1})	$\alpha_{(200°-700°C)}$ (°C^{-1})
CMAS1 basic system	$9.21 \cdot 10^{-6}$	$8.15 \cdot 10^{-6}$
CMASTi1	$9.85 \cdot 10^{-6}$	$9.90 \cdot 10^{-6}$
CMASMn1	$8.00 \cdot 10^{-6}$	$8.09 \cdot 10^{-6}$
CMASZn1	$24.06 \cdot 10^{-6}$	$20.44 \cdot 10^{-6}$
CMAS2 basic system	$8.01 \cdot 10^{-6}$	$8.15 \cdot 10^{-6}$
CMASTi2	$10.66 \cdot 10^{-6}$	$10.75 \cdot 10^{-6}$
CMASMn2	$12.41 \cdot 10^{-6}$	$11.27 \cdot 10^{-6}$
CMASZn2	$13.57 \cdot 10^{-6}$	$11.93 \cdot 10^{-6}$
CMASSn2	$8.23 \cdot 10^{-6}$	$8.36 \cdot 10^{-6}$
CMAS3 basic system	$9.32 \cdot 10^{-6}$	$8.15 \cdot 10^{-6}$
CMASTi3	$12.00 \cdot 10^{-6}$	$8.93 \cdot 10^{-6}$
CMASMn3	$13.45 \cdot 10^{-6}$	$12.03 \cdot 10^{-6}$
CMASZn3	$9.22 \cdot 10^{-6}$	$8.77 \cdot 10^{-6}$
CMSASn3	$8.64 \cdot 10^{-6}$	$8.26 \cdot 10^{-6}$
CMAS4 basic system	$8.11 \cdot 10^{-6}$	$8.03 \cdot 10^{-6}$
CMASTi4	$8.04 \cdot 10^{-6}$	$8.49 \cdot 10^{-6}$
CMASMn4	$8.26 \cdot 10^{-6}$	$7.99 \cdot 10^{-6}$
CMASZn4	$8.66 \cdot 10^{-6}$	$8.06 \cdot 10^{-6}$

Table 3.6.1 Thermal expansion coefficients of all glasses in range 200°-500°C and 200°-700°C.

From the results, we can conclude that:

1. Among the parent glasses belonging to the CMAS series, only CMAS4 exhibits a considerable decrease of CTE in the range 200°C-700°C;
2. All the CMASTi glasses show suitable values of CTEs in both temperature ranges. CMASTi4 exhibits the lowest CTE values because of the higher field strength of Ti^{4+} ions (1.25);
3. CTEs of CMASMn are larger compared with the other systems. However, with the exception of CMASMn3, CTEs of the other Mn-modified glasses fall within the required range for SOFC sealants; for its large CTE value, the CMASMn3 glass should be excluded from potential glass sealants;
4. A similar situation is found for CMASZn glasses. In this case, CMASZn1 is considered not suitable for SOFC sealing, due to too high CTE values. The CTE value for CMASZn4 is lower compared with the other glasses doped with ZnO, suggesting that the high content of ZnO tends to decrease CTE because of the higher field strength of Zn^{2+} ions (0.52-0.59).
5. Both samples in the CMASSn series exhibit a good CTE for sealing applications.

From the above reported results we can conclude that also isolated additive distribution, for i.e. CMASZn1, plays an important role in the expansion behavior of glasses. The results obtained for CMASTi4 and CMASZn4

confirm some evidence previously reported in the literature, where it has been demonstrated that in mixed alkaline earth oxide glass, addiction of TiO_2 >5.5 mol% and ZnO >4.8mol%-tends to decrease CTE compared with basic glasses[170-171-172]. This effect can be attributed to the higher field strength of Ti^{4+} ions and Zn^{2+} ions. In the second part of the sample characterization (see Section 3.8), the CTEs obtained for the corresponding glass ceramic will be discussed.

From dilatometric measurements, the value of maximum nucleation temperature can also be derived. The most suitable nucleation temperature of the glass specimens can be determined according to the Day and Ray method [173] as follows: the specimens are first soaked at differing nucleation temperatures (T_N) in the range T_g-T_D for a specific time, where T_g and T_D are the glass transition and dilatometric softening temperature, respectively. Samples are then subjected to DTA runs and the T_c and T_N trend is analysed, where T_c is the DTA peak temperature. The minimum of this curve generally represents the most efficient nucleation temperature, because the specimen soaked at the most suitable nucleation temperature usually show the lowest exothermic peak temperature in the DTA runs. As an example, Figure 3.6.5. displays DTA plots for the specimen CMAS1 obtained according to the above procedure for a nucleation time of 3 hours at the indicated temperatures.

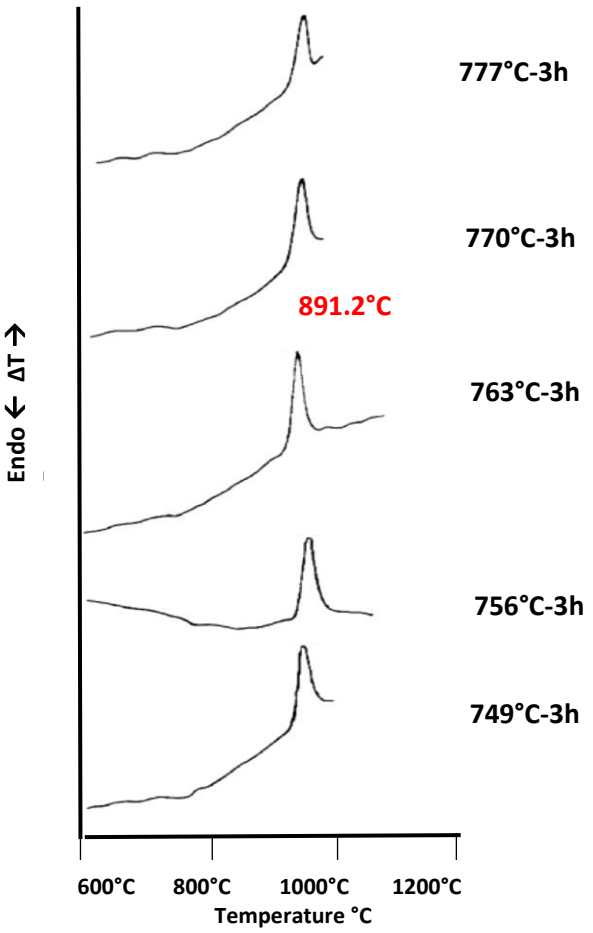

Figure 3.6.5 Differential thermal analyses traces of CMAS1 sample previously nucleated at the indicated temperature for 3h.

A continuous decrease in DTA peak temperature and an improvement in peak sharpness are observed upon the increase of the nucleation temperature up to 763°C. Higher nucleation temperatures resulted first in an increase of peak temperature and then in the shortening and broadening of peaks (despite the reduction of peak temperatures), which are the sign of crystallization decline and eventually decreasing of the peak to around 777°C. As a consequence, 763°C is chosen as the most suitable nucleation temperature for CMAS1 basic system glass. The crystallization growth temperature (T_{CG}) is considered the maximum temperature of exothermic peak in DTA run (for CMAS1 it is equal to 891.2°C, see Figure 3.6.5).

This method has been used for all series of glasses. In table 3.6.2. the data obtained from dilatometric and DTA measurements are summarized. The parameter ΔT in the last column is the difference between T_{CG} and T_N (its importance will be discussed later), T_{CG} is the maximum temperature of exothermic peak for samples nucleated at a given temperature T_N for 3 hours.

GLASS SAMPLE ID	T_g (°C)	T_D (°C)	T_N (°C)	T_{CG} (°C)	ΔT (°C)
CMAS1					
CMAS1 basic system	746	777	763	891.2	128,2
CMASTi1	720	786	772	899.4	127,4
CMASMn1	719	769	765	883.8	118,8
CMASZn1	730	768	766	887.3	121,3
CMAS2					
CMAS2 basic system	749	777	759	909.1	150,1
CMASTi2	699	779	770	903.7	133,7
CMASMn2	716	771	768	916.4	148,4
CMASZn2	735	781	765	909.8	144,8
CMASSn2	742	800	790	929.5	139,5
CMAS3					
CMAS3 basic system	733	772	749	911.7	162,7
CMASTi3	750	797	783	931.1	148,1
CMASMn3	716	763	757	919.0	162.0
CMASZn3	712	770	764	922.6	158,6
CMASSn3	748	798	791	949.4	158,4
CMAS4					
CMAS4 basic system	726	773	741	899.3	158,3
CMASTi4	723	768	768	905.9	137,9
CMASMn4	726	763	758	913.0	155,0
CMASZn4	712	759	747	880.2	133,2

Table 3.6.2 Summary of dilatometer glass transition (T_g) and softening (T_D) temperatures and the derived nucleation temperature (T_N).

From the data listed in table 3.6.2., we can conclude that generally the addition of network modifiers into pure glass-forming oxides disrupts glass network structure, creates non-bridging oxygen, and decreases T_g. In the presence of additive an increase of the nucleation temperature was observed, that improves the crystallization kinetics.

The effect of different types of transition metal oxides on T_g and T_D is then not significant and depends only on their arrangements in glass structure. Optimal T_g and T_D for SOFC seal glass can be obtained by a composition

containing 40-60 mol% glass formers, 20-40 mol% glass modifiers (alkaline earth oxides), 5-10 mol% intermediates and 3-10 mol% additives. The glasses under investigation respect these criteria.

Determining the nucleation temperatures is important also for another reason. For many years, researches have been working on new methods to reduce the manufacturing cost and carbon emissions in glass ceramic preparation. Usually, glass ceramics are produced by either sintering or two steps crystallization due to its poor crystallization ability [174-175-176]. However, both procedures suffer of not negligible drawbacks: in the sintering process, the quenching step wastes a lot of heat and generates a large amount of wastewater, resulting in environmental pollution; on the other hand, the two-step crystallization contains two heat treatment steps (nucleation and crystal growth) [177-178-179], which is highly energy-consuming and carbon-emitting. Thus, high cost of economic and environmental protection issues involving in glass ceramic production largely restrict their industrialized preparation and large-scale applications [180].

One very promising way is the one-step heat treatment where the nucleation and crystal growth are performed at the same temperature (T_{NC}) [181]. A small temperature difference (ΔT) between the optimal nucleation (T_N) and crystal growth (T_{CG}) temperatures is the necessary condition for one-step crystallization of glass-ceramics. As already mentioned, the T_N and T_{CG} of glass forming oxide systems are sensitive to the chemical composition of the parent glass [182-183]. Hence, optimizing the composition of the parent glass is considered as a feasible way to reduce ΔT, with the improvement of nucleation capacity or crystal growth capacity of the parent glass.

Recently, improving the nucleation capacity of the glass has been noticed to be significant to decrease ΔT. In this work, we found that adding a nucleation agent tends to increase the nucleation temperature and hence T_{CG} compared with the parent basic system glass.

The results we obtained for the nucleation temperatures indicate that all the modified glasses act to improve the nucleation capacity. However, to the best of our knowledge, just a few papers reported effective and direct relationships between ΔT and one-step crystallization and no clear correlation has not yet been established. Crystallization kinetic considerations will be useful to understand if the examined glass are suitable candidates for one step-crystallization. (see Section 8.1 “Crystallization kinetics”).

As reported in the literature by Yang et al. [184] a glass layer is created while the crystallization occurs. Indeed, during the crystallization of glass, glass network modifiers and nucleating agent ions are concentrated in the crystals, so that the glass layer between the crystals and the residual glass get richer in glass network formers such as Si and in some cases Al. Thus, the glass layer becomes a diffusion barrier layer for ions of the crystal phase such as Ca^{2+} and Mg^{2+} [185-186-187]. Figure 3.6.6 represents schematically the possible one step crystallization process.

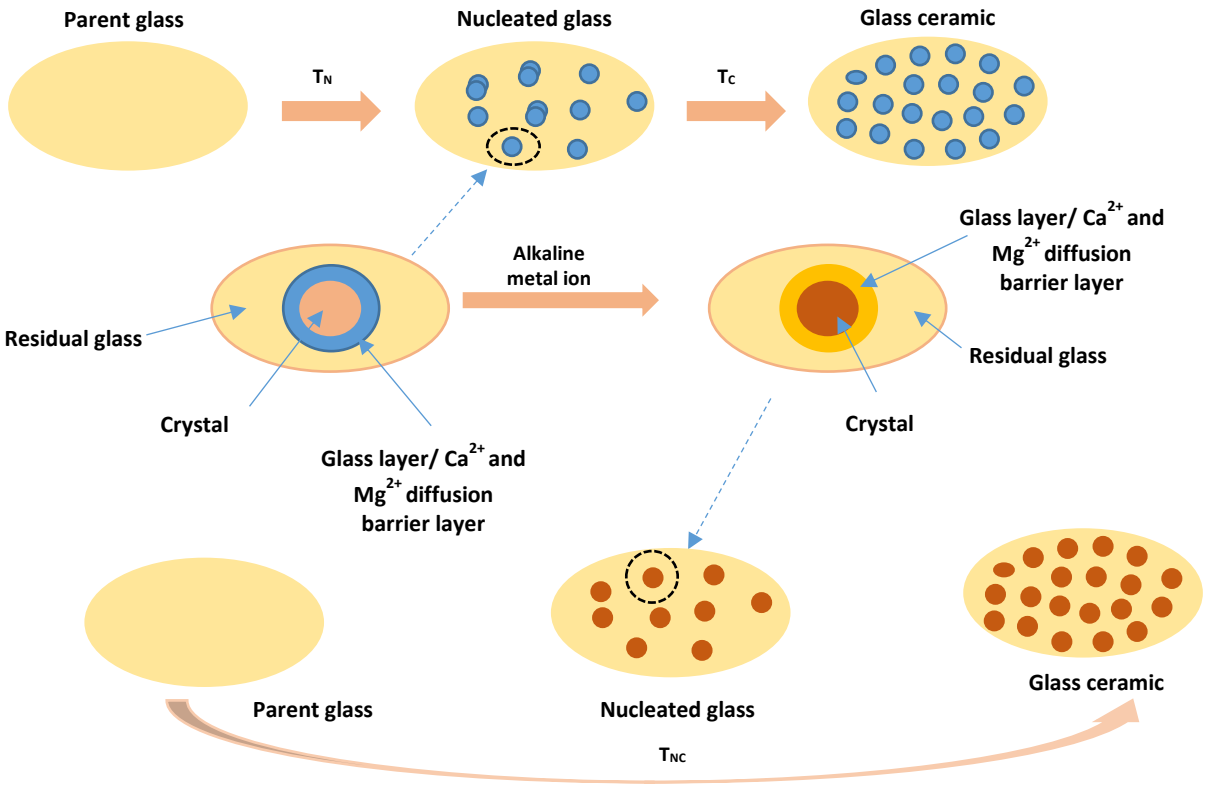

Figure 3.6.6 Schematic diagram of CMAS glass one-step crystallization accomplished by building Ca^{2+} and Mg^{2+} fast diffusion layer around the crystal.

According to this scheme, the diffusion layer would suppress the crystal growth [188-189-190]. Thereby, higher temperatures (T_{CG}) for crystal growth are necessary to overcome the diffusion barrier [191]. Therefore, avoiding the formation of diffusion barrier layer is necessary to improve the crystal growth capacity, decrease ΔT and achieve one-step crystallization of glass ceramic. Experimental data obtained from the analysis of crystallization kinetics will clarify the situations found in the studied glass series. (see. Section 3.8.1)

3.7 Temperature dependence of viscosity

Viscosity of a glass decreases with increasing temperature according to a logarithmic law. Arrhenius described the temperature dependence of viscosity by equation 3.16. More commonly used is the equation 3.17, usually called the Vogel-Fulcher-Tamman (VTF) equation, that is often expressed in the logarithmic form of equation 3.18.

$$\eta = \eta_0 e^{\frac{\Delta H_\eta}{RT}} \tag{3.16}$$

$$\eta = \eta_0 e^{\frac{B}{(T-T_0)}} \tag{3.17}$$

$$\log \eta = A + \frac{B}{T-T_0} \tag{3.18}$$

In eq. 3.16, η is the viscosity of the materials, η_0 is a pre-exponential factor, that can be considered constant for moderate temperature ranges, ΔH_η is the activation energy, which is also assumed constant, R is the gas

constant and T is the absolute temperature. In eq. 3.17 and 3.18 A, B and T_0 are constant parameters (see below). The behavior of viscosity in an Arrhenius plot has been used to classify glasses as strong and fragile. Strong glasses show linear behavior as expressed by eq.3.16, while fragile glasses display a non-linear trend as described by the VFT-equation, eq.3.17 [192]. The glass transition temperature, T_g, softening point, T_s, and melting temperature, T_M, are important parameter in characterizing viscous behavior of glass. Figures 3.7.1. - 3.7.4 present the viscosity of the different series of glasses (respectively CMAS1 series, CMAS2 series, CMAS3 and CMAS4 series) as a function of temperature. Has been demonstrated that VTF equation provides a good fit to viscosity data over wide range of temperature and therefore commonly used to estimate the viscosity of glasses. The experimental points, derived from HSM images, are situated between $log\,\eta$ values of 13 and 3 with in dPa s.

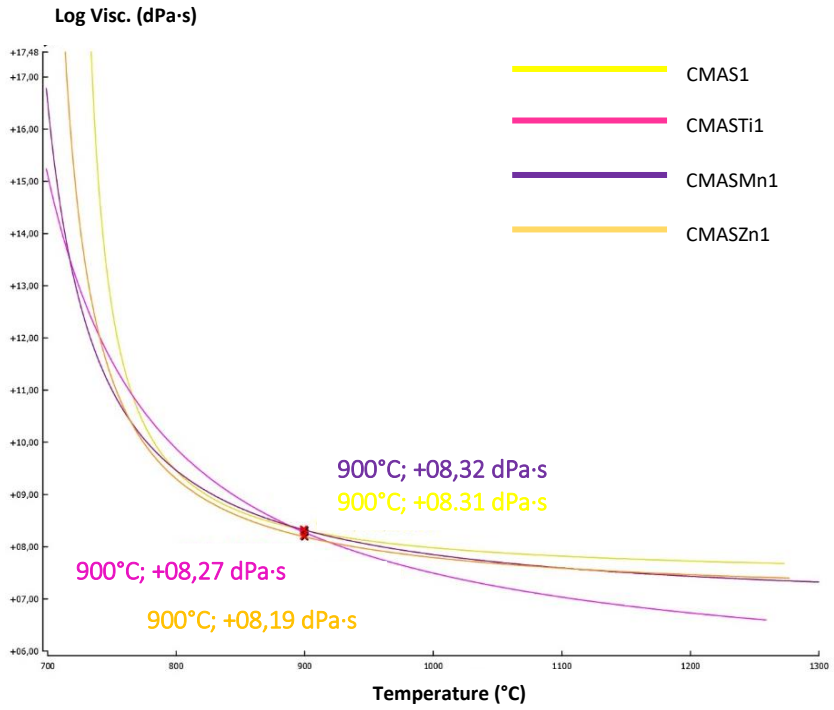

Figure 3.7.1 Viscosity of glasses belonging to the CMAS1 series.

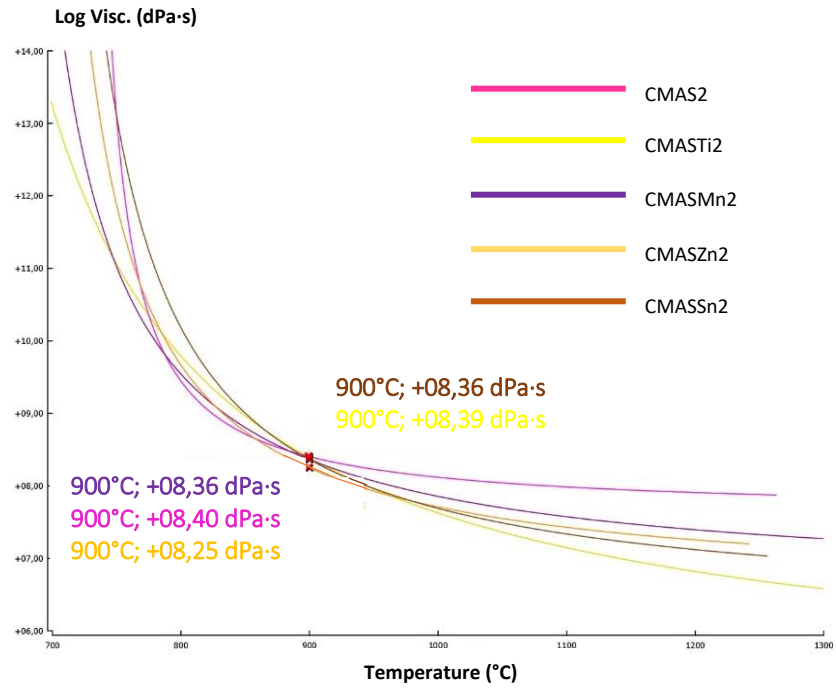

Figure 3.7.2 Viscosity of glasses belonging to the CMAS2 series.

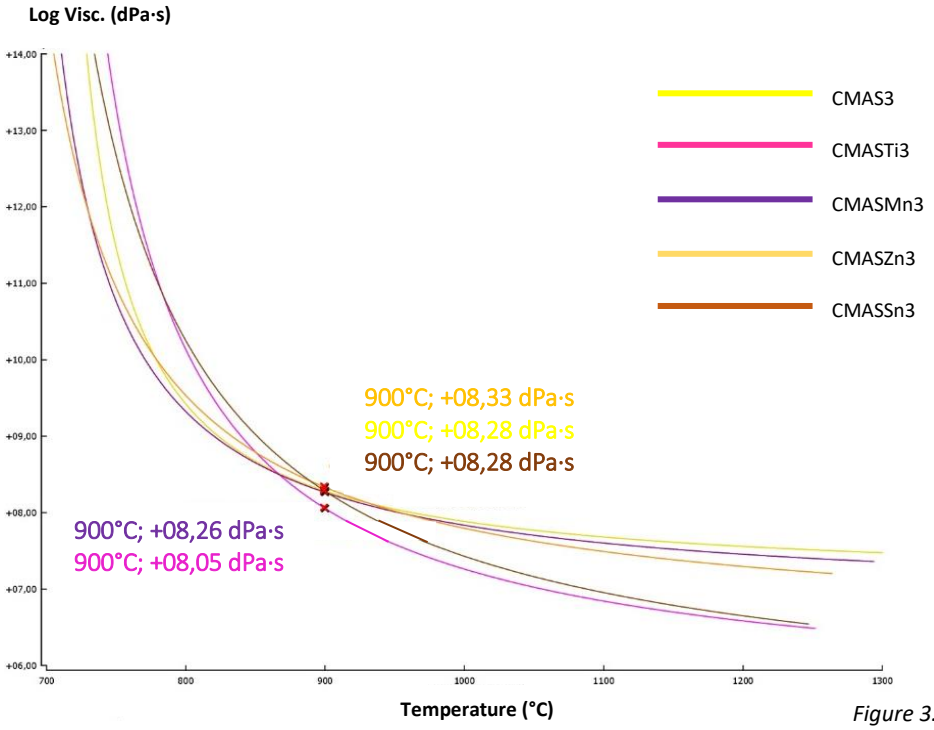

Figure 3.7.3 Viscosity of glasses belonging to CMAS3 series."

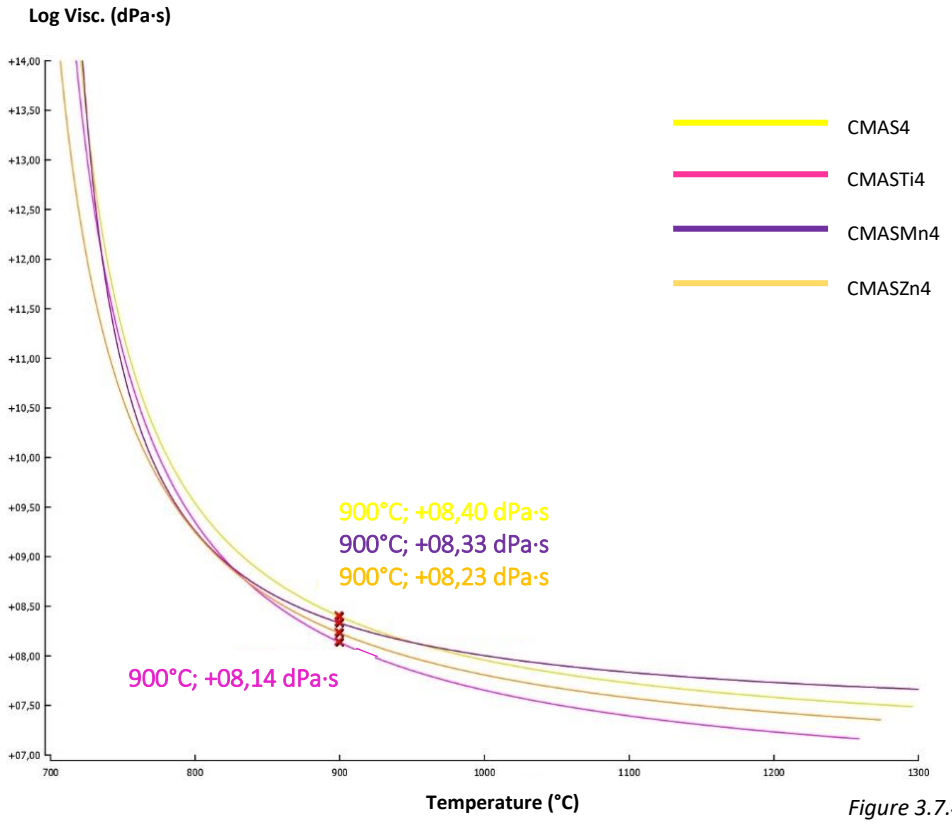

Figure 3.7.4 Viscosity of glasses belonging to CMAS4 series.

Calculated temperatures for dilatometric softening point T_D, softening point T_s and half ball T_{HB} for all series of glasses are summarized in table 3.7.1. together with the viscosity expressed as η (η is given in dPa s) for the glasses at T_s, T_{HB} and 900°C.

GLASS SAMPLE ID	T_D (°C)	T_S (°C)	T_{HB}(°C)	T_F (°C)	η (dPa s) T_S	η (dPa s) T_{HB}	η (dPa s) 900°C
CMAS1							
CMAS1 basic system	777	860	1257	1262	8.58	7.69	8.31
CMASTi1	786	843	1239	1248	8.80	6.65	8.27
CMASMn1	769	859	1456	1460	8.64	7.34	8.32
CMASZn1	768	839	1252	1266	8.69	7.42	8.19
CMAS2							
CMAS2 basic system	777	854	1243	1252	8.68	7.98	8.40
CMASTi2	779	854	1280	1313	8.91	6.62	8.39
CMASMn2	771	859	1409	1420	8.71	7.17	8.36
CMASZn2	781	839	1221	1231	8.79	7.23	8.25
CMASSn2	798	882	1228	1245	8.56	7.07	8.36
CMAS3							
CMAS3 basic system	772	858	1254	1263	8.59	7.39	8.28
CMASTi3	797	831	1233	1241	9.20	6.52	8.05
CMASMn3	763	855	1244	1253	8.71	7.17	8.36
CMASZn3	770	855	1259	1283	8.79	7.23	8.25
CMASSn3	800	865	1221	1236	8.76	6.60	8.28
CMAS4							
CMAS4 basic system	773	852	1271	1285	8.78	7.39	8.28
CMASTi4	769	857	1235	1249	8.62	7.52	8.40
CMASMn4	763	861	1421	1428	8.56	7.19	8.33
CMASZn4	759	834	1257	1263	8.77	7.37	8.23

Table 3.7.1 Characteristic temperature and viscosity values at T_S, T_{HB}, and 900°C calculated for all glasses.

The results obtained for all glasses are in good agreement. The calculated reduced viscosity of glasses at 900°C from VTF equation is close to ~8.0 dPa s, suitable for sealing applications.[193]

The results demonstrate that all glasses are no totally viscous at high temperatures. A smooth variation of the viscosity with temperature, i.e. low fragility, is one of the most important conditions for obtaining a good seal. The figures 3.7.1. - 3.7.4 show that viscosity varies between 6.0 and 9.0 dPa s, in the sealing range (700-900°C). Thus, all the glasses accomplish the η requirements for sealing.

All types of glasses underwent a more orderly structure or pass to a viscous liquid state depending on heating rate. As the firing temperature reaches above T_S, a further decrease is observed and the flow behavior of the glasses is similar to dense liquid.

A linear plot of $log\,\eta$ versus $\frac{1}{(T-T_0)}$ provides the calculation of A and B. T_0 is an empirical constant which used to linearize the viscosity curve. These parameters define the degree of association of molecules and depends on the type of glass and viscosity range. Moreover, the model parameter, A, is related to theoretical viscosity of completely free particles. It means the activation energy is required for mobility of particle into viscous flow and it is possible to obtain at an infinitely high temperature. Parameter T_0 is related to changes that occur in matrix of glass. In order to calculate the three unknown constants A, B, and T_0, it is necessary to input the three reference temperatures into the VFT equation.

In our case, a reference value of viscosity a T_g for all types of glasses is considered, together with the value of viscosity at half sphere has been selected. As mentioned, T_{HB} is the temperature in which a sample forms a half sphere shape during HSM analysis.

The temperature is obtained when the height of the sample is half of width corresponding to the contact angle 90°. The measured viscosity at T_{HB} temperature provides some important information and it is easily distinguishable during HSM measurement. The last standard temperature is the viscosity at T_S of multi oxides silicate derived from sintering curve.

Table 3.7.2. shows the VFT constants for each glasses belonging the different series.

GLASS SAMPLE ID	A (kPa·s)	B (kPa·s·°C)	T_0(°C)
CMAS1 basic system	9,7	0,14	709,1
CMAS2 basic system	8,4	0,44	629,6
CMAS3 basic system	8,9	0,22	667,9
CMAS4 basic system	9,5	0,15	689,1
CMASTi1	10,0	0,08	772,2
CMASTi2	7,0	0,86	562,9
CMASTi3	8,4	0,32	649,8
CMASTi4	9,1	0,23	678,8
CMASMn1	8,0	0,35	681,5
CMASMn2	8,5	0,22	687,4
CMASMn3	12,5	0,06	676,7
CMASMn4	7,7	0,29	663,2
CMASZn1	7,4	0,43	639,0
CMASZn2	8,5	0,45	647,8
CMASZn3	7,9	0,30	660,8
CMASZn4	7,8	0,34	660,8
CMASSn2	9,0	0,15	690,7
CMASSn3	8,5	0,26	658,7

Table 3.7.2 Constants of VFT equation for all types of glasses.

Generally, at temperatures below the dilatometric softening point, T_D (obtained from dilatometry experiments on bulk glasses), the pressed powders do not undergo viscous sintering.

All the modified glasses samples studied in this work, except CMASZn4, reach a maximum density at temperature close to the onset of crystallization and show evidence of viscous sintering. Beyond the first exothermal peak, no significant change of density occurs, whereas a drop of density is observed at the first endothermal peak, which correspond to melting point of the sample. The decrease might be related to the tendency of the glasses to crystallize, and to the volume change due to the crystallization or phase transitions.

3.8 Characterization of glass ceramic properties

After studying the properties of glasses, in the second step of our work we turned to examine the corresponding glass ceramics. To doing this, the glasses were subjected to a heat treatment in such a way to induce devitrification. Glass ceramic samples were prepared by re-firing the glass powders at different temperatures in the 850°C – 1100°C temperature range of for 1 hour to induce the crystallization process of the glass. A slow heating rate of 5°C/min is maintained in order to prevent the deformation of the samples. Glass powders pressed into a pellet and fired at various temperatures were then analyzed to investigate properties of the glass ceramic such as the crystallization kinetics, thermal expansion coefficient, formed phases and the microstructure of the different kinds of crystals.

Controlled crystallization of glass, starting from a heterogeneous or homogeneous nucleation process, can occur in two different ways depending on the nature of the nucleation mechanism. If nucleation occurs at a phase boundary between the vessel surface or air and the glass, the crystallization proceeds from the glass surface into the bulk material (surface crystallization). The other type of nucleation is the so-called internal crystallization and can be achieved with a simple two-step heat-treatment. The first one is an isotherm step at a temperature at which the mobility of atoms in the glass is sufficient for embryo formation and subsequent nucleus growth. The second step is necessary to enhance crystal growth up to the desired size homogeneously dispersed in the volume. Surface crystallization is usually favored compared to internal crystal nucleation, which generally requires the addition of nucleating agents. In fact, unless the first step of internal nucleation is induced, only the surface and impurities inside the glass act as nuclei and the crystalline phase starts to grow on them. Regardless the nucleation mechanism, during the crystal growth all mobile ions can move into the crystals leaving the glassy phase more and more viscous. This is indeed the case for many glass-ceramic systems where the materials are partially devitrified in some preferential areas, leading to a dangerous anisotropy in chemical and physical properties.

In this section, we investigate the natural trend of the MgO-CaO-Al_20_3-SiO_2 system towards nucleation in the absence and presence of nucleating agents, with the aim of identifying the nucleation mechanism and evaluating the crystallization activation energy. The emergence of great difference between the physico-chemical properties of the newly formed crystals and the remaining vitreous phase is a very common phenomenon. It seems thus very important, especially in view of possible industrial applications, to plan the devitrification of particular types of crystals which will have physical and chemical characteristics similar to those of the starting glassy phase.

3.8.1 Crystallization kinetics

Although numerous sealants have been proposed for SOFCs [194], very few studies dealing with crystallization kinetics of glass ceramic sealants have been reported in literature [195-196-197-198]. Crystallization process plays an important role in determining the properties and applications of glass ceramic sealants. For example, a recent installation process for the Siemens-SOFC required that the sealing glass should be partially viscous at 950°C for 2-3 hours to allow small displacement of the single stack elements after joining at 1000°C. This can be achieved by using a slow crystallization glass [199]. Also, the viscosity of glass ceramic sealants is affected by the parent glasses. Sakaki et al. [200] observed an increase in seal viscosity at about 950°C because of bulk crystallization of Wollastonite ($CaSiO_3$) in CaO-Al_2O_3-SiO_2 glass system. Moreover, as discussed in the previous section, sintering should precede crystallization to obtain a dense material suitable for a SOFC seal. Uncontrolled crystallization during the initial sintering process can adversely affect the SOFC operation. In the present investigation, crystallization kinetics of various glass ceramic sealants have been studied using different theoretical models.

Differential thermal analysis (DTA) has been extensively used as a rapid and convenient means for detecting a reaction process. The rate of a chemical reaction may be quantitatively analyzed by DTA and the activation energies evaluated. This method can be also used to obtain the activation energy for the crystallization of glasses, assuming that the process of crystallization is a first order reaction. In particular, DTA measurements are useful to obtain kinetic parameters related to the glass crystallization process in the non-isothermal mode, thanks to the rapidity of this method.

In crystallization kinetic studies, as cast (non-nucleated) and pre-nucleated samples can be used to recognize the effect of increasing and constant number of nuclei on the crystallization mechanism, respectively. For as-cast samples, when the nucleation takes place during the thermal analysis experiment, the number of nuclei is proportional to the heating rate. For the pre-nucleated samples, the number of nuclei does not depend on the heating rate. In our work, the amorphous samples are the starting materials, where no evidence of crystallization is detected by XRD analysis using a conventional Bragg-Brentano diffractometer with Ni-filtered Cu-K radiations.

Crystallization mechanisms of amorphous materials can be investigated based on various theoretical approaches discussed previously (see Section 2.3.1). In this work, the non-isothermal method was used. As mentioned, such measurements offer some advantages in comparison with isothermal studies. The measurements are performed using a constant heating rate until the devitrification of glasses is complete. Crystallization peak temperatures, T_C, and crystallized volume fractions, x, are determined from the thermal analysis curves. The volume fraction crystallized, x, at any temperature T is given by $x = \frac{S_T}{S}$, where S is the total area of the exothermic peak between the temperature, T_o, at which the crystallization begins and the temperature, T_f, at which the crystallization is complete and S_T is the partial area of the exothermic peak up to

the temperature T. Some authors have applied the Johnson-Mehl-Avrami equation (see Section 2.3.1) to the non-isothermal crystallization process, although this procedure is not strictly appropriate because the Johnson-Mehl-Avrami equation was derived for isothermal crystallization. The Kissinger equation is basically developed for studying the variation of the peak crystallization temperature with heating rate. According to Kissinger's method, the transformation under non-isothermal condition is represented by a first-order reaction. Moreover, the concept of nucleation and growth has not been included in Kissinger equation. Matusita et al. have developed a method based on the assumption that crystallization does not advance by an n^{th}-order reaction but by a nucleation and growth process. They emphasized that crystallization mechanisms such as bulk crystallization or surface crystallization should be taken into account for obtaining activation energies. In addition, the Matusita's method provides information about the Avrami exponent and dimensionality of growth. Augis and Bennett method is helpful in obtaining kinetic parameters such as frequency factor (k_o), rate constant (β) along with activation energy of crystallization and therefore is sometimes preferred over other models. Ozawa and Kissinger plots are the most commonly used methods to derive non-isothermal kinetic data, such as Avrami constant, *n* and crystallization activation energy, E_a, respectively. In the non-isothermal method, the values of the Avrami parameter, *n*, are determined from the Ozawa equation:

$$ln[-ln(1-x)] = -nln\beta + const \tag{3.19}$$

where *x* is the crystallized volume fraction at T for the heating rate β. From the slopes of the linear fits of the experimental data of a plot of $ln[-ln(1-x)]$ versus $ln\beta$, *n* values are calculated.

Crystallization mechanisms, i.e. *m* values, of the glass samples can be derived from Matusita et al.'s approach. The activation energy can be evaluated by the Kissinger equation as modified by Matusita et al.:

$$ln\left(\frac{T_C^2}{\beta^n}\right) = \frac{mE_a}{RT_c} + const \tag{3.20}$$

where T_c is the crystallization peak temperature for a given heating rate β, E_a is the activation energy, R is the gas constant, *n* is the Avrami parameter and *m* is the numerical factor of crystallization mechanism. The activation energy is calculated from the slopes of the linear fits to the experimental data from a plot of $ln\left(\frac{T_C^2}{\beta^n}\right)$ versus $\frac{1}{T_C}$. There exist also different approaches for the interpretation of the activation energy in the literature, such as the Ozawa equation modified by Matusita et al.:

$$ln\beta = -10.52\left(\frac{mE_a}{nRT_c}\right) - \left\{\frac{ln[-ln(1-x)]}{n}\right\} + const \tag{3.21}$$

where *m* is the parameter related to the crystallization mechanism. This equation is not widely used for activation energy determination, and it has not been considered in the present study.

The activation energy of crystallization can also be determined by an approximation proposed by Augis and Bennett. The pertinent relation is of the form:

$$ln\left(\frac{\beta}{T_C}\right) = -\frac{E_a}{RT_c} + lnk_0 \tag{3.22}$$

where, k_0 is the frequency factor and *R* the gas constant.

The plot of $ln\left(\frac{\beta}{T_C}\right)$ vs. + $\frac{1}{T_C}$ gives the activation energy of crystallization (E_a). This method has an extra advantage over the modifed Ozawa method, i.e. the intercept of the plot gives the value of the pre-exponential factor k_0 in thr Arrhenius equation, which can be viewed as the number of attempts per second made by the nuclei to overcome the energy barrier. This also provides information on the number of nucleation sites present in the material. The value of the activation energy can also be calculated also by using the variation of T_C with the heating rate β for both crystallization phases. By using relations similar to the Kissinger equation, the relations can be written in the form:

$$ln\left(\frac{\beta}{{T_C}^2}\right) = -\left(\frac{m}{n}\right)\frac{E_a}{RT_c} + const \quad (3.23)$$

$$ln(\beta) == -\left(\frac{m}{n}\right)\frac{E_a}{RT_c} + const \quad (3.24)$$

Table 3.8.1.1 shows a summary of the different approaches for the interpretation of the kinetic data obtained from thermal analysis measurements (see Section .2.3.1 for more details).

METHOD	APPROACH
Ozawa	$ln[-ln(1-x)] = -nln\beta + const$
Kissinger Modified By Matusita Et al.	$ln\left(\frac{T_C^2}{\beta^n}\right) = \frac{mE_a}{RT_c} + const$
Ozawa Modified By Matusita Et al.	$ln\beta = -1.052\left(\frac{mE_a}{nRT_c}\right) - \left\{\frac{ln[-ln(1-x)]}{n}\right\} + const$
Augis And Bennet	$ln\left(\frac{\beta}{T_C}\right) = -\frac{E_a}{RT_c} + lnk_0$
Afify	$ln\left(\frac{\beta}{{T_C}^2}\right) = -\left(\frac{m}{n}\right)\frac{E_a}{RT_c} + const$ $ln(\beta) == -\left(\frac{m}{n}\right)\frac{E_a}{RT_c} + const$

Table 3.8.1.1 Different methods for the interpretation of non-isothermal kinetic data.

Some approximations were assumed in considering these approaches:

1. primary nucleation occurs randomly and homogeneously over the whole portion of the material that has not yet transformed
2. the growth rate of a center does not depend on that of the other centers
3. the growth occurs at the same speed in all directions

The crystallization mechanisms in amorphous materials can be distinguished on the basis of the numerical parameters defined in the above discussed approaches. When the nucleation rate is zero, $n = m$, when nucleation takes place during thermal analysis, $n = m + 1$ and when surface crystallization is the predominant mechanism, $n = m = 1$, where the parameters of n and m represent the values of the growth morphology depending on the crystallization mechanism.

As seen in Table 3.8.1.2., different crystallization mechanisms appear for different numerical factors, such as rod-like for one dimensional growth or surface crystallization $(m = 1)$, disk-like for two-dimensional growth $(m = 2)$ and spherical for three-dimensional growth $(m = 3)$.

CRYSTALLIZATION MECHANISM	*n*	*m*
Bulk crystallization with a constant number of nuclei		
Three-dimensional growth of crystal	3	3
Two-dimensional growth of crystal	2	2
One-dimensional growth of crystal	1	1
Bulk crystallization with an increasing number of nuclei		
Three-dimensional growth of crystal	4	3
Two-dimensional growth of crystal	3	2
One-dimensional growth of crystal	2	1
Surface crystallization	1	1

Table 3.8.1.2 Value of n and m for different crystallization mechanism.

From microscopic analysis we found that the number of nuclei tends to increase during the crystallization process for all glasses examined. Considering these different approaches, the crystallization kinetics for all glasses were investigated by DTA analysis performed with different heating rates. The goal of this analysis is to study the crystallization mechanisms and their dependence on the chemical composition of the parent glasses. As a first step, XRD analysis is carried out on the as-cast sample glasses to confirm that no crystalline phases are present. An example of typical XRD spectra is reported in Figure 3.8.1.1.

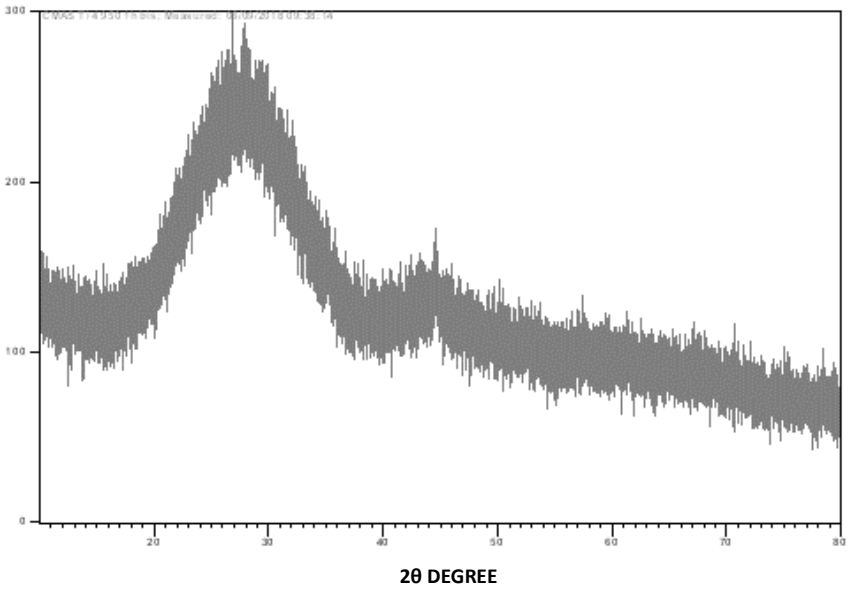

Figure 3.8.1.1 XRD patterns of the parent glasses.

As seen in Figure 3.8.1.1, samples are almost completely amorphous and no presence of crystallization is apparent. As already made for CTE measurements, the influence of different nucleating agents will be compared considering the series of glasses starting from the correspondent CMAS basic system. DTA analysis has been performed at different heating rate of 5, 10, 15, 20, 30 and 50°C/min. For all glasses at low heating

rates, the DTA thermogram is more defined and more exothermic peaks are recorded during the heat treatment.

Figures 3.8.1.2 - 3.8.1.5 show the DTA results obtained from the parent glasses in the series CMAS1 with the various additives.

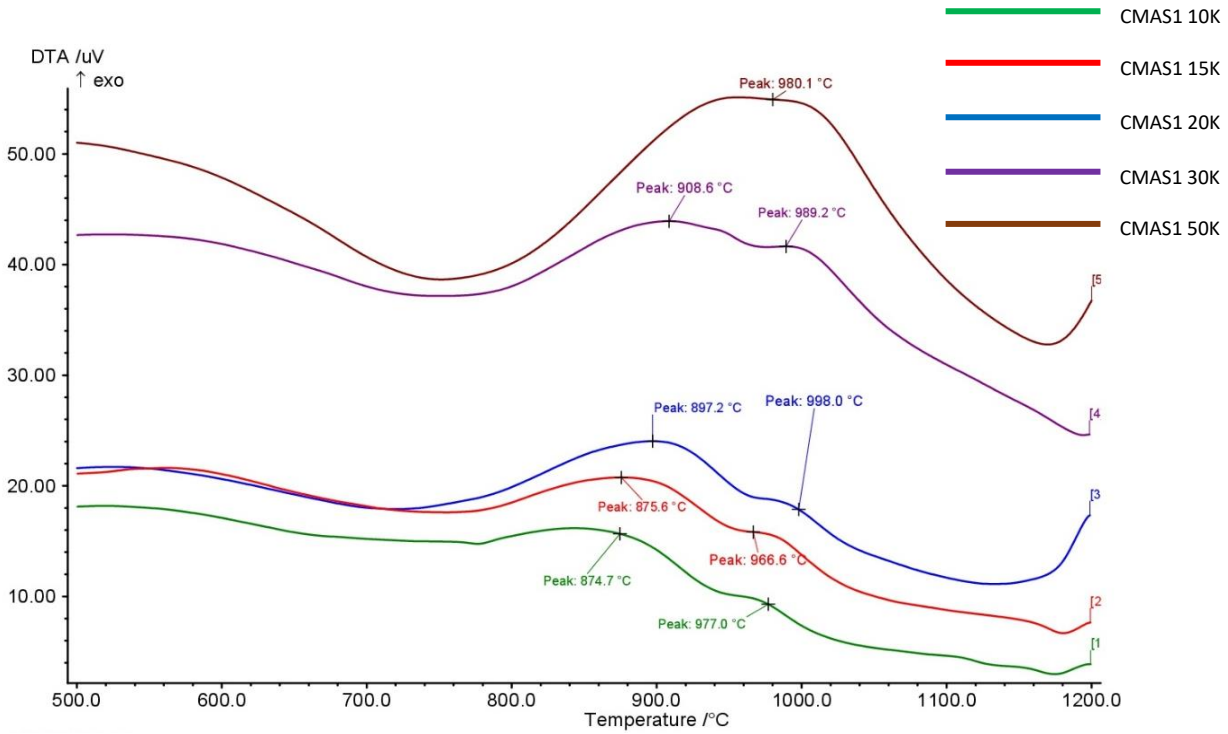

Figure 3.8.1.2 DTA curves of CMAS1 basic glass at different heating rates.

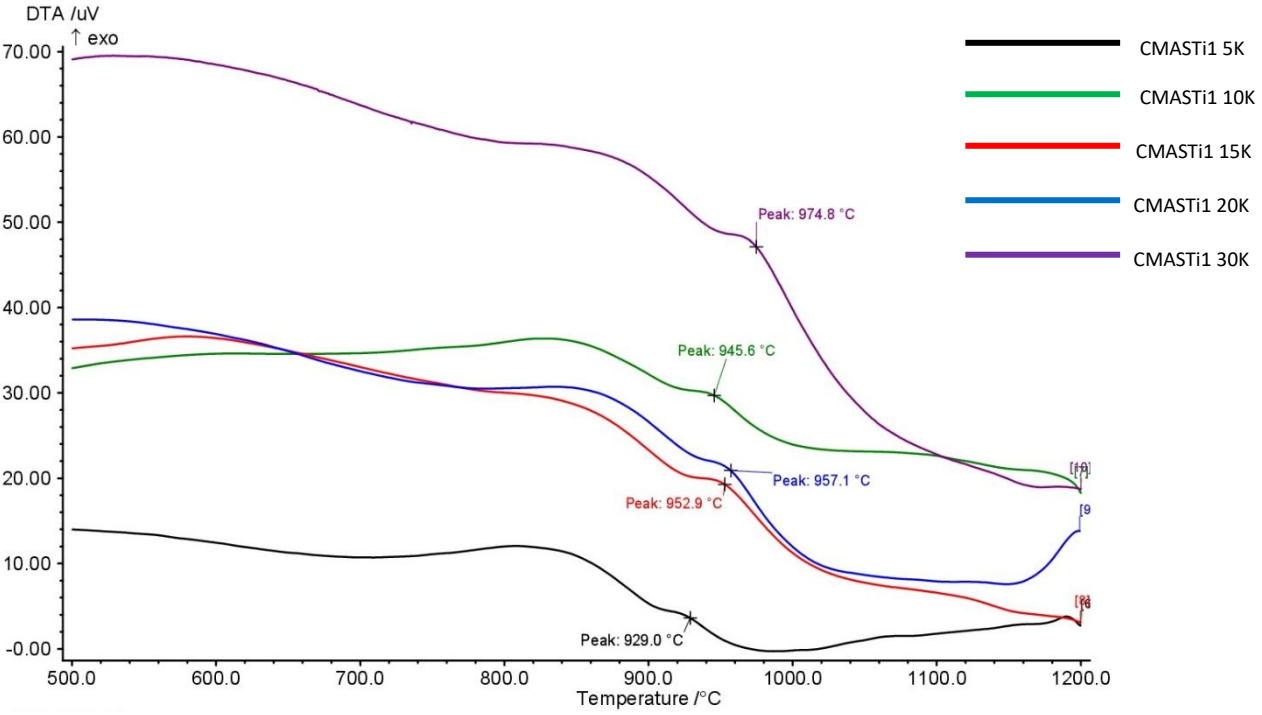

Figure 3.8.1.3 DTA curves of CMASTi1 glass at different heating rates.

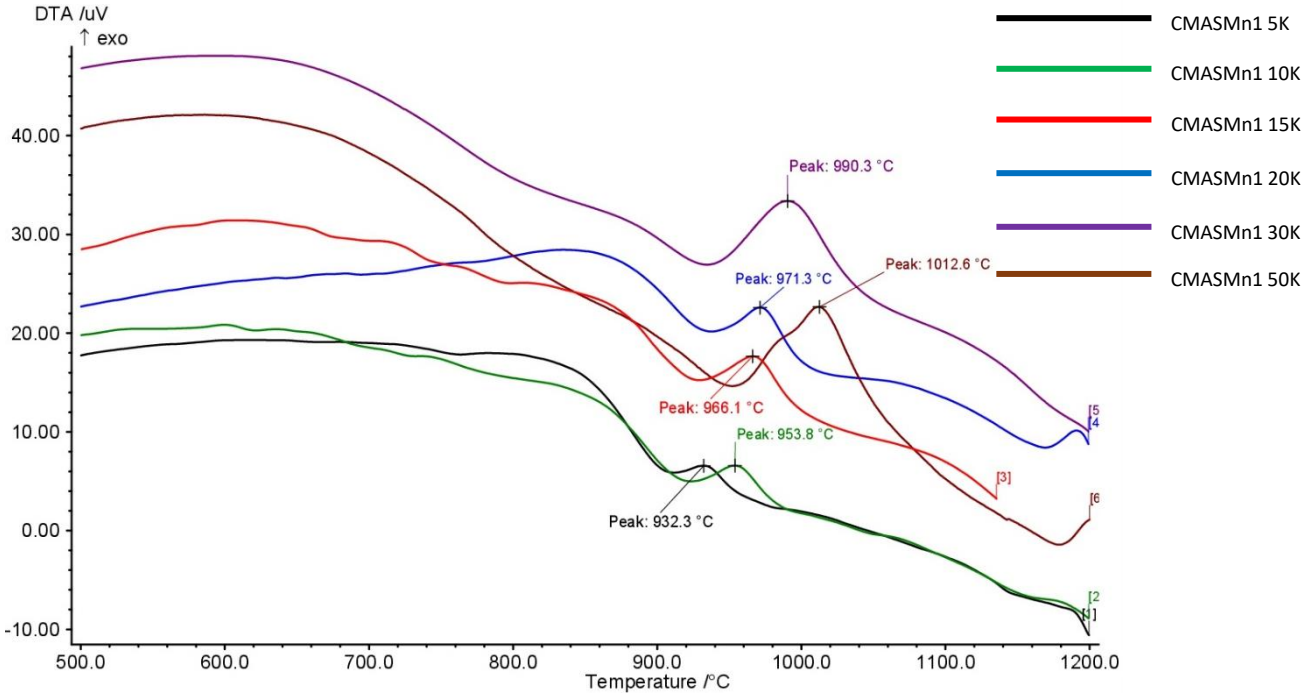

Figure 3.8.1.4 DTA curves of CMASMn1 glass at different heating rates.

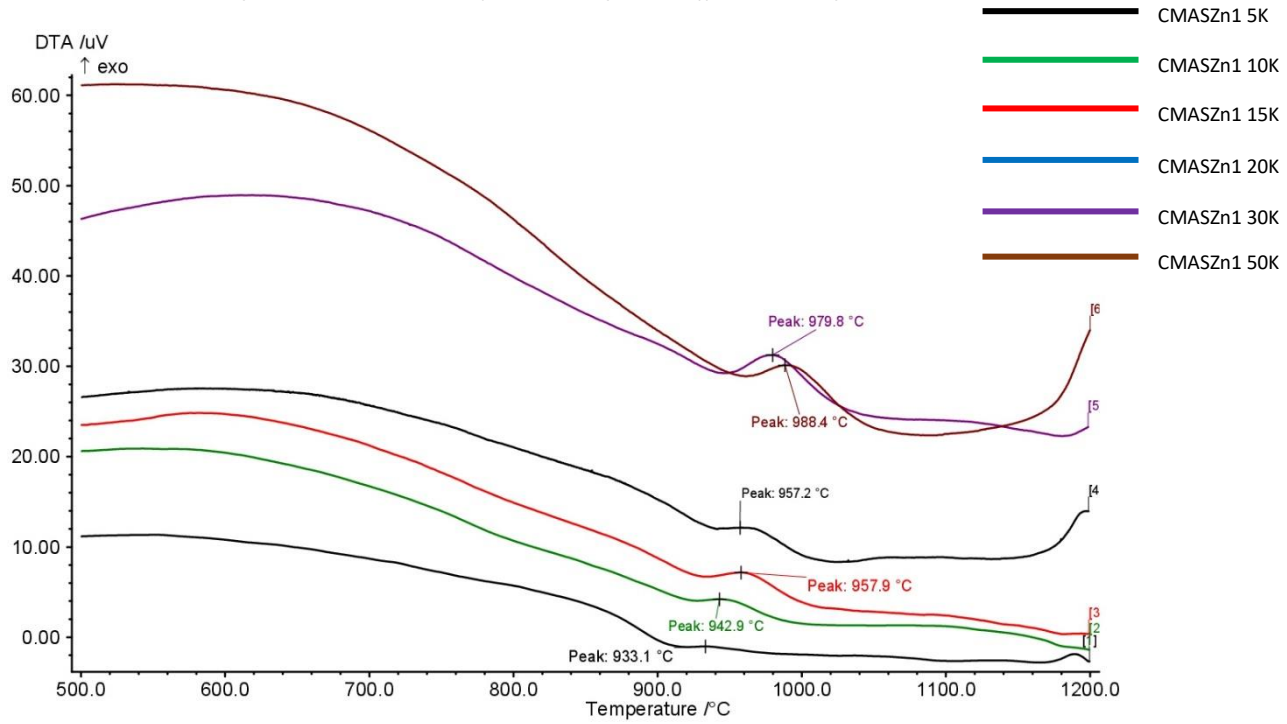

Figure 3.8.1.5 DTA curves of CMASZn1 glass at different heating rates.

From the above reported DTA thermograms emerge that with decreasing the heating rate, the maximum temperature of the exothermic peak is moved towards low temperatures. Furthermore, the area of the exothermic peak is larger when the heating rate is higher. For all glasses containing nucleating agents, there is just one exothermic peak located in the DTA curves, which may be associated with the formation of the main crystallization phases. To study the kinetics of crystallization the main exothermic peak has been considered

for all the investigated glasses. DTA data were analyzed to determine the crystallization parameters, i.e. the reaction order (*n*) and the activation energy (E_a) from the change in the crystallization peak temperature with the heating rate, using the equations illustrated above. Under the assumptions that 1) the crystallization mechanism do not change with temperature and heating rate, and 2) the deviation of the signal from the baseline in the initial stage of the reaction is proportional to the reaction rate (i.e. the maximum rate of a reaction is supposed to occur at the peak temperature), the modified Kissinger equation, Augis and Bennet equation and Afify equations (see Table 3.8.1.1) were applied. In Figure 3.8.1.6 the plot of $ln[-ln(1-x)]$ vs $ln\beta$ for the CMAS1 glass is shown. Based on the Ozawa equation, the Avrami exponents can be derived by a linear fit of the experimental data, as shown by Equation 3.19.

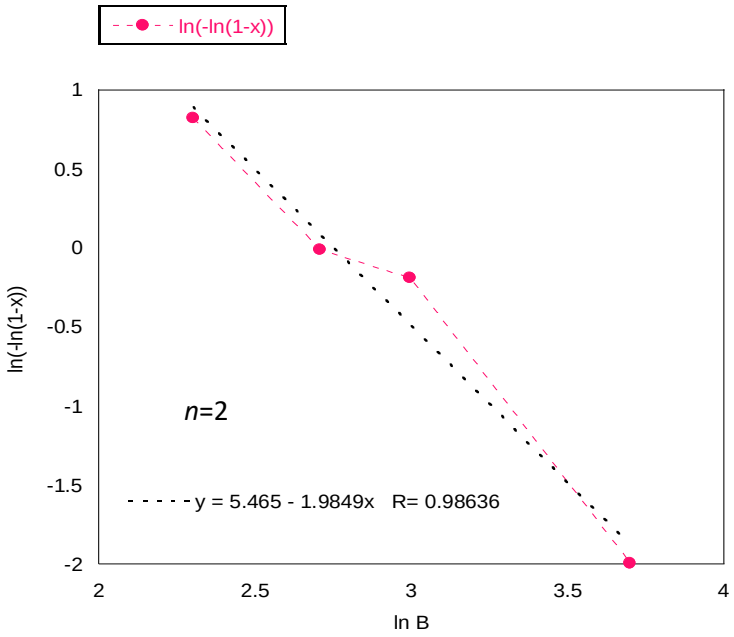

Figure 3.8.1.6 Plot ln(-ln(1-x)) vs ln β for CMAS1 basic glass.

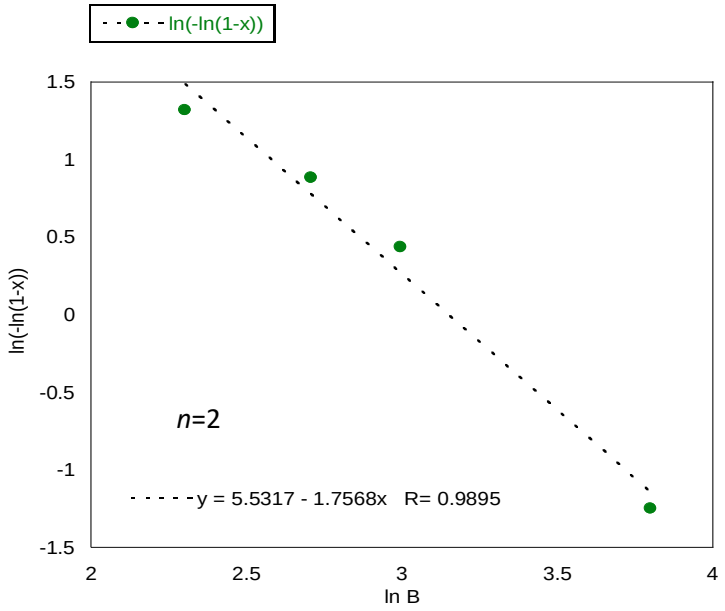

Figure 3.8.1.7 Plot ln(-ln(1-x)) vs ln β for CMASTi1 glass.

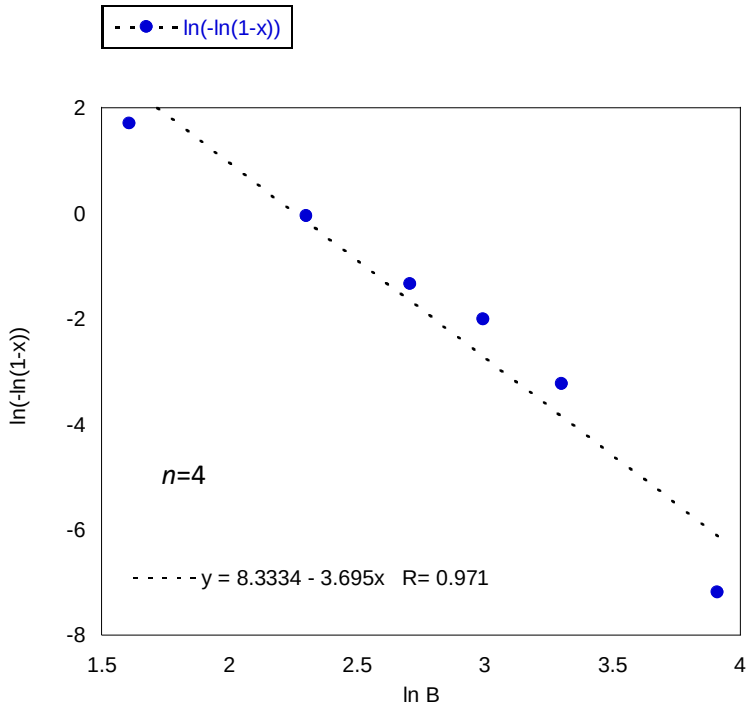

Figure 3.8.1.8 Plot ln(-ln(1-x)) vs ln β for CMASMn1 glass.

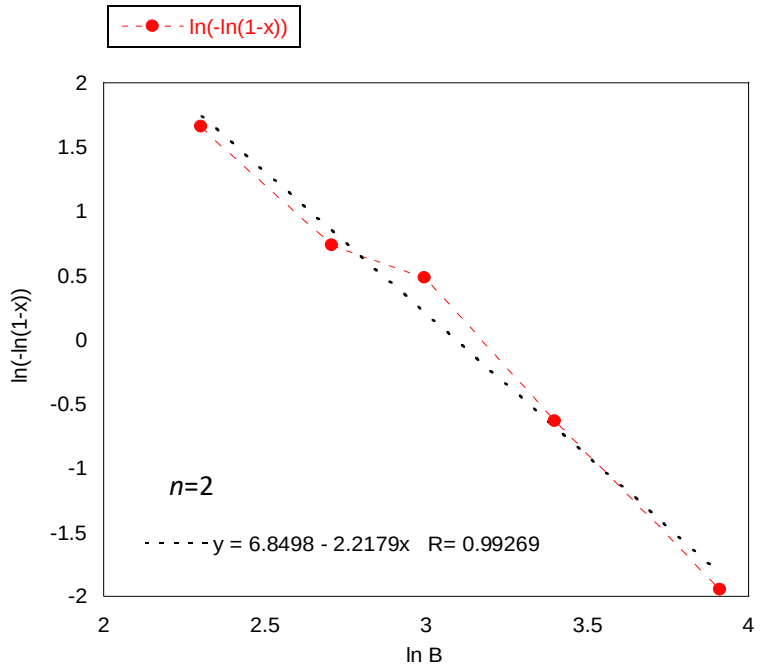

Figure 3.8.1.9 Plot ln(-ln(1-x)) vs ln β for CMASZn1 glass.

Once the Avrami exponents (*n* and *m*) were calculated, the activation energy is extracted from the slopes of the plots of the type reported in Figs. 3.8.1.10 - 3.8.1.13 (the CMASMn1 sample glass is chosen as an example), according to the different theoretical approaches previously discussed. This procedure has been carried out for all the examined glasses. According to *n* values, two types of glass devitrification are generally observed:

surface devitrification and bulk devitrification. The origins of surface devitrification are flaws, microheterogeneities, dust particles, and stress on the surface [201-202]. Surface devitrification is difficult to control since the origins of nucleation are very subtle. The origins of bulk devitrification are the very small nuclei formed during glass making and the microheterogeneities inside the glass. Bulk devitrification can be controlled to a certain extent and occurs preferentially in the phase-separated regions [203].

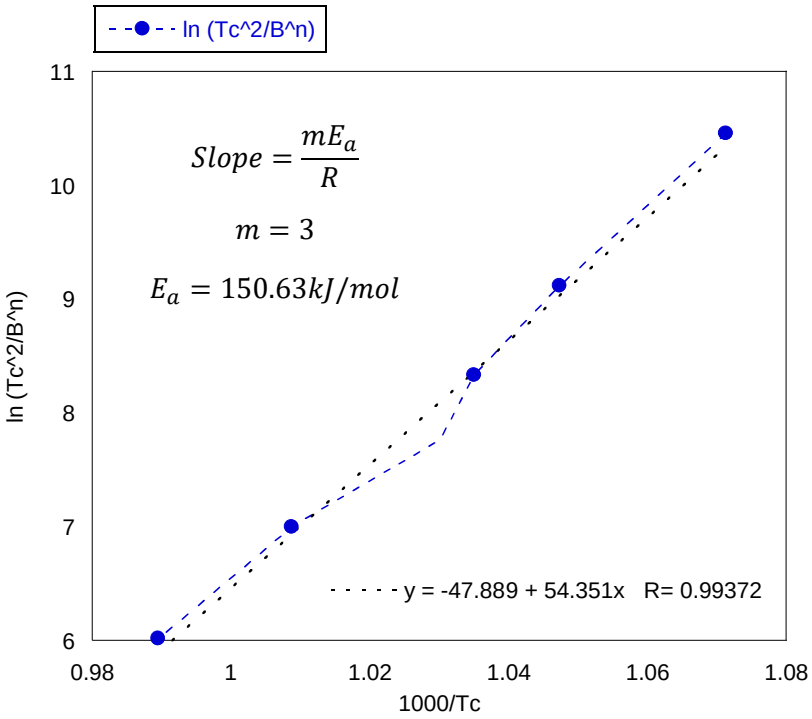

Figure 3.8.1.11 Determination of the activation energy according to Kissinger equation modified by Matusita (CMASMn1 sample).

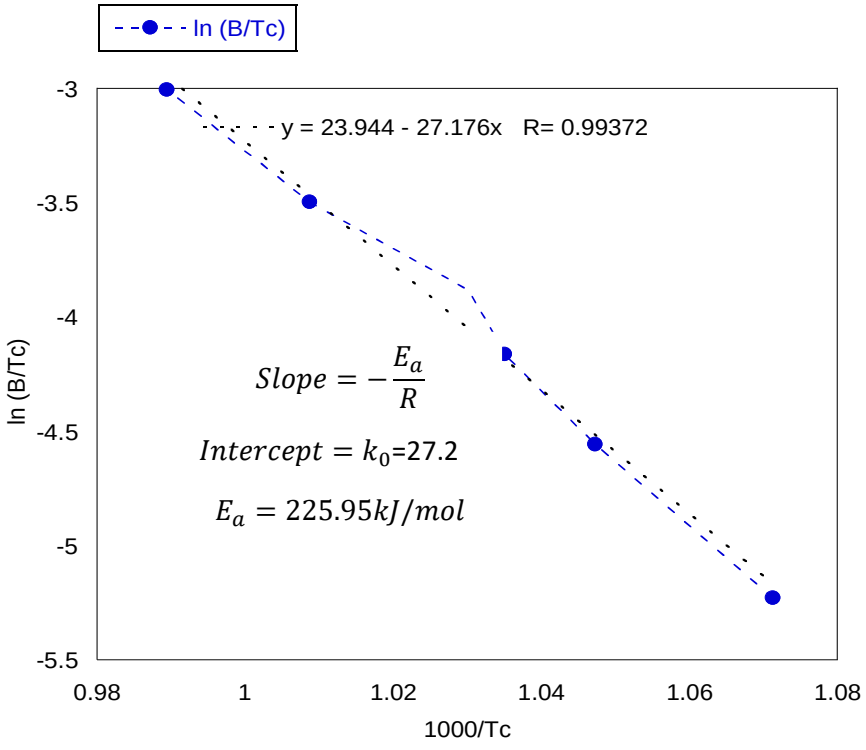

Figure 3.8.1.11 Determination of the activation energy according to the Augis and Benett equation (CMASMn1 sample).

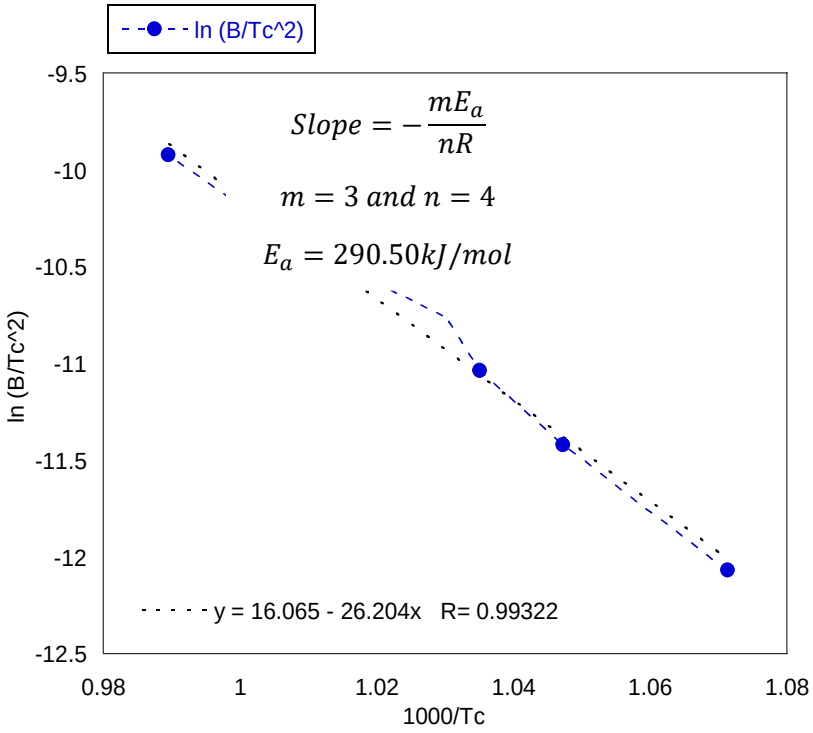

Figure 3.8.1.12 Determination of the activation energy according to the Afify I equation (CMASMn1 sample).

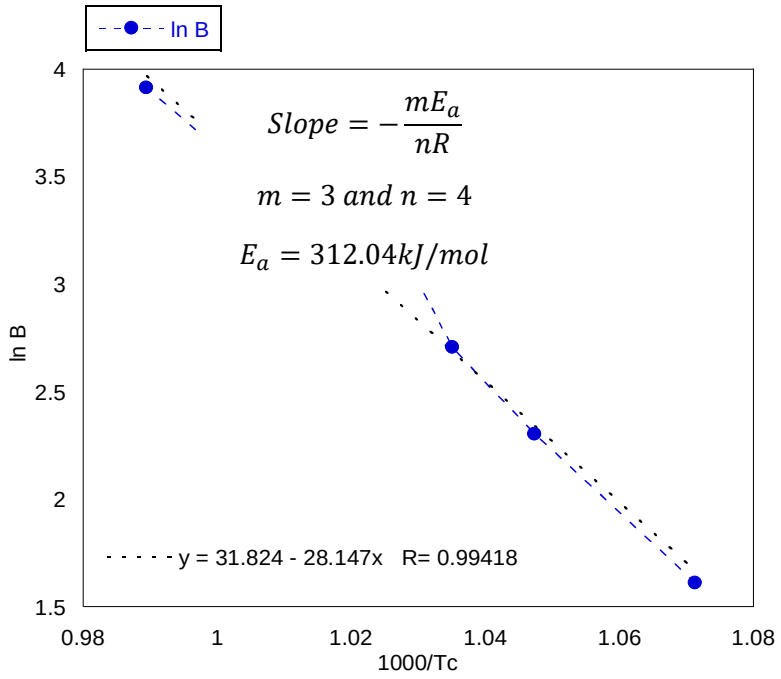

Figure 3.8.1.13 Determination of the activation energy according to the Afify II equation (CMASMn1 sample).

In table 3.8.1.3 the Avrami exponents and the activation energies (E_a) for all CMAS1 glasses are summarized.

GLASS SAMPLE ID	AVRAMI INDEX, *n*	m	E_a (kJ/mol) Kissinger and Matusita	E_a (kJ/mol) Augis and Bennett	E_a (kJ/mol) Afify I	E_a (kJ/mol) Afify II	K_0
CMAS1	2	1	763.5±1.2	381.7±0.8	747.2±0.7	779.8±1.2	42.5
CMASTi1	2	1	729.4±0.3	364.7±1.1	713.5±1.5	745.2±1.4	42.8
CMASMn1	4	4	150.6±0.7	225.9±0.9	290.5±1.3	312.0±2.1	27.2
CMASZn1	2	2	577.8±1.8	288.9±1.3	561.8±0.9	526.7±2.0	32.12

Table 3.8.1.3 Avrami exponents (n,m), crystallization activation energy (Ea) and k_0 of the glasses belonging to the CMAS1 series.

It can be noted that the energy values derived using the Augis and Bennet equation are heavily underestimated, most probably due to the fact that this method does not take into account in any manner the nucleation and crystal growth steps during the heat treatment.

Depending on the values found for *n*, hypotheses can be made on the dominant nucleation/crystal growth mechanism for the corresponding phase formation in the glass. If several phases grow in the same glass composition at different temperatures, the mechanisms are not necessarily the same for all phases. Similarly, the same phase appearing in different glasses can form under different mechanisms.

For the CMAS1 sample, the second exothermic peak was analyzed for determining the activation energy. The n value for CMAS1 is determined to be 2, indicating the one-dimensional growth of crystals. Data obtained for this sample show that the activation energy for the crystallization process is too high, hence the presence of Al^{3+}ions as network formers hinders the devitrification in the range of 970°-990°C. High contents of Al_2O_3, improve the thermal stability of the seal glass by hindering phase separation and devitrification [204-205]. When a suitable amount of Al_2O_3 is present, Al^{3+} ions are 4-coordinates, participate in network formation and homogenizes the glass structure. The TiO_2 nucleation agent, though slightly lowering the activation energy doesn't control totally the induction of crystallization, but at the same time CMASTi1 sample exhibits one-dimensional growth of crystals. This effect can be due to the dual role of TiO_2 as a glass former and a modifier. When TiO_2 exists as a network modifier, it has a lower field strength (1.25). When TiO_2 exists as a glass former, it has higher field strength (2.75). T_c and the activation energy for devitrification increase if TiO_2 participates in the glass network but decrease if it does not.

A similar growth behavior was recorder for the CMASZn1 glass, with ZnO promoting the crystallization process as shown by the lower activation energy compared to CMAS1, but the influence is more effective on the crystallization step if compared with CMASTi1. In both CMASTi1 and CMASZn1 the area of the exothermic peak observed in DTA thermograms is less than that recorded in the CMASMn1 glass. In the latter, the effect of MnO_2 nucleating oxide on the crystallization is dominant, and it tends to homogenize the devitrification toward an interface-controlled three-dimensional growth of crystals, as evident in Figure 3.8.1.4.

The values of k_0 demonstrate that the number of attempts per second made by nuclei to overcome the energy barrier is lower for low activation energy, because the nucleating agent actives the crystal growth.

The same considerations have been carried out for the other series of glasses. All the DTA thermograms obtained for glasses are reported in Appendix 1 with the corresponding plots used to derive the kinetic parameters according to the methods listed in Table 3.8.1.4.

In Table 3.8.1.4 are summarized the results obtained for the three different series of glasses. For CMAS2 and CMAS4 glasses, the second DTA peak has been taken into account for the kinetic analysis.

GLASS SAMPLE ID	*n*	*m*	E_a (kJ/mol) KISSINGER AND MATUSITA	E_a (kJ/mol) AUGIS AND BENNETT	E_a (kJ/mol) AFIFY I	E_a (kJ/mol) AFIFY II	k_0
CMAS2							
CMAS2 basic system	2	1	587.5±0.6	597.1±2.3	571.5±2.3	603.5±0.7	33.1
CMASTi2	3	2	196.1±1.0	196.1±1.1	282.1±1.5	305.9±1.5	21.0
CMASMn2	4	3	159.4±1.3	239.1±0.8	308.1±1.1	329.6±1.3	25.9
CMASZn2	3	2	270.4±0.7	270.4±1.4	393.7±0.9	386.5±1.3	26.7
CMASSn2	2	1	497.4±1.5	531.4±0.4	489.5±0.8	505.3±2.0	29.1
CMSA3							
CMAS3 basic system	4	3	339.7±1.3	359.6±1.6	479.5±0.9	490.8±0.9	41.7
CMASTi3	4	3	154.8±1.2	232.2±1.2	298.9±1.6	320.7±1.1	24.5
CMASMn3	4	3	210.3±08	315.5±1.8	410.2±2.0	388.3±1.2	35.8
CMASZn3	3	2	256.4±0.9	256.4±1.1	372.6±1.8	367.4±1.6	27.9
CMASSn3	3	2	262.4±1.1	262.0±0.7	381.0±1.9	385.6±1.5	26.7
CMAS4							
CMAS4 basic system	3	2	284.9±1.1	284.9±1.2	415.8±1.6	439.0±1.6	33.1
CMASTi4	3	2	183.0±0.7	183.0±0.8	262.7±1.3	286.2±1.7	19.5
CMASMn4	3	2	252.4±1.0	253.4±0.9	368.1±1.8	352.4±1.0	27.7
CMASZn4	4	3	169.6±0.8	254.5±1.0	329.2±1.4	349.5±2.0	29.3

Table 3.8.1.4 Avrami exponents (n and m), crystallization activation energy (Ea) and k0 of the glasses belonging to CMAS2, CMAS3 and CMAS4 series.

Considering the parent glasses CMAS2, CMAS3 and CMAS4, in which the composition is rich in alkaline earth oxides, the crystallization ability is better than that recorded in CMAS1.

From the result listed in the Table 3.8.1.4 one can deduce that:

1. For all the glasses belonging to CMAS2, CMAS3 and CMAS4 series, adding an additive in the parent glass composition brings about a high crystallization ability [206]. All types of nucleating agents improve the crystallization ability of CMAS parent glasses.
2. As the amount of Al_2O_3 in the parent glasses lowers, also the activation energy for the devitrification step decreases.
3. When the nucleation occurs as bi-dimensional growth of the crystals, the results of activation energy obtained from the Kissinger modified and Augis and Bennett equations are in good agreement. From this result is clear that the nucleation process during the heating treatment does not influence considerably the frequency with which the nuclei formed across the energy barrier for the crystallization.
4. The activation energy decreases with the alkaline earth oxides contents, what can be related to the "field strength" of cations as defined by Dietzel. The alkaline earth elements, which constitute the network modifier in the glass structure, weaken the glass network and favor the crystal growth. The lower the field strength, the higher is the weakening, and the higher is the tendency to crystallize.

5. In all series of glasses, the activation energy is lower when the nucleating agent participate in the crystallization process inducing a three-dimensional growth of the crystals.
6. In the last series of glasses it can be noted that TiO_2 acts as network modifier and hence it promotes the devitrification.

In CMASZn glasses, the amount of ZnO compared with the amount of alkaline earth oxides (CaO and MgO) in the composition plays an important role to improve the crystallization kinetics. In Figure 3.8.1.14 the activation energies of CMASZn glasses derived from the Kissenger equation are plotted as a function of the $\frac{CaO+MgO}{ZnO}$ ratio. This consideration is true only when Al_2O_3 acts as network modifier.

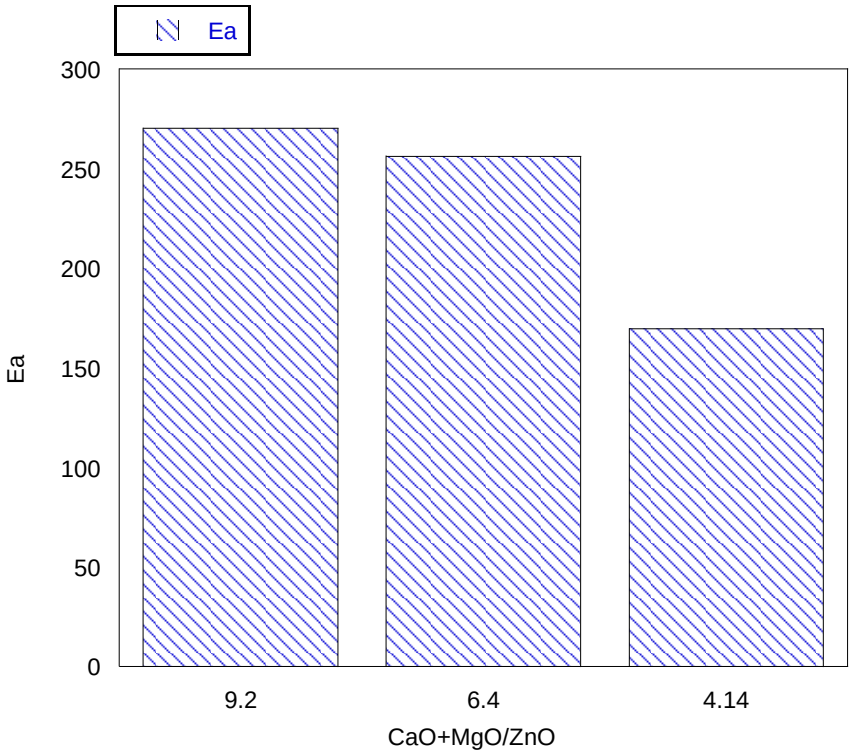

Figure 3.8.1.14 Activation energy derived from Kissenger equation of CMASZn glasses as a function of the (CaO+MgO)/ZnO ratio.

The higher the ratio $\frac{CaO+MgO}{ZnO}$, the lower is the influence of ZnO in promoting the overcoming the energy barrier. This behavior is not shown by the other additives.

In the CMAS2 series, SnO_2 exhibits less influence on crystallization, and the exothermic peak is moved to higher temperatures. Hence, SnO_2 delays the beginning of crystallization. In these modified glasses, the crystallization is improved by introducing into the mass glassy of insoluble crystals which they act as nucleation sites. In this way the heterogeneous nucleation is catalyzed on active substrate consisting of small nucleation agent crystal able to direct the atoms of the glass matrix toward an orderly growth leading to the formation of crystalline phases.

As mentioned in Section 3.6, the analysis of kinetic data is crucial to understand if the examined glasses are suitable candidates for one-step crystallization. Crystallization kinetic information allows to verify if the nucleating agents could act favoring "one step crystallization" as well as glass network modifiers. According to the findings of Yang, only the alkali metal ions could transform the glass network. Generally, alkali metal ions are considered as glass network modifiers and some of them will bond with the TO_4 tetrahedron, if trivalent cations, T, are present, to balance the local charge in the crystal lattice [207]. The remaining alkali-metal ions will escape from the crystal phase moving into the glass layer between the crystal particle and residual glass [208-209]. Then, alkali metal ions help to increase the Si-O-M bond (where M=alkali metal ion) content in the glass layer by transferring the Si-O-Si bonds to Si-O-M bonds. Consequently, the diffusion rate of Ca^{2+} and Mg^{2+} in the glass layer increases, enhancing the crystal growth ability of glass [210]. In other words, alkali metal ions change the Ca^{2+} and Mg^{2+} diffusion barrier layer to a Ca^{2+} and Mg^{2+} fast diffusion layer, as shown in Figure 3.6.6. Further, the Ca^{2+} and Mg^{2+} fast diffusion layer will promote the one step crystallization of glass ceramics. Yang et al. compared the influence of an alkaline oxide like Na_2O with a nucleating agent like CaF_2 on the crystallization kinetics of the system SiO_2-CaO-MgO-Al_2O_3-Fe_2O_3-Cr_2O_3 and from the activation energy data obtained from Kissinger and Augis/Bennet equations, they conclude that only Na_2O tend to decrease E_a in comparison with the alkali oxide free system. The values of activation energy recorded by Yang et al. are summarized in Table 3.8.1.5.

SAMPLE GLASS ID	E_a (kJ/mol)	*n*
GC-1 SiO_2-CaO-MgO-Al_2O_3-Fe_2O_3-Cr_2O_3	301.2	1.2
GC-2 SiO_2-CaO-MgO-Al_2O_3-Fe_2O_3-Cr_2O_3-CaF_2	337.3	3.4
GC-3 SiO_2-CaO-MgO-Al_2O_3-Fe_2O_3-Cr_2O_3-Na_2O	195.4	2.8
GC-4 SiO_2-CaO-MgO-Al_2O_3-Fe_2O_3-Cr_2O_3-Na_2O- CaF_2	216.6	2.9

Table 3.8.1.5. Crystallization activation energy (Ea) and Avrami index of glass samples evaluated from Kissinger and Augis-Bennett equations [210].

From kinetic data and SEM images, Yang concluded that the one step crystallization was successfully achieved by adding Na_2O into the parent glass, whereas CaF_2 did not have the ability to promote this phenomenon and it contributes only to refine the grains and to improve the microstructure of Na_2O-containing glass ceramics. On the contrary, from the results obtained in the present study on modified glasses by addition of nucleating agents, such as TiO_2, MnO_2, and ZnO, the presence of these metal oxides and SnO_2 increases the crystallization ability of the parent glass. Hence, these additives could influence the glass network acting also as network modifiers. As mentioned, the activation energy of the modified glasses is lower than the CMAS basic systems. This can be explained considering that these nucleating agents contribute to promoting phase separation and nucleation [211-212]. Indeed, during the heat treatment the amorphous glass will separate into phase-separated regions and residual glass phase. The phase separated regions are rich in certain elements, bringing the composition closer to that of the resulting crystal nucleus [186-213] and making easier the formation of the crystal

nucleus, because the atomic species required for crystal nucleus growth are sufficient. Besides this, the interface between the two regions can act as heterogeneous nucleation sites, which further reduces the nucleation barrier. As a result, the nucleation activation energy will be decreased. The low E_a values for modified glasses indicated that nucleation and crystallization occur easily. We can deduce that especially when the Avrami exponent *n* is close to 3 there will be enough nuclei grown up during the crystal growth stage [214]. As an example, in Figure 3.8.1.15. the SEM image of the CMASMn4 glass ceramic crystallized at T_C for 1 hour is presented.

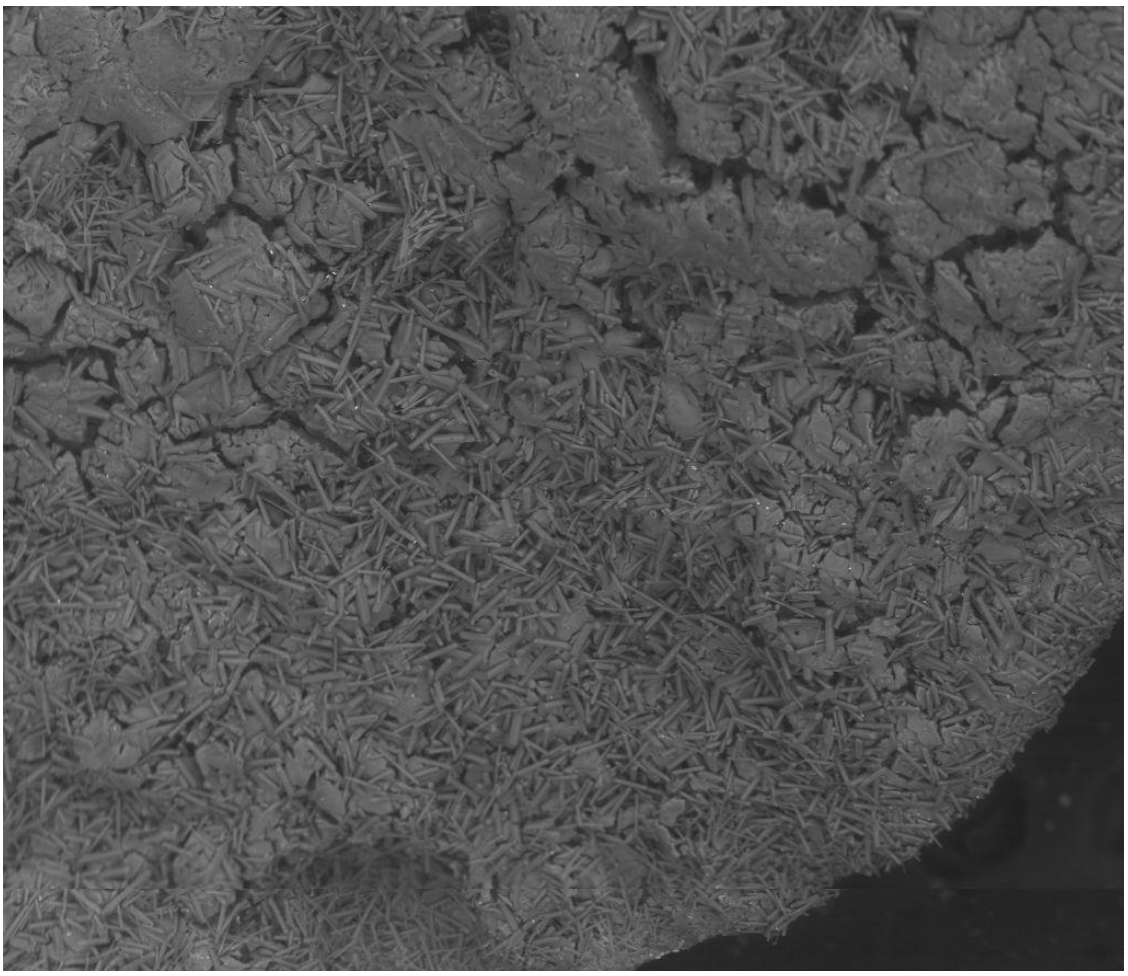

Figure 3.8.1.15 SEM image of CMASMn4 glass sample crystallized at 1100°C for 1 hour.

This image confirms that a large number of granular crystals are uniformly located in the glass-ceramic with Avrami exponent equal to 3, forming a typical three-dimensional crystallization microstructure. This suggests that the majority of crystalline nuclei grew uniformly with the addition of additive. All these results demonstrate a high degree of crystallization together with the formation of uniform crystal particles. These samples could then complete nucleation and crystal growth continuously at T_{CN}. According to the above hypothesis, the one-step crystallization of modified glass samples takes place through the formation of Ca^{2+} and Mg^{2+} fast diffusion layer. Thus, two experimental phenomena should be observed:

1. the ions derived from the nucleation agent, Ti^{4+}, Mn^{4+}, Zn^{2+} and Sn^{4+} will prefer to diffuse into the glass layer around the crystals
2. the residual glass will eventually transform into Ti^{4+}, Mn^{4+}, Zn^{2+} or Sn^{4+}-containing crystal phase in the midst of crystallization, with the existence of Ca^{2+} and Mg^{2+} fast diffusion layer.

From EDX spectra we can deduce that the Ti^{4+}, Mn^{4+}, Zn^{2+} and Sn^{4+}content in the crystal particle is clearly lower than that in the glass layer around the crystal, giving direct evidence of point 1. above. The reason for this phenomenon is most probably that the chemical potential of Ti^{4+}, Mn^{4+}, Zn^{2+} and Sn^{4+} in the glass phase is lower than in the crystal phase. As a result, Ti^{4+}, Mn^{4+}, Zn^{2+} and Sn^{4+}distrupt the Si-O-Si bonds to create new bonds like Si-O-X (where X is the ion derived from nucleating agents) in the glass layer. As a consequence, the silica network of the glass layer will be more "open". Bonds like Si-O-X contribute to Ca^{2+} and Mg^{2+} fast diffusion layer. This layer will help the crystals to grow, which is proven by the low E_a value, especially when the three dimensional crystallization mechanism occurs.

In summary, for all the modified glasses examined, the one-step crystallization could be successfully achieved by adding nucleating agents like TiO_2, MnO_2, ZnO and SnO_2, without the presence of any alkali metal ion. Thus, one-step crystallization of these glass ceramics can be made feasible and practical.

From the results discussed above, it is reasonable to assume that the increase of the specific surface area does not significantly influence the glass transition temperatures, whereas the crystallization peak maxima doesn't shift toward lower temperatures, remaining in the same range of temperature for all glasses. This observation and the absence of the splitting of the exothermic peak strongly suggest that the mechanism of crystal growth is essentially determined by surface nucleation. It is also noted that the transition temperatures of these glasses lie in a very narrow temperature range (700-740°C) which does not change even with changing the heating rate or particle size. This suggests that glasses from these compositions are quite stable up to the glass transformation temperature.

3.9 Phase content and microstructures

In parallel to the analysis of initial crystal growth kinetics, the phase content and microstructure of glass ceramics after mid and long term annealing at high temperatures is investigated.

The phase formation is studied with dependence on the chemical composition in the major oxide system and in particular with various additions of minor nucleating oxides in order to understand their effect on crystallization mechanism.

To understand the crystalline phase evolution during the heat treatment, a piece (~ 1-3g) of each glass composition has been crystallized in air at five different holding temperatures (900C°,950C°, 1000C°, 1050C°, 1100°C) for 1 hours in a gradient kiln and placed on an alumina sample holder.

The heating rate is 15°C/min and cooling was performed by moving the alumina sample holder to the cold end of the furnace and turning off the power. After 15 minutes the samples were removed from the furnace. Qualitative powder X-ray diffraction (XRD) analysis was performed on samples milled to particle size <45µm by using a conventional Bragg-Brentano diffractometer (Panalytical) with Ni-filtered Cu-Kα radiation.

The quantitative phase analysis of GCs was made by combined Rietveld-R.I.R (reference intensity ratio) method. 10% corundum (NIST RSM 676a) was added to all GC samples as an internal standard. Data were recorded in 2θ angle range 20-80° (step 0.02° s^{-1}).

The phase fractions extracted by Rietveld-R.I.R. refinements, using GSAS software and EXPGUI as graphical interface, were rescaled on the basis of the absolute weight of corundum originally added to their mixtures as an internal standard, and therefore, internally renormalized.

The background was successively fitted with a Chebyshev function with variable number of coefficients depending on its complexity. The peak profiles were modeled using a pseudo-Voigt function with one Gaussian and one Lorentzian coefficient.

Lattice constants, phase fractions, and coefficients corresponding to sample displacement and asymmetry were also refined.

3.9.1 Phase formation in the CMAS1 series

The crystallization temperatures of the bulk glasses where chosen taking into account the temperatures of glass transition, the exothermic peak of crystallization obtained from DTA thermograms, and the result of dilatometry measurements of as-pressed glass-powder compacts, which showed the sintering start. A test at 850°C for three hours revealed not completely dense and amorphous samples for modified glasses, whereas for parent glass CMAS evidence of crystallization was obtained. The samples fired at 900°C show evidence of sintering due to viscous flow, giving the compact a glassy appearance with a pale green color. Crystallization occurred above 900°C, accompanied in all samples by a color change to white. The surface of the material becomes shiny and smooth, with a rounded shape occurring at higher firing temperature due to the lower viscosity of the glassy phase.

The Figures 3.9.1.1 - 3.9.1.4 show the XRD patterns of samples heat treated at different temperatures for 1 hour.

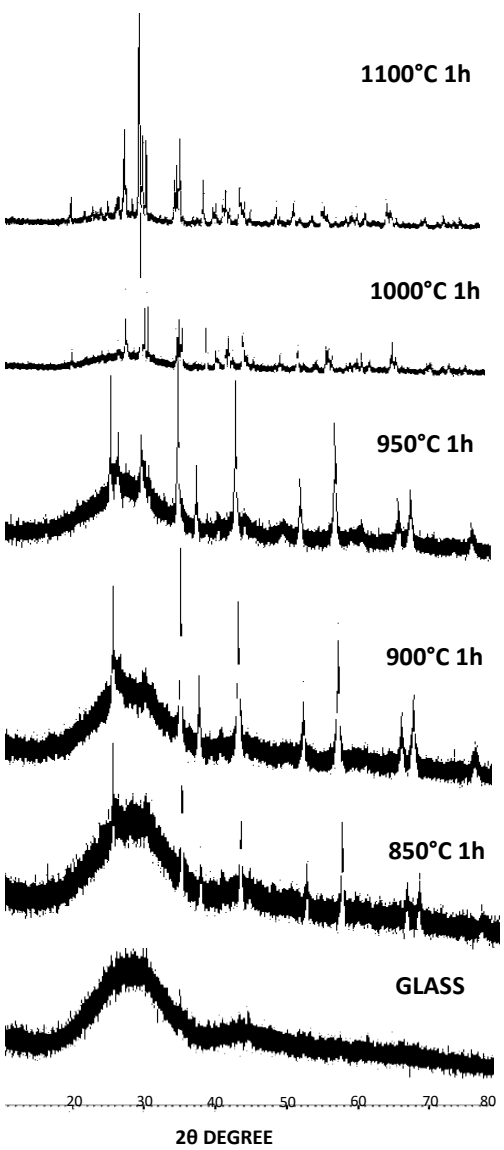

Figure 3.9.1.1 X-ray diffractograms of CMAS1 basic glass crystallized at different temperatures.

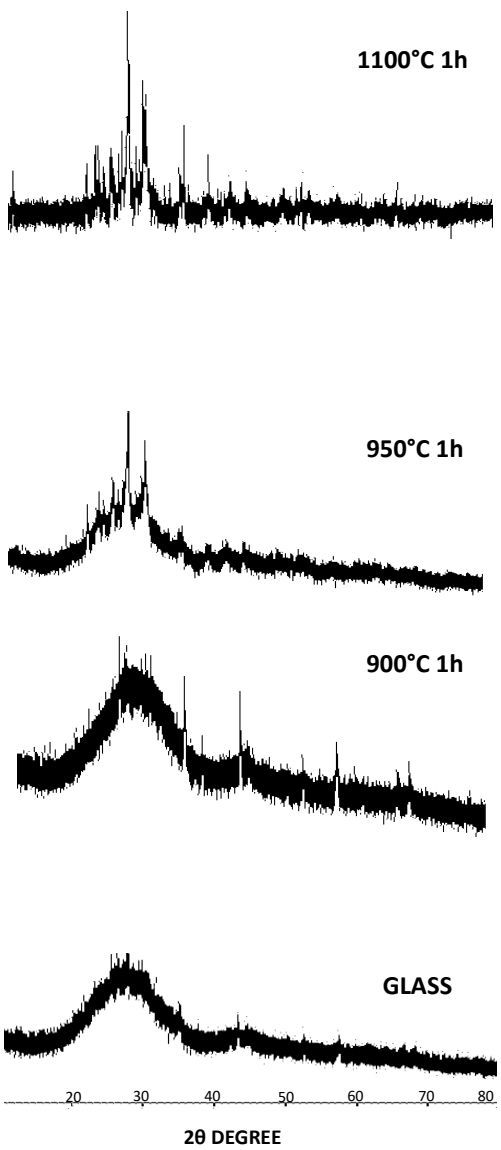

Figure 3.9.1.2 X-ray diffractograms of CMASTi1 glass crystallized at different temperatures.

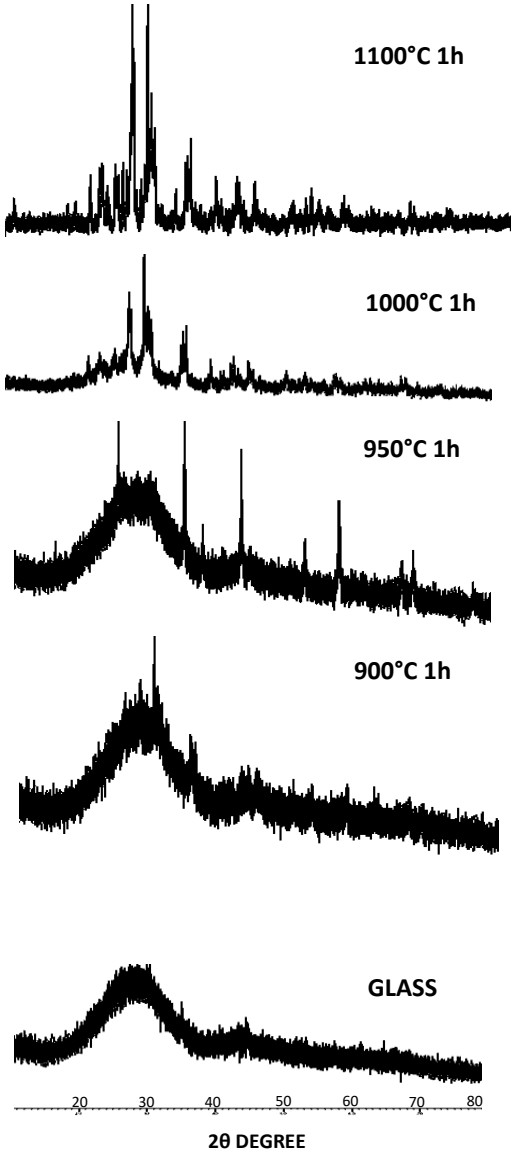

Figure 3.9.1.3 X-ray diffractograms of CMASMn1 glass crystallized at different temperatures.

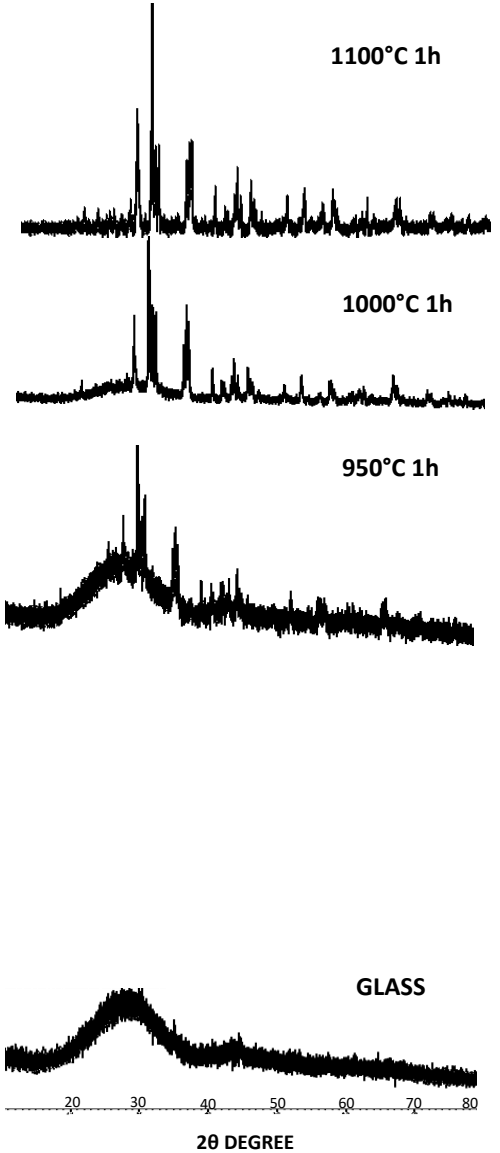

Figure 3.9.1.4 X-ray diffractograms of CMASZn1 glass crystallized at different temperatures.

From the XRD pattern at 1100°C we can observe that one hour is sufficient to reach almost a total devitrification for CMAS1 basic glass. Samples taken out below the onset of crystallization showed the characteristic amorphous scattering of the glassy state for all these glass series. In the case of the CMAS basic glass, devitrification stars at 850°C, the lowest temperature compared with the modified materials, as already seen in DTA thermograms. The main crystalline phase is Anorthite (Ca ($Al_2Si_2O_8$) ICDD 01-089-1460), the first exothermic peak in DTA curve being assigned to this phase. Augite (($Ca(Mg_{0.70}Al_{0.30})((Si_{1.70}Al_{0.30})O_6$ ICDD 01-078-1392) and Diopside ($CaMg(SiO_3)_2$ ICDD 01-073-6374) are the two minor phases formed upon heat treatment at 900°C, indicating that MgO intervenes in the phase formation when the holding temperature is higher. In modified glasses belonging to the CMAS1 series, crystallization is delayed compared to the basic glass as the XRD patterns of samples treated at 900°C still show an amorphous state.

For the modified glasses, the crystallization process occurs at about 950°C, with the formation of Anorthite ($Ca(Al_2Si_2O_8)$ ICDD 01-089-1460) as the main phase. By analyzing the XRD patterns at temperatures above 950°C, the presence of a silicate like $Ca_{0.88}Al_{0.12}Al_{1.77}Si_{2.23}O_8$ (ICDD 00-052-1344) is recorded. Like in CMAS1, Augite (($Ca(Mg_{0.70}Al_{0.30})((Si_{1.70}Al_{0.30})O_6$ ICDD 01-078-1392) and Diopside ($CaMg(SiO_3)_2$ ICDD 01-073-6374) are two phases present in considerable quantity. Other minor phases are present in the modified glasses, such as Wollastonite ($CaSiO_3$ ICDD 00-003-0626), detected in CMASTi1, Albite calcian ordered $(Ca(Si, Al)_4O_8$ ICDD 00-020-0548) in CMASMn1 and Clinoenstatite calcian ($Mg_{0.916}Ca_{0.084}SiO_3$ ICCD 01-076-0524) in CMASZn1.

In Tables 3.9.1.1 and 3.9.1.2. the main phases observed are listed with the corresponding quantification and the Rietveld parameters on glass ceramics at 1100°C.

SAMPLE GLASS ID	Anorthite (%)	Augite(%)	Diopside(%)	Wollastonite(%)	Albite(%)	Clinoenstatite(%)
CMAS1 BASIC SYSTEM	51.06	5.36	15.01	-	-	-
CMASTi1	20.25	10.6	7.21	3.35		
CMASMn1	30.64	12.96	8.24	-	4.26	-
CMASZn1	27.81	11.73	6.55			2.69

Table 3.9.1.1 Quantification of phases using Rietveld R.I.R method for CMAS1 glass series.

SAMPLE GLASS ID	GLASS (%)	χ^2	R_F^2	w_{rf}	r_p
CMAS BASIC SYSTEM	15.41	1.251	0.325	0.156	0.112
CMASTi1	62.42	1.325	0.463	0.177	0.115
CMASMn1	42.36	1.269	0.541	0.201	0.126
CMASZn1	51.12	1.147	0.226	0.125	0.301

Table 3.9.1.2 Fraction of amorphous part and Rietveld parameters for CMAS1 glass series.

We can conclude that the nucleation agents do not take part to the formation of new phases because they are not observed in phase composition. In Figures 3.9.1.5. - 3.9.1.8 the images acquired with SEM microscope are shown.

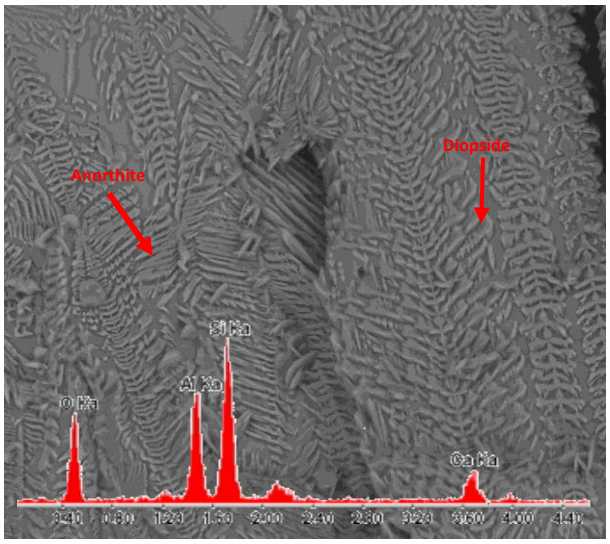

Figure 3.9.1.5 SEM micrograph of CMAS1 basic glass crystallized at 1100°C for 1h and EDS spectrum of Anorthite.

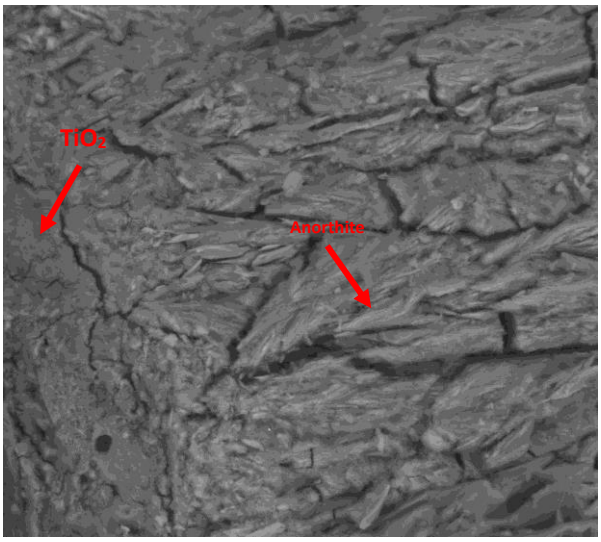

Figure 3.9.1.6 SEM micrograph of CMASTi1 basic glass crystallized at 1100°C for 1h.

Results of EDS spectroscopy confirm that additives are isolated and surround the crystals. SEM observations reveal that large amount of crystals occurred in the glass ceramic materials. The glass ceramic samples for SEM test were eroded in HF solution and the samples were repeatedly washed by ultrasonic cleaning after erosion. By this procedure, the glass phase of the glass ceramic structure is eroded and dissolved, and the microcrystalline phase is retained. It could be seen from the micrographs that the microstructure of the sample is dense and the glass phase and crystalline phases adhered to each other. This structure is beneficial to improve the integral density and wear-resistance of materials.

As mentioned, in CMASTi1 sample TiO_2 acts as network and the high value of activation energy could be confirmed also from the SEM micrograph. If compared to CMAS1 basic glass, the crystals between the amorphous phase are not well defined. This behavior could be explained by the configuration of titanium ions in the glass network. As reported in the literature[215-216], Ti^{4+} ions maintain a 4-fold coordination during the heat treatment, but this structural unit is a metastable state, and a heating treatment at $T>T_g$ may lead to depolymerization, with Ti^{4+} depleting from $[TiO_4]$ units and turning to a 6-fold coordination structure $[TiO_6]$. The depolymerized silica tetrahedron may bond together to form a new network. The network free Ti^{4+} ions bond with CaO and MgO that can supply non-bridging oxygens to form a modifier cation rich phase. Then the phase separation occurs. Ma et al. studied the effect of TiO_2 content on phase separation in the CaO-MgO-Al_2O_3-SiO_2-Na_2O glass, and found that increasing the TiO_2 amount the phase separation in the glass is promoted more effectively [217]. Wang et al.[218-219] found that doping with iron can promote the phase separation in the MgO-Al_2O_3-SiO_2-TiO_2 glass. In this situation, Ti atoms are concentrated in the small amorphous droplets which distribute homogeneously among the glass matrix, Si and Al rich phase.

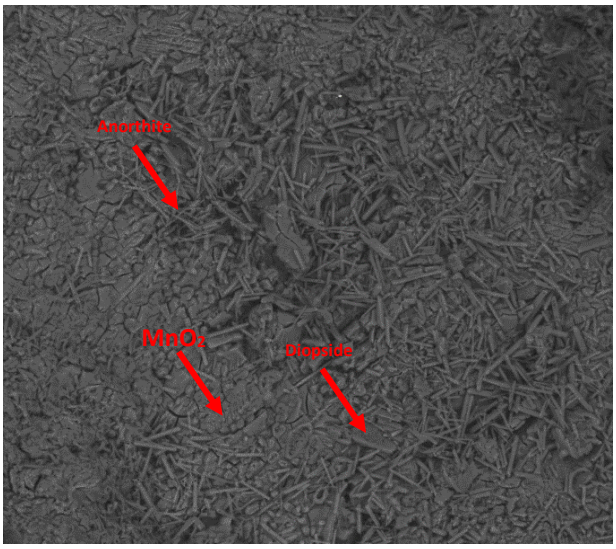

Figure 3.9.1.7 SEM micrograph of CMASMn1 glass crystallized at 1100°C for 1h.

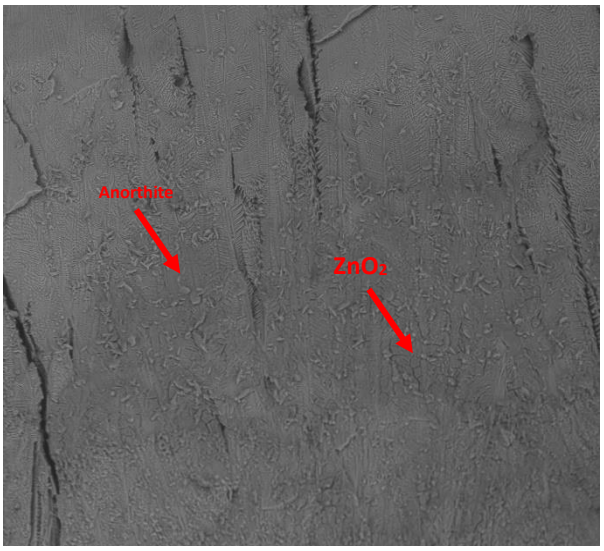

Figure 3.9.1.8 SEM micrograph of CMASZn1 glass crystallized at 1100°C for 1h.

In general, SEM images confirmed the kinetic results, i.e. one-dimensional growth of crystals for CMAS1 basic glass, CMASTi1 and CMASZn1 and three –dimensional growth for CMASMn1. Only in the latter sample the crystals structure is well defined, as confirmed by a low activation energy for crystallization. From EDS analysis, cylindrical-like crystals indicate the presence of Anorthite phase. The sample shows a residual glassy phase. For these glasses, the separation of phases occurs by nucleation and crystal growth where:

1. the crystal growth occurs on each single nucleation site
2. the phases tend to separate and they are well defined
3. an energy barrier exists between the phases
4. the so called "Droplet in Matrix" morphology emerges, in which the crystalline phases are distributed in the glassy phase

After the heat treatment at 1100°C for 1 hour, the resulting glass ceramics were tested to ascertin if the formed phases could affect considerably the CTE of the materials.

In Table 3.9.1.3 are listed the thermal expansion coefficient of the main phases formed in temperature ranges of 200°-500°C and 200°-700°C (error is within the range $\pm 0.10 \cdot 10^{-6}$ °C^{-1}).

SAMPLE GLASS ID	*α (200-500°C) (°C^{-1})*	*α (200-700°C) (°C^{-1})*
Anorthite	$4.82 \cdot 10^{-6}$	-
Augite	$5.21 \cdot 10^{-6}$	-
Diopside	$4.48 \cdot 10^{-6}$	-
CMAS1 BASIC SYSTEM	$9.29 \cdot 10^{-6}$	$8.23 \cdot 10^{-6}$
CMASTi1	$9.91 \cdot 10^{-6}$	$9.99 \cdot 10^{-6}$
CMASMn1	$8.10 \cdot 10^{-6}$	$8.15 \cdot 10^{-6}$
CMASZn1	$23.81 \cdot 10^{-6}$	$19.89 \cdot 10^{-6}$

Table 3.9.1.3 CTE values for the main phases formed and for all glasses belonging to the CMAS1 series.

The CTE values for the resulting glass ceramics differ only slightly from the CTEs of the corresponding glass samples. The different phases don't affect significantly the thermomechanical properties. This result confirms that CMASZn1 is not suitable for sealing application in SOFC.

3.9.2 Phase formation in CMAS2 series

The glasses belonging to the CMAS2 series present a higher amount of network modifiers compared to CMAS1 glasses and this composition influences the type of phases formed during the heat treatment. From DTA thermograms the crystallization is observed to occur at about 900°C, with the exception of the CMAS2 basic glass. Figures 3.9.2.1. - 3.9.3.5 show the X-Ray diffraction spectra of powder pressed samples.

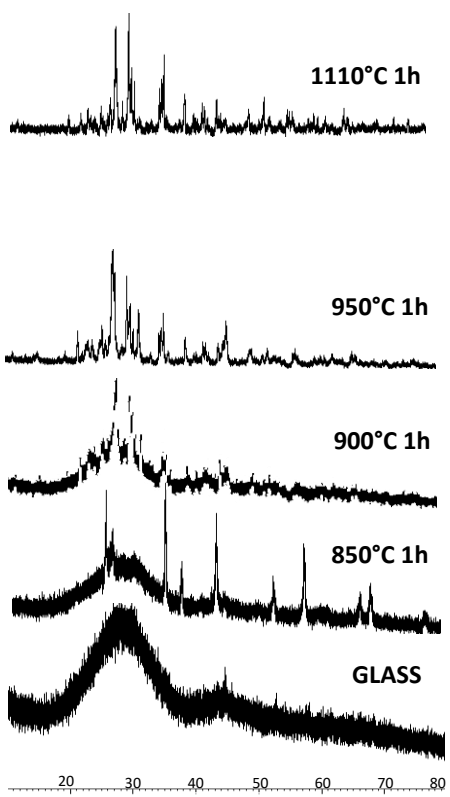

Figure 3.9.2.1 X-ray diffractograms of CMAS2 basic glass crystallized at different temperatures.

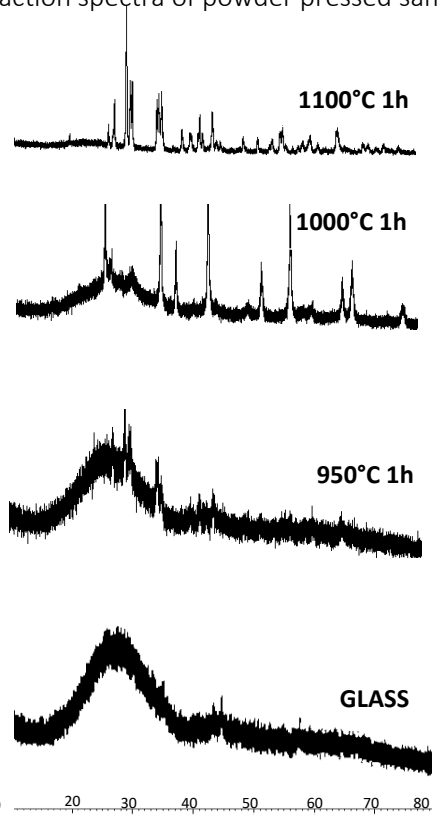

Figure 3.9.2.2 X-ray diffractograms of CMASTi2 basic glass crystallized at different temperatures.

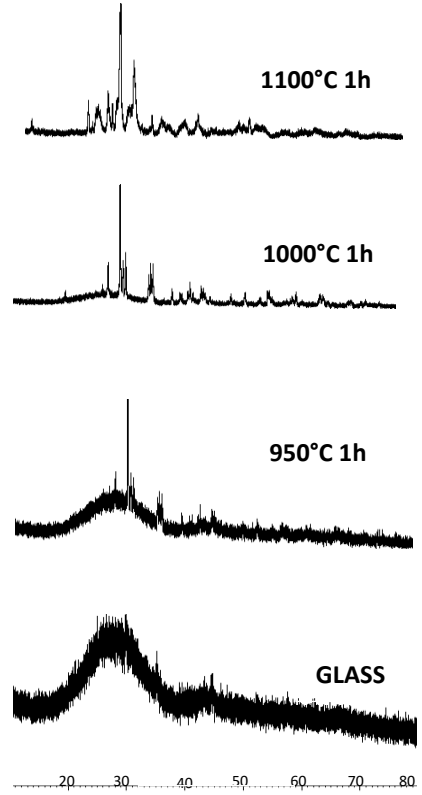

Figure 3.9.2.3 X-ray diffractograms of CMASMn2 glass crystallized at different temperatures.

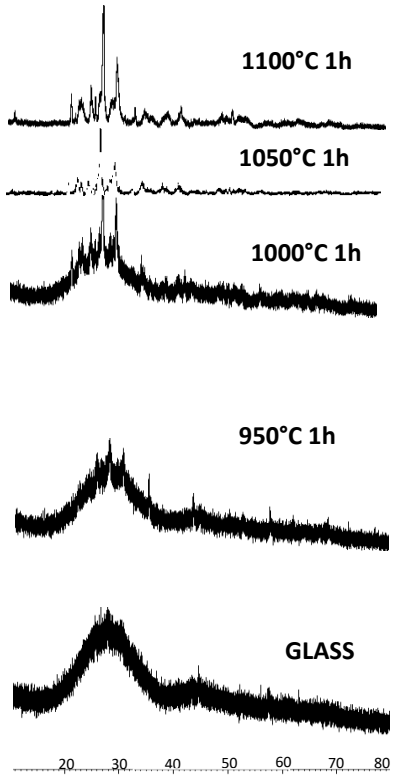

Figure 3.9.2.4 X-ray diffractograms of CMASZn2 glass crystallized at different temperatures.

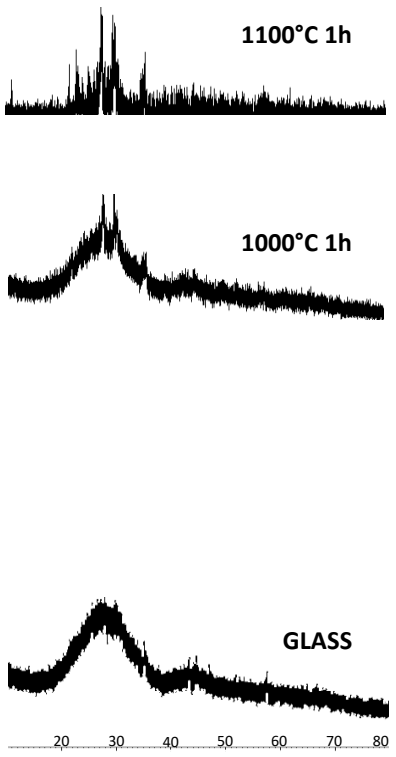

Figure 3.9.2.5 X-ray diffractograms of CMASSn2 glass crystallized at different temperatures.

Diffraction spectra confirm that, except for the CMAS2 basic glass, crystallization is not detectable below 900°C. Anorthite (Ca ($Al_2Si_2O_8$) ICDD 01-089-1460) is the main phase. In all glasses, Diopside ($CaMg(SiO_3)_2$ ICDD 01-073-6374) is present in smaller quantity due to the low MgO content in the glass composition, and Augite ($(Ca(Mg_{0.70}\ Al_{0.30})((Si_{1.70}\ Al_{0.30})O_6$ ICDD 01-078-1392) is revealed as the second most abundant phase. Small amounts of Albite calcian ordered $(Ca(Si, Al)_4\ O_8$ ICDD 00-020-0548) were detected in the CMAS2 basic glass. In CMASMn2 the presence of Diopside aluminian $(Ca(Mg, Al)(Si, Al)_2O_6$ ICDD 00-025-01549) is observed, while in CMASZn3, $Mg_2(Si_2O_6)$ ICDD 01-086-0433 is identified.

A different behavior is displayed by the CMASSn2 glass, in which the crystallization occurs at higher temperature (about 1000°C). From the XRD pattern we deduce that even 1 hour at holding time of 1100°C is not enough for a complete crystallization. After the heat treatment this glass consists prevalently of the amorphous phase, only the Anorthite phase being detected. The nucleating agents also in these case promote the devitrification but do not participate to phase formation.

In Tables 3.9.2.1 and 3.9.2.2 the result of the Rietveld R.I.R analysis are listed together with the CTE values for the obtained glass ceramics at 1100°C (error within the range $\pm 0.10 \cdot 10^{-6}$ °C^{-1}).

SAMPLE GLASS ID	Anorthite (%)	Augite (%)	Diopside(%)	Albite(%)	$Mg_2(Si_2O_6)$ (%)	Diopside aluminian (%)
CMAS2 basic system	51.23	13.01	7.51	2.01	-	-
CMASTi2	63.14	11.07	6.78	-	-	-
CMASMn2	61.79	10.27	6.88	-	-	1.23
CMASZn2	49.20	8.42	5.83	-	2.01	
CMASSn2	23.12	-	-	-	-	-

Table 3.9.2.1 Quantification of phases using Rietveld R.I.R method for CMAS2 glass series.

SAMPLE GLASS ID	GLASS (%)	χ^2	R_F^2	w_{rf}	r_p	α *(200-500°C) (°C^{-1}))*	α *(200-700°C) (°C^{-1})*
CMAS2 basic system	36.21	1.381	0.265	0.156	0.104	$8.15 \cdot 10^{-6}$	$8.21 \cdot 10^{-6}$
CMASTi2	19.32	1.465	0.513	0.177	0.145	$10.71 \cdot 10^{-6}$	$10.81 \cdot 10^{-6}$
CMASMn2	18.45	1.209	0.429	0.201	0.139	$12.52 \cdot 10^{-6}$	$11.35 \cdot 10^{-6}$
CMASZn2	39.87	1.007	0.207	0.125	0.157	$13.66 \cdot 10^{-6}$	$11.88 \cdot 10^{-6}$
CMASSn2	81.21	1.324	0.215	0.200	0.429	$8.34 \cdot 10^{-6}$	$8.41 \cdot 10^{-6}$

Table 3.9.2.2 CTE values for main formed phases and Rietveld R.I.R. for CMAS2 glass series.

The CTE values display the same trend as the CMAS1 series, the formed phases having a minimal influence (a slightly increase) on this property. It is concluded that the CMASZn2 can be considered not suitable for sealing application.

Figures 3.9.2.6 - 3.9.2.10 show the SEM images of the glasses treated at 1100°C for 1 hour.

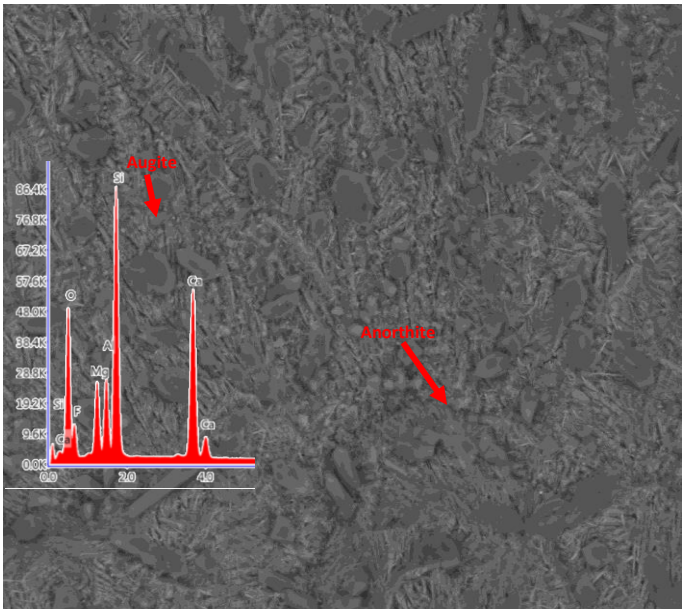

Figure 3.9.2.6 SEM micrograph of CMAS1 basic glass crystallized at 1100°C for 1h and EDS spectrum of AUGITE.

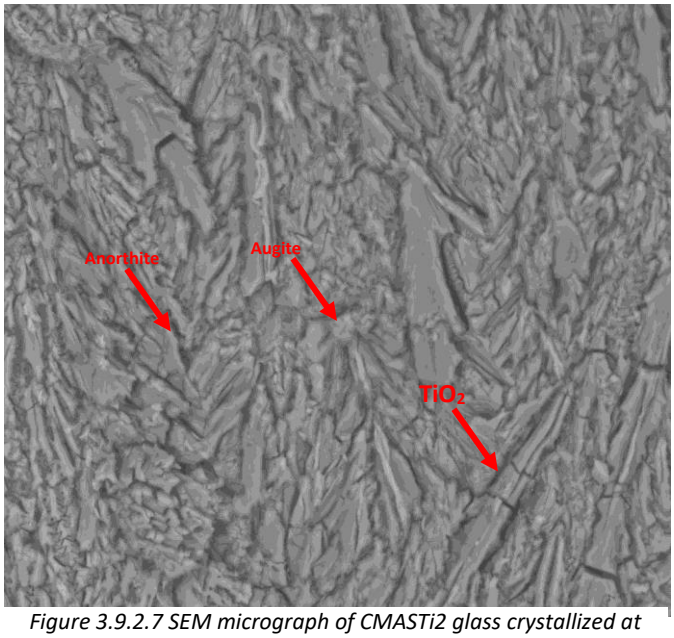

Figure 3.9.2.7 SEM micrograph of CMASTi2 glass crystallized at 1100°C for 1h.

In both cases, large amount of crystals are dispersed in the glassy phase. One-dimensional growth in CMAS2 basic glass and two-dimensional growth in CMASTi2 are consistent with the kinetic analysis previously discussed. TiO_2 is not included in the network glassy structure, but rather it surrounds the crystals. In both cases the interconnected microstructure as revealed by SEM images indicate than a spinodal decomposition occurs. This phenomenon is evident when one-dimensional growth and separation of phases are observed. A separation of phases occurs within an immiscibility region when the kinetic and thermodynamic conditions enable it to take place. From the thermodynamic point of view, it is necessary that the free energy of mixing is positive, in this case the separated phases will be in a lower energy state than the initial phases. From the kinetic point of view, it is necessary that the viscosity be lower enough to allow the separation of phases in a reasonable period of time.

The spinodal decomposition is characterized by the following properties:

1. the interfaces between the different phases are widespread and tend to define over time
2. it occurs spontaneously
3. the separation of phases takes place in a widespread way
4. an interconnected morphology is generated

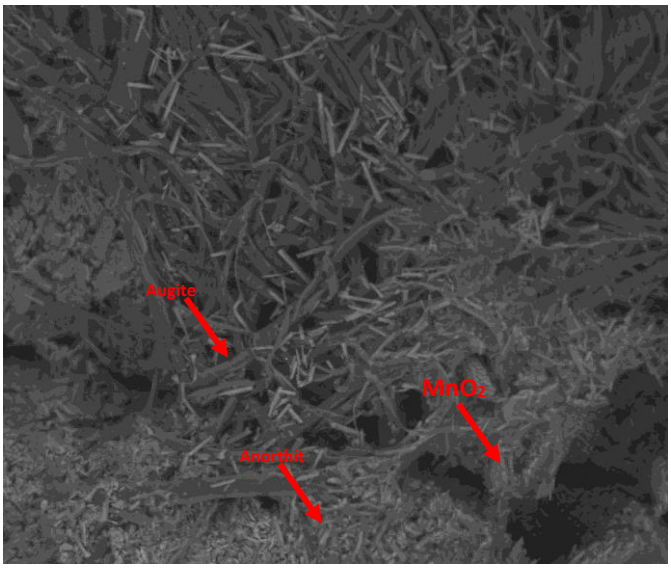

Figure 3.9.2.8 SEM micrograph of CMASMn2 glass crystallized at 1100°C for 1h.

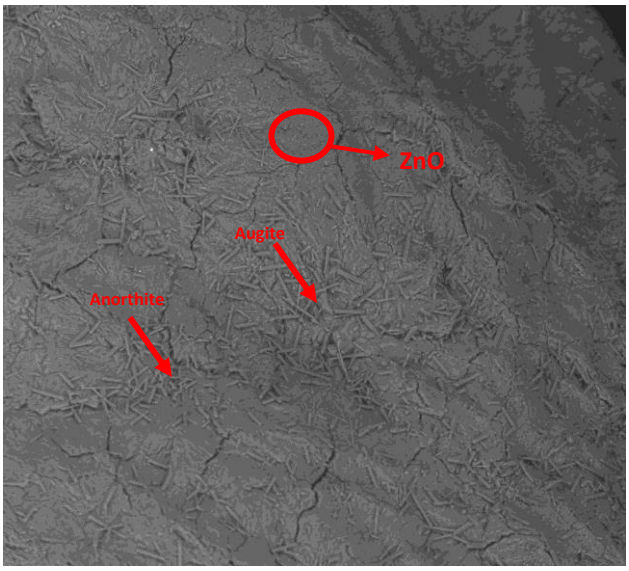

Figure 3.9.2.9 SEM micrograph of CMASZn2 glass crystallized at 1100°C for 1h.

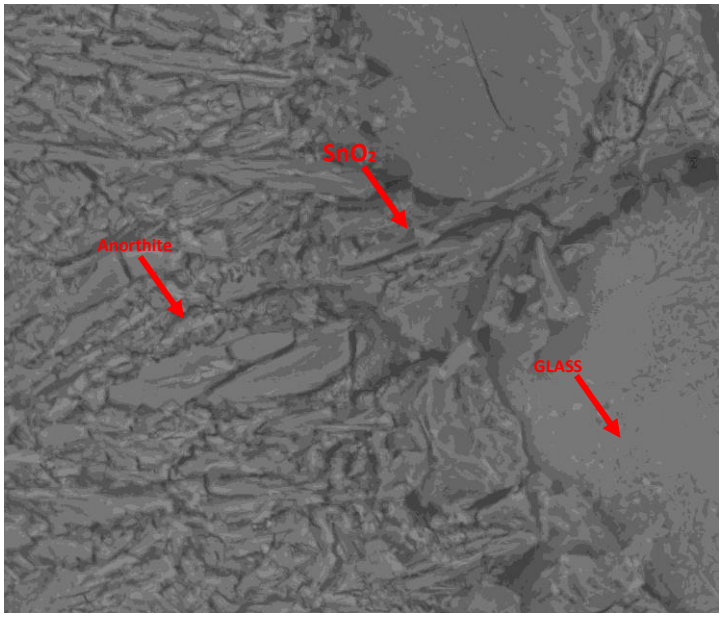

Figure 3.9.2.10 SEM micrograph of CMASSn2 glass crystallized at 1100°C for 1h.

The crystallization mechanisms derived from kinetic considerations are once again confirmed by SEM images. In CMASMn2 the crystals are well developed and homogeneously distributed into the glassy phase, as already evaluated by its low activation energy. Crystals are less evident in the CMASSn2 glass. In all the modified glasses, isolated accumulation of nucleating agents are detected.

3.9.3 Phase formation in CMAS3 series

The glasses belonging to the CMAS3 series exhibit the highest content of CaO, and are suitable candidates for one-step crystallization considering their low values of activation energies. The content of additive is about half of CaO and this could play an important role in phase formation. All these results are confirmed by a high degree of crystallization in XRD patterns and SEM micrographs.

In figures 3.9.3.1 - 3.9.3.5. the XRD patterns of the glass ceramic crystallized at different temperatures for 1 hour are reported.

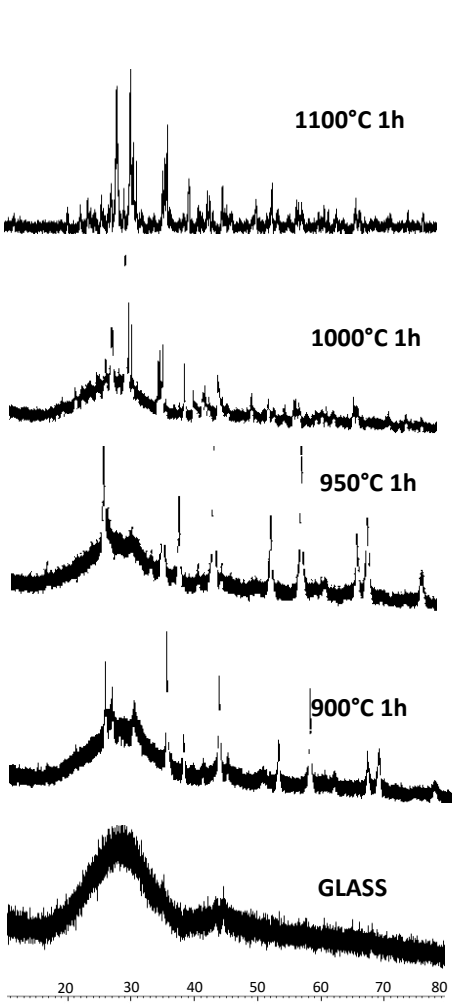

Figure 3.9.3.1 X-ray diffractograms of CMAS3 basic glass crystallized at different temperatures.

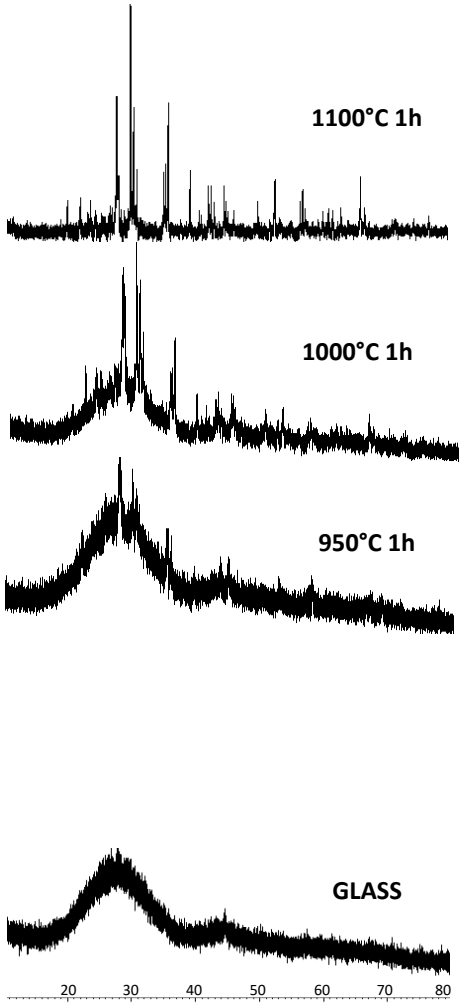

Figure 3.9.3.2 X-ray diffractograms of CMASTi3 glass crystallized at different temperatures.

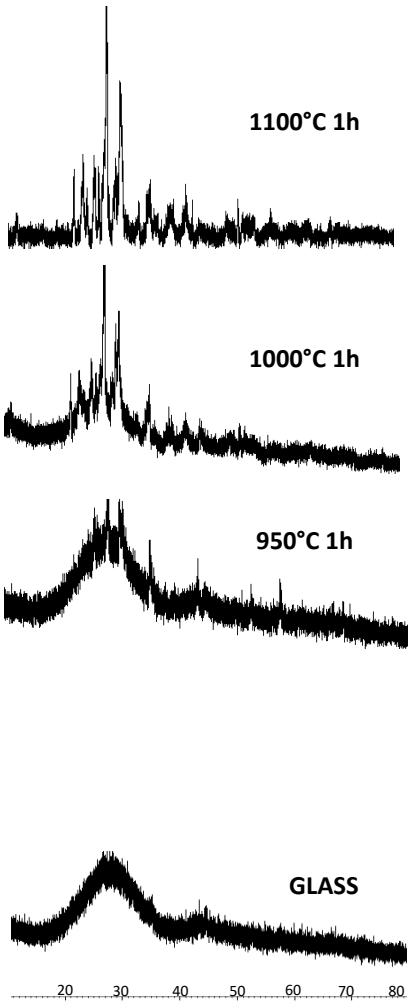

Figure 3.9.3.3 X-ray diffractograms of CMASMn3 glass crystallized at different temperatures.

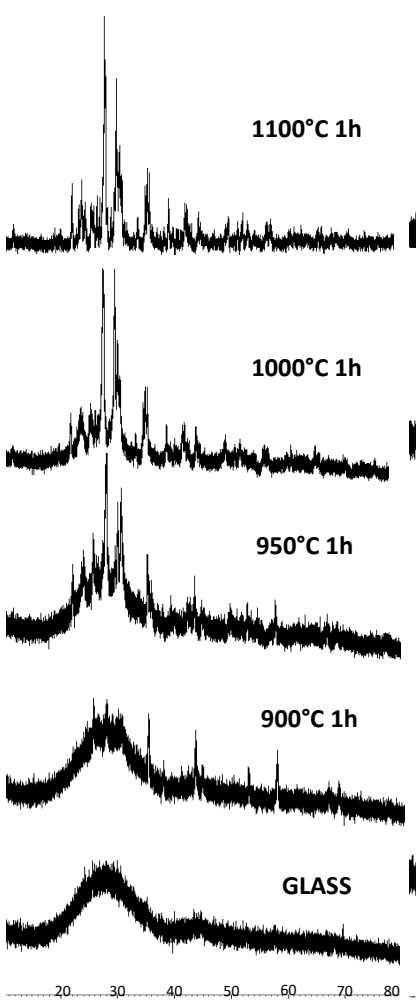

Figure 3.9.3.4 X-ray diffractograms of CMASZn3 glass crystallized at different temperatures.

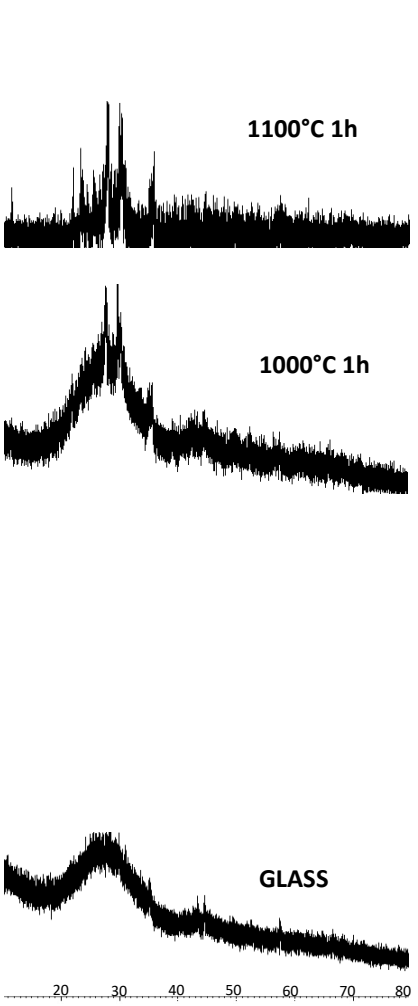

Figure 3.9.3.5X-ray diffractograms of CMASSn3 glass crystallized at different temperatures.

Unlike the other series, the crystallization of the CMAS3 basic glass starts above 900°C, and the amount of network modifier and additive tend to homogenize the devitrification process (only one exothermic peak observed in the DTA curve).

In all glass ceramics, the main crystalline phases are Anorthite ($Ca(Al_2Si_2O_8)$ ICDD 01-089-1460) and Diopside, the latter present in large quantity than other examined systems. In the CMASTi3, CMASMn3 and CMASZn3 modified glasses, the presence of additives could facilitate the phase separation. The interface of these two phases provides the core of heterogeneous nucleation for the precipitation of Diopside crystals. The compositions of the Diopside crystal are much different from that of the base glass, indicating that the growth should be diffusion-controlled.

In the CMAS3 basic glass, the Diopside crystals exist as $CaMgSi_2O_6$ ICDD 01-071-1067, in CMASTi3 as $Ca_{0.8}Mg_{1.2}(SiO_3)_2$ ICDD 01-076-0237, in CMASMn3 as Ca(Mg, Al)(Si, Al)$_2$ O_6 ICDD 00-041-1370 and in CMASZn3 as $Ca_{0.89}Mg_{1.11}Si_{1.98}O_6$ ICDD 01-072-1498. This behavior can be explained considering that, because Si^{4+} ion is a network former and does not tend to diffuse, the only ions available for diffusion under crystallization are Mg^{2+} and Ca^{2+}. When the $\frac{SiO_2}{(CaO+MgO)}$ ratio increases, the viscosity of the base glass also increases, and the diffusion of Mg^{2+} and Ca^{2+} ions becomes more difficult. Therefore, the crystallization activation energy increases too. The Ca^{2+} ion is known to be one of the largest ions, with an effective radius close to those Pb^{2+} and Ba^{2+} which shows a very limited mobility in the glass network, while Mg^{2+} has a smaller size and higher mobility [220]. Therefore, the diffusion of Ca^{2+} ions is the rate-limiting step in forming Diopside. In the CMAS3 glass series, the above ratio is lower (1.18) than the other glass series and the diffusion of Ca^{2+} ions is favored. The viscosity of the other glasses is relatively high due to the high $\frac{SiO_2}{(CaO+MgO)}$ ratio, so the mobility of Ca^{2+} ions is greatly limited and the crystallinity of Diopside is reduced accordingly. In addition, the increase of Mg^{2+} and Ca^{2+} ions is another important reason for the increase of the Diopside content. Moreover, Karamanov et al. [114] have proposed that the crystallization of Diopside may cause formation of additional porosity due to the significant difference between the density of Diopside in glassy (2.75 g/cm^3) and crystal state (3.27 g/cm^3). Note that the difference of density is negligible in the case of wollastonite (2.87 g/cm^3 and 2.92 g/cm^3 for the glass and the crystals, respectively). The effect of this phenomenon is evident in the crystallization of the bulk glasses, i.e. formation of big pores in the core of bulk samples. With the heat treatment around the temperature of the exothermic peak in the DTA curve, Mg^{2+} ions combine with Al^{3+} ions to form also Spinel phase ($MgAl_2O_4$ ICDD 00–21–1152). As the crystallization temperature increases, the reduced viscosity promote the diffusion of the ions, thus accelerating the crystal growth

In the CMAS3 basic glass, Augite ($(Ca(Mg_{0.70}Al_{0.30})((Si_{1.70}Al_{0.30})O_6$ ICDD 01-078-1392), Akermanite ($Ca_2MgSi_2O_7$ ICDD 00-003-0703) and Wollastonite ($CaSiO_3$ ICDD 00-002-0689) are detected. From XRD patterns, the modified glass ceramics consist of several different minor phases:

1. CMASTi3 shows Augite ($(Ca(Mg_{0.70}Al_{0.30})((Si_{1.70}Al_{0.30})O_6$ ICDD 01-078-1392), Wollastonite ($CaSiO_3$ ICDD 00-002-0689) and $Mg_2(Si_2O_6)$ ICDD 01-086-0433 crystalline phases.
2. CMASMn3 reveals the presence of aluminosilicates such as $Ca_{0.88}Al_{0.12}Al_{1.77}Si_{2.23}O_8$ ICCD 00-052-1344 and $Ca(Al_2Si_2O_8)$ ICDD 01-085-1660 together with Akermanite ($Ca_2MgSi_2O_7$ ICDD 01-074-0990)
3. CMASZn3 presents the same phases recorded in CMASMn3 but $Mg_2(Si_2O_6)$ ICDD 01-086-0433 is also detected
4. for CMASSn3 a different situation was found, with only a small amount of Akermanite ($Ca_2MgSi_2O_7$ ICDD 01-074-0990) detected, consistent with its poor tendency to grow crystals.

In Tables 3.9.3.1 and 3.9.3.2 the results derived from Rietveld R.I.R method are listed (quantification of phases and Rietveld parameters) together with the CTE values for the resulting glass ceramics at 1100°C (error within the range $\pm 0.10 \cdot 10^{-6}$ °C^{-1}).

SAMPLE GLASS ID	CMAS3 BASIC GLASS	CMASTi3	CMASMn3	CMASZn3	CMASSn3
Anorthite	39.41	29.53	25.04	35.76	18.70
Augite	9.31	8.21	9.12	9.88	-
Diopside	6.22	7.03	4.33	4.07	-
Wollastonite	1.52	2.33	1.74	-	-
$Ca_{0.88}Al_{0.12}Al_{1.77}Si_{2.23}O_8$	-	-	3.65	4.83	-
$Ca(Al_2Si_2O_8)$	-	-	3.81	3.86	-
$Mg_2(Si_2O_6)$	1.23	4.61	-	1.17	-
Akermanite	3.78	-	2.78	1.97	2.03

Table 3.9.3.1 Quantification of phases using Rietveld R.I.R method for CMAS3 glass series.

SAMPLE GLASS ID	GLASS (%)	χ^2	R_F^2	w_{rf}	r_p	α (200-500°C) (°C^{-1})	α (200-700°C) (°C^{-1})
CMAS3 BASIC SYSTEM	37.25	1.031	0.240	0.149	0.163	$9.44 \cdot 10^{-6}$	$8.24 \cdot 10^{-6}$
CMASTi3	42.13	1.420	0.637	0.207	0.207	$11.87 \cdot 10^{-6}$	$9.01 \cdot 10^{-6}$
CMASMn3	46.97	1.471	0.123	0.192	0.143	$13.01 \cdot 10^{-6}$	$12.21 \cdot 10^{-6}$
CMAZn3	39.41	1.530	0.337	0.320	0.211	$9.28 \cdot 10^{-6}$	$8.81 \cdot 10^{-6}$
CMASSn3	72.14	1.112	0.014	0.117	0.349	$8.75 \cdot 10^{-6}$	$8.11 \cdot 10^{-6}$

Table 3.9.3.2 CTE values for the main formed phases and Rietveld R.I.R. for CMAS3 glass series.

The CTE values present the same trend observed for the other glass series, with a low the influence of the formed phases on CTEs. As a consequence, all these glass ceramic materials are suitable for sealing application, with the exception of CMASMn3 that should be excluded for its CTE value slightly higher that the recommended limit.

In figures 3.9.3.6 - 3.9.3.10. the SEM micrographs of the glass ceramics obtained after a thermal treatment of 1 hour at 1100°C are reported

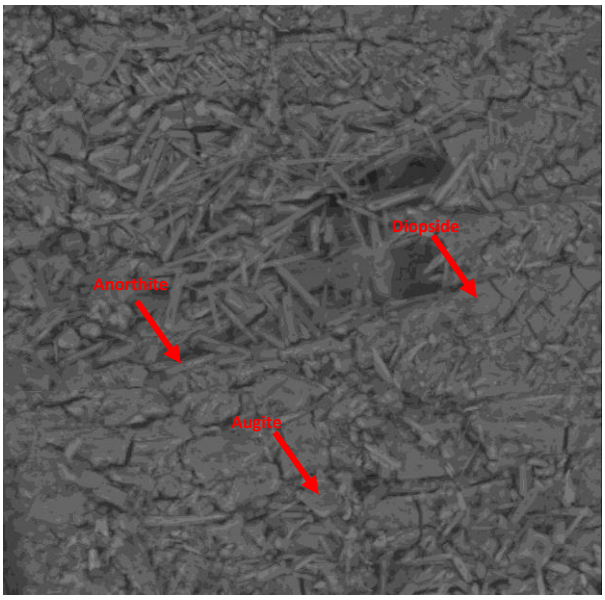

Figure 3.9.3.6 SEM micrograph of CMAS3 basic glass crystallized at 1100°C for 1h.

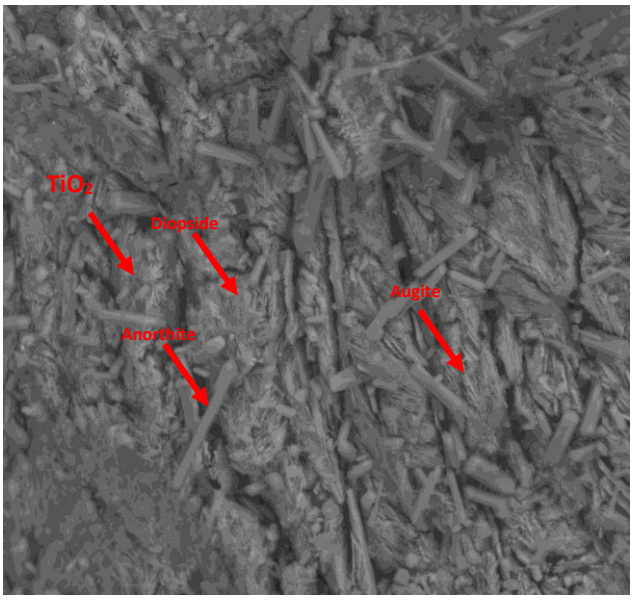

Figure 3.9.3.7 SEM micrograph of CMASTi3 glass crystallized at 1100°C for 1h.

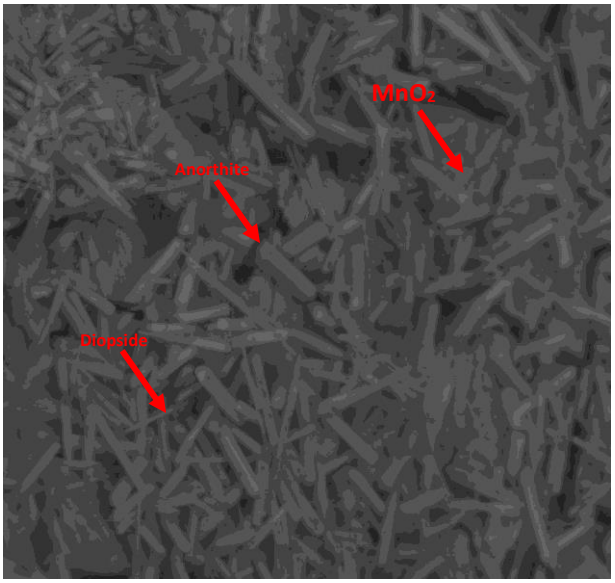

Figure 3.9.3.8 SEM micrograph of CMASMn3 basic glass crystallized at 1100°C for 1h.

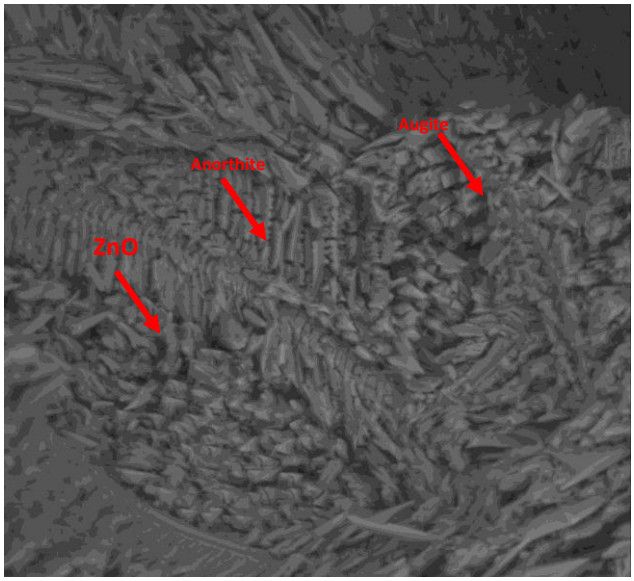

Figure 3.9.3.9 SEM micrograph of CMAZn3 basic glass crystallized at 1100°C for 1h.

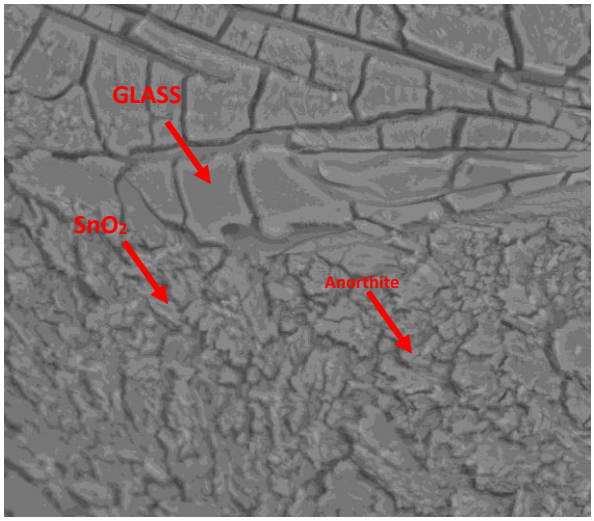

Figure 3.9.3.10 SEM micrograph of CMASSn3 basic glass crystallized at 1100°C for 1h.

The nucleating agents are isolated in the glass matrix and do not participate to phases formation as confirmed by SEM images and the separation of phases could be attributed to the segregation of calcium and magnesium ions as demonstrated in the De Vekey and Mahumdar work [221].

With decreasing the $\frac{SiO_2}{(CaO+MgO)}$ ratio, the average grain size decreases, consistent with the XRD analysis. This effect is associated with the decreasing in the number of non-bridging and the increasing in degree of polymerization.

The growth of Diopside is promoted by the lower viscosity and higher diffusion of cations. When the glasses are heated at their T_C the average grain size decreases, and the morphology of the crystals changes. The crystallinity and morphology have direct effects on the mechanical and chemical properties of the glass ceramics. With increasing the content of CaO, the amount and the size of crystal particles also grew up.

In glass ceramic samples like the CMAS3 basic glass, CMASTi3 and CMASMn3 where three-dimensional growth is dominant, well defined and rod like crystals together with smaller acicular ones are embedded in the glass matrix. The cylindrical like crystals are highly packed and significantly bigger in the glass ceramics. EDS analyses allow to assign these crystals to Anorthite phase, while the acicular crystals are attributed to Diopside phase. In CMAS3 basic glass and CMASTi3, the crystals assigned to Diopside feature a slightly excess in Ca compared to the stoichiometric phase, while the crystals assigned to Wollastonite displays a slight deficiency of Si. In CMASZn3 and CMASSn3 a two-dimensional growth of crystals is dominant. In CMASSn3 the glass phase is also prevailing.

3.9.4 Phase formation in CMAS4 series

As previously shown, in the CMAS4 basic glass the crystallization process is detected at lower temperature, and two exothermic peaks are visible in the DTA thermogram.

In this last series of glasses, the amount of nucleation agent is higher and equal to the MgO content. From DTA and HSM measurements, the beginning of crystallization was observed to occur just after the maximum densification temperature, except in the CMAS4 basic glass and CMASZn4. Therefore, well sintered samples are subjected to devitrification at temperature near 950°C. The XRD patterns confirm this behavior. For CMASZn4 the influence of the ZnO content affect significantly the crystallization because this additive tends to weaken the structure of the glass network.

XRD patterns of the glass ceramic materials resulting from different holding temperatures are reported below (Figures 3.9.4.1 - 3.9.4.4)

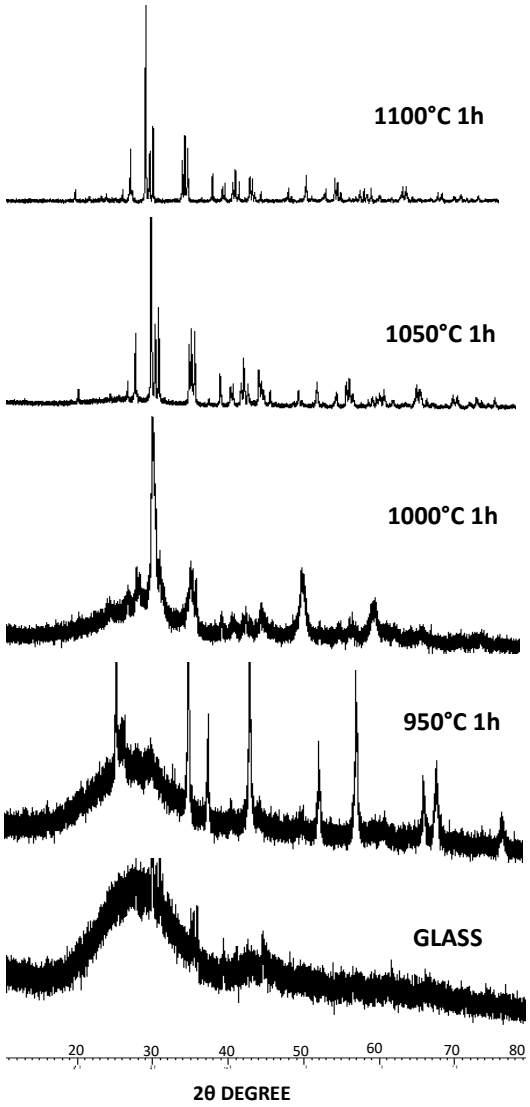

Figure 3.9.4.1 X-ray diffractograms of CMAS4 basic glass crystallized at different temperatures.

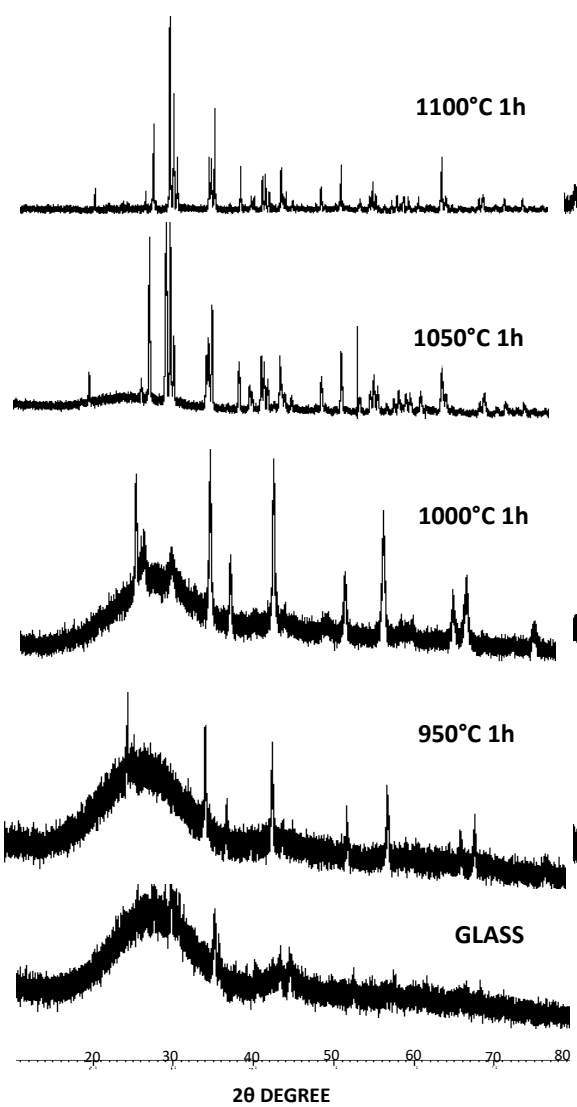

Figure 3.9.4.2 X-ray diffractograms of CMASTi4 glass crystallized at different temperatures.

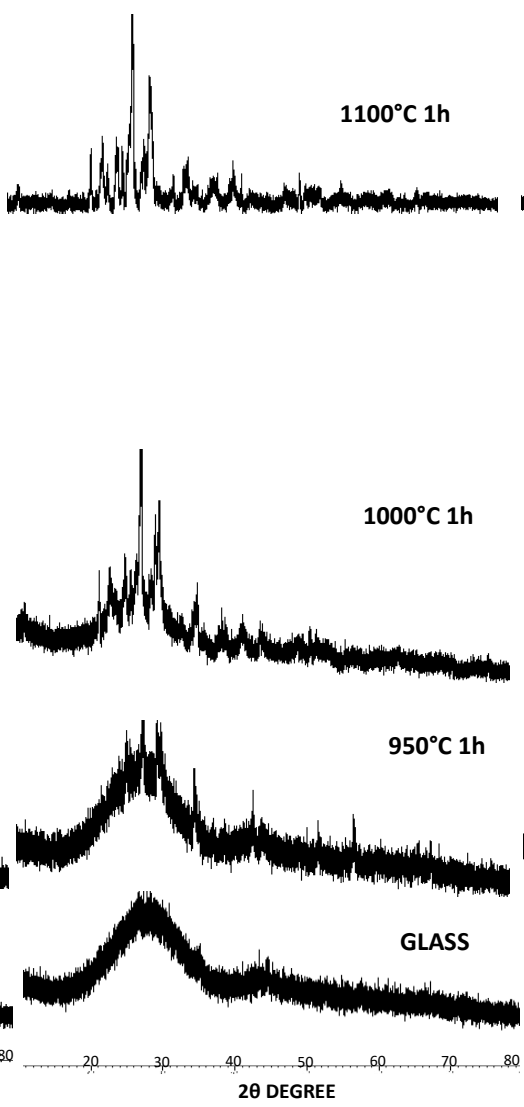

Figure 3.9.4.3 X-ray diffractograms of CMASMn4 glass crystallized at different temperatures.

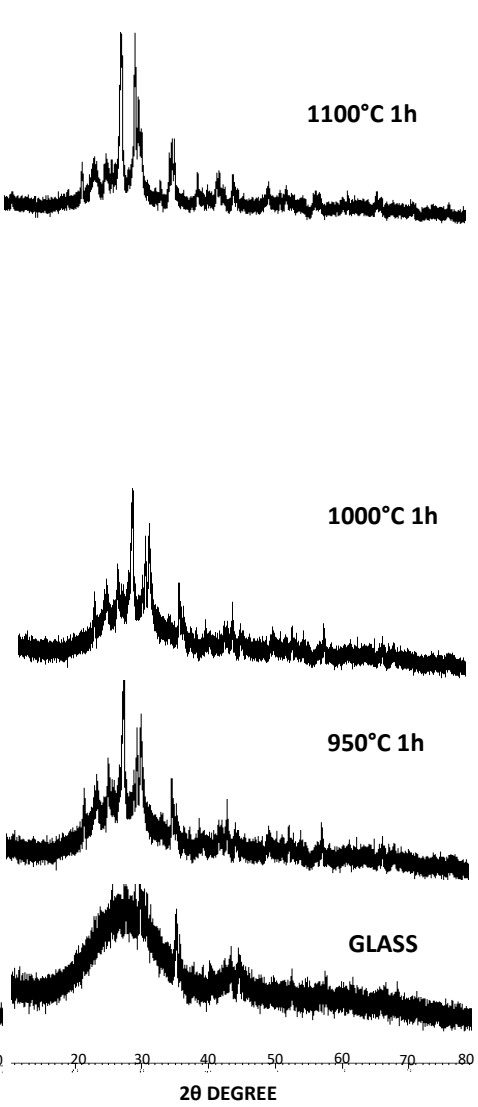

Figure 3.9.4.4 X-ray diffractograms of CMASZn4 glass crystallized at different temperatures.

From the XRD patterns at 1100°C we can deduce that a 1 hour treatment is sufficient to reach almost the totally devitrification for CMAS4 and CMASTi4, as also confirmed by the quantitative analysis. Unlike the other systems, the nucleating agents participate to phase formation, because XRD patterns recorded at high temperatures evidence the presence of new phases in which the additives take part to their formation. In all glasses belonging to this series the main crystalline phases are Anorthite ($Ca(Al_2 Si_2 O_8)$ ICDD 01-089-1460) and Diopside aluminian (Ca(Mg, Al) (Si, Al)$_2$ O_6 ICDD 00-025-0154). Augite (Ca ($Mg_{0.70}$ $Al_{0.30}$) (($Si_{1.70}$ $Al_{0.30}$)O_6) ICDD 01-078-1392) is present in smaller quantities compared to the other glasses. In CMAS4 basic glass, Wollastonite-2M ($CaSiO_3$ ICDD 00-027-0088), $Mg_2(Si_2O_6)$ ICDD 01-086-0433 and Clinopyroxene ($Ca_{0.20}$ $Mg_{1.80}$)(Si_2 O_6) ICDD 01-074-7827 are the minor phases. With regard to the latter, in CMASTi4 we have recorded the corresponding titanium-containing phase, Clinopyroxene titanium aluminian (Ca(Ti, Mg, Al)(Si, Al)$_2$ O_6 ICDD 00-025-0306), together with $CaAl_2Si_2$ ICDD 00-036-1342. In CMASMn4 glass ceramics, Diopside manganoan ((Ca, Mn)(Mg, Fe, Mn) Si_2O_6 ICDD 00-025-0154), a variant of Diopside, is a minor phase, with $Mg_2(Si_2O_6)$ ICDD 01-086-0433 and a Diopside like $Ca_{0.89}$ $Mg_{1.11}$ $Si_{1.98}$ O_6 ICDD 01-072-1498. Instead, the glass with ZnO contains small amount of Gahnite ($ZnAl_2O_4$ ICDD 00-074-1136) and Willemite ($2ZnO\ SiO_2$ ICDD 09 00-800-9761). In this glass higher percentages of the crystalline phases are recorded, the decrease of the glassy phase being due to replacement of calcium and magnesium with zinc oxide and. In CMASZn4, $CaAl_2Si_2$ ICDD 00-036-1342 and $Mg_2(Si_2O_6)$ ICDD 01-086-0433 are also observed.

In tables 3.9.4.1 and 3.9.4.2 the results obtained from Rietveld R.I.R method (quantification of phases analysis and the Rietveld parameters) are summarized together with the CTE values for the obtained glass ceramics at 1100°C (error within the range $\pm 0.10 \cdot 10^{-6}$ $°C^{-1}$).

SAMPLE GLASS ID	CMAS4 basic glass	CMASTi4	CMASMn4	CMASZn4
Anorthite	41.75	51.73	31.08	29.98
Augite	18.21	21.49	15.47	13.77
Diopside aluminian	-	4.12	5.33	5.04
Wollastonite-2M	2.11	-	-	-
Clinopyroxene	1.26	-	-	-
Clinopyroxene titanium aluminian	-	2.37	-	
$Ca(Al_2 Si_2 O_8)$	-	1.98	-	2.51
$Mg_2(Si_2O_6)$	0.97		2.64	1.43
Diopside manganoan	-	2.55	2.44	-
$Ca_{0.89}$ $Mg_{1.11}$ $Si_{1.98}$ O_6	-	-	3.19	-
Gahnite	-	-	-	1.94
Willemite	-	-	-	0.99

Table 3.9.4.1 Quantification of phases using Rietveld R.I.R method for CMAS4glass series.

SAMPLE GLASS ID	GLASS	χ^2	R_F^2	w_{rf}	r_p	α *(200-500°C) (°C^{-1})*	α *(200-100°C) (°C^{-1})*
CMAS4 basic system	19.35	1.122	0.274	0.166	0.552	$8.24 \cdot 10^{-6}$	$8.13 \cdot 10^{-6}$
CMASTi4	23.58	1.397	0.563	0.694	0.108	$8.33 \cdot 10^{-6}$	$8.61 \cdot 10^{-6}$
CMASMn4	52.47	1.674	0.442	0.227	0.237	$8.39 \cdot 10^{-6}$	$8.11 \cdot 10^{-6}$
CMASZn4	61.20	1.339	0.117	0.710	0.337	$8.78 \cdot 10^{-6}$	$8.15 \cdot 10^{-6}$

Table 3.9.4.2 CTE values for main formed phases and Rietveld R.I.R. for CMAS4 glass series.

The CTE values of glass ceramics are in agreement with those of the corresponding glasses with only a slightly increase observed. Therefore, we can conclude that also glass ceramics belonging to these systems possess good features to be used as sealants for SOFC.

SEM micrographs reported below (Figures 3.9.4.5 - 3.9.4.8) confirm that the nucleating agents play an important role in phase formation.

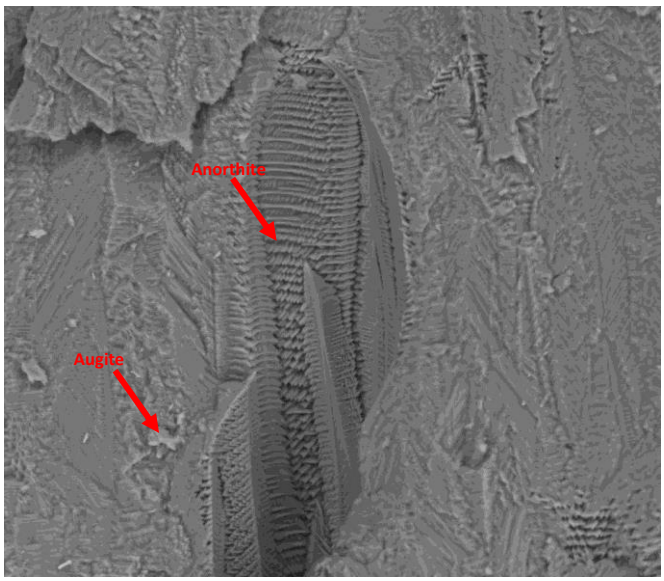

Figure 3.9.4.5 SEM micrograph of CMAS4 basic glass crystallized at 1100°C for 1h.

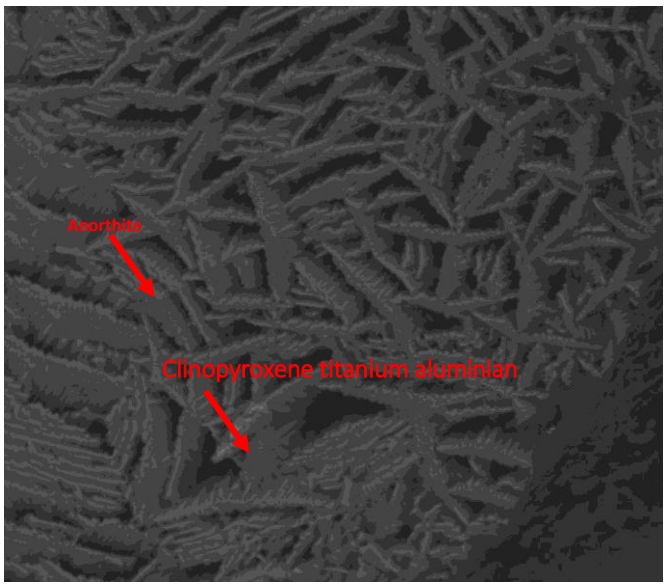

Figure 3.9.4.6 SEM micrograph of CMASTi4 glass crystallized at 1100°C for 1h.

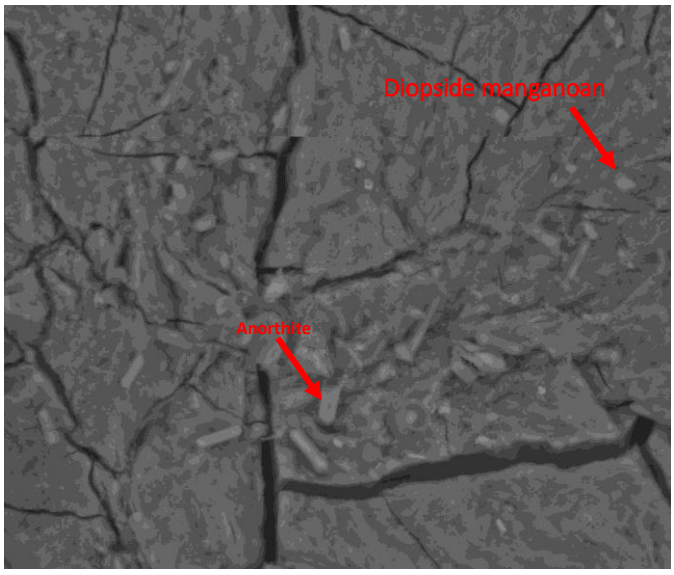

Figure 3.9.4.7 SEM micrograph of CMASMn4 glass crystallized at 1100°C for 1h.

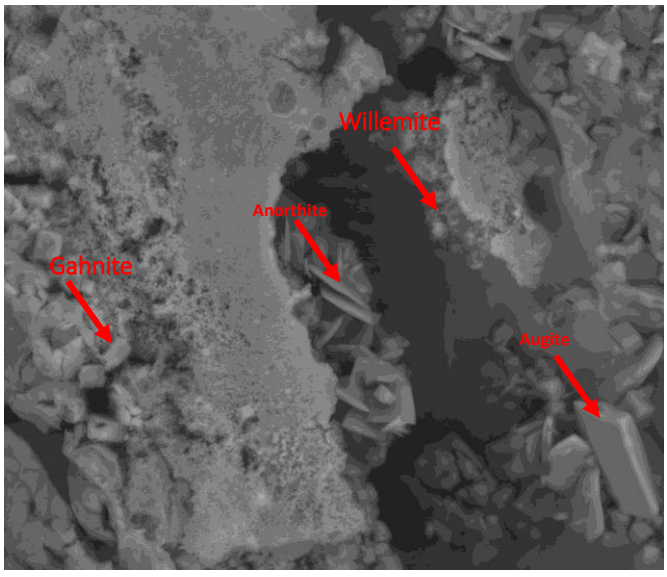

Figure 3.9.4.8 SEM micrograph of CMASZn4 glass crystallized at 1100°C for 1h.

In CMAS4, the arrangement of coexisting Diopside and Anorthite is confused with the glass phases. With the addition of TiO_2, the crystalline phases show a sheet shape with neat arrangement, high crystallinity and large crystal size. In CMASMn4, MnO_2 tends to promote the formation of crystal arrangements with strip-like shape and low crystallinity. The ZnO presence contributes to the formation of a quite different microstructure, the flaky crystals (Gahnite) with small size interwined stack together and more small grains (Willemite) between

flaky crystals, which result from volumetric crystallization and the anisotropy of crystal growth. These findings are consistent with the crystallization kinetics and XRD results.

We can conclude that the thermomechanical behavior of the parent glass and the crystallized materials are very similar, ensuring the absence of stresses during the ceramization process. All the compositions investigated belong to the region of glass formation in the ternary phase diagrams (Figure 3.9.4.9) where pyroxenes (e.g. Diopside) or Anorthite are more stable.

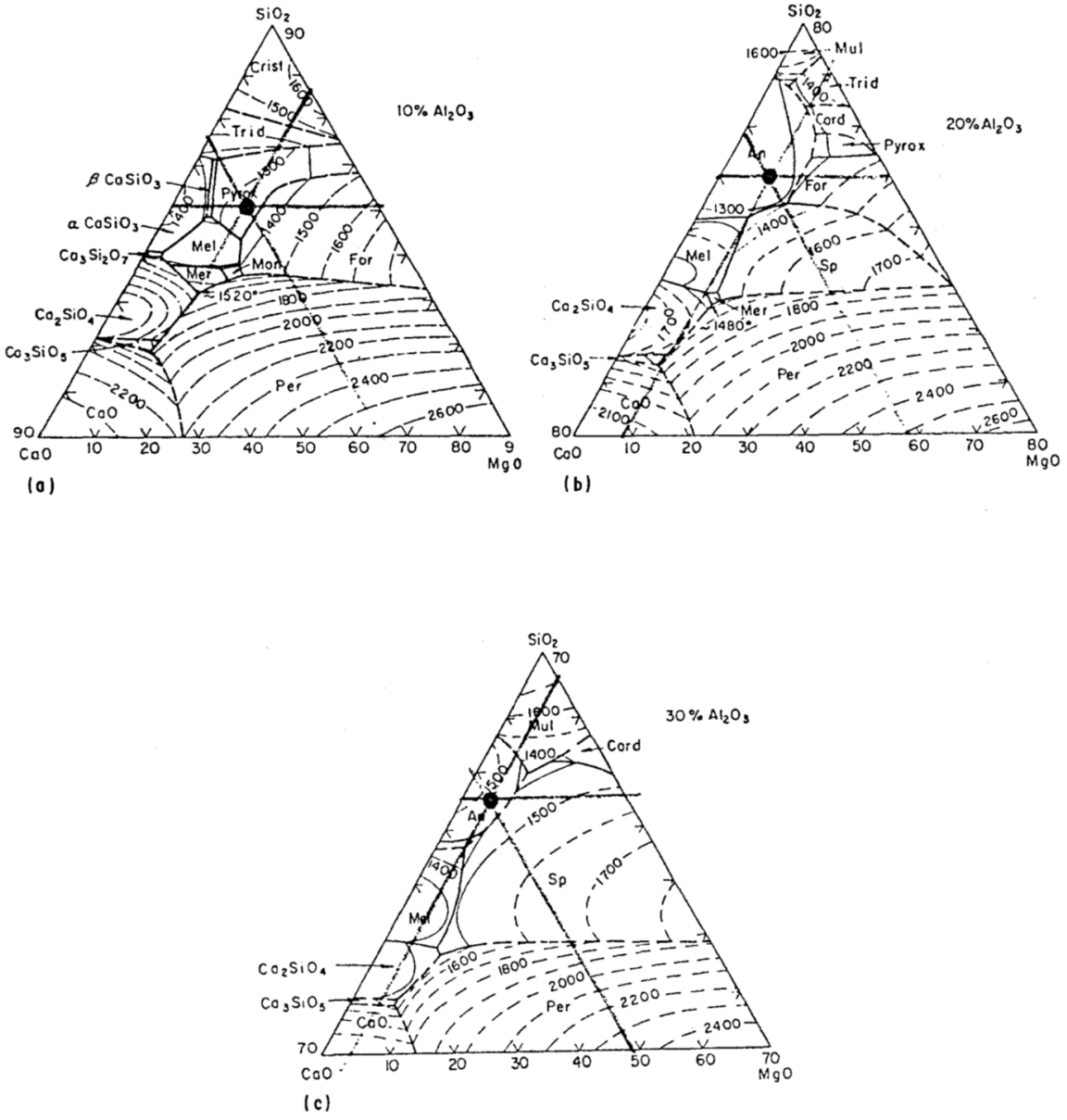

Figure 3.9.4.9 Phase diagrams of the system CaO-MgO-SiO_2 at different Al2O3 contents: a) Al_2O_3 36.78wt%, b) Al_2O_3 19.45wt% and c) Al_2O_3 14.44wt%.

The composition of the residual glassy phase suggests that the crystal phases are mainly controlled by the ratio MgO/Al_2O_3.

The crystals have a slightly higher density than the parent glass, suggested by the presence of interlocking crystals with a homogeneous distribution and a circular cavity inside.

Chapter 4

Synthesis and characterization of Borosilicate glass ceramics (CMASB) and their variants containing TiO_2, MnO_2, ZnO and SnO_2

In the second part of this research work, we turn to analyze a system modified by the presence of a further network former oxide, B_2O_3. The aluminoborosilicate (CMASB) glasses play an important role in glass technology, mainly because B_2O_3 decreases the glass viscosity, the network rigidity and the characteristic temperatures T_g and T_s [222-223-224-225-226]. The decrease in T_g and T_s can be understood as follows: a pure B_2O_3 glass has a low T_g (~275°C) due to its planar trigonal structure and B_2O_3 increases non-bridging oxygen containing silicate structural units and trigonal boroxyl groups. These structural change decrease the glass network connectivity and thus T_g and T_s. The interest in the study of borosilicate glasses is related to their good thermophysical properties, but the presence of B_2O_3 in the glass composition has also one important drawback: B_2O_3 tends to form volatile compounds with water vapor leading to seal degradation [36]. Of the components of potential sealing glasses, boron is of particular interest due to its desirable effect on the viscosity of glass, which is critical for the joining process [227]. On the other hand, the volatilization of boron-containing species restricts its application as a main component for SOFC sealing applications. Glasses with B_2O_3 as the only glass former have shown up to 20% weight loss under humidified H_2 environment and extensive interactions with cell components materials both in air and wet fuel gas [228]. Thus, high amount of B_2O_3 in a sealant is not recommended. For a seal glass, two main aspects of chemical stability should be considered: vaporization of the seal glass itself and its chemical interaction with oxidizing and reducing atmospheres.

Vaporization changes glass composition and overall network structure, and can adversely affect the desired thermal, mechanical, and electrical properties. Alkali oxides and B_2O_3 have a higher tendency to vaporize at SOFC operating temperatures due to their high vapor pressures.

Generally, alkaline earth oxides, rare earth metal oxides, and Al_2O_3 do not vaporize appreciably from a seal glass [60-169-229] and pure silica glass does not vaporize in dry air at the temperatures of interest, due to its low vapor pressure. However, SiO_2 in a silicate glass can vaporize in a wet atmosphere due to formation of $Si(OH)_4$ species [88]:

$$SiO_2 + 2H_2O = Si(OH)_4 \quad (4.1)$$

Water can exist in hydroxyl (OH^-) form, depending on water concentration and composition of the glass under examination [230-231]. In silicate glass, the interaction with water can break Si– O–Si network bonds and create siloxane (Si–OH) bonds [232-233]. The reaction rate of a silicate glass with water decreases when alkali oxides are replaced by alkaline earth oxides [232]. Vaporization of silica in a wet hydrogen atmosphere has also been reported [234]. A silica glass reacts with H_2 and H_2O and forms SiO and $Si(OH)_4$ species at 1000°C, respectively [235]. Generally, the $Si(OH)_4$ species dominates. The vapor transport of $Si(OH)_4$ species is linearly dependent on time. BaO- and Na_2O-containing silicate glasses tend to interact with water and to form silica-rich secondary phases [236-237]. For a Na_2O–silicate glass, T_g decreases steeply from ∼450 to ∼250°C as water content increases from 0 to 4 wt.% and then decreases gradually to ∼200°C as water content increases to 8 wt.% [230]. However, a MgO- and CaO-containing silicate glass does not show any silica loss in a wet reducing atmosphere at high temperatures [235]. Alkali oxide containing borate glass and borosilicate glass are prone to vaporization. Such glasses vaporize in the form of gaseous borates and alkaline metaborates [238]. Na_2O vaporizes from an alkaline oxide containing silicate seal glass at 750°C [239] and a sodium borate glass at 1000°C with as much as 13 wt.% loss [240]. Vaporization of B_2O_3 from a seal glass is more pronounced in the presence of water [229-239]. When a glass is free of alkali oxides, B_2O_3 reacts with water, forms HBO_2 gaseous species, and breaks the glass network [241]. When a glass contains alkali oxide(s), boron vaporization occurs in the form of RBO_2 (R = Na, K) and $B(OH)_3$ species [242]. Consequently, T_g of a glass can increase by 50–100°C because of the B_2O_3 content decrease and hydroxyl group formation [241-243]. Vaporization of BO_2 species from a CaO–SrO–ZnO–B_2O_3–Al_2O_3–TiO_2–SiO_2 seal glass increases with temperature and square root of time [229]. After thermal treatment at 800°C for 168 h, the weight loss due to gaseous $B_3H_3O_6$ vaporization increases from 0.16 to 0.98 mg/cm^2 when the atmosphere is changed from oxidizing to 30% H_2O reducing atmosphere. The weight loss of this glass increases from 0.03 to 0.16 mg/cm^2 as the B_2O_3 content increases from 2 to 20 mol% [229].

In this chapter, a systematic study of five different systems is presented, namely a basic composition CMASB and four glass containing B_2O_3 and a nucleating agent, respectively TiO_2, MnO_2, ZnO and SnO_2.

4.1 Chemical compositions

Glasses belonging to the CMAS3 series (see chapter 3) has been taken as starting material for the boroaluminosilicates, obtained by replacing a given amount of SiO_2 with B_2O_3. For the borosilicate glasses, the chemical composition has been investigated using inductively coupled plasma (ICP-OES). This method enables a quantitative analysis of the main elements (> 1 wt.%) with a relative experimental error of ± 3 %, while minor elements (> 0.1 %) and impurities (> 0.01 %) are detected with larger errors of 10 to 20 %. The results obtained for the five boroaluminosilicates as reported in table 4.1.1.

Sample ID	SiO_2 (%)	B_2O_3 (%)	Al_2O_3 (%)	CaO (%)	MgO(%)	TiO_2 (%)	MnO_2 (%)	ZnO (%)	SnO_2 (%)	Impurities (%)
CMASB 1	39.89	12.00	14.45	30.69	2.51	-	-	-	-	0.46
CMASBTi1	38.89	12.00	14.45	26.21	2.51	4.49	-	-	-	1.05
CMASBMn1	38.89	12.00	14.45	26.21	2.51	-	4.49	-	-	1.05
CMASBZn1	38.89	12.00	14.45	26.21	2.51	-	-	4.49	-	1.05
CMASBSn1	38.89	12.00	14.45	26.21	2.51	-	-	-	4.49	1.05

Table 4.1.1 Chemical compositions of boroaluminosilicate glasses

The glasses under examination present a fixed ratio between the two network former SiO_2 and B_2O_3 ($\frac{SiO_2}{B_2O_3} = 3.3$). Based on this assumption, our aim is to evaluate how the B_2O_3 as network former affects the glass properties.In this kind of glass system, it is important to understand how the network former oxide, B_2O_3, can modify the properties of the aluminosilicate-based glasses. To this end, the attention has to be focused on the ratio SiO_2/B_2O_3 and on the structural units in which B_2O_3 exists. Indeed, in borosilicate glasses, the structural units can be boroxyl (B_3O_6), diborate (B_4O_9), pentaborate (B_5O_{10}), dipentaborate (B_5O_{12}), tetraborate (B_8O_{16}), metaborate (B_3O_6), pyroborate (B_2O_5) or orthoborate (BO_3). As reported in literature, the 4-coordinated borate structural units may be dominant for lower B_2O_3 content glass while the 3-coordinated borate structural units may be prevalent in higher B_2O_3 content glass. It has been demonstrated that when the $\frac{SiO_2}{B_2O_3}$ ratio is higher than 3, 4-coordinated borate units prevail in the glass network. S. Huang et al. [244] demonstrated from IR absorption spectra that the presence of B_2O_3 in this amount favours the formation of boroxyl rings and the transformation from [BO_3] triangles to [BO_4] tetrahedrons. However, the decrease in [AlO_4] and [SiO_4] units is associated with the increase of [BO_4] units and, as a consequence, it is difficult to identify the variation of the glass network rigidity. In all the studied glasses Al_2O_3 acts as network modifier $\left[\frac{(CaO+MgO)}{Al_2O_3} > 1\right]$. It must also be taken into account that the alkaline earth oxide in the borosilicate glasses may convert the boroxyl groups into three-dimensional borate groups. This phenomenon is known as “boron anomaly” and frequently affects the characteristic temperatures of the glasses, such as T_g and T_s. In our study, we will examine the effect of network modifiers in the presence of B_2O_3 on thermal properties. CaO-MgO-borosilicate glasses were reported to show exceptions compared to the normal trends exhibited by mixed alkaline earth oxide borosilicate glasses [245-246]. To complete the analysis of boroaluminosilicates, the influence of the nucleating oxides is also investigated.

4.2 Density, chemical resistance and particles size

Firstly, the density of glasses and glass ceramics obtained after heat treatment was evaluated for the series of boroaluminosilicates under exam.The results of Archimede’s test are listed in table 4.2.1.

SAMPLE GLASS ID	Density of glass (g/cm^3)	Density of glass ceramic (g/cm^3)	Molar volume (cm^3/mol)
CMASB	3.24	3.61	30.51
CMASBTi	3.01	3.22	31.97
CMASBMn	3.98	4.06	30.99
CMASBZn	3.41	3.69	31.27
CMASBSn	3.07	3.18	31.43

Table 4.2.1 Density of glass and glass ceramic belonging to the CMASB series.

The density of glasses is higher than CMAS. The corresponding glass ceramics also show a slightly increase of density. When subjected to chemical resistance tests in acid (HCl 5%) and basic (NaOH 5%) environments all the examined CMASB glasses do not show any visible alterations. These results indicate that all the examined compositions are suitable from the viewpoint of chemical corrosion resistance. We can then conclude that the presence of B_2O_3 does not compromise the chemical resistance properties. When considering the durability test in water, these types of glasses show sign of reaction. After only 15 minutes soaking, gas bubbles are visible on the surface and after a longer period of about three days the samples are covered by a white dusty layer. Hence, these glasses exhibit the same behavior recorded for CMAS glass series, suggesting that also in this case the high content of alkaline earth oxide like CaO leads to reaction. The XRD pattern (Figure 4.2.1) of the treated samples demonstrated the formation of hydrate and hydrate carbonate phases.

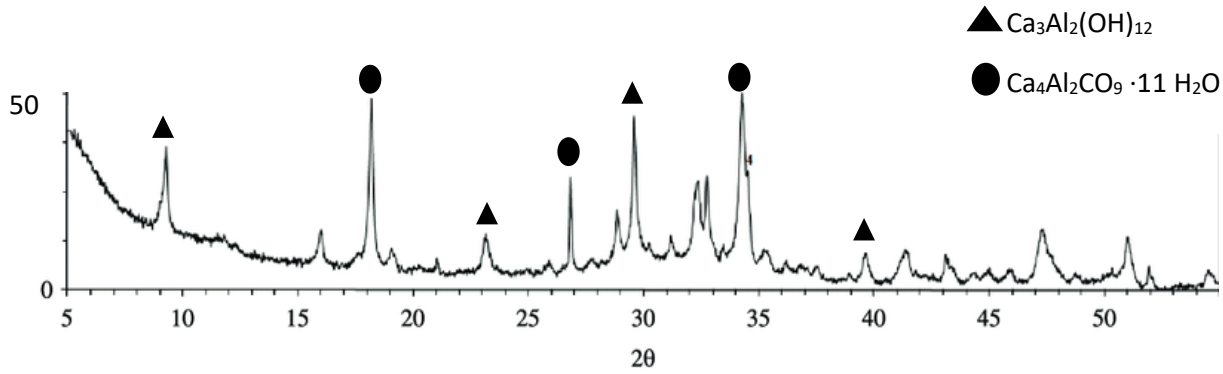

Figure 4.2.1 XRD pattern of treated samples with dusty layer.

This can be justified by the fact that alkaline earth elements, especially CaO, tend to easily form carbonates and the reaction goes faster when water is involved. According to the ISO 10545-3:1995 standard, the water absorption in air and under vacuum has been evaluated using the equations reported in Par.3.5.1. The so derived parameters such as open porosities, external volume and volume of closed and open pores, are summarized in the table 4.2.2 together with the apparent density in the fraction of sample with less easily refillable porosities.

Sample ID	E_b	E_v	V(cm^3)	p	V_0(cm^3)	V_1(cm^3)	T(g/cm^3)
CMASB	8,96	4,82	0,13	61,53	0,08	0,05	33,24
CMASBTi	6,81	3,72	0,24	29,16	0,07	0,17	31,05
CMASBMn	7,34	3,94	0,25	32,00	0,08	0,17	31,94
CMASBZn	5,16	4,52	0,16	56,25	0,09	0,07	28,42
CMASBSn	6,76	5,16	0,29	27,58	0,08	0,21	30,38

Table 4.2.2 Characteristic values calculated from the ISO 10545:1995 method.

These results show that no pronounced water absorption occurs for all samples, although it is higher than in CMAS glasses. The density values are in good agreement with the results obtained by the Archimede's method. As mentioned, the particle size distribution of the glass powders can affect the properties of the glasses. Hence, it is important to control the particle size distribution after subjecting the samples to a 2 h milling time. In figure 4.2.2 the size distribution of glasses belonging to the CMASB series are presented.

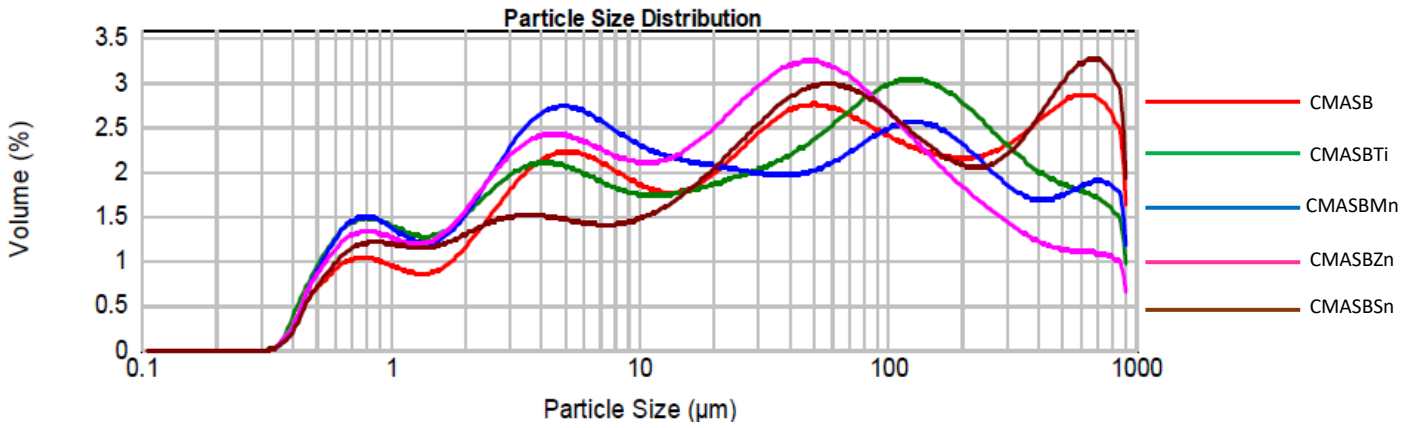

Figure 4.2.2 Particle size distribution of CMASB glasses.

The different hardness of the glasses explains the small differences recorded.

Typical resulting grains size are reported in the table 4.2.3 below.

GLASS SAMPLE	d(0.1) µm	d(0.5) µm	d(0.9) µm
CMSAB	2.194± 0.030	43.781± 0.030	536.097± 0.030
CMASBTi	1.392± 0.030	38.731± 0.030	392.894± 0.030
CMASBMn	1.452± 0.030	23.631± 0.030	399.541± 0.030
CMASBZn	1.580± 0.030	26.174± 0.030	261.057± 0.030
CMASBSn	1.780± 0.030	51.576± 0.030	576.570± 0.030

Table 4.2.3 Particle size distribution of the glass powders.

Considering the results of the grain size analysis, we conclude that the borosilicate glasses present higher hardness compared to CMAS glasses. With the exception of CMASBSn, the modified glasses exhibit low particle sizes compared to CMASB basic glass. Monitoring the glass particle size is essential because this property affects considerably the onset of crystallization. The size distribution is related to the surface area for nucleation and crystal grow.

4.3 Thermophysical and thermomechanical properties

In the following sections, the characteristic temperatures such as T_g, T_s and T_c of CMSAB glasses are discussed based on their effect on sealing glass performances. The influence of the B_2O_3 content can lead to significant changes compared to the results obtained for glasses belonging to the CMAS series. Generally, a decrease in T_g and T_s is expected under B_2O_3 addiction, but two different phenomena such as “boron anomaly” and “effect of combined ions” may change the overall network structure and then the properties of the glasses. Influence of the different oxides in the glass composition plays an important role on thermal properties, as discussed below. The sintering ability and the heat flow as a function of temperature were obtained by HSM and DTA measurements, respectively. As already done for CMAS glasses, the comparison between these two curves allows to understand the behavior of glasses during the heat treatment. In figures 4.3.1 - 4.3.5 the HMS curves and DTA thermograms at the heating rate of 15°C/min, are reported for the CMASB basic glass and for CMASBTi, CMABMn, CMASBZn and CMASBSn variants.

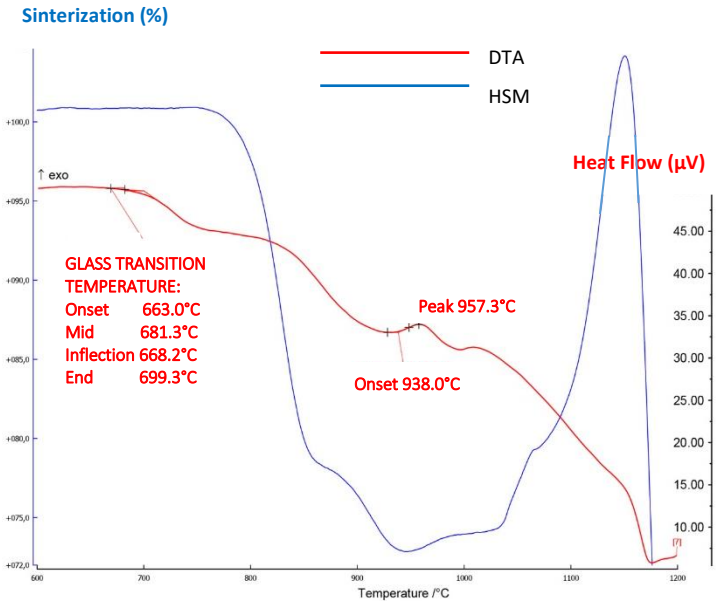

Figure 4.3.1 HSM and DTA curves on the temperature scale for basic glass CMASB1

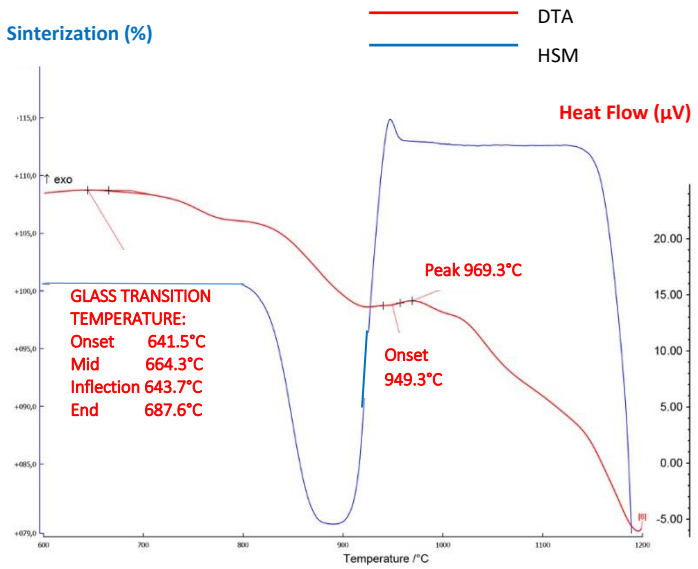

Figure 4.3.2 HSM and DTA curves on the temperature scale for CMASBTi

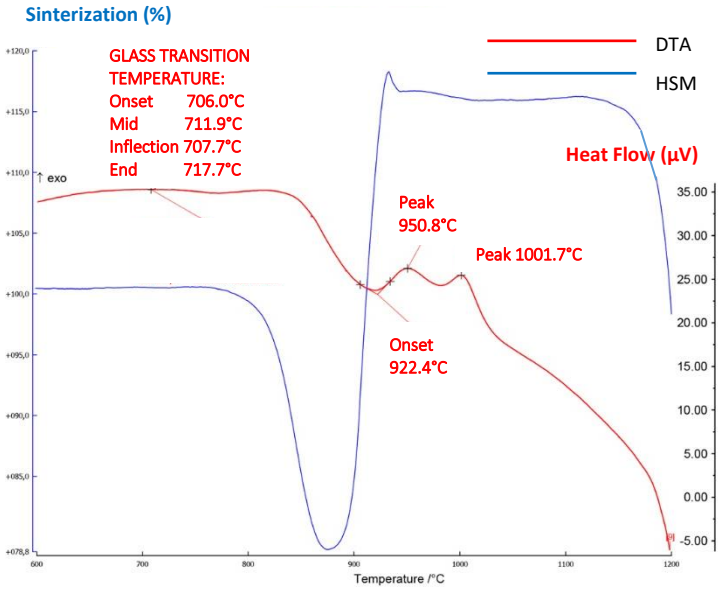

Figure 4.3.3 HSM and DTA curves on the temperature scale for CMASBMn

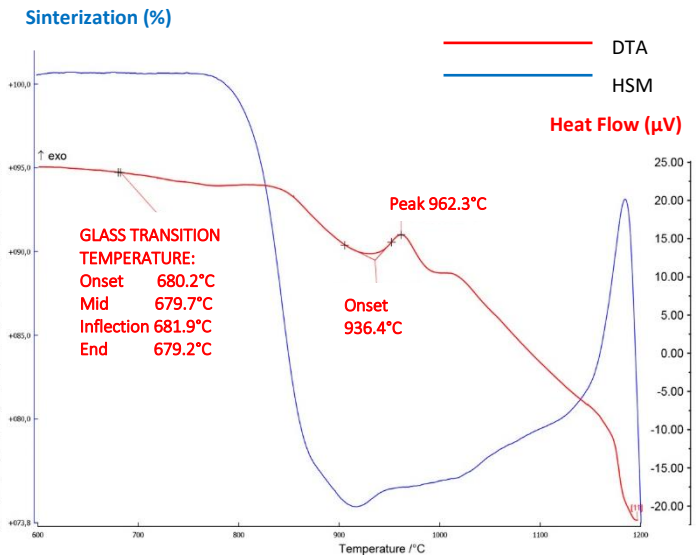

Figure 4.3.4 HSM and DTA curves on the temperature scale for CMASBZn

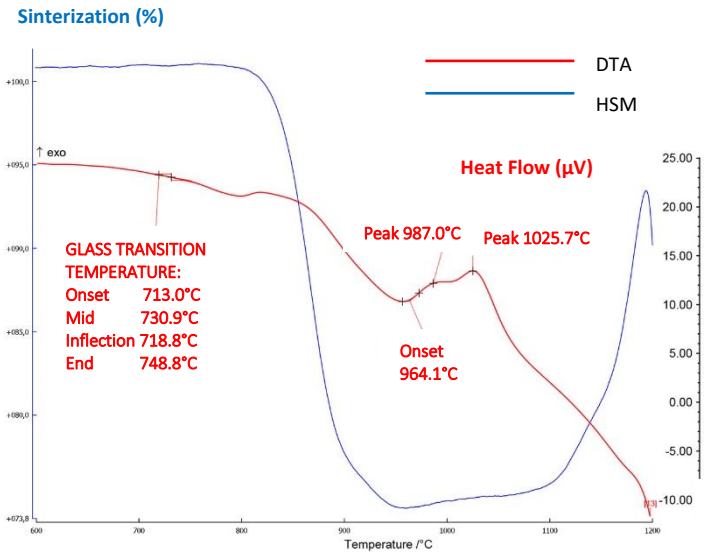

Figure 4.3.5 "HSM and DTA curves on the temperature scale for CMASBSn"

From the above reported curves, we can conclude that, except for CMASBSn, the first sintering temperature is lower than that recorded for glass belonging to the CMAS series. The same trend is found for glass transition temperatures, T_g. The characteristic temperatures of all glasses belonging to the CMASB series are listed in table 4.3.1.

GLASS SAMPLE ID	T_s (°C)	T_{FS}(°C)	T_{MS}(°C)	T_{HB} (°C)	T_F (°C)	T_g (°C)	T_c(°C)	T_o (°C)	T_{c1}(°C)	T_{o1} (°C)
CMASB	812	788	857	1183	1191	685	957.3	938.0	-	-
CMASBTi	838	810	872	1201	1205	647	969.3	949.3	-	-
CMASBMn	831	784	867	1210	1120	707	950.8	922.4	1001.7	-
CMABZn	827	793	897	1206	1211	670	962.3	936.4	-	-
CMABSn	851	817	932	1215	1222	728	987.0	964.1	1025.7	-

Table 4.3.1 Characteristic temperatures obtained by HSM and DTA tests.

Figure 4.3.6 shows the glass transition temperature trend for CMAS3 glass series and CMASB glass series.

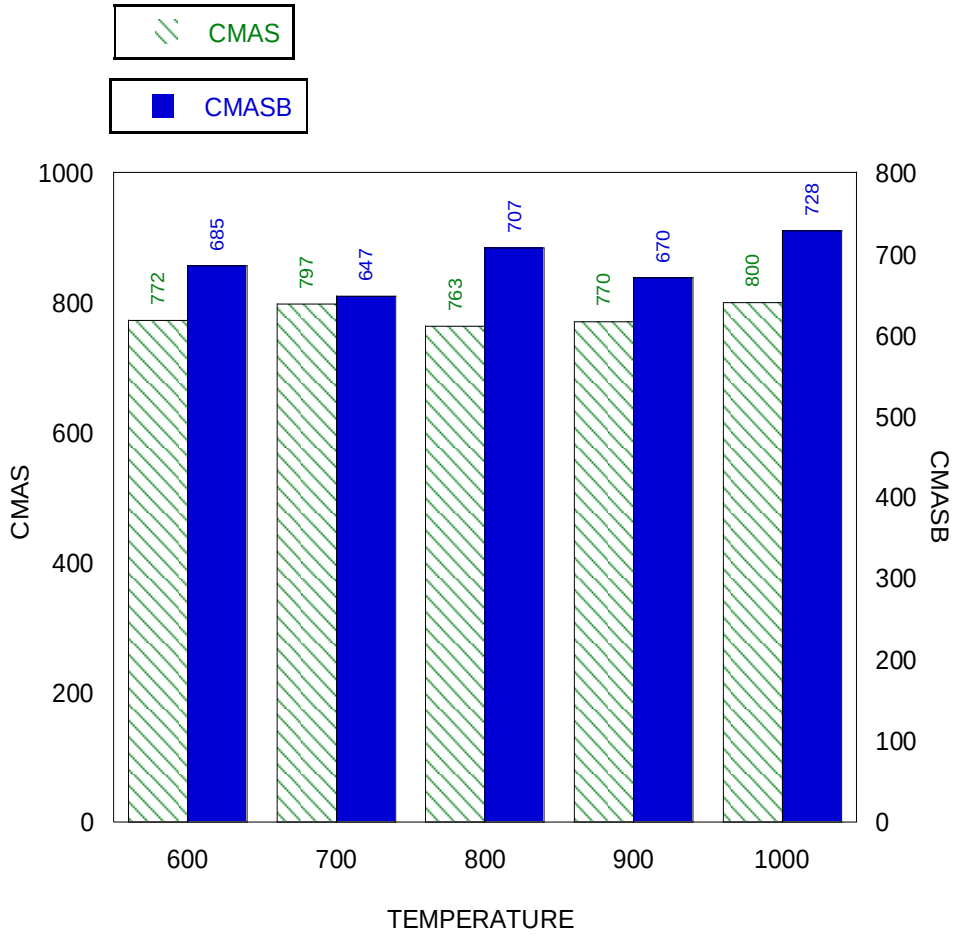

Figure 4.3.6 Glass transition temperature trend for the CMAS3 glass series and the CMASB glass series.

It is clear how the presence of B_2O_3 as network former decreases the T_g values due to the lower connectivity of the glass network.

The temperature range in which the maximum exothermic peak falls is rather different for the various glasses. Since in all the investigated glasses sintering is complete after the crystallization occurs, well-sintered and mechanically strong glass powders should be expected in the first stage of heat treatment. This property allows to suggest that these glasses are suitable candidates as sealants for SOFCs. The sintering ability parameter S_c ($S_C=T_C-T_{MS}$) [152] calculated for all CMASB glasses is significantly high. High S_c values indicate a delayed crystallization event, so allowing a wider processing window for a glass composition to attain maximum densification. Greater is S_c, the more independent are kinetics of sintering and crystallization. While the effect of B_2O_3 is to improve the sintering process, two exothermic less defined and broader peaks are observed in DTA thermograms. This behavior implies that the nucleating agents do not control the crystallization step.

From HSM curves a considerable expansion is observed for all glasses in the temperature range in which crystallization takes place (900-1000°C), which is generally an undesirable effect for sealing purposes.

From the data obtained, the glass stability for all samples has been calculated using the equations reported in Section 3.5.1 based on different models. All the results obtained for this series of glasses are presented in table 4.3.2.

GLASS SAMPLE ID	K_T	K_1	K_2	K_W	K_H	K_3
CMSAB	0,58	506	272,30	0,23	1,17	4,10
CMSABTi	0,54	558	322,30	0,27	1,37	5,02
CMSABMn	0,63	413	243,80	0,22	1,44	5,46
CMSABZn	0,55	541	292,30	0,24	1,18	5,70
CMSABSn	0,60	494	259,00	0,21	1,10	4,42

Table 4.3.2 Results of glass stability parameters for all the examined CMSAB glasses.

All the tested glasses exhibit a fairly good stability.

With regard to the K_2 parameter, high values are recorded when compared with the CMAS glass series, indicating that the crystallization is more difficult and that higher stability is exhibited during the formation. Unlike the CMASX (with X=nucleating oxides) series of glasses, the exothermic peak is broad even when a nucleation agent is added in the glass composition.

The values of K_W, K_H and K_3 are also higher than those found for CMAS glasses, because the melting starts first. The use of B_2O_3 as network former can issue problems due to high polarizability (low melting point). Indeed, in borosilicate glasses boroxyl rings mix with silicate tetrahedral units but borate tetrahedra do not, then the configurational entropy difference between silicate and borate tetrahedra induces phase separation.

B_2O_3 often decreases seal glass thermal stability by decreasing network connectivity and inducing phase separation. For borosilicate glasses, the presence of nucleating agents decreases the stability of glass forming in CMASBMn and CMASBSn, whereas stability increases in CMASBTi and CMASBZn.

As a result, the parameters, K_W and K_3, calculated for all glasses, fall within the range established in literature by Weinberg for simple glass systems , i.e. $0.1< K_W<0.5$ and $K_3>1.5$. The same remark could apply to K_H according to the Hruby interpretation (K_H must fall in the interval between 0.3 and 2..

To test the efficiency of the glasses belonging to CMASB series, the CTE must be then evaluated.

Generally, the CTE of an alkaline earth oxide containing silicate glass decreases with the SiO_2 content and increases with the B_2O_3 content [150-22-223]. The reason for the CTE increase with B_2O_3 content is twofold: the asymmetric structure of the planar boroxyl groups and the increase of non-bridging oxygens (decrease in network connectivity) in glasses [225-247].

However, the CTE of borosilicate glasses depends on $\frac{B_2O_3}{SiO_2}$ ratio [222-223-225].

As a rule, the CTE increases by ~ $1.0 \cdot 10^{-6}$ as the $\frac{B_2O_3}{SiO_2}$ ratio increase from 0.0 to 0.25, whereas a further increase of the $\frac{B_2O_3}{SiO_2}$ ratio to 1.5 does not change the CTE, probably because the B_2O_3 effect has leveled off. In the examined glasses, the $\frac{B_2O_3}{SiO_2}$ ratio is 0.31 and no significant change has been recorded in CTE values compared with CMAS glass series.

In figure 4.3.7 are reported the thermal expansion curves obtained for all glasses.

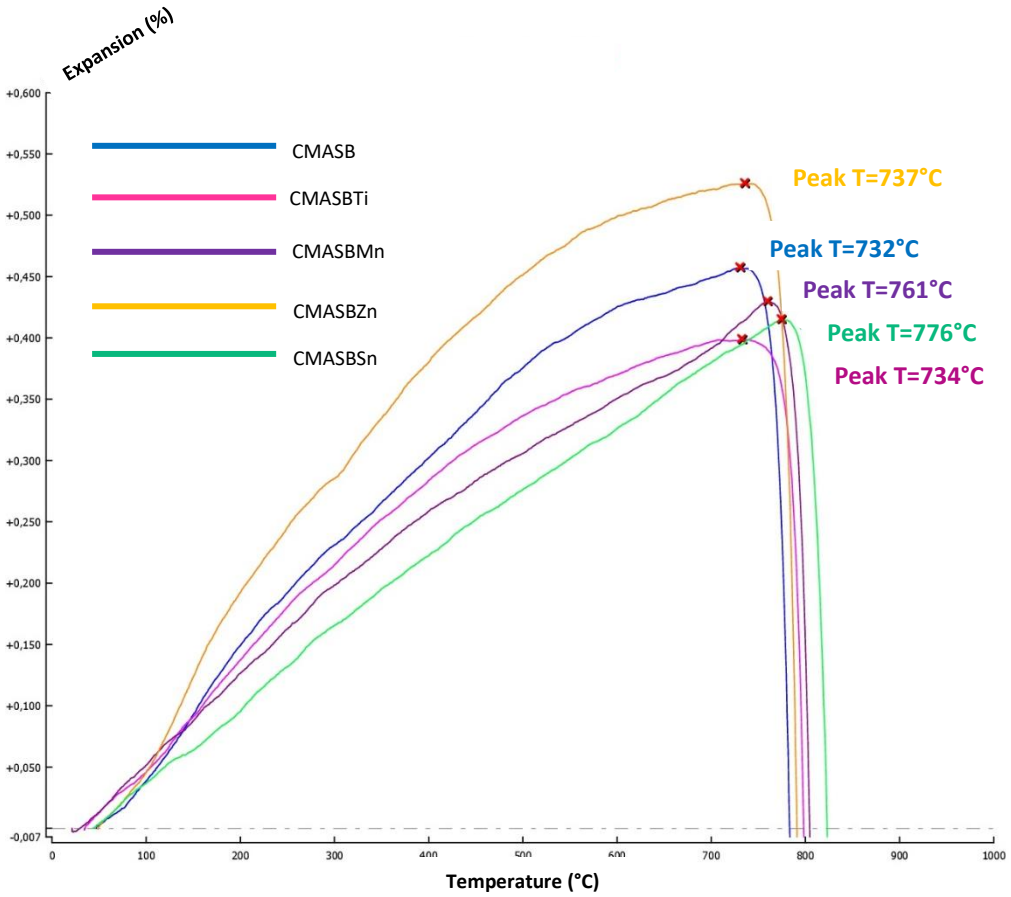

Figure 4.3.7 Thermal expansion curves obtained for all CMASB glass series.

In table 4.3.3 the CTE values recorded in the common temperature ranges of 200°C-500°C and 200°C-700°C are listed. The standard deviations for the reported CTE values are within the range $\pm 0.10 \cdot 10^{-6}$ °C^{-1}.

GLASS SAMPLE ID	$\alpha_{(200°-500°C)}$ (°C^{-1})	$\alpha_{(200°-700°C)}$ (°C^{-1})
CMASB basic system	$8.11 \cdot 10^{-6}$	$7.99 \cdot 10^{-6}$
CMASBTi	$8.21 \cdot 10^{-6}$	$8.07 \cdot 10^{-6}$
CMASBMn	$8.63 \cdot 10^{-6}$	$8.57 \cdot 10^{-6}$
CMASBZn	$8.42 \cdot 10^{-6}$	$8.51 \cdot 10^{-6}$
CMASBSn	$8.01 \cdot 10^{-6}$	$8.12 \cdot 10^{-6}$

Figure 4.3.3 CTE values recorded in the common temperature ranges of 200°C-500°C and 200°C-700°C for CMASB glass series.

From the above reported results, we can conclude that all the investigated glasses belonging to CMASB series could be suitable as sealant for SOFC. In particular the CTE values fall into the required range of 8.0 10^{-6} °C^{-1} to 12.0 10^{-6} °C^{-1} for sealing use.

As mentioned in Par.3.7, the viscosity of glasses has been calculated using Vogel-Fulcher-Tamman equation. As a rule, B_2O_3 is added in most glass compositions to decrease the viscosity. However, for sealing purposes the viscosity should be >10^9 Pa·s in order to provide hermetic sealing at the cell operating temperatures.

In Figure 4.3.8 the viscosity of the different CMASB glasses is reported as a function of temperature.

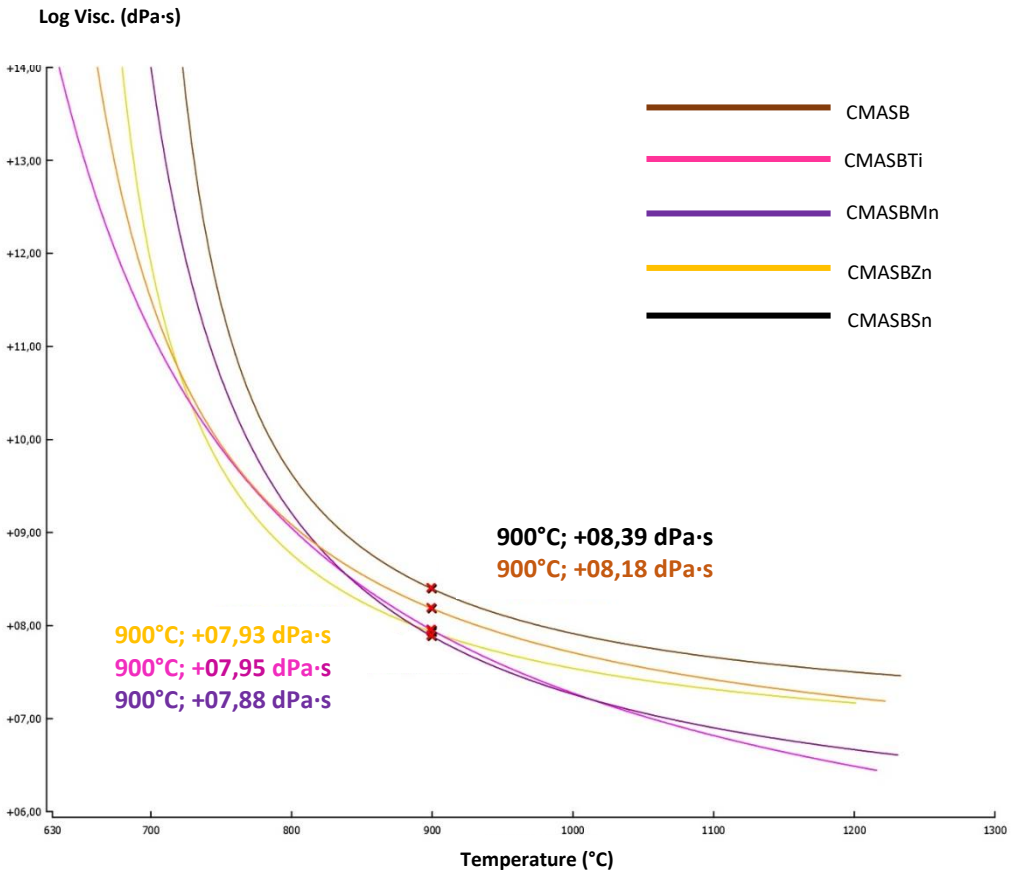

Figure 4.3.8 Viscosity of the different CMASB glasses as a function of temperature.

Calculated temperatures for dilatometric softening point T_d, softening point T_s and half ball temperature T_{HB} for the whole series of glasses are summarized in table 4.3.4 together with the viscosity expressed as $log\,\eta$ (η is given in dPa s) for the glasses at 900°C.

GLASS SAMPLE ID	T_D (°C)	T_S (°C)	T_{HB}(°C)	T_F (°C)	η (dPa s) T_S	η (dPa s) T_{HB}	η (dPa s) 900°C
CMASB basic system	732	812	1183	1191	8.62	7.19	7.93
CMASBTi	734	838	1201	1205	8.56	6.49	7.95
CMASBMn	761	831	1210	1220	8.66	6.63	8.01
CMASBZn	737	827	1206	1211	8.77	7.21	8.18
CMASBSn	776	851	1215	1222	8.83	7.48	8.39

Figure 4.3.4 Characteristic temperature and viscosity values at T_S, T_{HB}, and 900°C calculated for all the examined glasses.

Since the glasses viscosity at 900°C evaluated from the VTF equation is close to ~8.0 dPa s, we can deduce that glasses belonging to the CMASB series are suitable for sealing applications [248]. As recorded for aluminoslicate glasses, the viscosity varies between 6.0 and 9.0 dPa s, in the sealing range (700-900°C). Thus, all the glasses meet the η requirements for sealing.

In table 4.3.5 are presented the result for VFT constants deriving from the procedure described in Par. 3.7.

GLASS SAMPLE ID	A (kPa·s)	B (kPa·s·°C)	T_0(°C)
CMASB basic system	7,5	-0,16	626,82
CMASBTi	5,2	-0,08	481,72
CMASBMn	8,0	-0,29	622,97
CMASBZn	14,7	-0,30	731,08
CMASBSn	8,6	-0,22	674,45

Table 4.3.5 VFT constants for glasses belonging to CMASB series.

4.4 Crystallization kinetics

To fully understand how the presence of B_2O_3 as network formers can influence the properties of these potential glass ceramic seal for SOFCs, kinetics of crystallization must be analyzed. To this end, the same approach discussed in Section 3.8.1 for CMAS glass series has been followed.

The non-isothermal method has been used. The activation energy, E_a, for the crystallization process has been evaluated using the Kissinger modified by Matusita, Augis and Bennet and Afify equations.

DTA analysis has been performed at different heating rate of 5, 10, 15, 20, 30 and 50°C/min.

At low heating rates, the DTA thermogram presents more exothermic peaks during the heat treatment.

Figures 4.4.1 - 4.4.5 show the DTA results obtained from the glasses in the series CMASB, respectively CMASB parent glass, CMASBTi, CMASBMn, CMASBZn and CMASBSn.

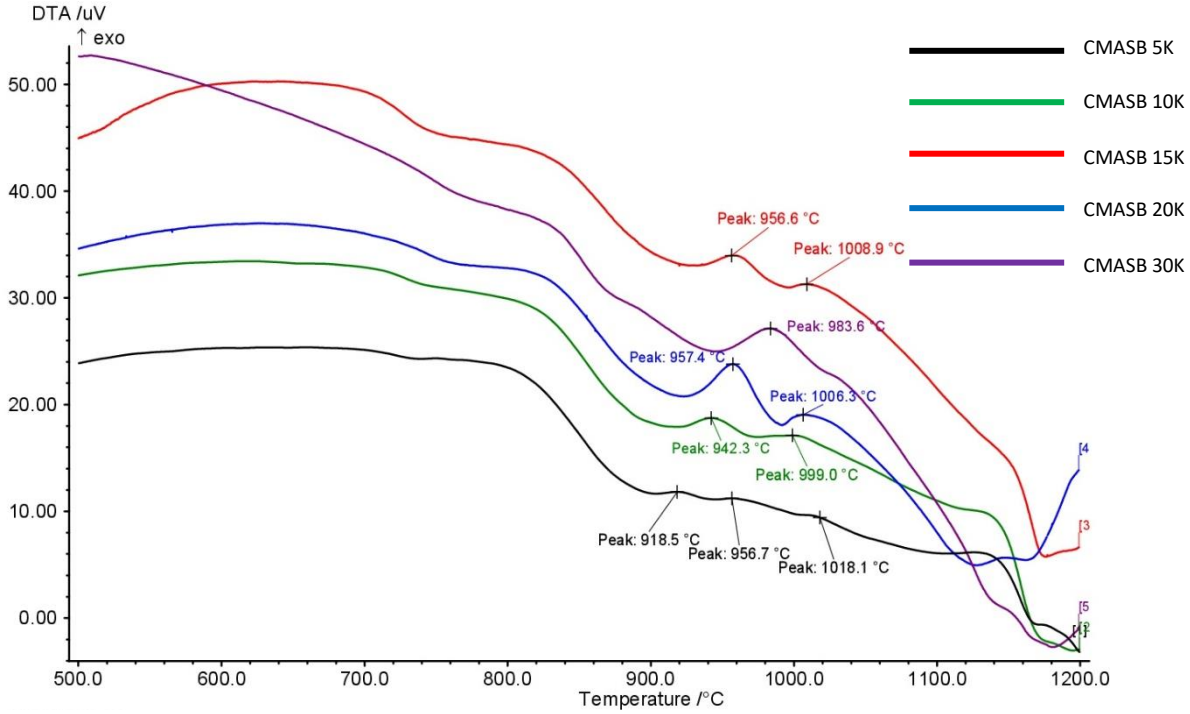

Figure 4.4.1 DTA curves of CMASB basic glass at different heating rates.

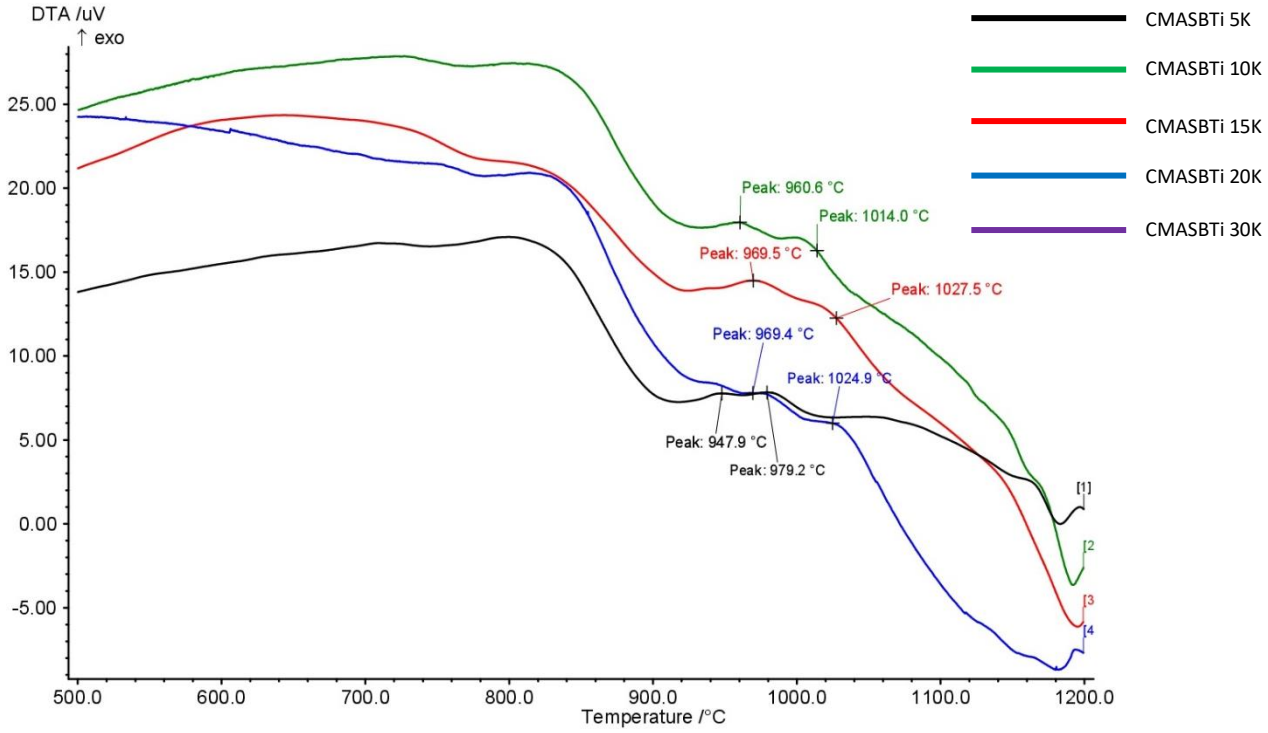

Figure 4.4.2 DTA curves of CMASBTi glass at different heating rates.

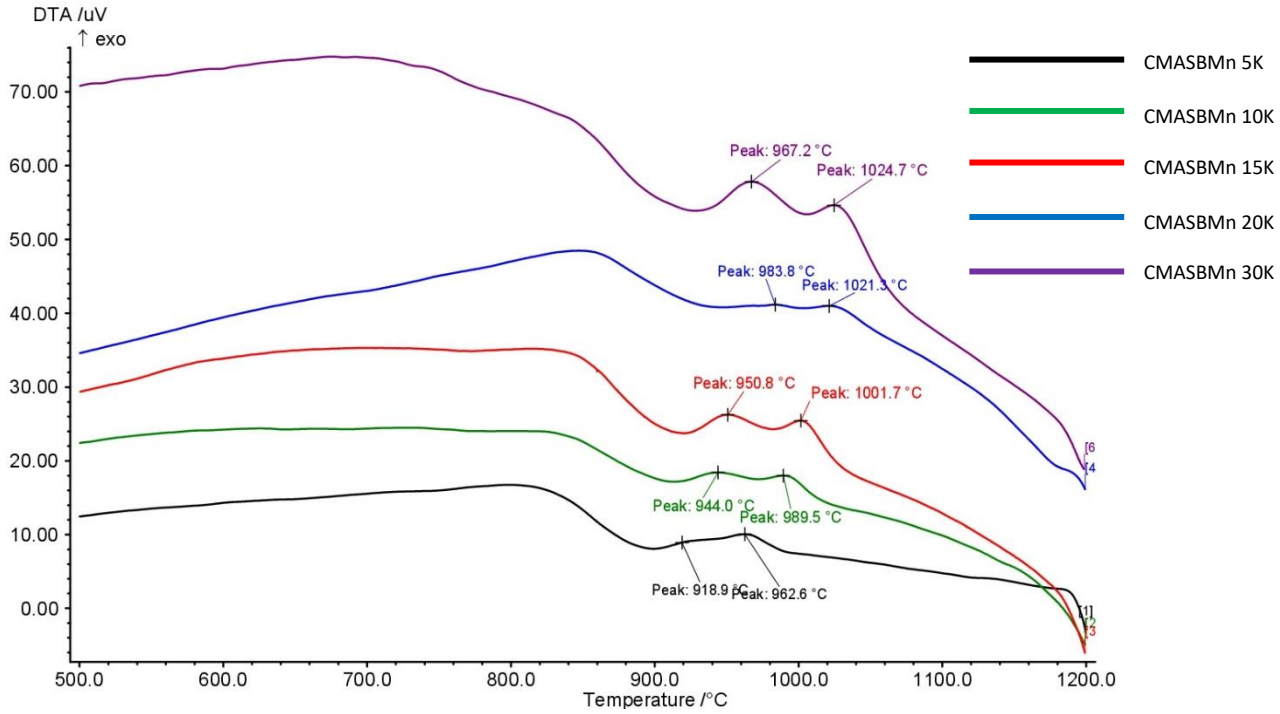

Figure 4.4.3 DTA curves of CMASBMn glass at different heating rates.

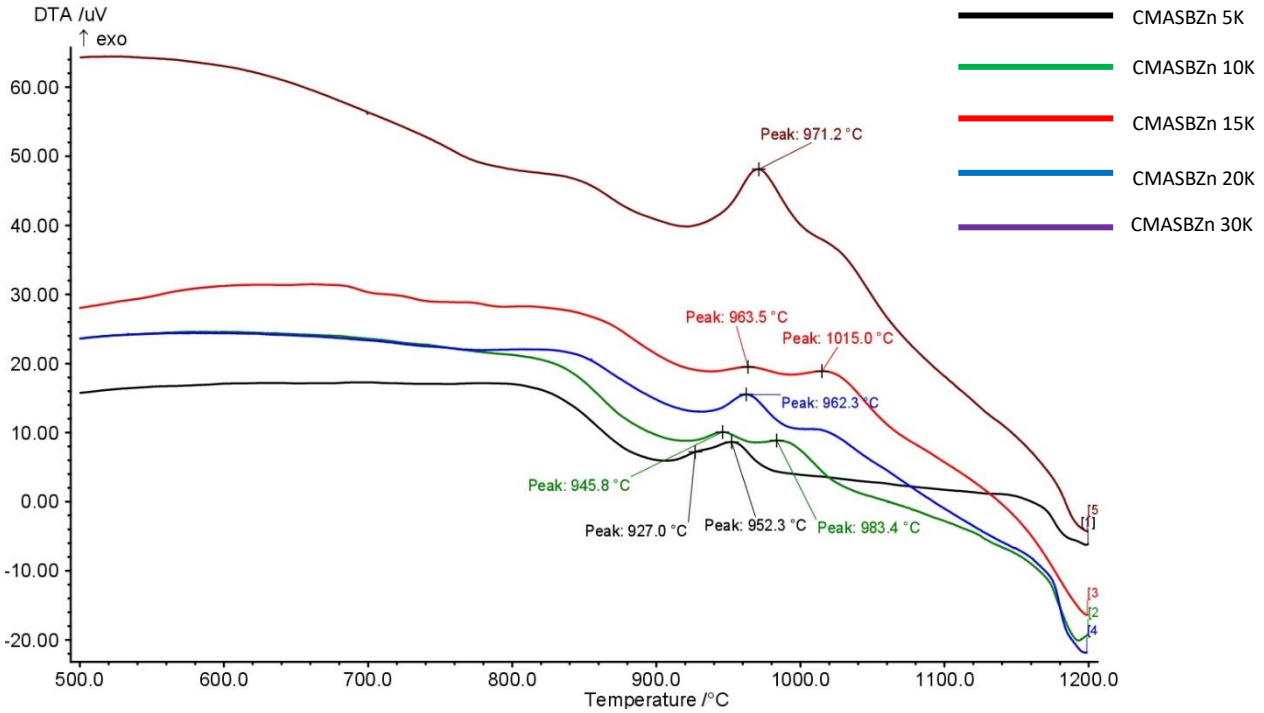

Figure 4.4.4 DTA curves of CMASBZn glass at different heating rates

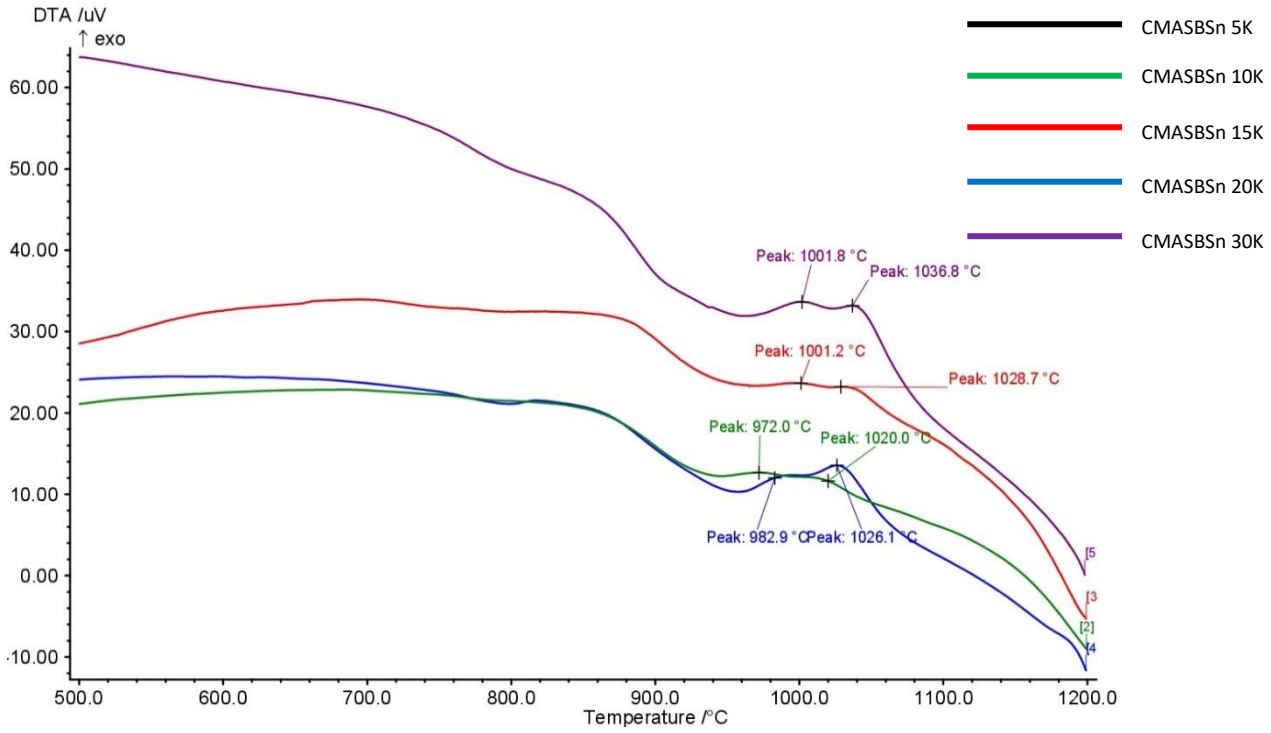

Figure 4.4.5 DTA curves of CMASBSn glass at different heating rates.

In all examined glasses, the DTA run performed at 50°C/min is not reported because the heating rate is too high to see a definite exothermic peak for the crystallization step.

DTA thermograms show that with decreasing the heating rate, the maximum temperature of the exothermic peak is moved towards low temperatures. Two exothermic peaks are recorded in all DTA runs.

In order to study the kinetics of crystallization the first exothermic peak has been considered for all the glasses. The results obtained for the basic and modified glass are very different compared with the CMAS glass series. Indeed, the addiction of nucleating agents do not affect significantly the thermograms, suggesting that the additive doesn't control and doesn't homogenize the crystallization process. In all DTA measurements, the exothermic peaks are broad and not well defined, especially at lower heating rate. Also in this series, CMASBSn exhibits the crystallization peak at higher temperature, around 1000°C. Generally, several phases grow in the same glass composition at different temperatures, and the mechanism are not necessarily the same for all phases. Similarly, the same phase appearing in different glasses can form under different mechanisms.

DTA data were analyzed in order to determine the crystallization parameters, i.e. the reaction order (*n*) and the activation energy (E_a) from the change in the crystallization peak temperature with the heating rate.

Based on the Ozawa method, the Avrami exponents for each glass can be extrapolated from the slopes of $ln[-ln(1-x)]$ against $ln\beta$ plots. Once obtained the calculated Avrami exponents (*n* and *m*), the activation energy is derived from the slopes of the plots reported below obtained by different methods summarized in table 4.3.4.

In table 4.4.1 are reported the results of Avrami exponents and the activation energies (E_a) for all the CMASB glasses.

GLASS SAMPLE ID	CMASB basic system	CMASBTi	CMASBMn	CMABSZn	CMABSSn
Avrami index, *n*	4	2	4	2	4
m	3	2	3	2	3
E_A (kJ/mol) Kissinger and Matusita	133.42±1.20	307.83±1.03	166.38±1.00	306.44±1.02	152.31±1.36
E_A (kJ/mol) Augis and Bennett	200.14±1.41	307.83±0.91	249.57±1.74	306.44±2.01	228.47±1.28
E_A (kJ/mol) Afify I	256.20±1.71	299.77±1.22	322.17±1.59	298.47±1.45	293.70±1.03
E_A (kJ/mol) Afify II	206.35±2.01	315.89±1.09	294.05±1.33	306.45±1.27	315.56±1.77
K_0	21.04	33.92	27.30	34.50	23.64

Table 4.4.1 Avrami exponents (n,m), crystallization activation energy (Ea) and k_0 of the glasses belonging to CMASB series.

As mentioned, the energy values recorded using the Augis and Bennet equation are seriously underestimated, probably because this method does not include the concept of nucleation and crystal growth during the heat treatment. In all glasses, the value of the activation energy tends to increase considerably if the nucleation factor is considered.

From the above reported results, we can conclude that the studied borosilicate glasses display a different behavior in comparison with the CMAS glass series.

The activation energy for the crystallization process of the basic system CMASB is lower that the modified glasses. Hence, the nucleation agents do not improve the beginning of crystallization, meaning that the intermediate oxides here considered delay the formation of crystals.

Usually, TiO_2, MnO_2, ZnO and SnO_2 are considered as nucleating agents, which contribute to promote phase separation and nucleation. It is then rather surprising that the E_a values of modified glasses are higher than that of the CMASB basic glass with no addition. A possible explanation for this phenomenon could be that, following the addition of TiO_2, MnO_2, ZnO and SnO_2, a large crystal nucleation density occurs during the isothermal hold. The crystal nucleus grows to a small extent because of the open glass network. Indeed, as mentioned, the presence of B_2O_3 in the glass tends to decrease the network connectivity forming non-bridging oxygens. This could lead to a situation where there is less Ti, Mn, Zn and Sn presence in the residual glass surrounding the nuclei. When the nucleation ends, a layer of the intermediate oxide is absent around the nuclei. Then crystal nuclei growth is suppressed because of the closed network and lower ions diffusion mobility, which is shown by the increase of E_a.

This effect is more evident for CMASBTi and CMASBZn glasses, because in these cases, the samples show a two-dimensional growth of crystals, and according to SEM image a bulk crystallization with a constant number of nuclei occurs. It is evident also the agreement between the results obtained for these glasses. For CMASBTi this behavior could be explained by the dual role of TiO_2 as a glass former and a modifier.

When TiO_2 exists as a network modifier, it has a lower field strength (1.25). When TiO_2 exists as a glass former, it has higher field strength (2.75). T_c and the activation energy for devitrification increase if TiO_2 participates in the glass network but decrease if it does not. It is not clear if this consideration could be attribute to MnO_2 oxide.

A different behavior is exhibited by CMASB basic glass and CMASBMn and CMASBSn, where three-dimensional growth of crystal is dominant and the number of nuclei tends to increase during the heat treatment.

Based on these assumptions, one-step crystallization is not suitable for modified glasses, because the addition of additives does not have the ability to promote this phenomenon.

If we compare the CMAS3 and CMASB basic glasses, the results obtained from activation energy evidence that CMASB is a better candidate for one-step crystallization.

Low value E_a for CMASB parent glass indicates that it can easily nucleated and crystallized, then Ca^{2+} and Mg^{2+} fast diffusion layer is forming.

The decrease in E_a with B_2O_3 addition may be attributed to the lower activation energy of viscous flow of B_2O_3 which allows to promote the crystallization process.

4.5 Phase content and microstructures of glass ceramic

Crystalline phases in the heat-treated samples are selectively analyzed using powder X-Ray diffraction.

All glass samples are previously heat treated in a furnace at six different temperatures for 3 hours.

The influence of B_2O_3 and nucleation agents has been tested using XRD spectra.

From the DTA curves discussed in the previous sections we have concluded that for all glasses the first exothermic peak is detected at about 950°C, so that a decreasing in the amorphous phase should be observed for samples thermally treated a T > 950°C. As mentioned, the B_2O_3 presence tends to delay the starting temperature of crystallization.

The same experimental procedure has been performed as reported in Section. 3.9.

In figures 4.5.1 - 4.5.5 (respectively CMASB basic glass, CMASBTi, CMASBMn, CMASBZn and CMASBSn) are reported the XRD patterns for all the examined glasses.

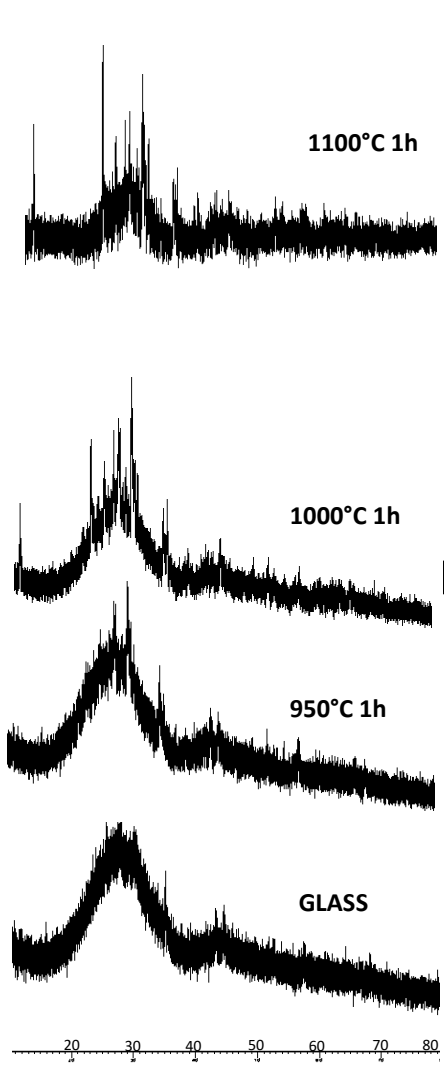

Figure 4.5.1 X-ray diffractograms of CMASB basic glass crystallized at different temperatures

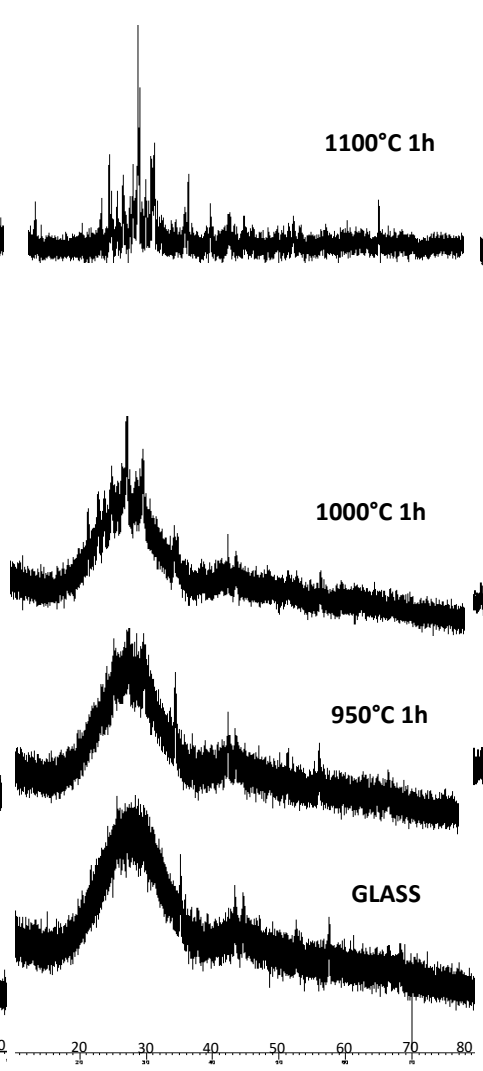

Figure 4.5.2 X-ray diffractograms of CMASBTi glass crystallized at different temperatures

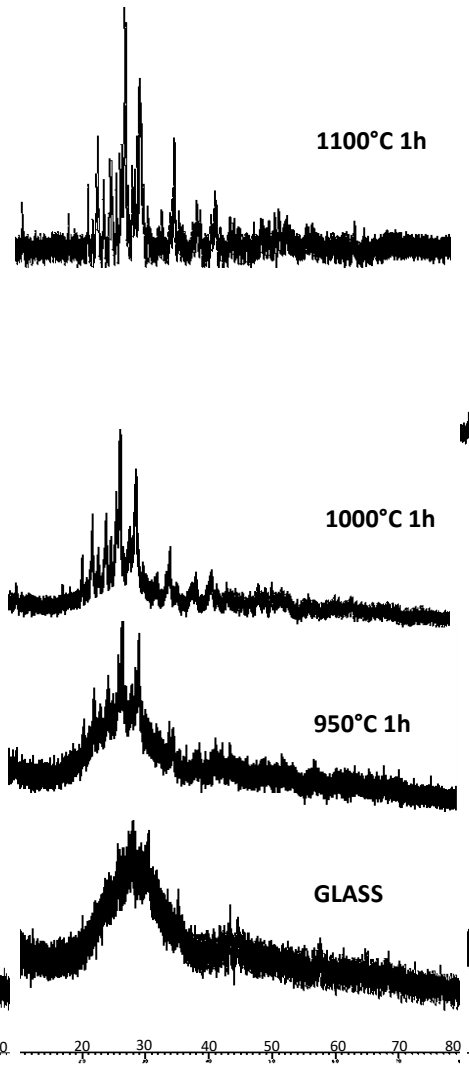

Figure 4.5.3 X-ray diffractograms of CMASBMn glass crystallized at different temperatures

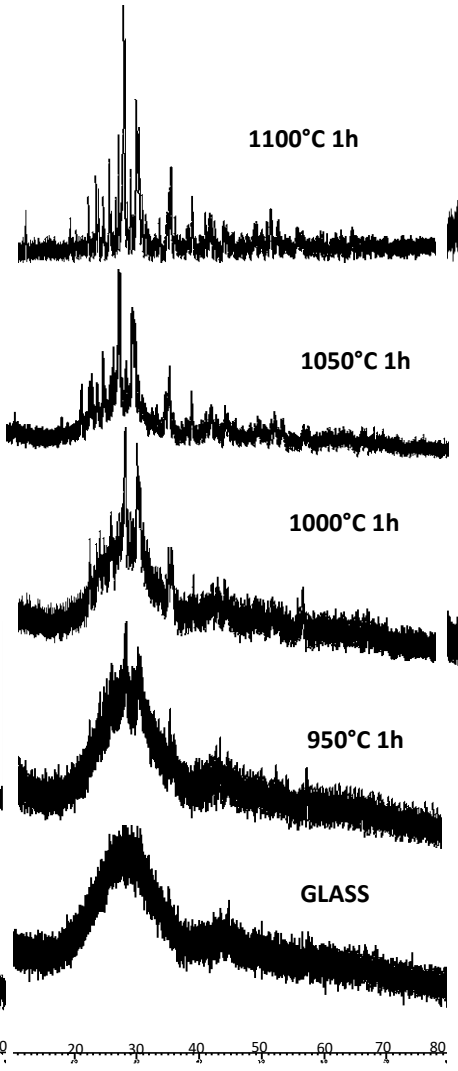

Figure 4.5.4 X-ray diffractograms of CMASBZn glass crystallized at different temperatures

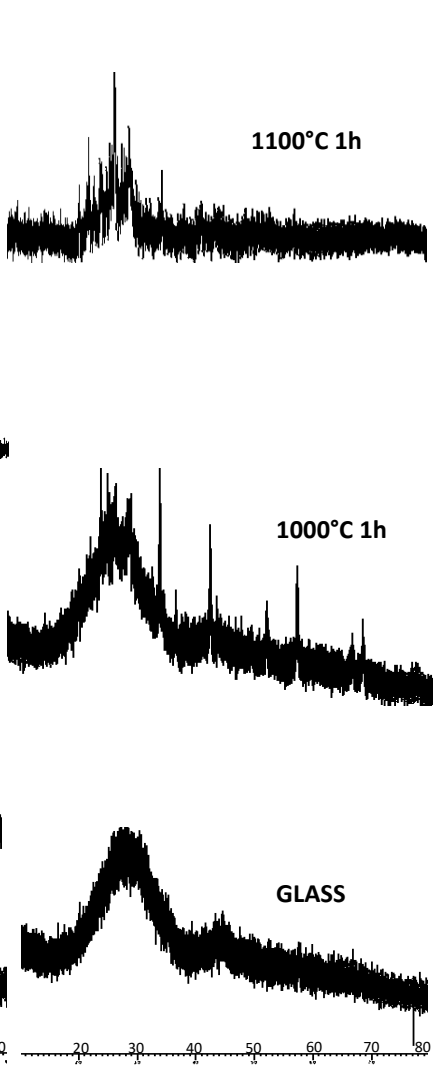

Figure 4.5.5 X-ray diffractograms of CMASBSn glass crystallized at different temperatures

From the above reported XRD patterns it is clear that a larger amount of glassy phase still remains after one hour at the holding temperature, so confirming the results obtained from DTA measurements. These glasses are too refractory and a long heating is required to obtain a homogeneous crystalline phase. The general study of glasses heated at different temperature between 900°C and 1100°C under standard heating programs indicated the formation of Anorthite ($CaAl_2Si_2O_8$ ICDD 00-041-1486) and Diopside ($CaMgSi_2O_6$ ICCD 01-075-1092) as main crystalline phases, similar to what we recorded for CMAS3 glass series. The relative amount of the two phases is dependent on both the final temperature and the glass composition, and on the influence of additives. In all glasses, the crystalline phases detected are similar, and the nucleation agents don't participate to phase formation. Minor phases detected for all glass ceramics are Augite aluminian (Ca (Mg, Fe, Al) (Si, Al)$_2$ O_6 ICDD 00-041-1483) and Wollastonite-1A ($CaSiO_3$ ICDD 00-027-1064). No other phases was detected. Then, the presence of a network former such as B_2O_3 does not modify the process of phases formation, the obtained results being in agreement with the CMAS3 glass series, and it does not take part to the phase formation step. Crystallization starts at around 950°C and is enhanced by increasing the temperature near to 1000°C, resulting in the formation of Anorthite as a major phase, and Diopside as secondary phase. In table 4.5.1 and 4.5.2 are reported the results obtained from Rietveld R.I.R method (quantification of phases analysis and the Rietveld parameters) together with the CTE values for the obtained glass ceramics at 1100°C (error within the range $\pm 0.10 \cdot 10^{-6}$ °C^{-1}).

SAMPLE GLASS ID	CMASB basic glass (%)	CMASBTi (%)	CMASBMn (%)	CMASBZn (%)	CMASBSn (%)
Anorthite	17.52	24.34	26.31	31.21	15.91
Diopside	4.21	7.46	8.99	12.57	4.77
Augite aluminian	3.99	6..77	4.14	3.11	0.87
Wollastonite-1A	1.23	2.19	1.62	1.50	0.21

Table 4.5.1 Quantification of phases using Rietveld R.I.R method for the glasses belonging to CMASB series.

SAMPLE GLASS ID	GLASS (%)	χ^2	R_F^2	w_{rf}	r_p	α (°C^{-1}) (200-500°C)	α(°C^{-1}) (200-700°C)
CMASB basic system	71.24	1.102	0.271	0.206	0.473	$8.27 \cdot 10^{-6}$	$8.12 \cdot 10^{-6}$
CMASBTi	57.21	1.447	0.412	0.594	0.176	$8.39 \cdot 10^{-6}$	$8.34 \cdot 10^{-6}$
CMASBMn	61.98	1.391	0.673	0.317	0.391	$8.81 \cdot 10^{-6}$	$8.89 \cdot 10^{-6}$
CMASBZn	49.30	1.007	0.114	0.244	0.388	$8.79 \cdot 10^{-6}$	$8.73 \cdot 10^{-6}$
CMASBSn	78.10	1.377	0.286	0.193	0.211	$8.33 \cdot 10^{-6}$	$8.51 \cdot 10^{-6}$

Table 4.5.2 CTE values for the main phases formed and Rietveld R.I.R. for the glasses belonging to CMASB series.

As see for CMAS glass series, the CTE values of glass ceramics are comparable to those of the corresponding glasses but a slightly increase is observed, due to the formation of the same main phases.

This suggests that also these glass ceramics possess good features to be used as sealants for SOFC, the CTE values respecting the limit for sealing application ($8.00 \cdot 10^{-6}$ °C^{-1} - $12 \cdot 10^{-6}$ °C^{-1}). The main microstructural changes for boron oxide containing glasses to final glass ceramics are evident in SEM images (Figure 4.5.6 - 4.5.10 respectively CMASB basis glass, CMASBTi, CMASBMn, CMASBZn and CMASBSn).

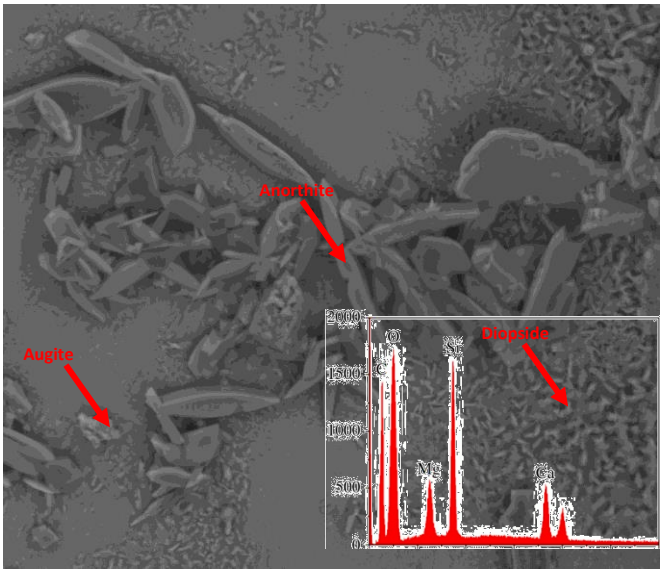

Figure 4.5.6 SEM micrograph of CMASB basic glass crystallized at 1100°C for 1 h and EDS spectrum of Diopside.

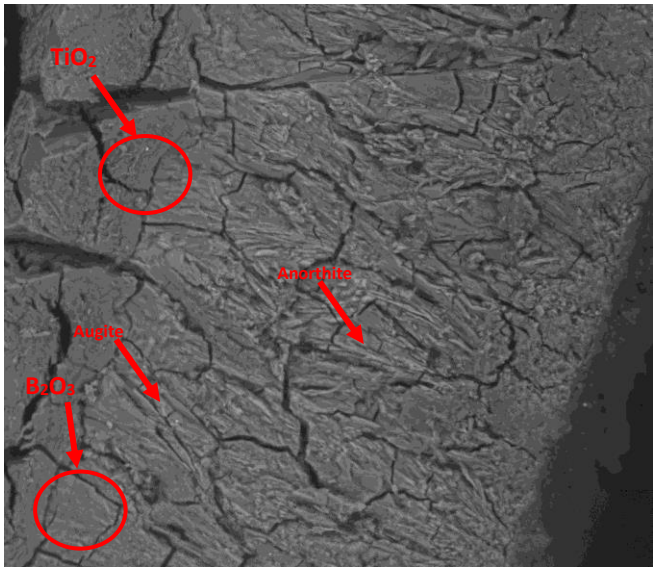

Figure 4.5.7 SEM micrograph of CMASBTi glass crystallized at 1100°C for 1 h.

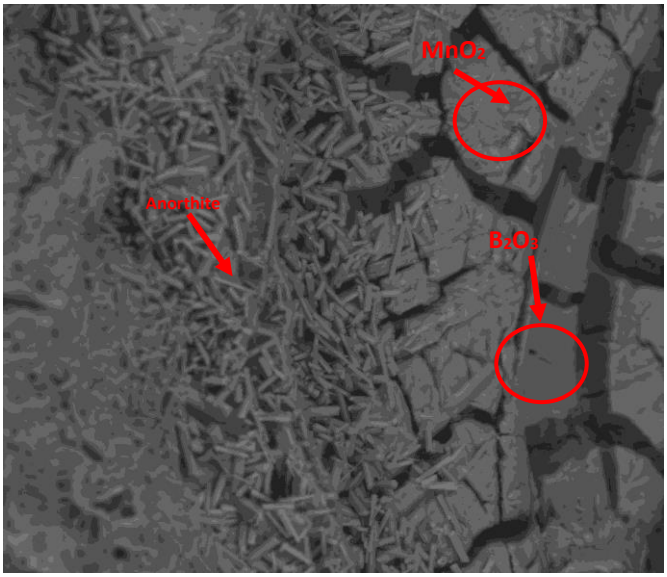

Figure 4.5.8 SEM micrograph of CMASBMn glass crystallized at 1100°C for 1 h.

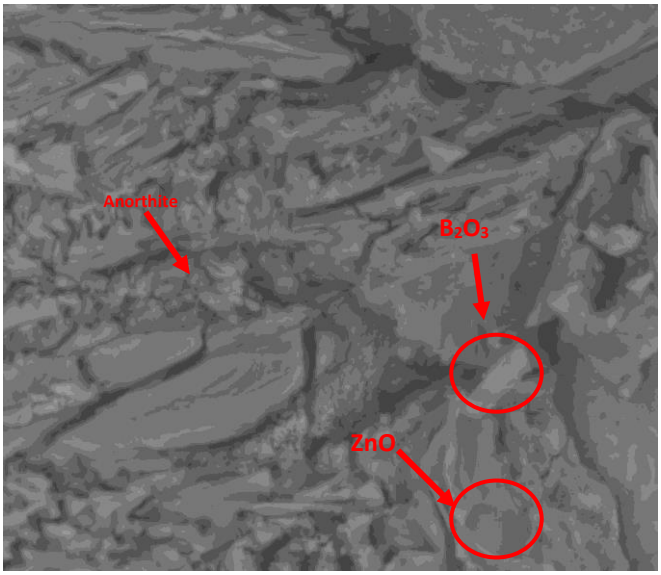

Figure 4.5.9 SEM micrograph of CMASBZn glass crystallized at 1100°C for 1 h.

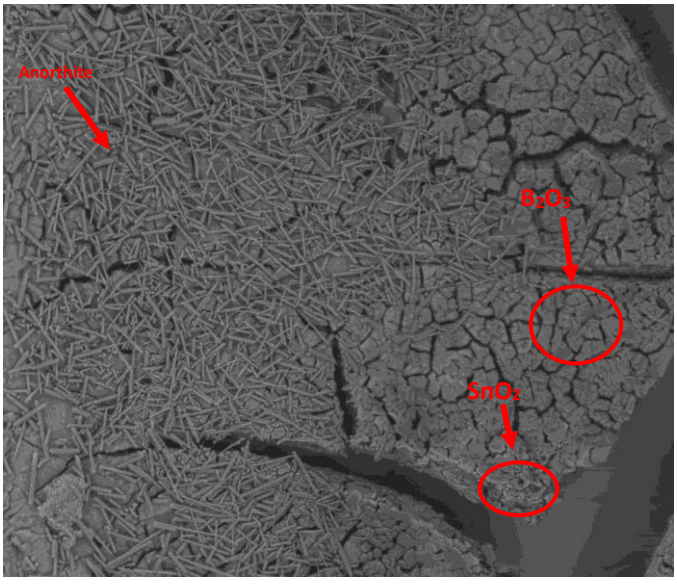

Figure 4.5.10 SEM micrograph of CMASBSn glass crystallized at 1100°C for 1h.

The surface of the particles displays a bright contrast, as a consequence of fluorhydric etching. A heterogeneous distribution of small crystals can be observed in the dark contrast. From EDS analysis we can confirm that boron and other nucleating agents are isolated and located on the surface of the glass ceramics sample, and they are not involved in phase formation. With the exception of CMASB, CMASMn and CMASBSn, where the three dimensional growth of crystals is dominant, the CMASTi and CMASZn glass ceramics exhibit a two-dimensional growth, where the separation of phase could be observed. In general, for this kind of crystallization mechanism the larger is the amount of boron oxide, the greater number of phase separated small droplets. As mentioned, De Vekey and Majumdar [221] stated that the phase separation, which takes place at about 950°C in CMAS3 glass series, is due to the segregation of calcium and magnesium ions after their diffusion. The texture of B_2O_3 has a limited solubility into some aluminosilicate glasses and we can see also high tendency to create ordered zones with high alumina content [249]. This feature can enhance the tendency to produce a phase separation process. In all glass ceramics, after 1 hour at 1100°C, small aggregates of needle-like crystals are formed in the early surface of particles (on increasing the final temperature the number of aggregates of Anorthite crystal tends to increase). The general microstructure of these B_2O_3-containing glass ceramics is similar and we can assume that the boron oxide is mainly located at the residual glassy phase.

In summary, the above discussed characterization of modified borosilicate glasses allows us to conclude that these kind of glass ceramics are suitable for sealing application in SOFC. They present good thermal and viscous properties, their thermal expansion coefficients are in good agreement with the required ranges for seal and the phases formed during heat treatment do not affect significantly the glass properties.

4.6 Vaporization experiments: Knudsen Effusion Mass Spectrometry

As mentioned, one of the main drawbacks in the use of borosilicates for sealing purposes in SOFC technology is the tendency to produce volatile species under oxidant and, even more, water-containing atmospheres. For example, the available literature data shows that the formation of gaseous species such as BO_2 (dry air) and $H_3B_3O_6$ (wet forming gas with 30% vol. H_2O) is thermodynamically favoured at 700-800 °C for pure B_2O_3.[229] Besides oxygen- and water-induced volatilization, some borosilicate glasses can also display a not negligible intrinsic (under *vacuo*) volatility at higher temperatures, leading to the release of B_2O_3(g) and, in case of alkali metal-containing glasses, ternary species such as $NaBO_2$(g) and KBO_2(g).

The extent of the above volatilization processes in glass systems depends on the thermodynamic activity of B_2O_3. In order to test the stability towards vaporization of the borosilicate glasses studied in this work, some preliminary experiments were carried out by the Knudsen Effusion Mass Spectrometry technique available at the Department of Chemistry of Sapienza, University of Rome. In this method, the sample is placed in a closed cell having a small orifice on the top. The whole assembly is kept under ultra-high vacuum and heated by an electric resistance. The vapors produced by vaporization/decomposition of the sample effuse from the orifice

and are analysed by a mass spectrometer. Under the so-called “molecular flow” regime (established for cell pressure lower than 10^{-3} bar), the mass spectral intensities of the detected species can be easily related to the corresponding partial pressures in the vapor phase. The latter can be considered to approximate closely the equilibrium pressures provided that the effusion orifice area is much smaller than the vaporizing surface.

Two experiments were carried out on the CMASB glass, using different materials for the cell (platinum and alumina) in order to check possible interaction with the sample at high temperature. In both experiments, no signal was detected for any of the gaseous species expected to form, such as B_2O_3, BO_2, and $Ca(BO_2)_2$, even at the highest temperatures reached (around 1150 °C, close to the melting point of the glass). Since a conservative estimate of the lowest detectable partial pressure value by the KEMS apparatus at this temperature is about 10^{-9} bar, on the basis of vapour pressures reported in the literature for pure B_2O_3, we can estimate an upper limit for the B_2O_3 activity in the CMASB glass of less than 10^{-3}. Such a low upper limit value indicates that the reactivity of B_2O_3 in the glass under study is orders of magnitude reduced compared to the pure oxide, suggesting that this material could be capable to withstand water- and oxygen atmospheres somehow better than expected.

Chapter 5

Preparation and properties of Mullite based glass ceramic derived from industrial process waste

The proper re-use of the various waste generated by industrial and everyday human activities has become a crucial problem in all the economically advanced societies. The largest part of waste are presently re-used as raw materials for cement production, i.e. slag cement using blast furnace slag [250] and eco-cement made from municipal waste [251]. It is, however, highly desirable to develop other uses. As discussed in the above sections, glass-ceramics are used in various applications such as building materials, cooking ceramics, machinable ceramics, bio-ceramics, optical material and sealant for electrochemical device like SOFC. Numerous silicate-based wastes, such as coal combustion ash, slag from steel production, fly ash and filter dusts from waste incinerators, mud from metal hydrometallurgy, different types of sludge as well as glass cullet or mixtures of them have been considered for the production of glass-ceramics.

In the last 40 years, the production of glass ceramics from waste using different processing methods received much attention and considerable knowledge and expertise has been accumulated on the transformation of silicate waste into useful glass-ceramic products.

The last part of this research project deals with this important topic. As mentioned, our work has been mainly developed in X-Tech lab. in Civita Castellana (VT), a private research laboratory working for the companies operating in this important ceramic industry district. Civita Castellana has been for longtime one of the most famous sanitary ware production area in Italy. The development of ceramic industry in this area is related to the local availability of good clay resources. During the stage of industrial process, different types of wastes are produced, the amount being estimated in about 500.000 t per year. Large amount of kaolin waste is derived, consisting mostly of mica and quartz alongside kaolinite as well as other minor constituents.

The kaolin waste generally discarded in the open air causes significant environmental problems, affecting fauna, flora and people's health. Numerous studies have been dedicated to recycling of kaolin processing waste aimed at the production of glass ceramics. In this scenario, this research aims to investigate the potential reuse of waste to obtain a new type of glass ceramic for use as sealant for SOFC. Recycling and reuse of wastes should be seen not only from an environmental point of view but also in terms of economic viability. In this sense, the development of applied research toward higher added value technical solutions encourages optimized ways for enhancing the culture of recycling and reuse.

5.1 Characterization of waste

Most ceramic products are clay-based and are made from a single clay or one or more clays mixed with mineral modifiers such as quartz and feldspar. The types of commercial clays used for ceramics are primarily kaolin and ball clay.

The main waste from production in industrial processes consist of quartz, clay (kaolinite - $Al_2Si_2O_5(OH)_4$) and/or mica and feldspars (orthoclase - $KAlSi_3O_8$ or albite - $NaAlSi_3O_8$), and contain only small amounts of coloring components such as Fe_2O_3, TiO_2 and/or other transition metal oxides. Regarding sanitary ware production, this mixture derives from ceramic bodied and glaze processing. In general, traditional ceramic products are made of naturally raw materials such as clay, feldspar, silica, alumina, calcium carbonate, etc [252].

In sanitary ware manufacturing, many treatments are done on raw materials to obtain the finished products. Figure 5.1.1 presents a general process flow diagram for ceramic products manufacturing. The basic steps include raw material procurement, beneficiation, mixing, forming, green machining, drying, presinter thermal processing, glazing, firing, final processing, and packaging.

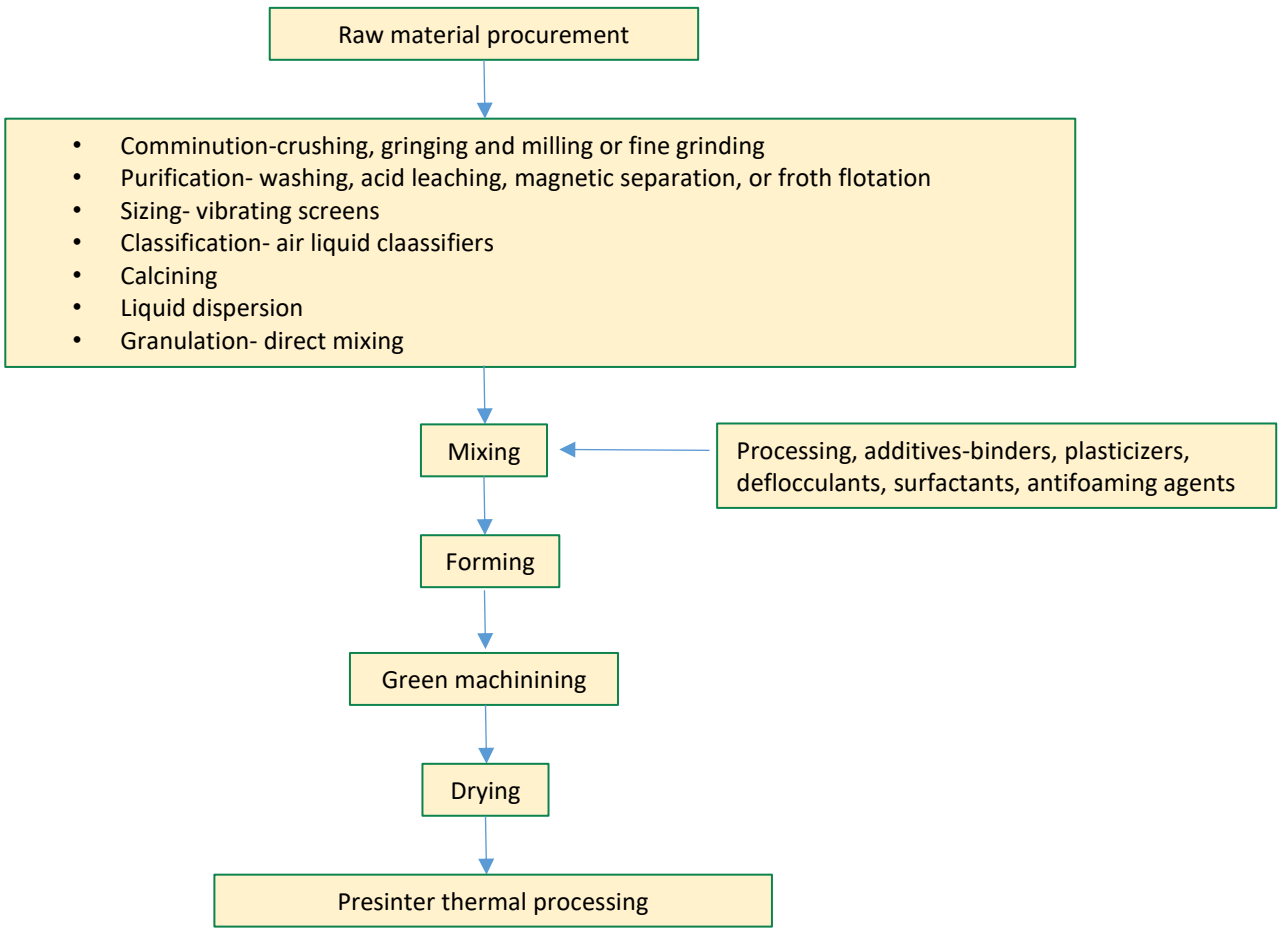

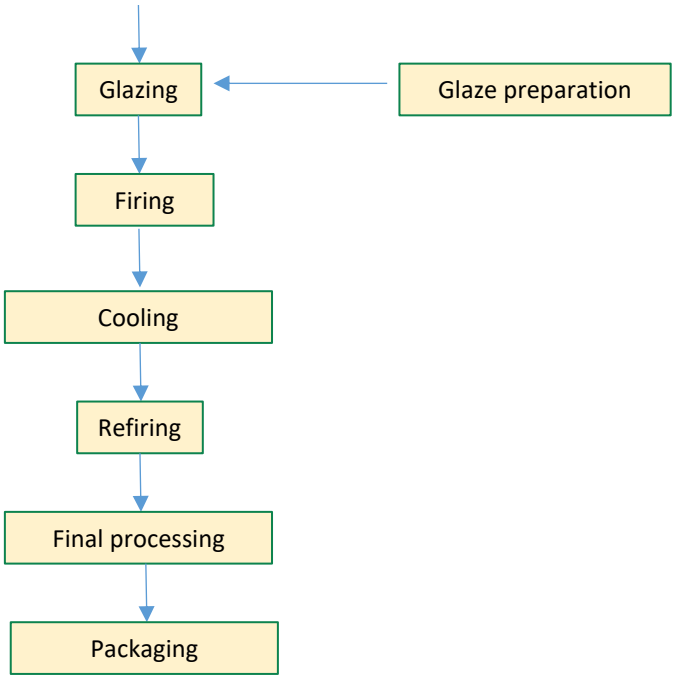

Figure 5.1.1 Process flow diagram for ceramic products manufacturing.

The raw materials used in the manufacture of ceramics range from relatively impure clay materials mined from natural deposits to ultrahigh purity powders prepared by chemical synthesis. Naturally occurring raw materials used to manufacture ceramics include silica, sand, quartz, flint, silicates, and aluminosilicates (e.g. clays and feldspar). For traditional ceramics, glaze coatings are often applied to dried or bisque-fired ceramic ware prior to sintering. Glazes consist primarily of oxides and can be classified as raw glazes or frit glazes. In raw glazes, the oxides are in the form of minerals or compounds that melt readily and act as solvents for the other ingredients. Some of the more commonly used raw materials for glazes are quartz, feldspars, carbonates, borates, and zircon. Hence, considering that numerous studies have been dedicated to the recycling of aluminosilicate-based wastes, this kind of materials are possible candidates for transformation into glass-ceramic. Moreover, many recent studies have been reported on the synthesis of CaO-MgO-Al_2O_3-SiO_2 glass ceramics using various wastes as starting materials for glass ceramic synthesis. For instance, glass ceramics rich in Diopside and in Anorthite were obtained by sintering glass powders originated from mixture of “Kira” and dolomite. “Kira” is the name attributed to the waste derived from the refining process of kaolin clay, and consist mainly of quartz, kaolinite and feldspar, similarly to our case. In this study, only the fine fraction of the mined kaolin clay is used for porcelain production, the coarse fraction that remains after processing being normally reburied as a waste product. The authors highlighted one of the key benefits of Kira as being low in Fe_2O_3 and TiO_2, which normally provide the dark coloring to the end product. Considering also these assumptions, the idea arises to convert the ceramic waste from sanitary ware industry into glass ceramic which can be used as sealant for SOFC. The need to found an alternative use of these materials is related to the large amount of waste produced during the sanitary ware manufacturing. In this contest, the sanitary-ware companies have an obligation to landfill the solid process scrap at least one each year. A code is assigned to

this kind of waste for its management in landfills. In our case, 10.12.01 is the European Waste Catalogue attributed. It is important to highlight that this kind of waste derived from materials not thermally treated. In table 5.1.1 is presented a common waste analysis performed by the companies to assign the code referring to the required parameters listed in the Legislative Decree 152/06. In table 5.1.1 the standard methods adopted and the danger indication according to the Regulation CE N. 1272/2008 are also summarized.

Parameter	Values measured	Unit of measure	Methods of analysis	Danger indication
Physical state	Solid	-	-	-
Density	1015	kg/mc	Gravimetric	-
COD	<10	mg/l	APAT CNR IRSA 5130	-
Ammonia nitrogen	<5	mg/l	STANDARD METHODD VERS. 19TH 4500 NH_3	-
pH	8.0	Un pH	IRSA CNR 1 Book 64 Vol.3 1985	-
Fixed residue at 105°C	3.1	$\%_{P/P}$	UNI EN 14346:2007	-
Antimony	<0.50	mg/kg	UNI EN 13857:2004 UNI EN ISO 11885:2009	H314, H411
Arsenic	1.41	mg/kg		H301, H331. H350, H400, H410
Beryllium	<0.50	mg/kg		H301, H315, H317, H319, H330, H335, H350I, H372. H411
Boron	<0.50	mg/kg		H271, H302, H332, H411
Cadmium	<0.50	mg/kg		H301, H330, H340, H350, H360FD, H372, H400, H410
Cobalt	<0.50	mg/kg		H317, H350, H400, H410
Chromium	<0.50	mg/kg		H300, H310, H330, H373, H400, H410
Mercury	<0.50	mg/kg		H302, H323, H360DF, H373, H400, H410
Nickel	<0.50	mg/kg		H302, H315, H319, H400, H410
Lead	1.12	mg/kg		H301, H331, H373, H400, H401
Copper	3.12	mg/kg		H314, H412
Selenium	1.18	mg/kg		H300, H330, H373, H411
Tin	<0.50	mg/kg		H302, H332, H335, H341, H361D, H372, H411
Thallium	<0.50	mg/kg		H302, H318, H400, H410
Vanadium	<0.50	mg/kg		H225, H304, H315, H319, H340, H350, H372
Zinc	9.25	mg/kg		H225, H304, H332, H373

Benzene	<5	mg/kg	EPA 5021A 2003+EPA 8015D 2003	H225, H304, H315, H361D. H373
Toluene	<5	mg/kg		H226, H312, H315, H332
Ethylbenzene	<5	mg/kg		H226, H312, H315, H332
Xilene	<5	mg/kg		H226, H312, H315, H332
Chlorinated solvents	<5	mg/kg	IRSA CNR 1 Book 23a Vol.3 1985	-
Hydrocarbon C_{10}-C_{40}	<50	mg/kg	UNI EN 14039:2005	H411

Table 5.1.1 Analysis of chemical composition of CER 10.12.01 waste.

It can be seen that trace of transition metals are present in the sample, but the concentration is under the limits imposed by law.Considering the nature of the starting material, four types of different waste have been tested. Wastes have been taken from four different companies to account for composition variation. An example e of the chemical composition of a waste sample as determined by X-ray fluorescence is reported in table 5.1.2 (the error on results is ±0.01). While the chemical composition of the samples varies according to their origin, the variation in each waste type is relatively small. In all wastes, the major components are SiO_2 (65.7-75.3 mass%) and Al_2O_3 (21.9-29.5 mass%), totaling > 87.6 mass%. The remaining components are K_2O ~ 1.5 mass% and Fe_2O_3, TiO_2 and Na_2O < 1 mass%.

Compound	wt%
SiO_2	67.63
Al_2O_3	27.92
K_2O	1.52
Fe_2O_3	0.86
Na_2O	0.68
TiO_2	0.58
CaO	0.30
MgO	0.12
P_2O_5	0.12
SO_3	0.12
ZrO_2	0.04
ZnO	0.02
SnO_2	0.01
MnO_2	0.01
OTHER IMPURITIES	0.07

Table 5.1.2 Analysis of waste by X-ray fluorescence.

Considering the origin of the waste, its compositions derive from mixing ceramic bodied and glazes used during sanitary ware manufacturing. The elementary composition of these starting materials for production are reported in the tables 5.1.3 and 5.1.4 (the error on results is ±0.01).

BODY GREEN	
Compound	wt%
SiO_2	65.91
Al_2O_3	27.92
K_2O	1.74
Fe_2O_3	1.50
CaO	1.22
TiO_2	0.74
Na_2O	0.29
MgO	0.24
BaO	0.10
OTHER IMPURITES	0.34

Table 5.1.3 Analysis of body green by X-ray fluorescence.

GLAZE	
Compound	wt%
SiO_2	57.09
Al_2O_3	11.94
CaO	10.37
ZrO_2	8.53
ZnO	2.68
MgO	2.27
SnO_2	2.20
K_2O	1.60
Na_2O	1.34
MnO_2	1.16
OTHER IMPURITIES	0.39

Table 5.1.4 Analysis of glaze by X-ray fluorescence.

From these results, we can conclude that the main constituents of ceramic bodies are silica, alumina, alkali and alkaline earth oxides together with two kinds of metal transition oxides. Indeed, in glaze composition other different types of oxide are also recorded such as ZrO_2, ZnO, SnO_2 and MnO_2.

To develop a glaze for sanitary-ware sector four kinds of oxides are used with different functions:

1. Vetrificant oxides such as SiO_2 and B_2O_3
2. Stabilizing oxides mainly Al_2O_3
3. Fluxing oxide such as PbO, Na_2O, K_2O, CaO, MgO, BaO, Li_2O, ZnO
4. Coloring oxides such as SnO_2, ZrO_2, Fe_2O_3, CuO_2, Co_3O_4, Cr_2O_3, MnO_2, NiO, V_2O_5 and TiO_2

Analyzing the results listed in the tables, it is evident that:

1. industrial waste contains the characteristic chemical constituents of glass
2. glaze introduces additive like Fe_2O_3 that could increase the tendency toward crystallization and ZnO that could decrease the melting temperature and the melt viscosity without affecting the chemical properties of the material
3. alkali oxide like Na_2O could decrease the viscosity of the melt

Based on the above reported compositions, this waste can be considered a suitable candidate for producing glass ceramic material, because it is constituted by a network former such as SiO_2, an intermediate oxide like Al_2O_3, network modifiers (alkali and alkaline earth oxides) and nucleating agents. We can then consider this material as a rather complex system, an evolution of the basic glasses examined in the previous chapters.

In this scenario, understading how the different components could affect the properties of the resulting material is a prohibitively difficult task.

The idea here is rather to wonder if a complex system of this type can meet the requirements to be used as sealant for SOFC.

The mineralogical information is important to understand the features of the starting material for producing glass ceramics. XRD spectra are shown in figure 5.1.2

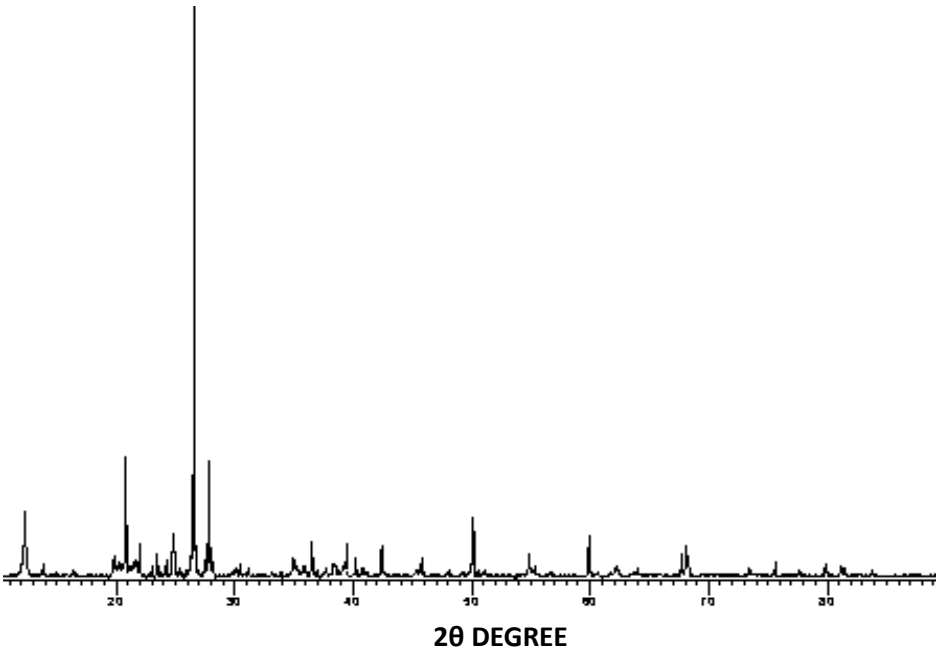

Figure 5.1.2 XRD patterns of waste derived from industrial process.

The XRD pattern of waste shows that the main crystalline phases are the following:

1. Quartz, SiO_2 ICDD 01-0703755
2. Albite ordered, $NaAlSi_3O_8$ ICDD 00-009-0466
3. Kaolinite-1A, $Al_2Si_2O_5(OH)_4$ ICDD 00-058-2005
4. Dolomite, $CaMg(CO_3)$ ICDD 01-075-3698
5. Mullite, $Al_{4.64}Si_{1.36}O_{9.68}$ ICDD 01-074-4145
6. $Na(AlSi_3O_8)$ ICDD 01-083-1614
7. Mica Muscovite ($KAl_2Si_3AlO_{10}(OH)_2$) ICCD 00-568-9856

In Tables 5.1.5. and 5.1.6 the results obtained from the Rietveld R.I.R method are listed.

Phases	wt%
Quartz,	25.31
Albite ordered	12.07
Kaolinite-1A	38.89
Dolomite	3.74
Mullite	10.98
$Na(AlSi_3O_8)$	2.21
Muscovite	1.22

Table 5.1.5 Quantification of phases using the Rietveld R.I.R method for CER 10.12.01 waste.

SAMPLE ID	χ^2	R_F^2	w_{rf}	r_p
WASTE CER 10.12.03	1.122	0.147	0.296	0.403

Table 5.1.6 Rietveld R.I.R. parameters for CER 10.12.01 waste.

Kaolinite is an excellent structure forming in a wide range of firing temperatures, with mica acting as a fluxing agent at high sintering temperatures.

The mineral quartz causes an increase in the mechanical strength and a decrease in the firing shrinkage, acting as a "skeleton" during the formation of the liquid phase. According to the methodology of rational analysis, the kaolin clay used in this study is mainly composed of kaolinite (86.7 wt%) and quartz (9 wt%). The amount of mica can be considered small (4.3 wt%). According to the same methodology, the main minerals present in the kaolin waste are kaolinite (49.65 wt%) and mica (40.5wt%). The amount of quartz was found to be 9.85 wt%. These mineralogical results suggest that the studied raw materials have a good potential to be used in the manufacturing of mullite based ceramics.

With regard to the thermophysical properties of the waste, the sintering behavior and the thermal expansion coefficient have been evaluated. Dilatometric tests have been performed to understand if the thermal expansion coefficient is in agreement with the required limit of sealant for SOFC. The resulting waste CTE is equal to $10.74 \cdot 10^{-6}$ °C^{-1} $\pm 0.10 \cdot 10^{-6}$ °C^{-1} in the temperature range 200-500°C and 6.81 10^{-6} °C^{-1} $\pm 0.10 \cdot 10^{-6}$ °C^{-1} for 200-700°C. It can be seen that CTE tends to decrease considerably in the higher temperature range, perhaps due to chemical transformation during high heating treatment. Furthermore, the waste sample derives from a mixture of not thermally treated raw materials, which makes possible decomposition phenomena during the heat treatment.

HSM measurements showed that the sintering process starts at high temperature (T_{FS}=1160°C) and ends around 1411°C, T_{MS}; the melting temperature is then too high, around 1560°C. The latter property is an important drawback for glass production purposes. To by-pass the problem, a new synthesis route has been devised. The waste powder has been mixed with one of the glass system studied in the previous chapter. This procedure is inspired by the preparation technique of ceramic glaze in industrial process. For traditional ceramics, glaze coatings often are applied to dried or bisque-fired ceramic ware prior to sintering. As mentioned above, glazes consist primarily of oxides and can be classified as raw glazes or frit glazes. In raw former, oxides are in the form of minerals or compounds that melt readily and act as solvents for the other ingredients. Typical raw materials are quartz, feldspars, carbonates, borates, and zircon. The frit glazes are

traditional glazes mixed with "frits", a ceramic composition that has been fused in a special oven, quenched to form a glass, and granulated. Basically, the word "frit" indicates "a calcinated mixture of sand and fluxes ready to be melted in a crucible to make a glass". The unheated raw materials of glass making are more commonly called "glass batch". Frits form an important part of the batches used in compounding enamels and ceramic glaze; the purpose of this pre-fusion is to render any soluble and/or toxic components insoluble by causing them to combine with silica and other added oxides. However, not all glasses that are quenched in water are a frit, as this method of cooling down very hot glass is also widely used in glass manufacture.

Frits are indispensable constituents of most industrial ceramic glazes which mature at temperatures below 1150°C. They are typically intermediates in the production of raw glass, as opposed to pigments and shaped objects, but they can be used in a number of high-tech contexts. Frit made predominantly of silica, diboron trioxide (B_2O_3), and soda are used as enamels. Frits are also used as fluxing agents for reducing the melting point of the ceramic glaze. Considering these features, a frit can be compared with the glass systems previously analyzed. Hence, CMASB glass system has been added to sample waste in order to decrease the melting temperature. The choice fell on a system doping with B_2O_3 for its low melting point.

5.2 Characterization of waste-derived glasses

5.2.1 Preparation and composition of glass

Based on the melting point of CMASB, batch composition are prepared by mixing 70.0 mass% of waste with 30.0 mass% of CMASB. Waste and CMASB powder are mixed by wet ball milling for 2 hours and dried at 110°C overnight. The dried powder mixtures are calcined at 900°C to decompose $CaCO_3$ contained in not thermally treated waste. They are then fired at 1400°C for 2 hours and quickly cooled into the kiln. The glass powder is ground in a ball mill and sieved <100 mesh to determine the crystallization conditions and <48 mesh for the determination of the thermophysical properties. In table 5.2.1.1 the chemical composition of the resulting glass is summarized, obtained using ICP-OES (the error on results is ±0.01). This method enables a quantitative analysis of the main elements (>1 wt.%) with a relative experimental error of ± 3 %, while minor elements (> 0.1 %) and impurities (> 0.01 %) are detected with larger errors of 10 to 20 %.

Sample ID	GC 10.12.01
SiO_2 (%)	63.06
Al_2O_3 (%)	23.18
CaO (%)	9.67
TiO_2 (%)	1.52
K_2O (%)	1.04
Fe_2O_3 (%)	0.84
MgO(%)	0.22
B_2O_3 (%)	0.11
Na_2O (%)	0.10
Impurities (%)	0.26

Figure 5.2.1.1 Analysis of glass GC 10.12.01 by X-ray fluorescence.

Based on the chemical composition, Al_2O_3 acts as a network former. Indeed, in this case three oxides, namely SiO_2, Al_2O_3 and B_2O_3, form the glass network, the presence of network modifiers is lower than in the previously examined glasses and the amount of additives is very small. The network modifiers are alkali and alkaline earth oxides. The GC 10.12.01acronym is assigned to the sample, related to the waste code assigned by the European Waste Catalogue.

5.2.2 Density, chemical resistance and particles size

Density of the glass sample is calculated using Archimede's test and ISO 10545-3:1995 standard method, as already done for the other systems. In tables 5.2.2.1. and 5.2.2.2. are listed the results obtained (for all details on the relevant properties see Section 3.2).

Sample ID	Density of glass (g/cm^3)	Density of glass ceramic (g/cm^3)	Molar volume (cm^3/mol)
GC 10.12.01	5.98	6.23	50.61

Table 5.2.2.1 Density of glass and glass ceramic belonging to CMASB series.

Sample ID	E_b	E_v	V(cm^3)	p	V_0(cm^3)	V_1(cm^3)	T(g/cm^3)
GC 10.12.01	12.78	8.37	0.21	80.95	0.17	0.04	50.75

Table 5.2.2.2 Characteristic values calculated from the ISO 10545:1995 method.

The values obtained are in good agreement with the results recorded for the other glass systems. The density is slightly higher than glasses belonging to CMAS and CMASB series, but the influence of B_2O_3 is minimal. No remarkable absorption of water has been recorded, although it results to be higher than the other glass samples. The open porosity is too high. The chemical resistance tests in acid (HCl 5%) and basic (NaOH 5%) environment show an optimal behavior against corrosion, indeed no visible alteration are evident on the sample surface after the treatments. Also the durability test in water highlights the high quality of the sample, with no sign of reaction observed. Even after a longer period of about two months soaked in distilled water, the sample does not appear covered by a white dusty layer. The low CaO content in the glass composition does not contribute to formation of hydrate and hydrate carbonate phases. Using a laser granulometer, the particle size distribution has been evaluated after subjecting the samples for a milling time of 2 hours. As mentioned, this property is important as it tends to influence considerably the onset of crystallization. In figure 5.2.2.1. the size distribution of glass particles is presented.

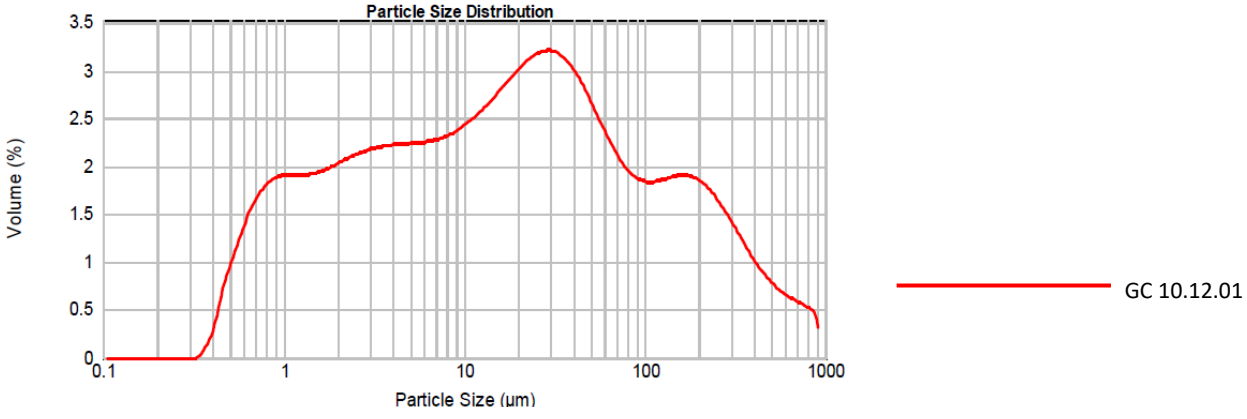

Figure 5.2.2.1 Particle size distribution of glass sample derived from waste.

Typical resulting grains size are reported in the table 5.2.2.3 below.

GLASS SAMPLE ID	d(0.1) µm	d(0.5) µm	d(0.9) µm
GC 10.12.01	1.555 ± 0.030	17.402 ± 0.030	209.636 ± 0.030

Table 5.2.2.3 Particle size distribution of the glass powder.

As previously discussed, the size distribution is related to the surface area for nucleation and crystal growth. Considering that 90% of the particles have dimensions below 209.636 µm, we can conclude that the glass exhibits a discrete hardness, lower than CMASB glass series, but comparable to CMAS glasses.

5.2.3 Thermophysical, thermomechanical and kinetic crystallization properties

By combining the data obtained from hot-stage microscopy analysis (HSM) and DTA, the sintering and crystallization behavior of the glass was evaluated. In particular, the thermophysical properties of glass were obtained by the HMS and DTA curves recorded at 15°C/min rate. Figure 5.2.3.1 shows the sintering behavior and DTA analysis.

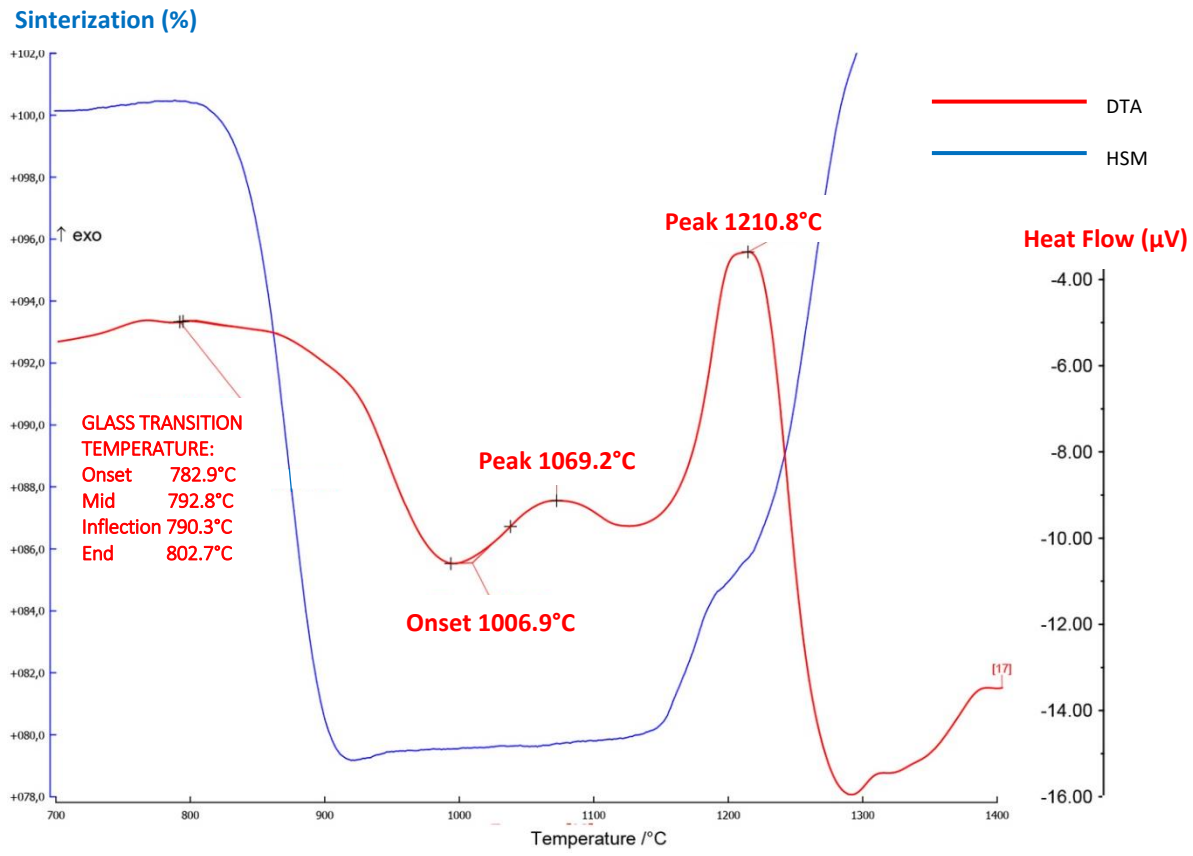

Figure 5.2.3.1 ***Sintering behavior and DTA analysis for glass derived from waste.***

By the analysis of these curves, we can deduce that the sintering process is perfectly complete when the crystallization starts, meaning that these two processes are totally independent. The sintering ability parameter S_c ($S_C=T_C-T_{MS}$) is significantly high, implying that the crystallization event is delayed (T_C=1069°C). As a consequence, well-sintered and mechanically strong glass powders should be formed before crystallization

occurs. This can be explained on the basis of the chemical composition of the glass, which is rich in SiO_2 and Al_2O_3 network formers with an amount of network modifiers and additives too small to control the crystallization process, and to improve the nucleation and growth of crystals. This kind of behavior makes this material suitable for glass sealant applications. The DTA thermogram show two exothermic peaks, as observed for the CMAS1 glass where Al_2O_3 acts as a network former. The second is the main crystallization peak.
In table 5.2.3.1. the characteristic temperatures of the GC 10.12.03 glass are listed.

GLASS SAMPLE ID	T_s (°C)	T_{FS}(°C)	T_{MS}(°C)	T_{HB} (°C)	T_F (°C)	T_g. (°C)	T_c(°C)	T_o (°C)	T_{c1}(°C)	T_{o1} (°C)
GC 10.12.01	858	826	915	1449	1460	786	1006.9	1069.2	-	1201.8

Table 5.2.3.1 Characteristic temperatures obtained from HSM and DTA tests.

The high value of the glass transition temperature is in agreement with the high content of silica.
From the data so obtained, the glass stability has been calculated using the equations reported in Par.3.5.1, based on different interpretations (table 5.2.3.2).

GLASS SAMPLE ID	K_T	K_1	K_2	K_W	K_H	K_3
GC 10.12.01	0,54	674	283,20	0,19	0,72	9,43

Table 5.2.3.2 Results of glass stability parameters for all examined glasses.

It can be concluded from the data in this table that the glass exhibits a good stability as shown by the high value of the K_1 parameter.
The values of K_1, K_W, K_H and K_3 are influenced by the high melting point, but respect the required limits.
As repeatedly discussed in this work, the thermal expansion coefficient is a property crucial for sealing purposes in SOFCs. Despite the high content of network formers, the CTE in the waste-derived material was found to be $9.75 \cdot 10^{-6}$ °C^{-1} $\pm 0.10 \cdot 10^{-6}$ °C^{-1} in the 200-500°C temperature range and 8.87 10^{-6} °C^{-1} $\pm 0.10 \cdot 10^{-6}$ °C^{-1} in the 200-700°C interval. This result indicates that the presence of all the other oxides limits the decrease of CTE. Unlike the sample waste, CTE decreases only by ~1 10^{-6} °C^{-1} in the temperature range 200-700°C.
On this basis, this glass can be considered as a suitable candidate for sealing applications (8.0 10^{-6} °C^{-1} to 12.0 10^{-6} °C^{-1}).

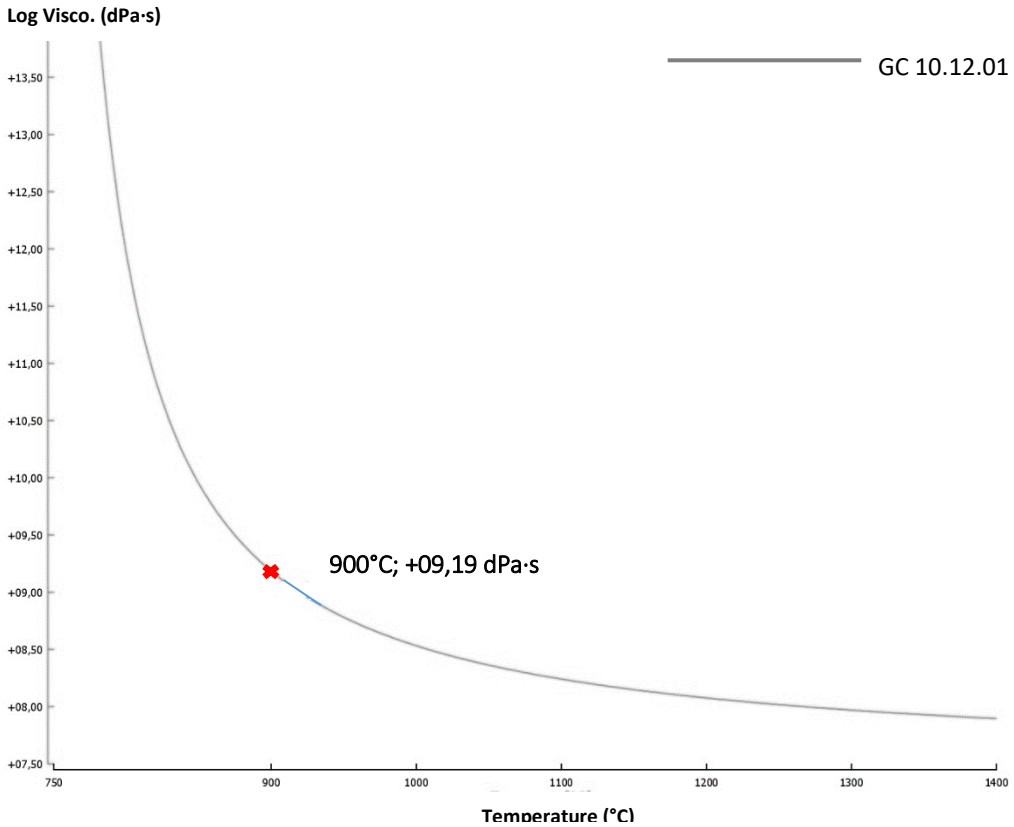

Figure 5.2.3.2 Viscosity curve of glass derived from waste.

The viscosity of the glass (Figure 5.2.3.2) has been obtained using the Vogel-Fulcher-Tamman equation (Section 3.7). The calculated temperatures for the dilatometric softening point T_d, softening point T_s and half ball temperature T_{HB} for this type of glass are summarized in table 5.2.3.3 together with the viscosity expressed as $log\,\eta$ (η is given in dPa s) at 900°C.

GLASS SAMPLE ID	T_D (°C)	T_S (°C)	T_{HB}(°C)	T_F (°C)	η (dPa s) T_S	η (dPa s) T_{HB}	η (dPa s) 900°C
GC 10.12.01	838	858	1449	1460	8.71	7.41	8.89

Figure 5.2.3.3 Characteristic temperature and viscosity values at T_S, T_{HB}, and 900°C calculated for all examined glasses.

The glass viscosity at 900°C from VTF equation is close to $\sim 10^{8.0}$ Pa s, appropriate for sealing applications [248]. As obtained for aluminoslicate and borosilicate glasses, viscosity varies between 6.0 and 9.0 dPa s, in the sealing range (700-900°C). Thus, the sample fulfills the η requirements for sealing.

Table 5.2.3.4. shows the VFT constants derived from the procedure described in Section 3.7.

GLASS SAMPLE ID	A (kPa·s)	B (kPa·s·°C)	T_0(°C)
GC 1.12.01	16.15	-0.05	781.45

Table 5.2.3.4 VFT constants for glass derived from waste.

In the final step of our characterization work, the crystallization kinetics has been evaluated in order to understand if the one-step crystallization could be performed. As previously discussed, a low value of the activation energy could promote this phenomenon.

DTA analysis has been performed at different heating rates of 20, 30 and 50°C/min, as shown in Figure 5.2.3.3

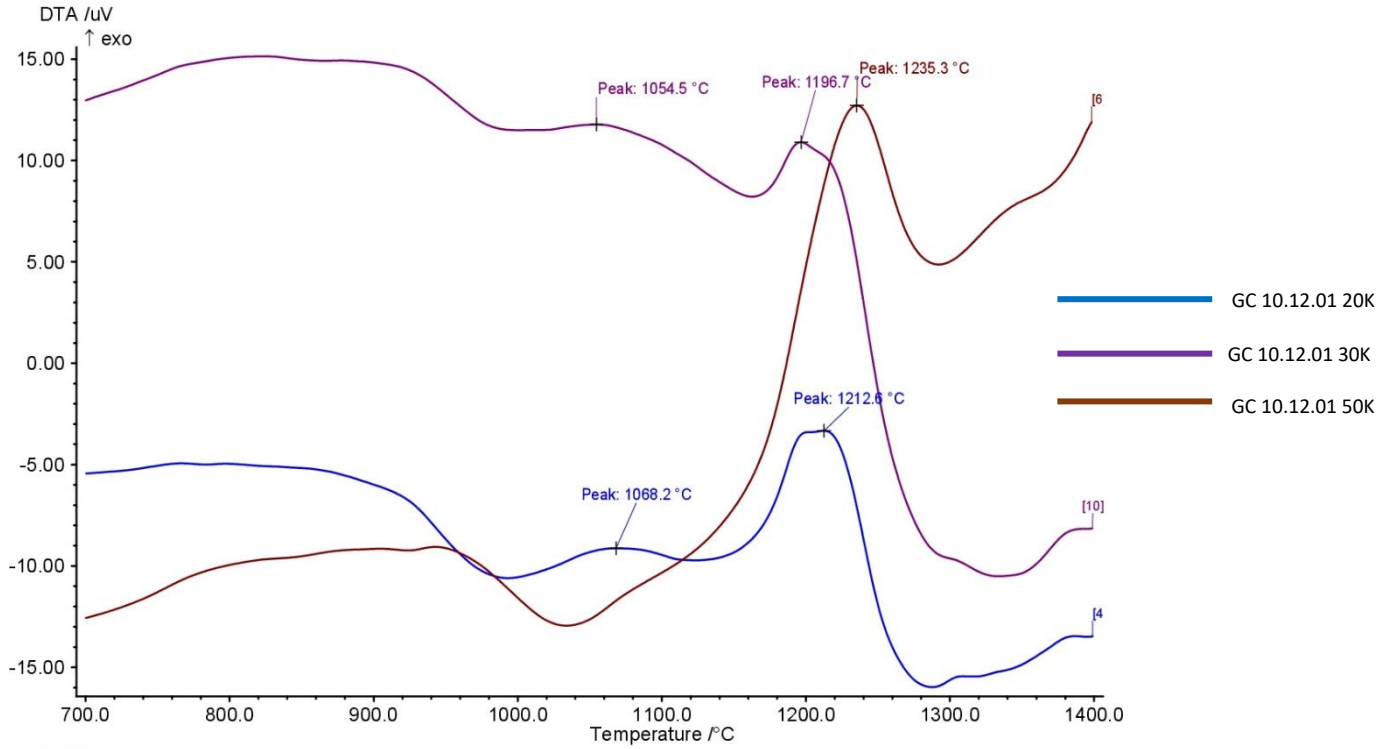

Figure 5.2.3.3 DTA curves at different heating rates for glass derived from waste.

Although the influence of the different oxides is difficult to analyze, a delay in the crystallization event is evident from the DTA curves. At the high heating rate of 50°C/min, the sample exhibits a poor tendency to crystallize, with broad and not well-defined exothermic peaks. The results derived from the kinetic equations (see Section 3.8.1) are listed in table 5.2.3.5.

GLASS SAMPLE ID	GC 10.12.03
Avrami index, *n*	4
m	3
E_A (KJ/mol) Kissinger and Matusita	259.18±
E_A (KJ/mol) Augis and Bennett	372.17±
E_A (KJ/mol) Afify I	436.95±
E_A (KJ/mol) Afify II	457.77±
K_0	37.21

Table 5.2.3.5 Avrami exponents (n,m), crystallization activation energy (Ea) and k_0 of the glass derived from waste.

As a result, the crystallization mechanism occurs with an increasing number of nuclei and three dimensional growth of crystals. The value of the activation energy doesn't fit with the one step crystallization behaviour, the low amount of network modifiers hindering the creation of Ca^{2+} and Mg^{2+} fast diffusion layer.

5.2.4 Evaluation of phase content

The nature and character of crystalline phases and the microstructure of the glass ceramic material are reported to be the most important factors affecting the technical properties of sealants for SOFC. In figure 5.2.4.1 the XRD patterns of the waste-derived glass recorded at different holding temperature for 1 hour are shown. It can be seen from this figure that at temperatures close to the first exothermic peak the glassy phase tends to convert totally in crystalline phases.

The main crystalline phases present in the glass ceramic sample are Mullite ($Al_{4.75}Si_{1.25}O_{9.63}$ ICDD 01-079-1454), Quartz (hexagonal silica, SiO_2 ICDD 00-046-1045) and Anorthite ($Al_2Ca(SiO_4)_2$ ICDD 00-002-0537). Little amount of Cristobalite (tetragonal silica, SiO_2 ICDD 00 03-0270), Anorthoclase disordered ($(Na, K)(Si_3Al)O_8$ ICDD 00-009-0478), Augite ($Ca_{0.818}Mg_{0.792}Fe_{0.183}Fe_{0.086}Al_{0.151}Al_{0.269}Si_{1.731}O_6$ ICCD 01-071-0721) and $Ca_{0.88}$ $Al_{0.12}$ $Al_{1.77}$ $Si_{2.23}$ O_8 ICDD00-052-1344.

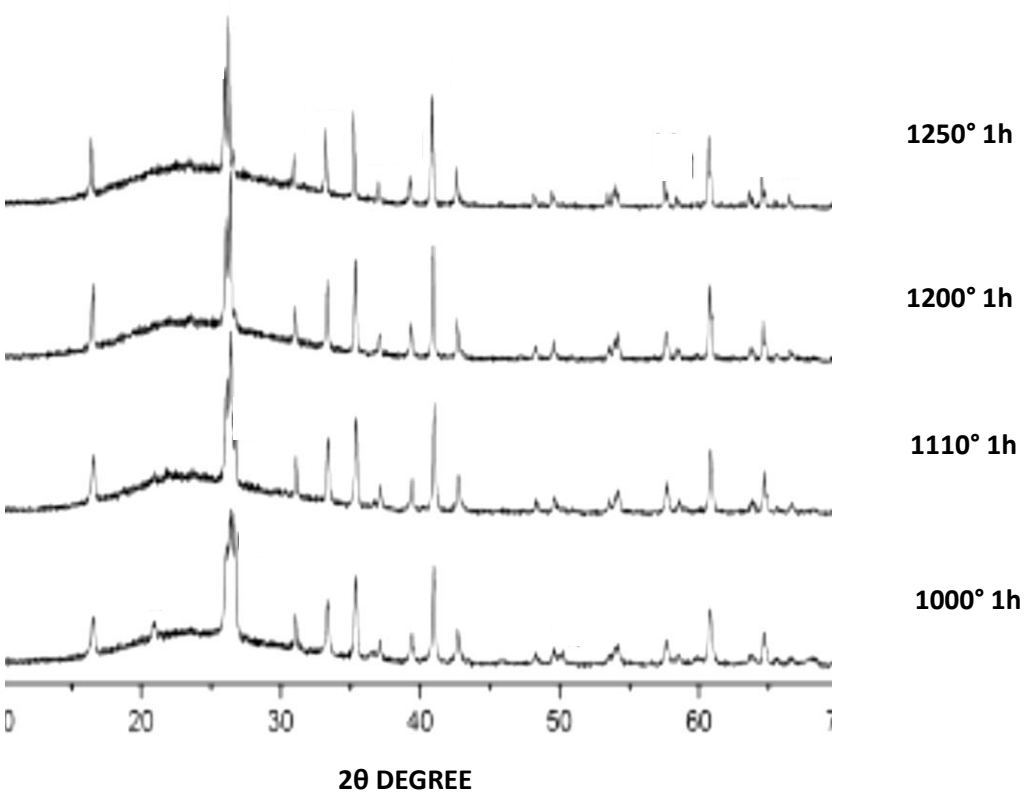

Figure 5.2.4.1 XRD patterns of GC 10.12.01 crystallized after different heat treatments.

In tables 5.2.4.1 and 5.2.4.2 the results obtained from the Rietveld R.I.R method (quantification of phases analysis and the Rietveld parameters on glass ceramic at 1100°C) and the CTE value (error within the range $\pm 0.10 \cdot 10^{-6}$ °C^{-1}) are reported, respectively.

Phases	wt%
Mullite	39.21
Quartz,	7.12
Anorthite	8.47
Cristobalite	1.32
Anorthoclase disordered	1.09
Augite	0.52

Table 5.2.4.1 Quantification of phases using Rietveld R.I.R method for GC 10.12.01.

SAMPLE ID	*GLASS*	χ^2	R_F^2	w_{rf}	r_p	$\alpha(°C^{-1})$ *(200-500°C)*	$\alpha(°C^{-1})$ *(200-700°C)*
GC 10.12.03	41.7	1.236	0.094	0.117	0.361	$8.99 \cdot 10^{-6}$	$8.75 \cdot 10^{-6}$

Table 5.2.4.2 Rietveld R.I.R. parameters for GC 10.12.01.

As mentioned, the CTE of the resulting glass ceramic material slightly decreases compared to the value recorded for glass, but it remains still suitable for sealing applications.

As seen in other glass systems, Anorthite is recorded as one of major phases and no Diopside is detected in the obtained glass ceramic. After the heat treatment, a certain amount of quartz is detected. The presence of glassy phase (mainly from Mica) is clearly observed by the occurrence of a halo in the region between 15° and 30° in 2θ scale. Since the amount of silica (SiO_2) in the kaolin clay is much higher than that in Mullite (~50 wt% vs. 28 wt%), it can be expected that the excess amount of silica will experience a series of transformations with increasing temperature. According to the literature [253-254], excess silica (in the form of quartz above 980°C) transforms to amorphous silica after heat treatment above 1200°C and crystallizes to form Cristobalite as temperature increases. A final transformation of Cristobalite to amorphous phase is also reported to occur above 1500°C [253].

Based on these literature information, we assume that the thermal transformation of the excess silica taking place in our kaolin clay (at 1300°–1550°C) can be expressed as

$$3Al_2O_3 \cdot 2SiO_2 + SiO_2(Quartz\ +\ Amorphous) \rightarrow 3Al_2O_3 \cdot 2SiO_2 + SiO_2(Quartz\ +\ Amorphous + Cristobalite)$$

According to this scheme, quartz and amorphous silica (most likely formed below 1300°C) crystallize into Cristobalite with increasing temperature. Part of the Cristobalite returns to the amorphous phase, with orthorhombic Mullite as the main crystalline phase at high temperature. The two reflections of Mullite at 2θ ~ 26°, planes (120) and (210), are classically attributed to the presence of orthorhombic Mullite (also known as secondary Mullite, the Mullite formed from the amorphous aluminosilicate phase).

As far as samples derived from formulations containing kaolin waste are concerned, acicular Mullite crystals dispersed in glass phase are observed at 1200°C, as can be seen in figure 5.2.4.1 (SEM image) together with the EDS spectrum of Mullite crystals.

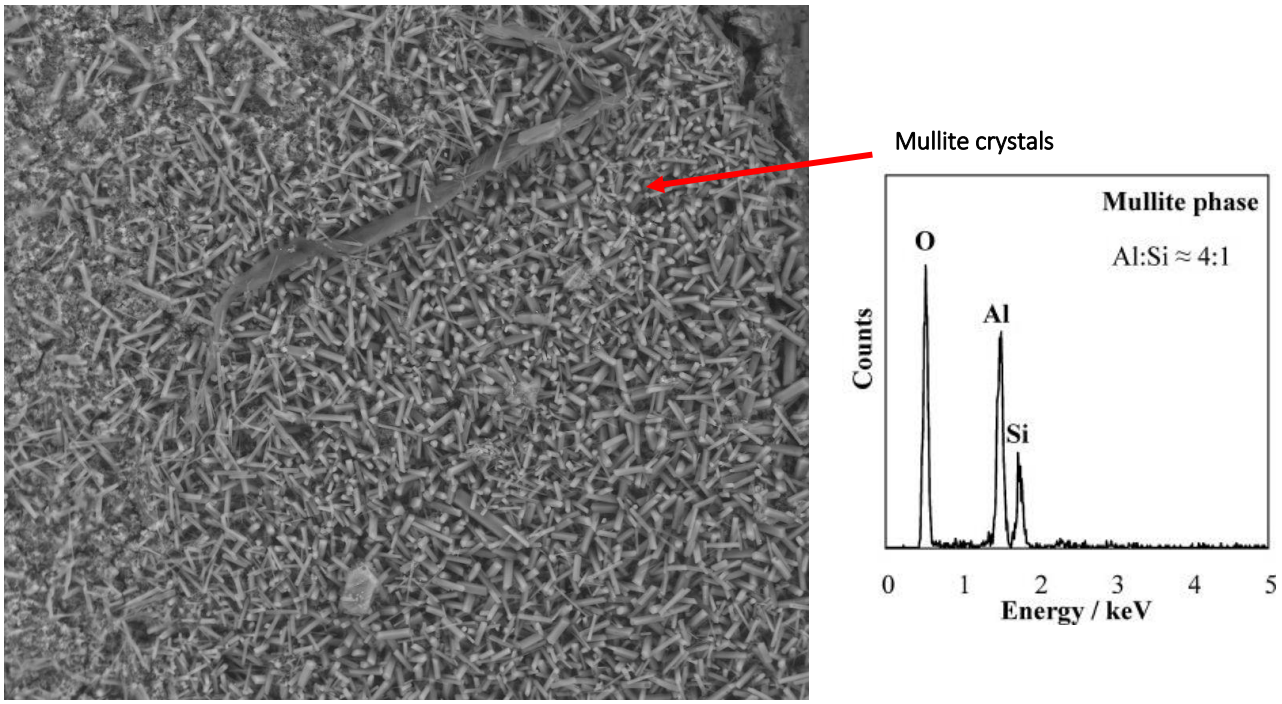

Figure 5.2.4.2 Acicular Mullite crystal dispersed in glassy phase after 1 hour at 1200°C and EDS spectrum of Mullite crystals.

SEM micrograph confirms the three dimensional growth of crystals obtained from kinetic considerations. Mullite has been qualified as one of the most important refractory ceramic material due to its special set of properties such as low density (3.17 g/cm^3), good chemical stability, high modulus of rupture and low coefficient of thermal expansion(~$4.5 \cdot 10^{-6}$°C^{-1}) [255-256].The production of Mullite by reactive sintering of silico-aluminous sources occurs by ionic diffusion of aluminum ions(Al^{3+}) to the interior of SiO_2 layers formed during the decomposition of Kaolinite (>500 °C). Hence, mullitization can be characterized as a slow and thermally activated process [258-259-260]. We can then conclude that also from the phase formation point of view, the glass sample we prepared starting from ceramic industrial processes waste could be considered as a suitable candidate for sealing applications in Solid Oxide Fuel Cell (SOFC) and other high temperature technologies.

Conclusions

In this work, a systematic investigation was presented on the synthesis and physicochemical properties of glass ceramic materials of selected compositions with a view to the possible use of such systems as sealants in Solid Oxide Fuel Cells (SOFC).

SOFC-based systems (see Chapter 1) are known to be among the most promising candidates for sustainable power generation either in stationary and in mobile applications, for their high efficiency energy conversion (70-80% with cogeneration) and their low emissions of pollutants. SOFCs convert directly chemical energy to electrical energy by a redox reaction. The most typical reactants are air and hydrogen which provide water as the only reaction product, with virtually no pollutant or greenhouse gas production. Other fuels, such as CH_4 can also be used. The reaction heat can be reused to supply the cell working temperature (600-800°C), and for example, to heat a water circuit. Current work on SOFCs is aimed in particular to optimize the constituents and to reduce the costs in order to allow SOFC to become a technology suitable for large-scale applications. Seal and sealing processes are an important part of SOFC design. Sealants must fulfill stringent requirements, what recently promoted a great number of studies aimed at identifying the optimal materials. Candidate sealing materials must be chemically inert respect the other cell components, must exhibit good chemical stability at high temperature under dual atmospheres of SOFCs and present constancy of its physical properties. Today, glasses and glass ceramics could satisfy these conditions and can be considered the best candidates.

In our research work, a number of aluminosilicate and borosilicate glass ceramic with different nucleating agents have been considered and investigated with various experimental techniques (briefly described in Chapter 2). In particular, the quaternary CaO-MgO-Al_2O_3-SiO_2 (CMAS) glass-forming oxide system was considered, and the effect of additional oxides such as TiO_2, MnO_2, ZnO, SnO_2 and B_2O_3 was investigated. This choice was in part motivated from the industrial context in which the study was carried out. On one hand, the underlying idea was to explore the possibility to perform the industrial production of these materials (still limited to few manufacturers in the world) and their appropriate characterization in house. On the other, the perspective to produce this kind of glass ceramic materials from waste of ceramic industry processes was considered.

In the first part of this work (Chapter 3) four different systems have been first considered, with the basic glass CMAS composition and no nucleating agent. Subsequently, four modified glasses with an additive oxide (namely, TiO_2, MnO_2, ZnO, SnO_2) have been synthesized and investigated. These additives act by promoting the nucleation and crystal growth during the heat treatments at high temperatures.

As a first step, the thermophysical properties of the selected glasses were investigated in dependence of the main oxide contents, and then with addiction of minor oxides by HSM (Hot Stage Microscope) and Differential

Thermal Analysis (DTA) measurements. The characteristic temperatures have been determined to understand how the glasses evolve during the heat treatment, with particular attention to the sintering ability and the crystallization process. Besides the glass transition temperatures T_g, which should be as high as 700°-750°C, and the melting temperature T_m, that should be relatively low (in the range 1200°-1300°C), a number of parameters proposed in the literature were determined and used to evaluate the glass stability against crystallization. In overall, the results highlight a good stability of the glasses during the heat treatments, especially in the quinary systems, in which the first exothermic peak of crystallization occurs in the temperature range 920°-970°C.

Besides the thermal behaviour, thermomechanical properties of the glasses were also studied as a function of composition. In particular, the evaluation of the coefficient of thermal expansion (CTE) is crucial for sealing applications. CTEs of sealants should match those of other SOFC components to avoid thermal stress and loss of sealing efficiency. With the exception of few Zn- and Mn- containing compositions, all the investigated glasses were found to satisfy the requirement usually recommended for SOFC applications (CTE ranging from $8.0 \cdot 10^{-6} °C^{-1}$ to $12.0 \cdot 10^{-6} °C^{-1}$). The viscosity of the selected glasses, another critical property for sealing operation, was determined and compared to the recommended values, that in all cases resulted fulfilled for the selected compositions.

In the second step, the study the kinetic of crystallization was tackled, in order to better understand the mechanism of devitrification. To this end, different models have been used, following in particular the work published by Kissinger and Matusita, Augis and Bennet and Afify. From the obtained results, we could evaluate the activation energy for the crystallization process and get information on how the nucleation growth takes place, in particular about superficial or bulk nucleation and one, two or three dimensional mechanisms. On this basis, we concluded that the presence of nucleation agents tends to improve the crystallization process lowering activation energy compared to basic aluminosilicate glasses, especially for glasses that exhibit a 3D growth of nuclei. Moreover, from the kinetic results we can conclude also that for modified aluminosilicate glasses, one step crystallization, where the nucleation and crystal growth occur at the same temperatures, is favoured. This phenomenon is possible because the nucleation agents contribute to promoting phase separation and nucleation. To complete the characterization of aluminosilicate glass ceramic, phase formation has been studied by using XRD and SEM analysis. The main phases recorded were Anorthite, Augite and Diopside in all glasses, with less amount of other phases. The SEM images highlighted that the nucleation agents do not participle to phase formation, except in samples where the additive oxide content is as high as the MgO network modifier (CMAS4 series of glasses).

In the second part of the work (Chapter 4), a set of boroaluminosilicates (CMASB, $CaO\text{-}MgO\text{-}Al_2O_3\text{-}SiO_2\text{-}B_2O_3$) has been examined in order to understand how the presence of a different network structure could influence the properties of the glass ceramics. The effect of the same nucleating agents used for CMAS compositions

was also investigated. The stability of these glasses resulted to be lower than aluminosilicates. The crystallization occurs in the range of temperature 920°-990°C, but the nucleation agents were found to have a minor influence in controlling the crystallization step, with the higher activation energy for crystallization promoting one step crystallization. On the basis of the measured thermomechanical properties, glasses belonging to CMASB series exhibit a good behavior with respect to sealing applications. Also in this case, Anorthite, Diopside and Augite are the main phases and either B_2O_3 and nucleation agents do not take part to phase formation.

In the last part of this work (Chapter 5), a new type of glass ceramics deriving from waste is proposed and analysed. The idea is to convert the ceramic waste from sanitary ware industry into glass ceramics which can be used as sealant for SOFC. The need to found an effective reuse/recycling of ceramic industry waste is justified by the large amount of them produced during the sanitary ware manufacturing. Kaoline waste from ceramic industrial process has been chosen as a starting materials. The properties of glass samples derived from waste were then investigated following the same procedures employed for the other systems. On the basis of the CTEs, viscosity and phase analysis, we concluded that these recycled materials can be considered as suitable candidate for sealing application. In particular, the CTE value falls in range required for sealing ($8.99 \cdot 10^{-6}$ $°C^{-1}$), viscosity at 900°C is 8.89 dPa s, an optimal value for sealing applications, and the main crystalline phase was found to be Mullite, one of the most important refractory ceramic material due to its special set of properties such as low density, good chemical stability, high modulus of rupture and low coefficient of thermal expansion.

In overall, appropriate synthesis procedures were put in place for a in house, laboratory scale production of selected glass ceramic compositions of potential use as sealants in high temperature devices, including some samples obtained from the treatment of ceramic industry waste. The thermal, thermomechanical and phase characterization of the synthesized materials showed that the selected materials are appropriate, with few exceptions, for sealing purposes in SOFC technology.

References

[1] L.S. Langston, Am. Soc. Mechanical Eng., Power & Energy, 1 (No.2) (2004).

[2] S.C. Singhal, K. Kendall, "High-temperature Solid Oxide Fuel Cells: Fundamentals, Design and Applications" Elsevier Ltd, Amsterdam, (2003).

[3] S.M. Haile, Acta Mater. 51 (2003) 5981.

[4] C.K. Lin,"Overview of Solid Oxide Fuel Cells", Conference, National Central University Taiwan, (2011).

[5] P. Knauth, H.L. Tuller, J. Am. Ceram. Soc. 85 (2002) 1654.

[6] R.Bove, S.Ubertini, "Perovskite Oxide for Solid Oxide Fuel Cells", Springer, New York, (2008).

[7] D. Stöver, H.-P. Buchkremer, J. P. P. Huijsmans, Handbook of Fuel Cells: Fundamentals, Technology and Applications", (Eds.), John Wiley & Sons, Chichester, U.K., vol. 4 (2003) 1015.

[8] J. Malzbender, E. Wessel, R. W. Steinbrech, L. Singheiser, Ceram. Eng. & Sci. Proc., vol. 25 (2004) 387.

[9] R.E. Loehman, T.Garino, R.Tandon, E. Corral, M.Brochu, S. Widgeon, "Filled Glass Composites for Sealing of Solid Oxide Fuel Cells", Coference, California, (2009).

[10] J.Y.Tian, "Analysis of mechanical properties for the joint of metallic interconnect and glass ceramic in Solid Oxide Fuel Cell", Conference, National Central University Taiwan, (2010).

[11] C.K. Lin, "Analysis of High-Temperature Mechanical Durability of SOFC Stack Joints", Conference National Central University Taiwan, (2011).

[12] J.W. Tian, "Analysis of thermal stresses and mechanical properties for the components of Solid Oxide Fuel Cell", Conference, National Central University Taiwan, (2010).

[13] J.W. Fergus, R. Hui, X. Li, D.P. Willinson, "Solid Oxide Fuel Cells", CRC Press, Boca Raton, (2009).

[14] S.P.S. Badwal, K. Foger, Ceram. Int. 22 (1996) 257.

[15] N.Q. Minh, J. Am. Ceram. Soc. 76 (1993) 563.

[16] W. Bujalski, "Sustainable Energy Systems", Conference Birmingham, (2009).

[17] P. Huczkowski, W.J.Quadakkers, "Effect of geometry and composition of Cr steels on oxide scale properties relevant for interconnector applications in Solid Oxide Fuel Cells (SOFCs)", Forschungzentrum Julich GmbH, Dissertation, (2005).

[18]. S.M. Haile, Acta Mater. 51 (2003) 5981.

[19] R.M. Ormerod, Chem. Soc. Rev. 32 (2003) 17.

[20] K. Somroop, P. Lorwichit, S. Charojrochkul, P. Limthongkul, Eur J Solid State Inorg Chem. 13 (2011) 1365.

[21] J.W. Fergus, R. Hui, X. Li, D.P. Willinson, "Solid Oxide Fuel Cells: Materials Properties and Performance", CRC Press, Boca Raton, 2010.

[22] A.B. Stambouli, E.Traversa, Renew Sust Energ Rev. 6 (2002) 433.

[23] R.M. Ormerod, Chem. Soc. Rev. 32 (2003) 17.

[24] W.Z. Zhu, S.C. Deevi, Mat. Sci. Eng. A362 (2003) 228.

[25] D.Stolten, B.Emonts, “Fuel Cell Science and Engineering”, Wiley-VCH, Weinheim, (2012).

[26] S.M. Haile, Acta Mater. 51 (2003) 5981.

[27] A.F. Sammels, M.V. Mundschau, “Nonporous Inorganic Membranes: for Chemical Processing”, Wiley-VCH Verlag GmbH & Co. KGaA (2006)

[28] N. Q. Minh, Ceramic Fuel Cell, J. Am. Ceram. Soc. 76 (1993) 563.

[29] J. Malzbender, E. Wessel, R. W. Steinbrech, L. Singheiser, Ceram. Eng. & Sci. Proc., Vol. 25 (2004) 387.

[30] W.Z. Zhu, S.C. Deevi, J. Mat. Sci. Eng. 348 (2003) 227.

[31] F.Tietz, D. Simwonis, P. Batfalsky, U. Diekmann, D. Stover, “Degradation phenomena during operation of Solid Oxide Fuel Cells”, in Proc. 12th IEA Workshop SOFC: Mater. & Mechanisms, K. Nisancioglu (Eds), Int. Energy Agency, (1999) 3.

[32] Z.G. Yang, S.P. Simner, P.Singh, G.G. Xia, “Electrochemical Materials and System”, Conference Washington, (2005).

[33] http://www.stubhollow.com/Transportation/Electric/boats/fuelcellboat.htm., (2012).

[34] A.B. Stambuoli, E. Traversa, Renew Sust Energ Rev. 8 (2008) 328.

[35] C. A. Handwerker, J. E. Blendell, W. Kaysser, Amer. Ceram. Soc., 7 (1990) 436.

[36] J. W. Fergus, J. Power Sources 147 (2005) 46.

[37] K. S. Weil, J. Mater. 58 (2006) 37.

[38] M. P. Mahapatra, K. Lu, J. Power sources 195 (2010) 7129.

[39] F. Smeacetto, M. Salvo, P.Leone, M. Ferraris, J. Eur. Soc. 30 (2009) 933.

[40] K.S. Weil, JOM 52 (2006) 37.

[41] K.D. Meinhardt, D.S. Kim, Y.S. Chou, K.S. Weil, J. Power Sources 182 (2008) 188.

[42] J. Malzbender, Y. Zhao, J. Mat. ScI. 47 (2012) 4342.

[43] J.E. Shelby, “Introduction to Glass Science and Technology: Edition 2” Royal Society of Chemistry, Cambridge, 2005.

[44] W. D. Kingery, H.K. Bowen, D.R. Uhlmann, “Introduction to ceramics”, John Wiley & Sons NY (1976).

[45] M. K. Mahapatra, K. Lu, J. Mat. Sci. Eng. 67 (2010) 65.

[46] Y-S Chou, J.W. Stevenson, R.N. Gow, J. Power Sources 168 (2007) 395.

[47] C. W. Parmelee, C.G. Harman, “Ceramic Glazes, third edition”, Chaners Books (1973).

[48] R. Zheng, S.R. Wang, H.W. Nie et Al., J. Power Sources 128 (2004) 165.

[49] G.V. Kukolev, “Silicon Chemistry and Physical Chemistry of Silicates”, Higher School Publ., Moscow, (1966).

[50] H.R. Fernandes, D.U. Tulyaganov, A. Goel, M.J. Ribeiro, M.J. Pascual, J.M.F. Ferreira, J. Eur. Ceram. Soc. 30 (2010) 2017.

[51] J.E. Shelby, “Introduction to Glass Science and Technology, Royal Society of Chemistry”, Cambridge, (1997).

[52] J.I. Kroschwitz, A. Seidel, Kirk-Othmer, "Encyclopedia of Chemical Technology", Wiley-Interscience, Chichester, (2006).

[53] W. Vogel, "Chemistry of Glass", American Ceramic Society (1985).

[54] H.G. Pfaender, "Schott Guide to Glass", Chapman & Hall, (1996).

[55] J. Schilm, in: 1st Joint European Summer School on Fuel Cell and Hydrogen Technology, Viterbo, Italy, (2011).

[56] W. Lui, X. Sun, M. Khaleel, "Advances in Ceramics", In Tech, Richland, (2011).

[57] S. Ghosh, P. Kundu, A.D. Sharma, R.N. Basu, J. Eur. Ceram. Soc. 28 (2008) 69.

[58] P. Geasee, T. Schwickert, U. Diekmann, R. Conradt, "Ceramic Materials and Components for Engines", J.G. Heinrich (Eds), Wiley-VCH Veralg GmbH, Weinheim (2001) 57.

[59] C. Lara, M. J. Pascual, A. Durán, J. Non-Crystal. Solids 348 (2004) 149.

[60] H. Scholze, "Glass. Nature, Structure, and Properties"Springer Verlag, New York, (1991).

[61] R. Conradt, H. Bach, D. Krause (Eds), "Fiberglass and Glass Technology: Energy-Friendly Compositions and Applications" Springer Verlag, Berlin (1999) 232.

[62] A.P. Tomsia, J.A. Pask, R.E. Loehmann, Engineering Materials Handbook, "Ceramics and Glasses", S. J. Schneider (Eds.), A.S.M. Int., vol.4 (1991).

[63] I.W. Donald, Review, J. Mater. Sci. 28 (1993) 2841.

[64] P. W. McMillan, Academic Press, London, (1979) 229.

[65] Z. Strnad, "Glass-Ceramic Materials: Liquid Phase Separation, Nucleation and Crystallization in Glasses (Glass Science and Technology)", Elsevier, Amsterdam (1986) 268.

[66] W.Holand, G.H. Beall, "Glass-ceramic technology", Am. Ceram. Soc., Westerville, OH (2002) 372.

[67] J.Malzbender, R.W. Steinbrech, J. Power Sources 173 (2007) 60.

[68] D.Bahadur, N. Lahl, K. Singh, L.Singheiser, K.Hilpert, J. Electrochem. Soc. A558 (2004) 151.

[69] T. Zhang, Q. Zhu, Z. Xie, J. Power Sources, 188 (2009) 177.

[70] J. W. Fergus, R.Hui, X. Lui, D.P. Willinson, "Cathodes in Solid Oxide Fuel Cells: Materials Properties and Performances", CRC Press, Boca Raton, (2009).

[71] Y.Sakaki, M. Hattori, Y. Esaki, S. Ohara, T. Fukui, K. Kodera, Y. Kubo, J. Electrochem. Soc. 97 (40) (1997) 652.

[72] S. Ohara, K. Mukai, T.Fukui, Y. Sakaki, M. Hattori, Y. Esaki, J. Ceram. Soc. Of Japan 109 (2001) 186.

[73] M. Guedes, A.C. Ferro, J.M. Ferreira, J. Eur. Ceram. Soc. 21 (2001) 1187.

[74] P. Geasee, T. Schwickert, R. Conradt, DVS Verlag, Düsseldorf 212 (2001) 304.

[75] N. Lahl, L. Singheiser, K. Hilpert, Honolulu, FL, Electrochem. Soc. Proc., Pennington, NJ, PV 99-19 (1999) 1057.

[76] N. Lahl, K. Singh, L. Singheiser, D. Bahadur, K. Hilpert, J. Mater. Sci. 35 (2000) 3089.

[77] P. Geasee, Thesis RWTH Aachen, Logos Verlag Berlin, (2003) 179.

[78] S. B. Sohn, S. Y. Choi, G. H. Kim, H. S. Song, G. D. Kim, J. Amer. Ceram. Soc. 87 (2004) 254.

[79] C. Lara, M. J. Pascual, M. O. Prado, A. Durán, Solid State Ionics 170 (2004) 201.

[80] N. P. Bansal, E. A. Gamble, J. Power Sources 147 (2005) 107.

[81] N. P. Bansal, M. J. Hyatt, Ceram. Eng. Sci. Proc.12 (1991), 1222.

[82] Y. S. Touloukian, "Thermophysical Properties of High Temperature Solid Materials", MacMillan Co., New York, 6 (1967).

[83] D. Bahat, J. Mater. Sci. 7 (1972) 198.

[84] K. Eichler, G. Solow, P. Otschik, W. Schaffrath, J. Europ. Ceram. Soc. 19 (1999) 1101.

[85] N. Lahl, K. Singh, L. Singheiser, D. Bahadur, K. Hilpert, J. Electrochem. Soc. 149 (2002) A607.

[86] Y. M. Sung, The, J. Mat. Sci. 31 (1996) 5421.

[87] B.C. Bunker, R.J. Kirkpatrick, R.K. Brow, G.L. Turner, C. Nelson, J. Am. Ceram. Soc. 74 (1991) 1430.

[88] J.E. Shelby, "Introduction of Glass Science and Technology", Royal Society of Chemistry, Cambridge, 2005.

[89] S. B. Sohn, S. Y. Choi, G. H. Kim, H. S. Song, G. D. Kim, J. Non-Crystal. Solids 297 (2002) 103.

[90] K. L. Ley, S. B. Sohn, S. Y. Choi, G. H. Kim, H. S. Song, G. D. Kim, J. Non-Crystal. Solids 321 (2005) 207.

[91] M. Krumpelt, R. Kumar, J. H. Meiser, I. Bloom, J. Mater. Sci. 11 (1996) 1489.

[92] M. Hillers, G. Matzen, E. Veron, M. Dutreilh-Colas, A. Douy, J. Am. Ceram. Soc. 90 (2007) 720.

[93] P. H. Larsen, P. F. James, J. Mater. Sci. 33 (1998) 2499.

[94] P. H. Larsen, F. W. Poulsen, R. W. Berg, J. Non-Crystal. Solids 244 (1999) 16.

[95] S. P. Jiang, L. Christiansen, B. Hughan, K. Foger, J. Mater. Sci. Letters 20 (2001) 695.

[96] T. Horita, H. Kishimoto, K. Yamaji, Y. Xiong, N. Sakai, M. E. Brito, H. Yokokawa, J. Electrochem. Soc. 153 (2006) A2007.

[97] Z. Yang, K. D. Meinhardt, J. W. Stevenson, J. Electrochem. Soc. 150 (2003) A1095.

[98] Z. Yang, J. W. Stevenson, K. D. Meinhardt, Solid State Ionics 160, (2003) 213.

[99] C. W. F. T. Pistorius, M. C. Pistorius, Z. Kristallogr, 117 (1962) 259.

[100] V. A. C. Haanappel, V. Shemet, S. M. Gross, T. Koppitz, N. H. Menzler, M. Zahid, W. J. Quaddakers, J. Power Sources 150 (2005) 86.

[101] N. H. Menzler, D. Sebold, M. Zahid, S. M. Gross, T. Koppitz, J. Power Sources 152 (2005) 156.

[102] L. Blum et al., Proc. 9th Int. Symp. Solid Oxide Fuel Cells (SOFC IX), Montreal, Quebec, Electrochem. Soc. Proc., Pennington, NJ, 2005-01 (2005) 39.

[103] S. Mukerjee et al., Proc. 9th Int. Symp. Solid Oxide Fuel Cells (SOFC IX), Montreal, Quebec, Electrochem. Soc. Proc., Pennington, NJ, (2005) 48.

[104] L. Blum, H. P. Buchkrmer, S.Gross et al, Forschungszetrum Julich Fuel Cells 7 (2007) 204.

[105] P. Jinhua, S. Kening, Z. Naiquing, et al., J. Rare Earth 25 (2007) 434.

[106] V. Kumar, A. Arora, O.P. Pandey et al., Int. J. Hydr. Energy 33 (2008) 434.

[107] V.A.C. Haanappel, V. Shemet, I.C. Vinke et al., J. Power Sources 141 (2005) 102.

[108] K.A. Nielsen, M. Solvang, F.W. Poulsen et al., "Advances in Solid Oxide Fuel Cells", Ceramic Engineering and Science Proceedings (2005) 239.

[109] N.H. Mentzler, D. Sebold, M. Zahid et al., J. Power Sources 152 (2005) 156.

[110] N.H. Menzler. M.B. Ram, H.P. Buchkremer et al., J. Ceram. Soc. 23 (2003) 445.

[111] H.N. Xiao, Y. Cheng, L.P. Yu, H.B. Liu, Mater. Sci. Eng. A 431 (2006) 191.

[112] A.A. Reddy, A. Goel, D.U. Tulyaganov, S. Kapoor, K. Pradeesh, M.J. Pascual, J.M.F.Ferreira, J. Power Sources 231 (2013) 203.

[113] W. Höland, G.H. Heall, "Glass–Ceramic Technology", Wiley, (2012). 346.

[114] A. Karamanov, L. Arriza, I. Matekovits, M. Pelino, Ceram. Int. 30 (2004) 2119.

[115] M. J. Pascual, L. Pascual, A. Duran, Phys. Chem. Glasses 42 (2001) 61.

[116] M. J. Pascual, A. Duran, M. O. Prado, Phys. Chem. Glasses 46 (2005) 512.

[117] W. A. Johnson, R. F. Mehl, Trans. Am. Inst. Min. Metall. Pet. Eng. 135 (1939) 416.

[118] M. Avrami, J. Chem. Phys. 7, (1939) 1103.

[119] D. W. Henderson, J. Non-Crystal. Solids 30 (1979) 301.

[120] M. C. Weinberg, J. Non-Crystal. Solids 142 (1992) 126.

[121] K. Matusita, S. Sakka, J. Non-Crystal. Solids 38-39 (1980) 741.

[122] K. Matusita, S. Sakka, Phys. Chem. Glasses 20 (1979) 81.

[123] K. Matusita, S. Sakka, Bull. Inst. Chem. Res., Kyoto Univ. 59 (1981) 159.

[124] A. Marotta, A. Buri, S. Saiello, J. Thermal Anal. 23 (1982) 239.

[125] F. Branda, A. Marotta, A. Buri, Thermochim. Acta 135 (1988) 91.

[126] H. J. Borchardt, F. Daniels, J. Am. Chem. Soc. 79 (1957) 41.

[127] H. J. Borchardt, J. Inorg. Nucl. Chem. 12 (1960) 252.

[128] G. O. Piloyan, I. D. Rybachikov, O. S. Novikova, Nature 5067 (1966) 1229.

[129] J. A. Augis, J. E. Bennett, J. Therm. Anal. 13 (1978) 283.

[130] H. E. Kissinger, J. Res. Natl. Bur. Stand. (U.S.) 57 (1956) 217.

[131] H. E. Kissinger, Anal. Chem. 29 (1957) 1702.

[132] T. Ozawa, J. Therm. Anal. 2 (1970) 301.

[133] T. Ozawa, J. Therm. Anal. 9 (1976) 369.

[134] T. Ozawa, Polymer 12 (1970) 150.

[135] P.W. McMillan, "Glass-Ceramics", 2nd EditionAcademic Press, London, 1979.

[136] M.H. Idris, G.A. Khater, Phys. Chem. Glasses 45 (2004) 141.

[137] G.H. Beal, J. Non-Cryst. Solids 129 (1991) 163.

[138] A.W.A. El-Shennawi, A.A. Omar, G.A. Khater, Glass Technol. 32 (1991) 131.

[139] M.H. Idris, Ph.D. Thesis, Cairo Univ., (2002).

[140] T. Maehara, T. Yano, S. Shibata, M. Yamane, Phil. Mag. 84 (2004) 3085.

[141] B.H.W.S.D. Jong, K.D. Keefer, C.M. Taylor, Geochim. Cosmochim. Acta 45 (1981) 1291.

[142] B.H.W.S.D. Jong, C.M. Schramm, V.E. Parziale, J. Am. Chem. Soc. 106 (1984) 4396.

[143] P. Taylor, A.B. Campbell, D.G. Owen, J. Am. Ceram. Soc. 66 (1983) 347.

[144] D. Turnbull, Contemp. Phys. 10 (1969) 473.

[145] D. R. Uhlmann, J. Non-Crystal. Sol. 7 (1972) 337.

[146] A. Hrubÿ, Czech J. Phys. B 22 (1972) 1187.

[147] M. C. Weinberg, Phys. Chem. Glasses 35 (1994) 119.

[148] M. L. F. Nascimento, L. A. Souza, E. B. Ferreira, E. D. Zanotto, J. Non-Crystalline Sol. 351 (2005) 3296.

[149] I. Avramov, E. D. Zanotto, M. O. Prado, J. Non-Crystal. Sol. 320 (2003) 9.

[150] C. Lara, M.J. Pascual, A. Duran, J. Non Cryst. Solids 348 (2004) 149.

[151] M.O. Prado, E.D. Zanotto, R. Muller, J. Non-Cryst. Solids 279 (2001) 169.

[152] J. Frenkel, J. Phys. 9 (1945) 385.

[153] J.K. Mackenzie, R. Shuttleworth, Proc. Phys. Soc. (London) 62 (1949) 833.

[154] K.Kanehashi, J.F. Stebbins, J. Non-Cryst. Solids 353 (2007) 4001.

[155] S. Morimoto, N. Kuriyama, J. Ceram. Soc. Jpn. 104 (5) (1996) 442.

[156] M. Rezvani, Y.B. Eftekhari, H.M. Solati, Ceram. Int., 31 (2005) 75.

[157] B.E. Yekta, P. Alizadeh, L. Rezazadeh, J. Eur. Ceram. Soc., 26 (2006) 3809.

[158] A. Goel, D U. Tulyaganov, E. R. Shaaban, R. N. Basu, J. M. Ferreira, J. Appl. Phys. 104 (2008) 043529.

[159] K. Roessler, “Gmelin’s Handbook of Inorganic Chemistry”, Chemie, Leipzig, (1992).

[160] I.W. Donald, B.L. Metcalfe, L.A. Gerrard, J. Am. Ceram. Soc. 91 (2008) 715.

[161] I.W. Donald, J. Mater. Sci. 28 (1993) 2841.

[162] R. Kirsch, ”Glass Science and Technology”, vol. 13, Elsevier, Amsterdam, (1993) 352.

[163] S.P. Jiang, S.H. Chan, J. Mater. Sci. 39 (2004) 4405.

[164] M. Radovic, E. Lara-Curzio, R.M. Trejo, H. Wang, W.D. Porter, Ceram. Eng. Sci. Proc. 27 (2006) 79.

[165] S. Majumdar, T. Clarr, B. Flandermeyer, J. Am. Ceram. Soc. 69 (1986) 628.

[166] E.A. Brandes, G.B. Brook, Smithells “Metals Reference Book”, 7th ed., Butterworth Heinemann, Oxford, (1992) 14.

[167] M. Mori, Y. Hiei, N.M. Sammes, G.A. Tompsett, J. Electrochem. Soc. 147 (2000) 1295.

[168] Z. Yang, Int. Mater. Rev. 53 (2008) 39.

[169] M.B. Volf, “Glass Science and Technology”, Elsevier, Amsterdam (1984).

[170] S.T. Reis, R.K. Brow, J. Mater. Eng. Perform. 15 (2006) 410.

[171] M.J. Pascual, A. Guillet, A. Dura´n, J. Power Sources 169 (2007) 40.

[172] S.T. Reis, R.K. Brow, T. Zhang, P. Jasinski, Ceram. Eng. Sci. Proc. 27 (2006) 297.

[173] M. Rezvani, B. Eftekhari Yekta, and K. Marghussian, J. Eur. Ceram. Soc. 25 (2005) 1525.

[174] H. Zheng, Y.Pu, X. Liu, J. Wan, J. Alloy. Compd. 672 (2016) 272.

[175] G. Qu, X. Hu, L. Cui, Ceram. Int. 40 (2014) 4213.

[176] S. Banijamali, B. Eftekhari Yekta, H.R. Rezaie, V.K. Marghussian, Thermochim. Acta 488 (2009) 60.

[177] R. W. Douglas, Nature 207 (1965) 674.

[178] C. Russel, Chem. Mater. 17 (2005) 5843.

[179] R. Casasola, J. M. Rincon, M. Romero, J. Mater. Sci. 47 (2011) 553.

[180] K. Zhang, J. Liu, W, Lui, J. Yang, Chemosphere 85 (2011) 689.

[181] R.D. Rawlings, J.P. Wu, A.R. Boccaccini, J. Mater. Sci. 41 (2006) 733.

[182] P. Alizadeh, V. K. Marghussian, J. Eur. Ceram. Soc. 20 (2000) 765.

[183] P. Alizadeh, V. K. Marghussian, J. Eur. Ceram. Soc. 18 (2003) 775.

[184] J. Yang, B. Liu, S. Zhang, A. A. Volinsky, J. of Alloys and Comp. 688 (2016) 709.

[185] L. N. Brush, E. Le, Cryst. Growth. Des. 6 (2006) 379.

[186] C. Patzig, T. Hoche, M. Dittmer, C. Russel, Cryst. Growth. Des. 12 (2012) 2059.

[187] S. Bhattacharyya, T. Hoche, J.R. Jinschek, I. Avramov, R. Wurth, M. Muller, C. Russel, Cryst. Growth. Des. 10 (2010) 379.

[188] T. Hoche, C.Patzig, T. Gemming, R. Wurth, C. Russel, I. Avramov, Crystal. Growth. Des. 12 (2012) 1556.

[189] V. S. Raghuwanshi, C. Russel, A. Hoell, Cryst. Growth. Des. 14 (2014) 2823.

[190] A. De Pablos-Martin, C. Patzig, T. Hoche, A. Duran, M. J. Pascual, Cryst. Eng. Comm. 15 (2013) 6979.

[191] S. Bhattacharyya, C. Bocker, T. Heil, J.R. Jinschek, T. Hoche, C. Russel, H. Kohl, Nano Lett. 9 (2009) 2493.

[192] J.E. Shelby, “Introduction to glass science and technology”, Royal Society of Chemistry (RSC)-Paperbacks (1997).

[193] M.J. Pascual, M.O. Prado, A. Duran, Phys. Chem. Glass, 46 (2005) 512.

[194] J.W. Fergus, J.Power Sources 147 (2005) 46.

[195] N.P. Bansal, E.A. Gamble, J. Power Sources 147 (2005) 107.

[196] A. Goel, D. U. Tulyaganov, I. K. Goel, E.R. Shaaban, J.M.F. Ferreira, J. Non Cryst. Solids 355 (2009) 193.

[197] T. Zhang, R.K. Brow, S.T. Reis, C.S. Ray, J. Am. Ceram. Soc. 91 (2008) 3235.

[198] M.J. Pascual, C. Lara, A. Duran, Phys. Chem. Glasses 47 (2006) 572.

[199] K. Eichler, G. Solow, P. Otschik, W. Schaffrath, J. Eur. Ceram. Soc. 19 (1999) 1101.

[200] Y. Sakaki, M. Hattori, Y. Esaki, S. Ohara, T. Fukui, K. Kodera, Y. Kubo, Electrochem. Proc. 18 (1997) 652.

[201] I. Avramov, J. Non-Cryst. Solids 353 (2007) 2889.

[202] H. Yinnon, D.R. Uhlmann, J. Non-Cryst. Solids 44 (1981) 37.

[203] T. Jin, K. Lu, J. Power Sources 195 (2009) 195.

[204] M.K. Mahapatra, K. Lu, W.T. Reynonds Jr., J. Power Sources 179 (2008) 106

[205] R. Zheng, S.R. Wang, H.W. Nie, T.L. Wen, J. Power Sources 128 (2004) 165.

[206] X. Guo, X. Cai, J. Song, G. Yang, J. Non-Cryst. Solids 405 (2014) 63.

[207] H. C. Li, D.G. Wang, J.H. Hu, C. Z. Chen, Matter. Lett. 106 (2013) 373.

[208] J. Cao, Z. Wang, J. Alloy and Comp. 557 (2013) 190.

[209] H.C. Li, D. G. Wang, C. Z. Chen, F. Weng, H. Shi, Ceram. Int. 42 (2016) 1439.

[210] L. Ren, H. Zhou, X. Li, W. Xie, X. Luo, J. Alloy and Comp. 646 (2015) 780.

[211] D. P. Mukherjeen, S. K. Das, Ceram. Int. 39 (2013) 571.

[212] G. A. Khater, Ceram. Int. 37 (2011) 2193.

[213] K. P. O'Flynn, K. T. Stanton, Crystal. Growth. Des. 10 (2010) 1111.

[214] E. Ercenk, J. Non-Cryst. Solids 387 (2014) 101.

[215] G. A. Khater, Ceram. Int. 37 (2011) 2193.

[216] M. Rezvani, B. Eftekhari-Yekta, M. Solati-Hashjin, V. K. Marghussian, Ceram. Int. 31 (2005) 75.

[217] M. S. Ma, W. Ni, Y. L. Wang, Z. J. Wang, F. M. Liu, J. Non-Cryst. Solids 354 (2008) 5395.

[218] S. M. Wang, Environ. Sci. Technol. 44 (2010) 4816.

[219] S.M. Wang, F.H. Kuang, Q. Z. Yan, C. C. Ge, L. H. Qi, J. Alloys Compd. 509 (2011) 2819.

[220] G. H. Chen, J. Mater. Sci. 42 (2007) 7239.

[221] R. C. De Vekey and A. J. Nakayama, Phys. Chem, Glasses,16 (1975) 36.

[222] S.B. Sohn, S.Y. Choi, G.H. Kim, H.S. Song, G.D. Kim J. Non-Cryst. Solids 297 (2002) 103.

[223] S.B. Sohn, S.Y. Choi, G.H. Kim, H.S. Song, G.D. Kim, J. Am. Ceram. Soc. 87 (2004) 254.

[224] K.L. Ley, M. Krumpelt, R. Kumar, J.H. Meiser, I. Bloom, J. Mater. Res. 11 (1996) 1489.

[225] M.K. Mahapatra, K. Lu, R.J. Bodnar, Appl. Phys. A, 95 (2009) 493.

[226] F. Smeacetto, M. Salvo, M. Ferraris, V. Casalegno, P. Asinari, J. Eur. Ceram. Soc. 28 (2008) 611.

[227] T. Shwickert, R. Sievering, P. Geasee, and R. Conradt, Mat-Wiss. U. J. Am. Ceram. Soc. 33 (2002) 363.

[228] K. D. Meinhardt, J. D. Vienna, T. R. Armstrong, L. R. Pederson, US patent 6430966 B1 (2002).

[229] T. Zhang, W.G. Fahrenholtz, S.T. Reis, R.K. Brow, J. Am. Ceram. Soc. 91 (2008) 2564.

[230] M. Tomozawa, M. Takata, J. Acocella, E.B. Watson, T. Takamori, J. Non-Cryst. Solids 56 (1983) 343.

[231] R.H. Doremus, Y. Mehrotra, W.A. Lanford, C. Burman, J. Mater. Sci. 18 (1983) 612.

[232] Y. Moriya, M. Nogami, J. Non-Cryst. Solids 38–39 (1980) 667.

[233] M. Tomozawa, J. Non-Cryst. Solids 73 (1985) 197.

[234] D. Carter, A. Call, M. Ferrandon, J. Kropf, V. Maroni, J. Mawdsley, D. Myers, B. Yıldız, CH16EL11 and N-AN07EL0101 FY'06 Report, Argonne National Laboratory, 2006.

[235] P. Singh, S.D. Vora, Ceram. Eng. Sci. Proc. 26 (2005) 99.

[236] M. ToMozawa, S. Capella, J. Am. Ceram. Soc. (1983) C24.

[237] C. Wang, L. Zhou, J. Non-Cryst. Solids 80 (1986) 360.

[238] V.L. Stolyarova, E.N. Plotnikov, Glass Phys. Chem. 31 (2005) 30.

[239] K. Ogasawara, H. Kameda, Y. Matsuzaki, T. Sakurai, T. Uehara, A. Toji, N. Sakai, K. Yamaji, T. Horita, H. Yokokawa, J. Electrochem. Soc. 154 (2007) B657.

[240] M. Cable, in: L.D. Pye, V.D. Frechette, N.J. Kreidl, "Borate Glasses: Structure, Properties, Applications (Materials Science Research)" vol. 12, Plemum Press, New York, (1978), 399.

[241] M.J. Snyder, M.G. Mesko, J.E. Shelby, J. Non-Cryst. Solids 352 (2006) 669.

[242] J. Simon, Ceram. Trans. 141 (2004) 389.

[243] E.M. Birtch, J.E. Shelby, Ceram. Trans. 141 (2003) 347.

[244] S. Huang, S. LI, F. Wu, Y. Yue, J. Inorg. Organomet. Polym. 14 (1975) 1014.

[245] C. Lara, M.J. Pascual, M.O. Prado, A. Dura´n, Solid State Ionics 170 (2004) 201.

[246] R.E. Loehman, H.P. Dumm, H. Hofer, Ceram. Eng. Sci. Proc. 23 (2002) 699.

[247] K. Lu, M.K. Mahapatra, J. Appl. Phys. 104 (2008) 074910.

[248] M.J. P.ascual, M.O. Prado, A. Duran, Phys. Chem. Glasses 46 (2005) 512.

[249] J. F. MacDowell and G. H. Beall, J. Am. Ceram. Soc. 52 (1969) 17.

[250] R. Kondo, M. Daimon, M. Asakawa, T. Ito, Annual Rep. Cemet Tech. 28 (1974) 94.

[251] H. Uchikawa, H, Obama, World Cement, (1995) 33.

[252] A. Bernasconi, V.Diella, N. Marioni, A. Pavese, F. Francescon, Ceram. Int. 38 (2012) 5859.

[253] C. Yhen, G. S. Lan, W. H. Tuan, Ceram. Int. 26 (2000) 715.

[254] N. Tezuka, I. M. Low, I. J. Davies, M. Prior, A. Studer, Physica B385 (2006) 555.

[255] H. Schneider, J. Schreuer, B Hildmann, J. Eur. Ceram. Soc. 28 (2008) 329.

[256] M. Bartsch, B. Saruhan, M. Schmucker, H. Schneider, J. Am. Ceram. Soc. 74 (1999) 2448.

[257] I.A.Aksay, J. A. Pask, J. Am. Ceram. Soc. 58 (1975) 507.

[258] S. H. Risbud, J. A. Pask, J. Mater. Sci. 13 (1978) 2449.

[259] M. V. Magliano, V. C. Pandolfelli, Ceramica 56 (2010) 368.

[260] M. Panneerselvam, K. J. Rao, Chem. Mater. 15 (2003) 2247.

Appendix 1

Annex 1: Thermophysical properties of CMAS glass series

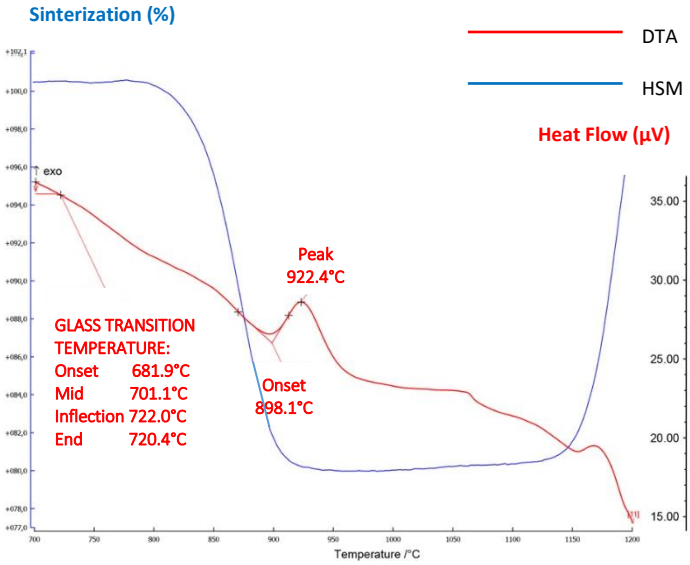

Figure A1 HSM and DTA curves on the temperature scale for CMASTi2.

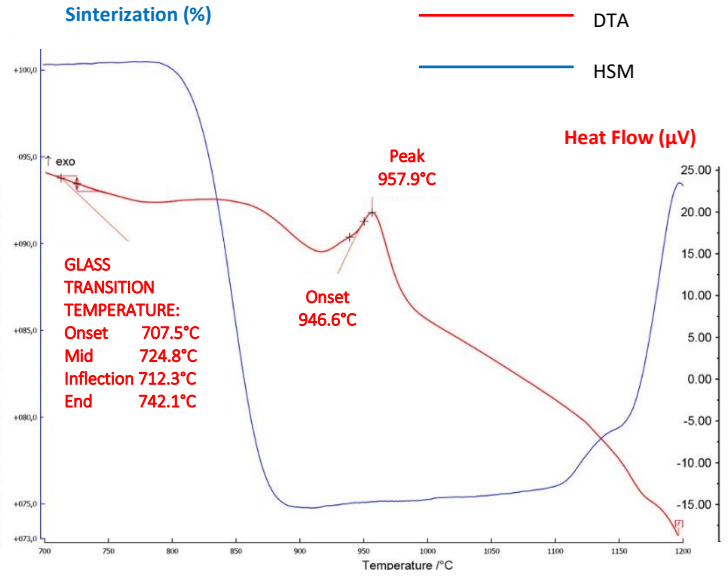

Figure A2 HSM and DTA curves on the temperature scale for CMASTi3.

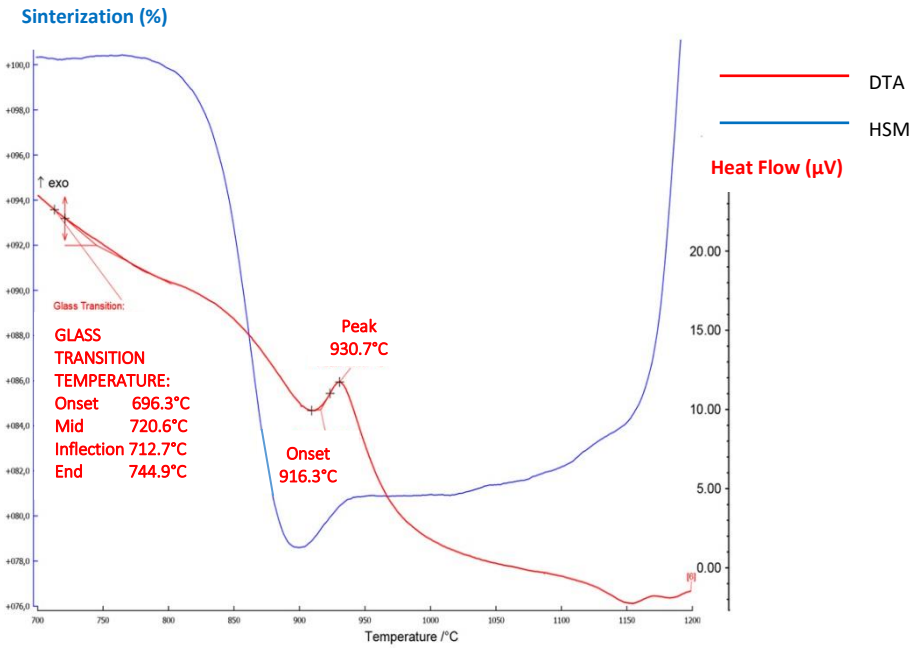

Figure A3 HSM and DTA curves on the temperature scale for CMASTi4.

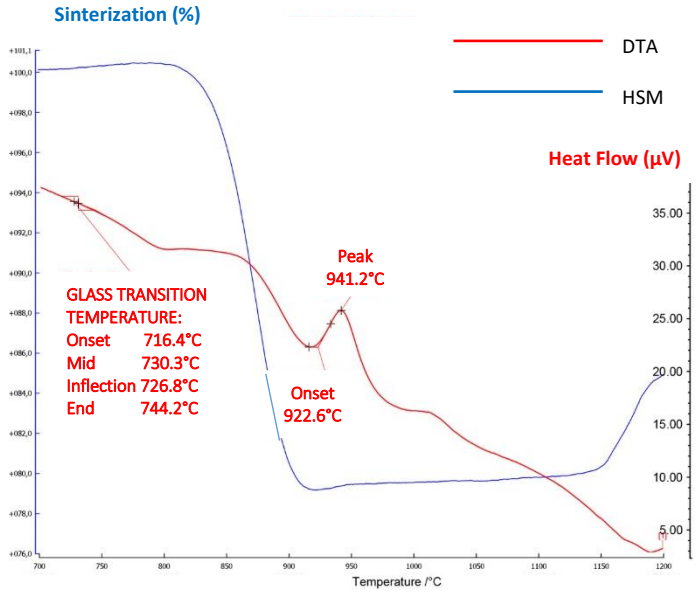

Figure A4 HSM and DTA curves on the temperature scale for CMASMn1.

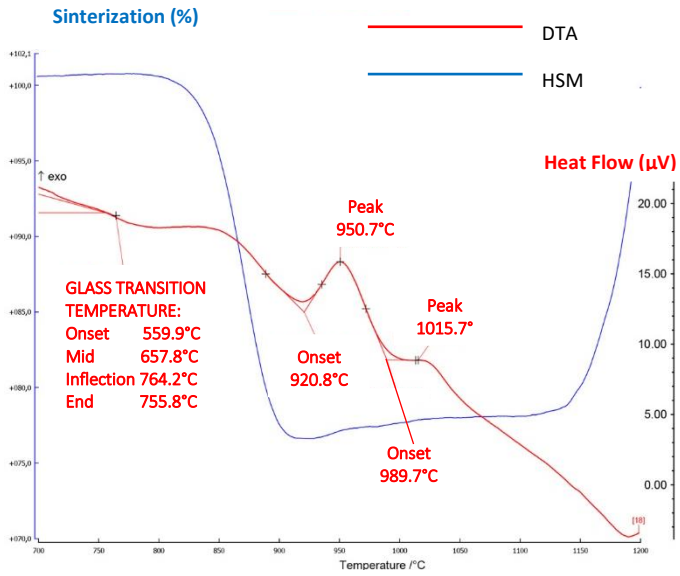

Figure A5 HSM and DTA curves on the temperature scale for CMASMn3.

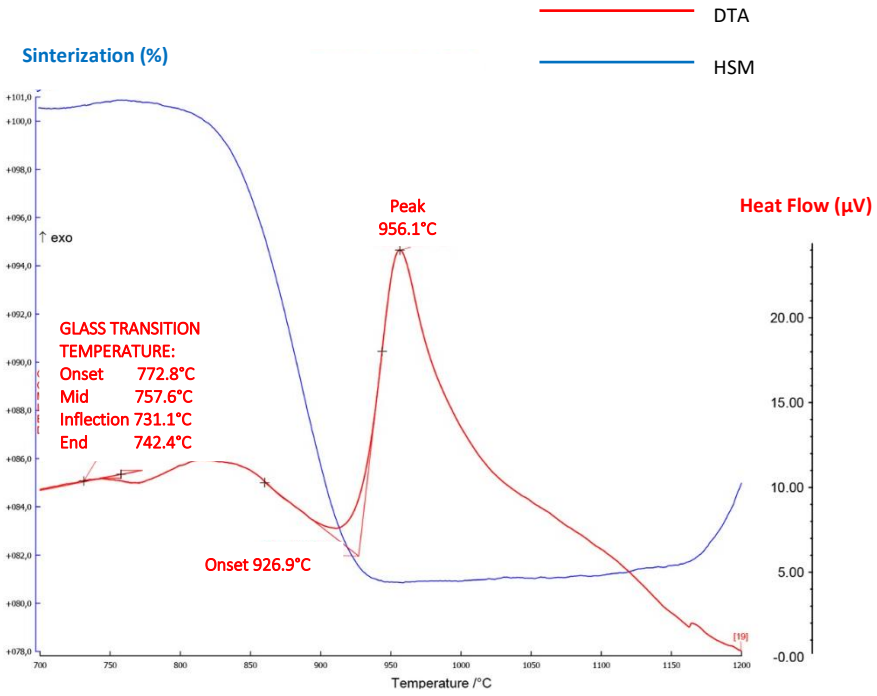

Figure A6 HSM and DTA curves on the temperature scale for CMASMn4.

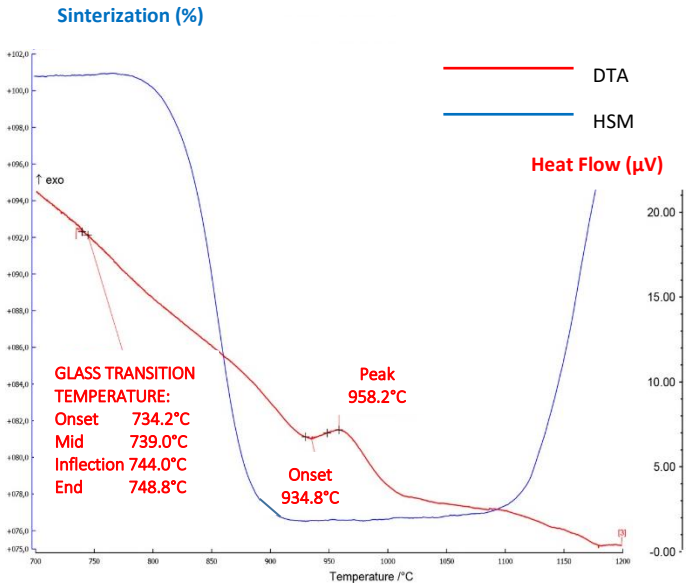

Figure A7 HSM and DTA curves on the temperature scale for CMASZn1.

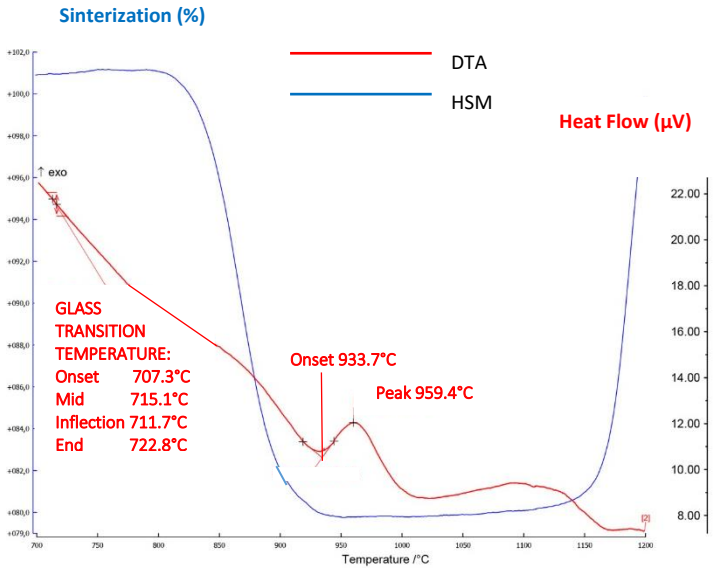

Figure A8 HSM and DTA curves on the temperature scale for CMASZn3

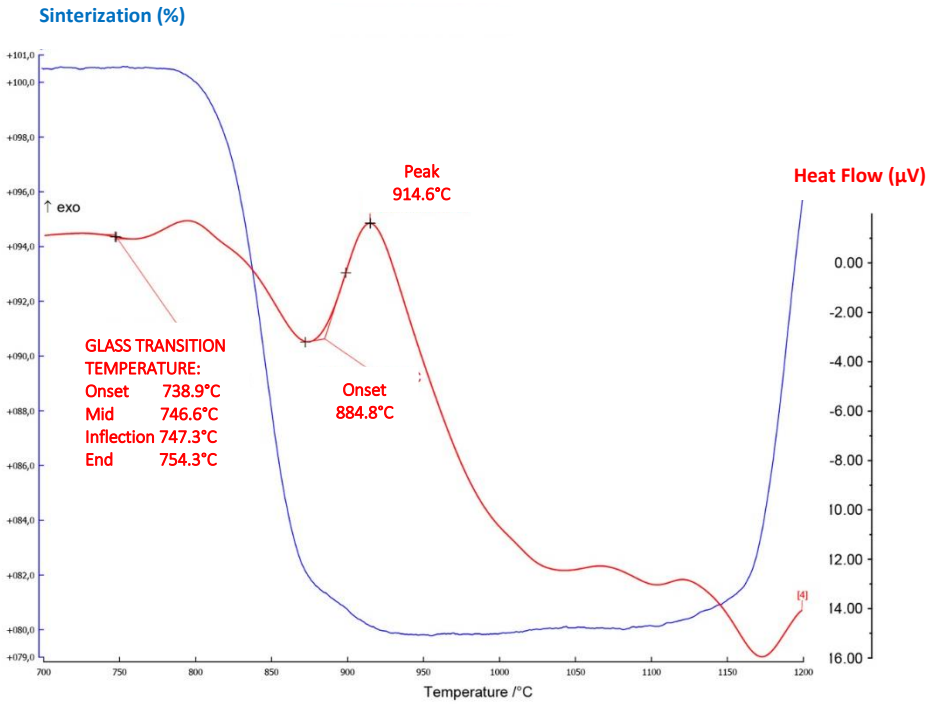

Figure A9 HSM and DTA curves on the temperature scale for CMASZn4.

Annex 2: Crystallization kinetics of CMAS glass series

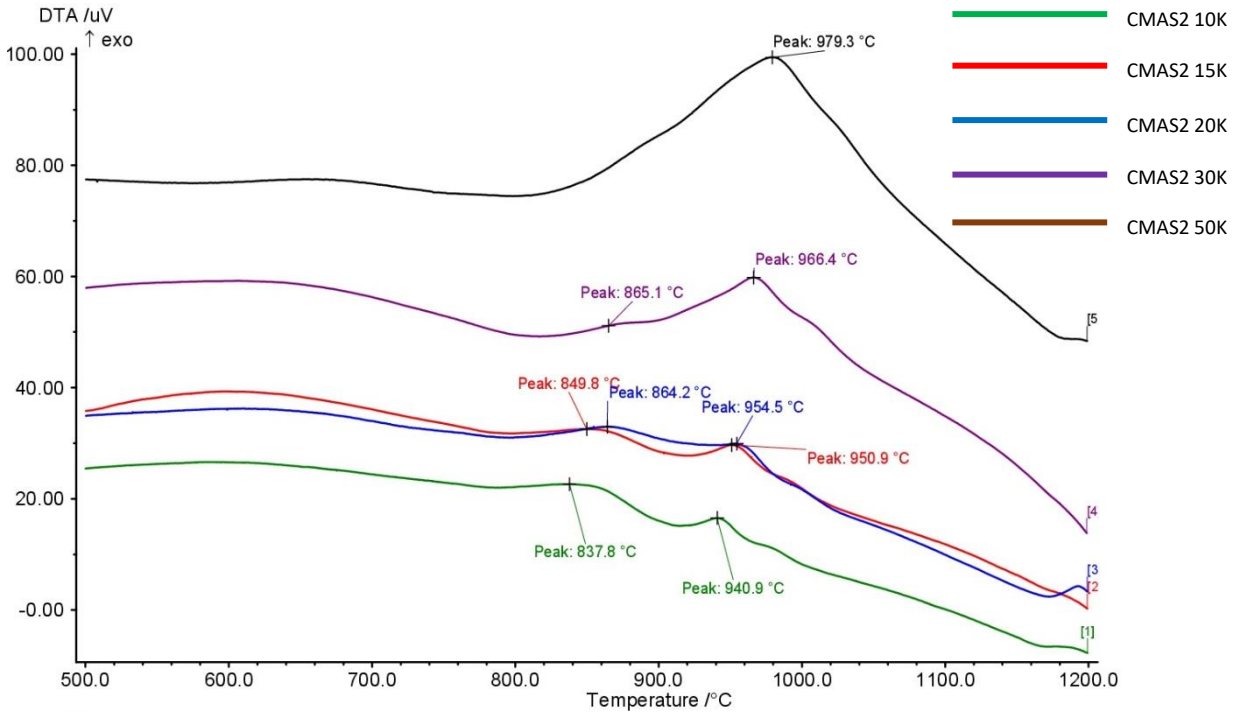

Figure A10 DTA curves of CMAS2 basic glass at different heating rates.

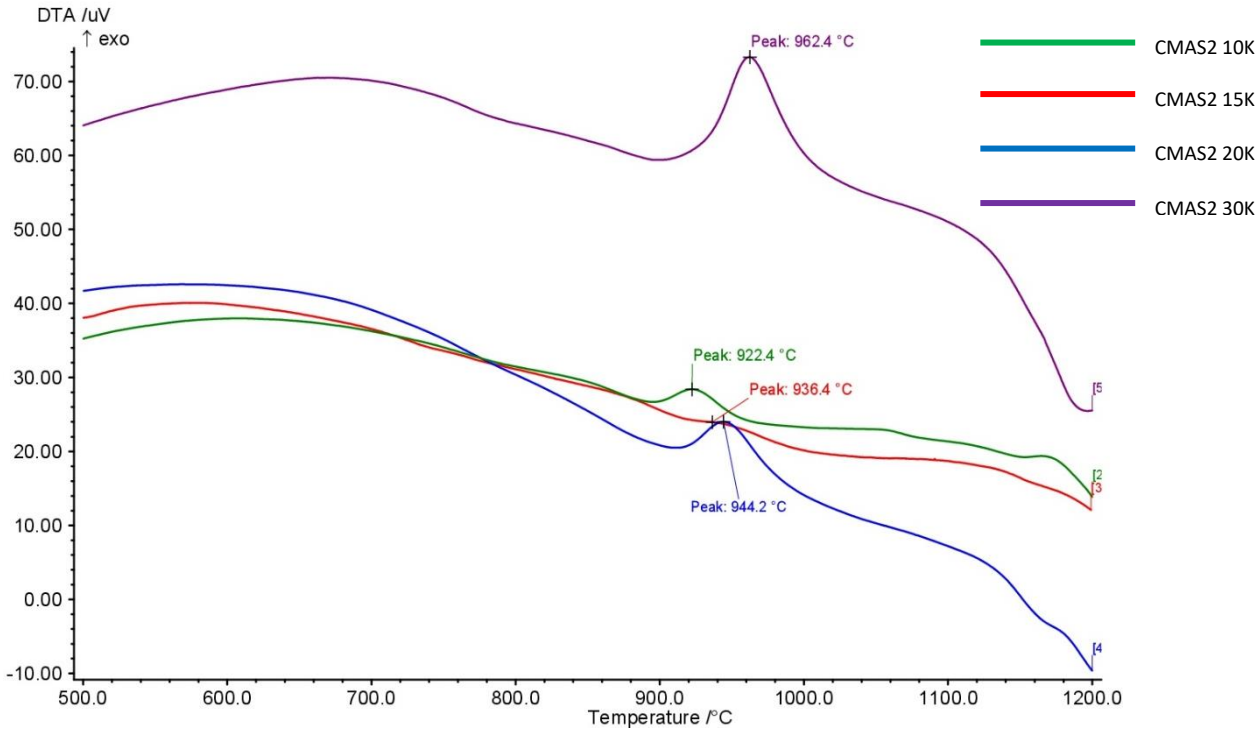

Figure A11 DTA curves of CMASTi2 glass at different heating rates.

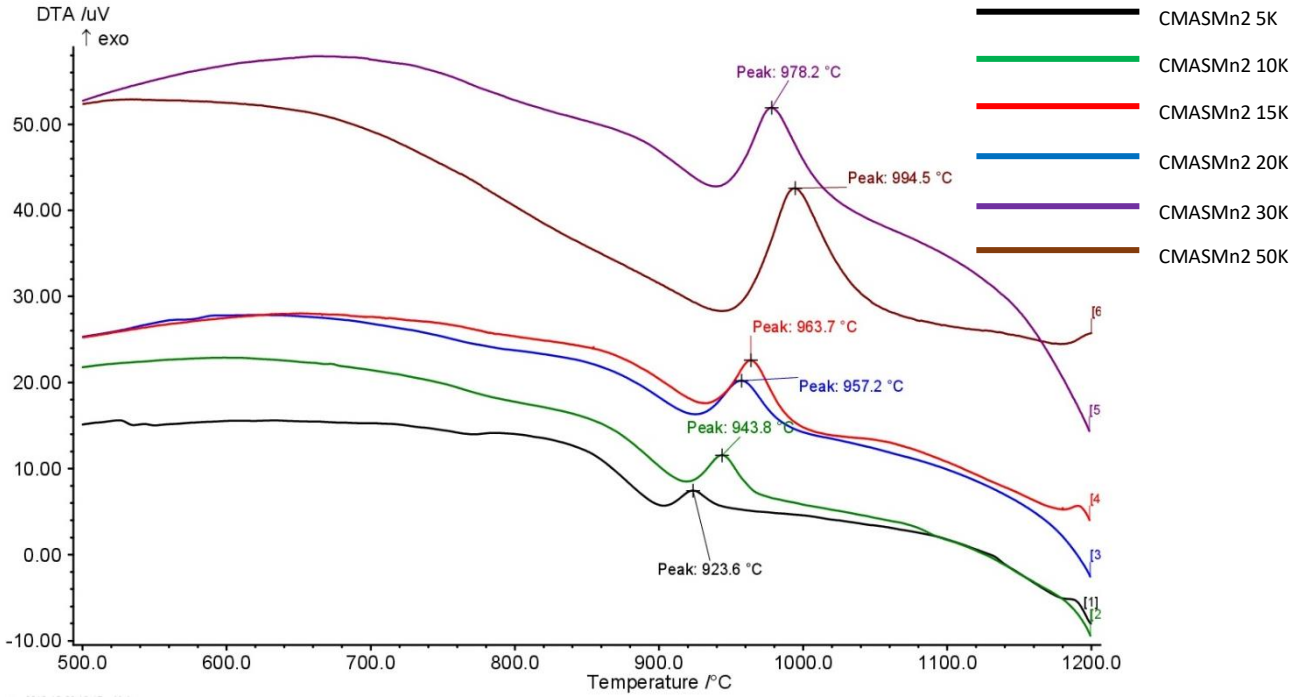

Figure A12 DTA curves of CMASMn2 glass at different heating rates.

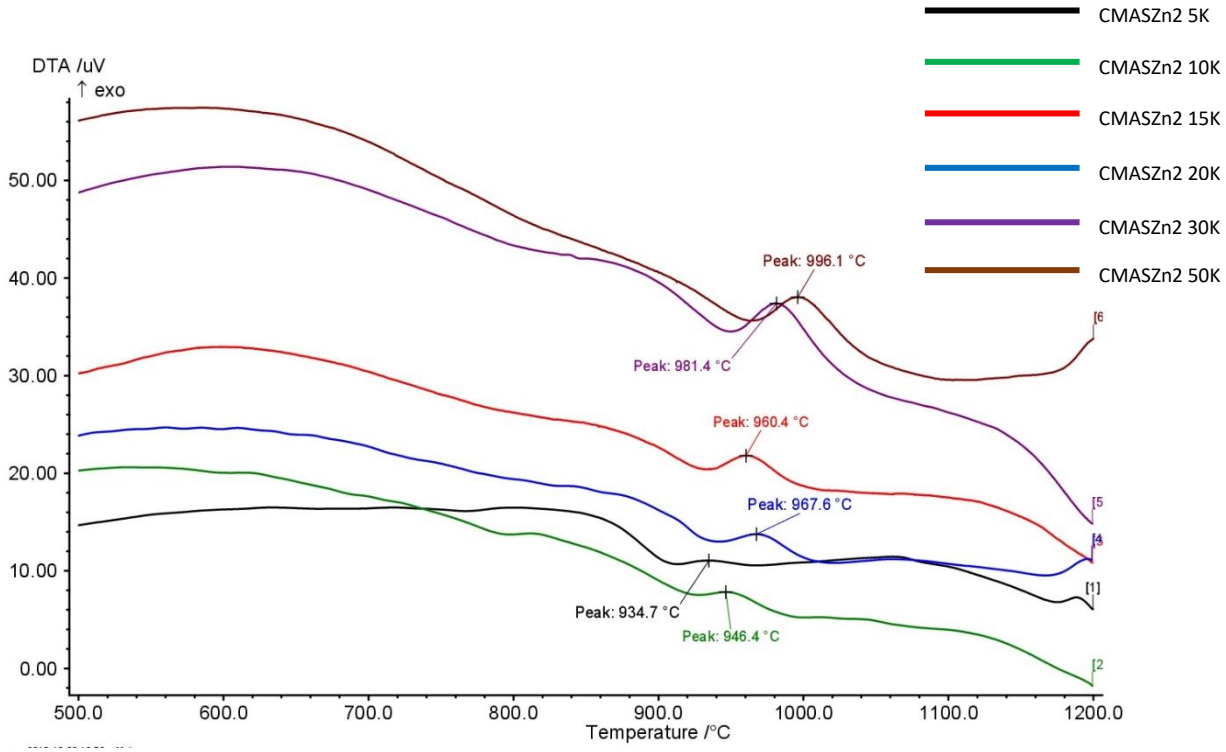

Figure A13 DTA curves of CMASZn2 glass at different heating rates.

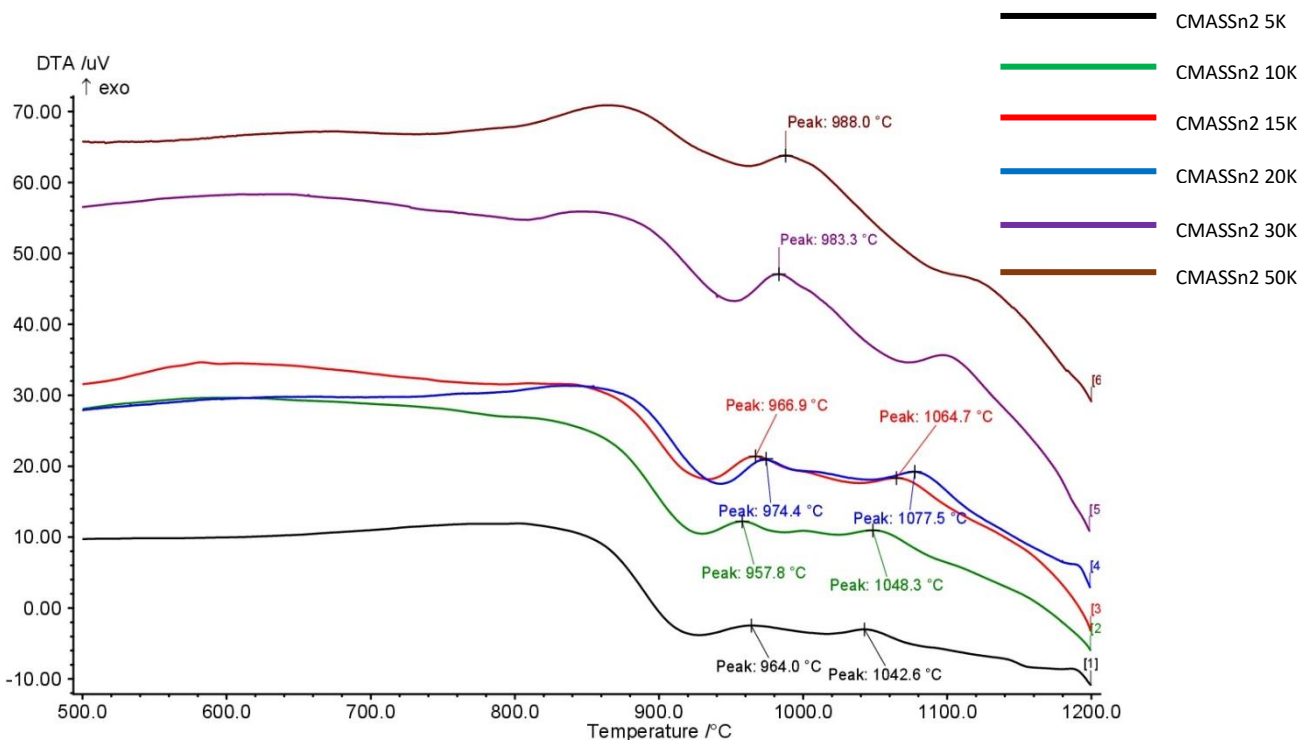

Figure A14 DTA curves of CMASSn2 glass at different heating rates.

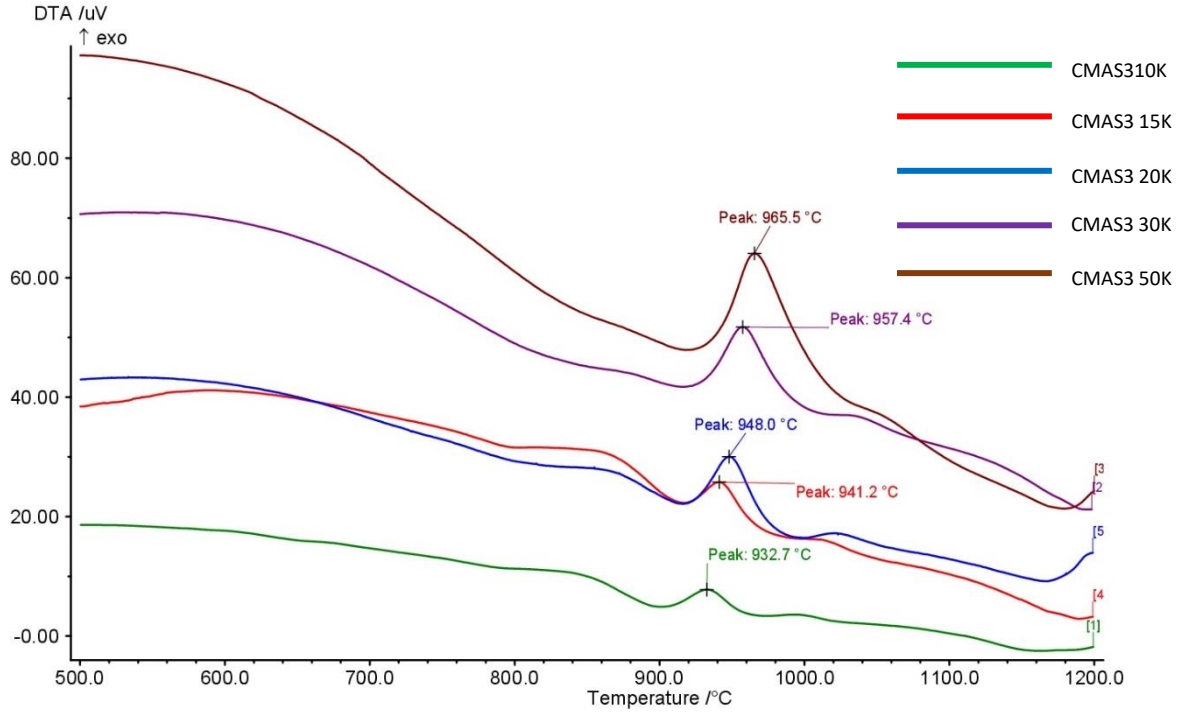

Figure A15 DTA curves of CMAS3 basic glass at different heating rates.

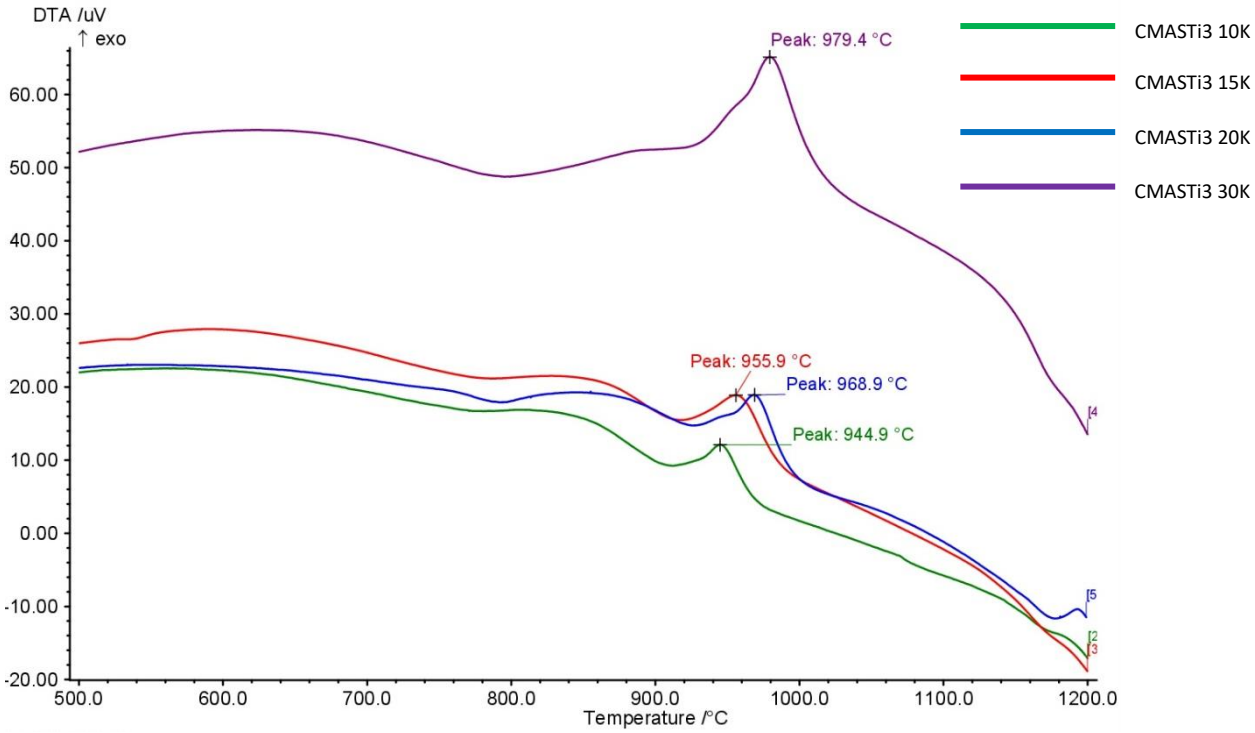

Figure A16 DTA curves of CMASTi3 glass at different heating rates.

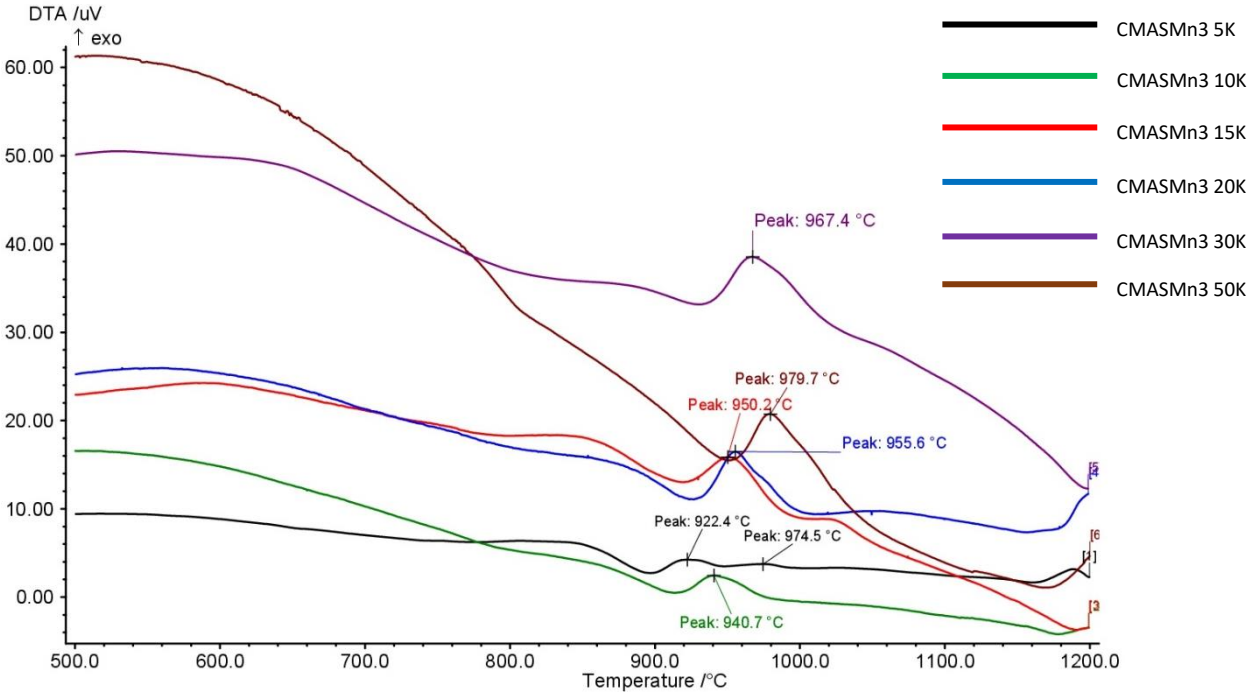

Figure A17 DTA curves of CMASMn3 glass at different heating rates.

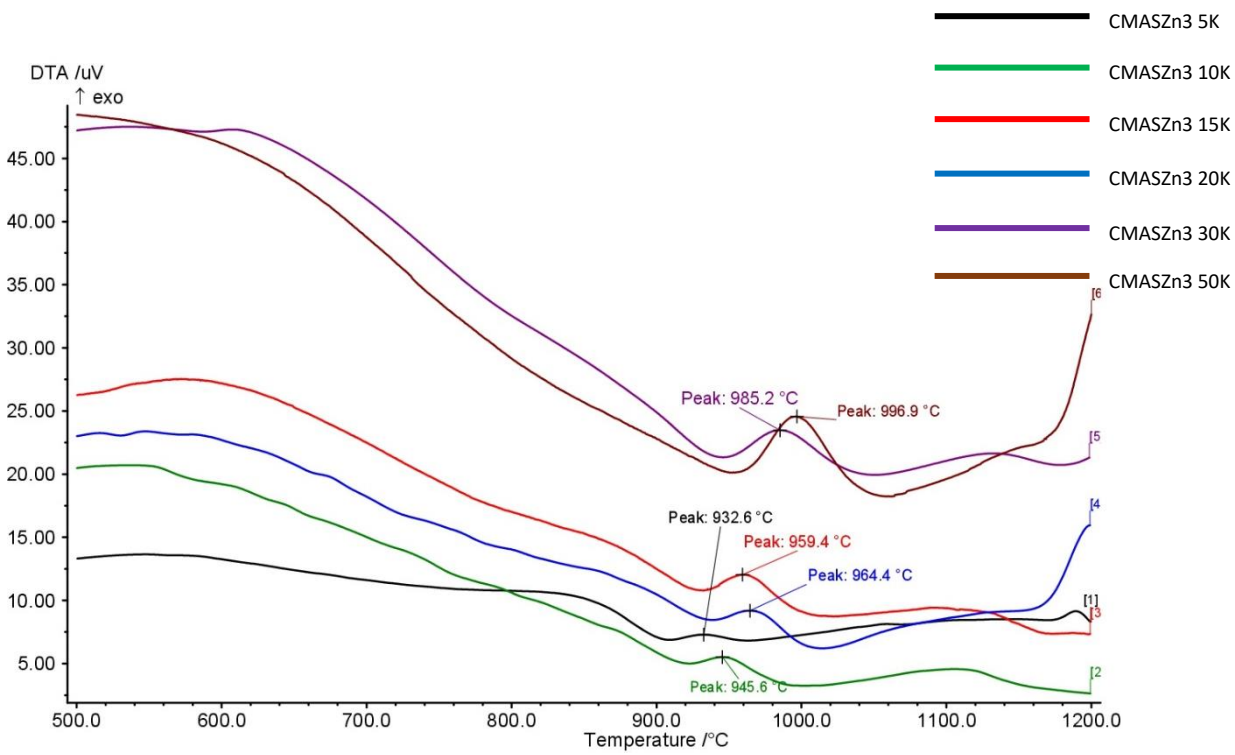

Figure A18 DTA curves of CMASZn3 glass at different heating rates.

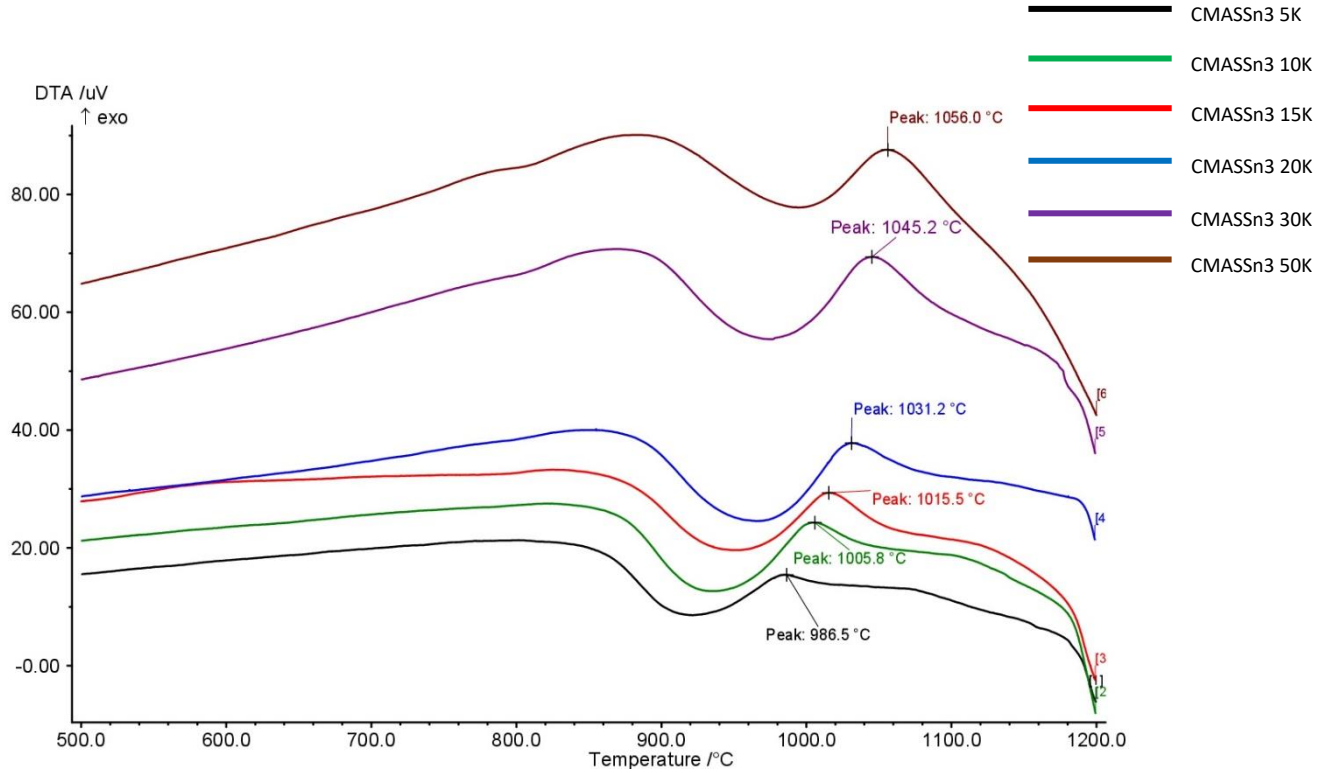

Figure A19 DTA curves of CMASSn3 glass at different heating rates.

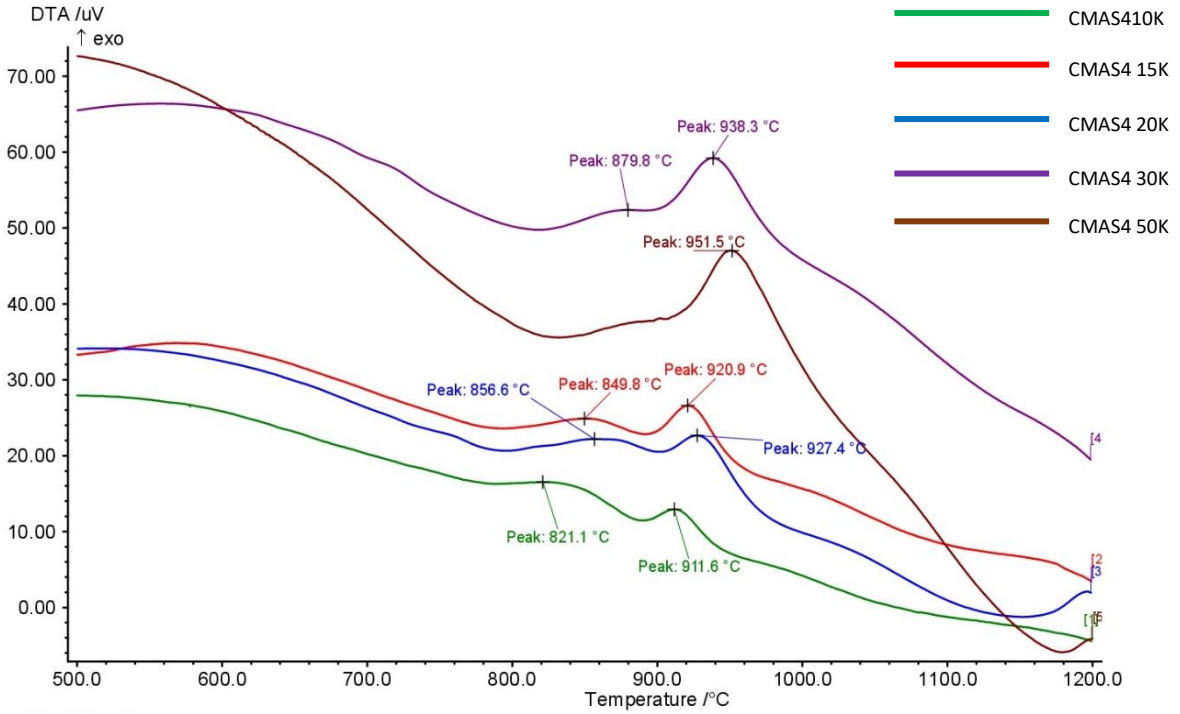

Figure A20 DTA curves of CMAS4 basic glass at different heating rates.

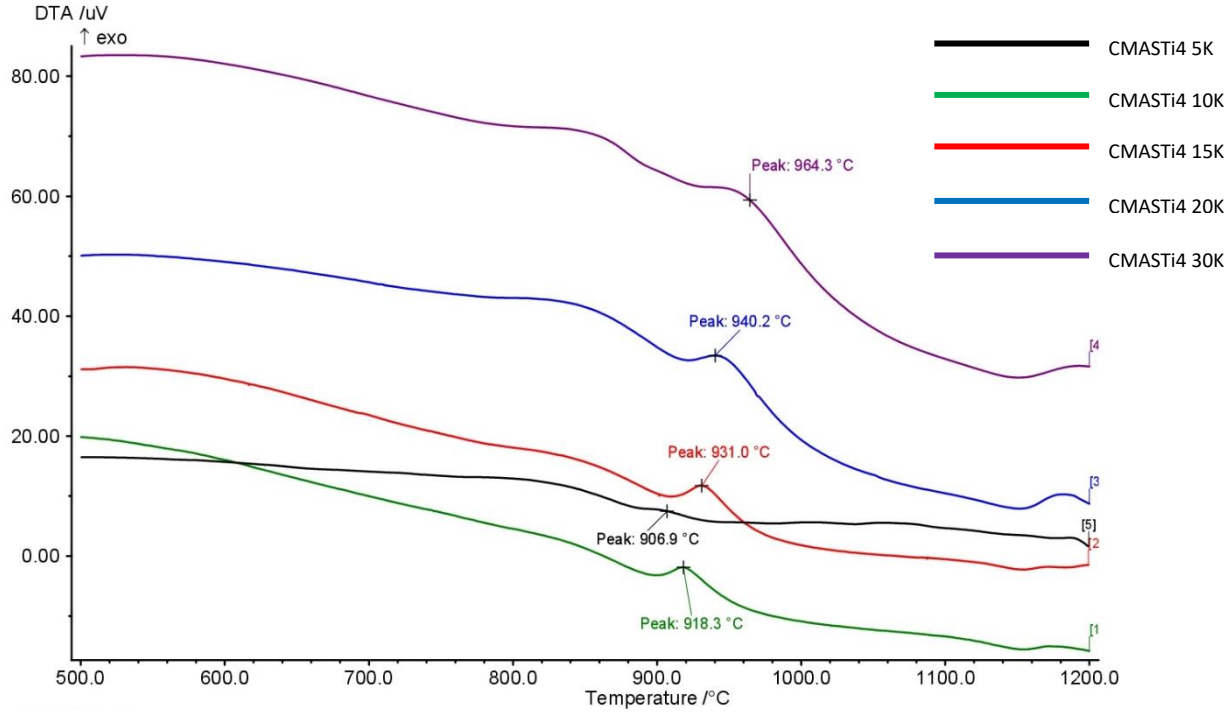

Figure A21 DTA curves of CMASTi4 glass at different heating rates.

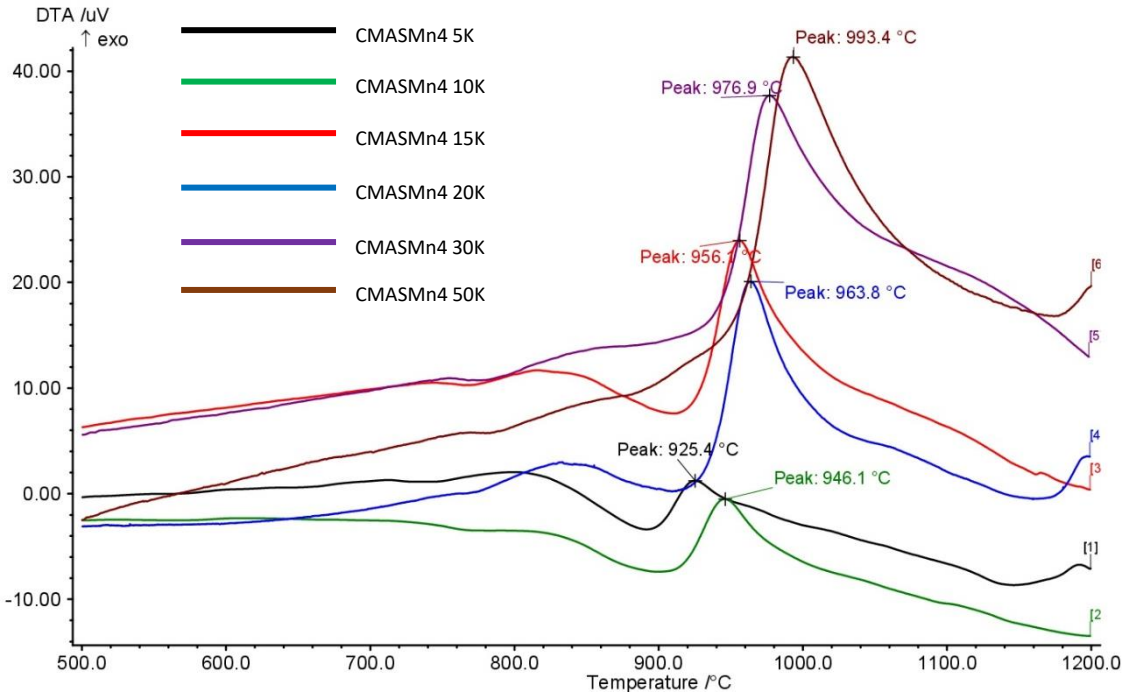

Figure A22 DTA curves of CMASMn4 glass at different heating rates.

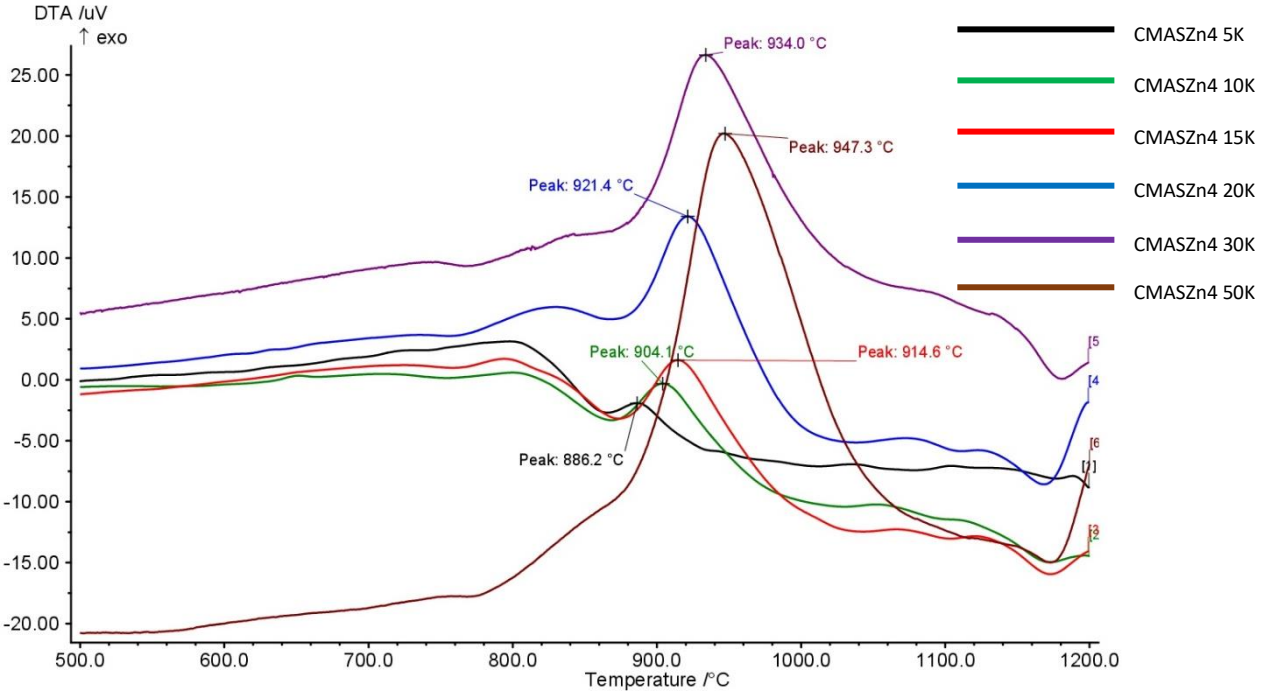

Figure A23 DTA curves of CMASZn4 glass at different heating rates.